

**Enclosure 1, Attachment 2 of
MFN 06-313S08**

ROAMM Review With Responses

SEVERE ACCIDENT MANAGEMENT
in SUPPORT of the ESBWR
DESIGN CERTIFICATION DOCUMENT

By

Theo G. Theofanous and Truc-Nam Dinh

Theofanous & Co. Inc.

September 27, 2005
Revised, July 30, 2006
Final, May 6, 2007
Santa Barbara, California

SEVERE ACCIDENT MANAGEMENT FOR ESBWR

Executive Summary

Abbreviations and Acronyms

A. Overview of ESBWR Design Features to Eliminate Hypothetical Severe Accident Threats to Containment Integrity

B. ROAAM-Based Treatment of Containment Threats; Interfaces to Level 1&2 PRA

1. Containment Performance against Direct Containment Heating (DCH)

- 1.1 Overall considerations
- 1.2 ESBWR Design
- 1.3 Previous Work
- 1.4 Present Assessment
 - 1.4.1 Key Physics in DCH
 - 1.4.2 Probabilistic Framework
 - 1.4.3 Quantification of DCH Loads
 - 1.4.4 Quantification of Fragility to DCH
 - 1.4.5 Prediction of Failure Probability
- 1.5 Summary and Conclusions for DCH
- 1.6 References for DCH

2. Containment Performance against Ex-Vessel Steam Explosions (EVE)

- 2.1 Overall considerations
- 2.2 ESBWR Design
- 2.3 Previous Work
- 2.4 Present Assessment
 - 2.4.1 Key Physics in EVE
 - 2.4.2 Probabilistic Framework
 - 2.4.3 Quantification of Loads for EVE
 - 2.4.4 Quantification of Fragility to EVE
 - 2.4.5 Prediction of Failure Probability
- 2.5 Summary and Conclusions for EVE
- 2.6 References for EVE

3. Containment Performance against Basemat Melt Penetration (BMP)

3.1 Overall considerations

3.2 ESBWR Design

3.3 Previous Work

3.4 Present Assessment

3.4.1 Key Physics in BiMAC Device Operation

3.4.2 Probabilistic Framework

3.4.3 Quantification of Thermal Loads on BiMAC Device

3.4.4 Quantification of BiMAC Device Fragility

3.4.5 Prediction of Failure Probability of BiMAC Device

3.5 Summary and Conclusions on BMP

3.6 References for BMP

4. Conclusions Summarized in the Form of CPETs.

Appendices:

A. Verification of the Transient CLCH Model

B. Validation of the Vent-Clearing Model for CLCH

C. Validation of the Codes PM-ALPHA and ESPROSE-m

D. Validation of Natural Convection Model for Corium Melts

E. Validation of 2-Phase Natural Circulation Model in BiMAC

Addendum[†]:

Independent Review Reports and Author Responses

Appendices 1, 2, and 3 to the Addendum.

[†] To maintain the connection to the reviewer comments any significant changes in the report are made in the form of Addenda that appear at the end of the chapter to which they pertain. Minor corrections are made in the form of notes or footnotes set in brackets [..]. In all cases the page numbers of the original document are maintained.

Executive Summary

With a Core Damage Frequency (CDF) of $\sim 10^{-8}$ per year, no water on the Lower Drywell (LDW) floor at the time of vessel breach in all but $\sim 1\%$ of this CDF, melt release at low RPV pressure in all but $\sim 1\%$ of this rate, and an inerted containment atmosphere, the central concern of Severe Accident Management (SAM) in ESBWR that had to be addressed was in-containment stabilization of melt progression, and coolability of the resulting core debris in a manner convenient to post accident recovery. This concern we addressed by inventing, designing, and incorporating the Basemat- Internal Melt Arrest and Coolability (BiMAC) device. In Chapter 3 we present activation and functional requirements of this device, and show that it would robustly intervene in all risk-significant Severe Accident (SA) sequences to present a melt-containing, impenetrable boundary, thus assuring long-term coolability, and absence of melt-concrete interactions and Basemat Melt Penetration (BMP).

The BiMAC device consists of a liner-like arrangement of a series of steel pipes that cover the LDW floor and side walls to a height of ~ 2 m. Flow inside these pipes is gravity-driven from the GDCS pools and it is established initially by activation of several LDW deluge lines, and by natural circulation once the water level in the LDW has risen to a height of ~ 2 m (~ 3 min). The activation requirement is that deluge line valves meet a 0.999 reliability criterion both in opening up on demand (immediately following vessel breach), and against opening up prematurely (prior to vessel breach). In addition there will be a diverse/passive deluge system. Functional requirements of BiMAC are that local Burnout (due to the thermal load exceeding the Critical Heat Flux, or CHF) as well as global flow conditions that lead to local dry-outs (due to flow instability) are avoided with great margins. While optimization of the design parameters is yet to be performed (along with experiments), we are able to show that the concept is in principle sound, and such margins will be possible to verify at a very high level of confidence. Furthermore, the design includes a 20 cm thick, (sacrificial) refractory layer which we show to effectively protect the BiMAC pipes under all conceivable conditions of melt release from the reactor pressure vessel.

Notwithstanding their marginal (or even minimal) risk significance, in this document we also treat (by analysis) Direct Containment Heating (DCH), due to melt dispersal from RPV failure at high pressure (the Class III, or HP scenarios), and Ex-Vessel Steam Explosions (EVE). For the former we examine energetic DW over-pressurization as well as the thermally stressed UDW liner, and we find that containment failure in both cases is physically unreasonable. For the latter we find, in a conservative treatment, that (a) fuel-coolant interactions in shallow, saturated water pools would be of no structural concern, and (b) the potential pulses from explosions in deep (> 1.5 m), subcooled water pools, receiving melt pours in the typical range of 100's of kg/s, could exceed the structural capacity of both the reactor pedestal wall, as well as that of the BiMAC. These outcomes we assume to constitute containment failure.

This work was performed under the overall philosophy of the Risk Oriented Accident Analysis Methodology (ROAAM), and it has benefited from prior work on SAM carried out for the US NRC (on SA issue resolution for existing plants), and US DOE (on the AP600, and AP 1000).

This report consists of two introductory chapters on ESBWR design and methodology of SAM, and three main chapters addressing DCH, EVE, and BMP (BiMAC) respectively. There is also an addendum with the Reviewer reports and our responses.

Abbreviations and Acronyms

ADS	Automatic Depressurization System
ALWR	Advanced Light Water Reactor
ATWS	Anticipated Transients Without Scram
BiMAC	Basemat Internal Melt Arrest and Coolability (Device)
BMP	Basemat Melt Penetration
BWR	Boiling Water Reactor
CBP	Containment Bypass and Leakage
CCFP	Conditional Containment Failure Probability
CCI	Corium-Concrete Interactions
CDF	Core Damage Frequency
CET	Containment Event Tree
CLCH	Convection-Limited Containment Heating (model for DCH)
COP	Containment Over-Pressurization
COPS	Containment Over-pressure Protection System
CPET	Containment Phenomenological Event Tree
CRD	Control Rod Drive
CRSS	Center for Risk Studies and Safety
CSET	Containment Systems Event Tree
CV	Containment Vessel
DCD	Design Control Document
DCH	Direct Containment Heating
DPV	Depressurization Valve
DW	Drywell
EPRI	Electric Power Research Institute
ESBWR	Economic Simplified Boiling Water Reactor
EVE	Ex-Vessel Steam Explosion
FCI	Fuel-Coolant Interaction
GDCS	Gravity-Driven Cooling System
GE	General Electric (Company)
GE-NE	GE Nuclear Energy
H ₂ C	Hydrogen Combustion
HP	High Pressure (core-melt Scenario)
HPME	High Pressure Melt Ejection
I&C	Instrumentation and Control
IC	Isolation Condenser
ICS	Isolation Condenser System
IGT	Instrumentation Guide Tube
IVR	In-Vessel Retention (severe accident management scheme)
LDW	Lower Drywell
LOCA	Loss-of-Coolant-Accident
LP	Low Pressure (core-melt Scenario)
MAAP	Modular Accident Analysis Program
MCCI	Molten Corium-Concrete Interactions

MSIV	Main Steam Isolation Valve
MSL	Main Steam-Line
NRC	Nuclear Regulatory Commission
O&M	Operation and Maintenance
PCC	Passive Containment Cooling
PCCS	Passive Containment Cooling System
PRA	Probabilistic Risk Assessment
PSA	Probabilistic Safety Assessment
PWR	Pressurized Water Reactor
ROAAM	Risk-Oriented Accident Analysis Methodology
RCCV	Reinforced Concrete Containment Vessel
RPV	Reactor Pressure Vessel
SA	Severe Accident
SAM	Severe Accident Management
SAMS	Severe Accident Management Strategy
SAT	Severe Accident Treatment
SBWR	Simplified Boiling Water Reactor
SP	Suppression Pool
SRV	Safety Relief Valve
TDH	Torispherical Drywell Head
UCCS	Upper Cylindrical Containment Section
UCSB	University of California, Santa Barbara (CRSS)
UDW	Upper Drywell
URD	Utility Requirement Documents
VB	Vacuum Breaker

A. Overview of ESBWR Design Features to Eliminate Hypothetical Severe Accident Threats to Containment Integrity

The results of Level 1 PRA (GE-NE, 2005a) show that core damage events (Severe Accidents) in ESBWR are *remote and speculative* (CDF~ 10^{-8}). Still efforts have been made, and design features and procedures have been included that provide an additional (diverse and redundant) layer of defense against all threats to containment integrity that such hypothetical events may conceivably entail.

Given a severe accident, threats to containment integrity may be enumerated as follows:

- (a) *Prompt, Energetic Loading*: explosive fuel-coolant interactions, high-pressure melt ejection leading to direct containment heating (and pressurization),
- (b) *Late, Gradual Loading*: melt ablation and penetration of the containment basemat, pressurization of containment atmosphere by steam and/or non-condensable gases, and
- (c) *Isolation Failure*: errors or malfunctions that leave existing flow paths open to the outside, activation of the containment overpressure protection system.

In this report we will deal with the phenomenological (physics) components of these threats; namely, Ex-vessel Steam Explosions (EVE), Direct Containment Heating (DCH), and Basemat Melt Penetration (BMP). Our treatment of the BMP will also provide the principal phenomenological input needed to assess Containment Over-pressurization, which, being a systems-driven event, is treated in the Level 2 PRA (GE-NE, 2005a). This is the case for Isolation Failure as well.

From a top level perspective a principal strategic decision we had to make for Severe Accident Management (SAM) in the ESBWR was in regards to arresting the melt propagation process and ensuring long term coolability within the containment boundary. As one potential option we examined the applicability and effectiveness of In-Vessel Retention (IVR)—an internationally pursued severe accident management approach, already developed and utilized for the passive PWR designs in the USA (Theofanous et al, 1996). We concluded that this could be a highly effective approach for the ESBWR as well, however, only if all equipment found hanging from the lower head penetrations were to be supported from the outside so as to maintain the melt-containing capacity of the lower head. This proved unworkable from the operational perspective, and the option was rejected by the design managers. On the other hand, we determined that the coolability question could be addressed ex-vessel and with a high degree of certainty.

Thus ex-vessel behavior is the principal focus of our treatment in this report. More specifically, we are to address manifestations of the above noted threats to containment integrity in a manner that is inclusive of all possible ex-vessel evolutions. Our approach is comprehensive and founded on the basic physics that underlie these evolutions.

As in the most recent ABWR design, the ESBWR features: an inert containment atmosphere to prevent deflagration or detonation of combustible mixtures; a Containment Over-pressurization Protection System (COPS) (but here it is manually operated—MCOPS) to guard against slow buildup of pressure due to non-condensable gas generation and/or heat-up of the suppression pool water; and a drywell spray system in support of accident recovery operations. Unlike the ABWR, or any other previous GE BWR, the ESBWR containment design includes the Passive Containment Cooling System (PCCS), to remove decay heat from the containment, and the (also passive) Basemat-Internal Melt Arrest and Coolability (BiMAC) device (invented in the course of this work— Theofanous and Dinh, 2005), to essentially eliminate the possibility of extended corium-melt interactions, non-condensable gas generation, and base-mat penetration. In addition the ESBWR is equipped with the Isolation Condensers (IC's), a system for ensuring decay heat removal from the RPV in sequences where the reactor is at high pressure. This is an improved version of system employed in some of the earlier BWR designs.

An overall illustration that summarizes all these systems in the framework of the ESBWR containment can be found in Figure A.1. Detailed descriptions, and performance assessments under severe accident conditions are provided in Chapters 1 through 3. Containment Phenomena Event Trees (CPET's) provide for all necessary links to the relevant/consistent sets of Plant Damage States (PDS's) through the Level 1 PRA (GE-NE, 2005a), and to Containment Systems Event Trees (CSET's) and potential release categories as employed in Levels 2 and 3 PRA (GE-NE, 2005a). The overall assessment methodology is summarized in the next Chapter.

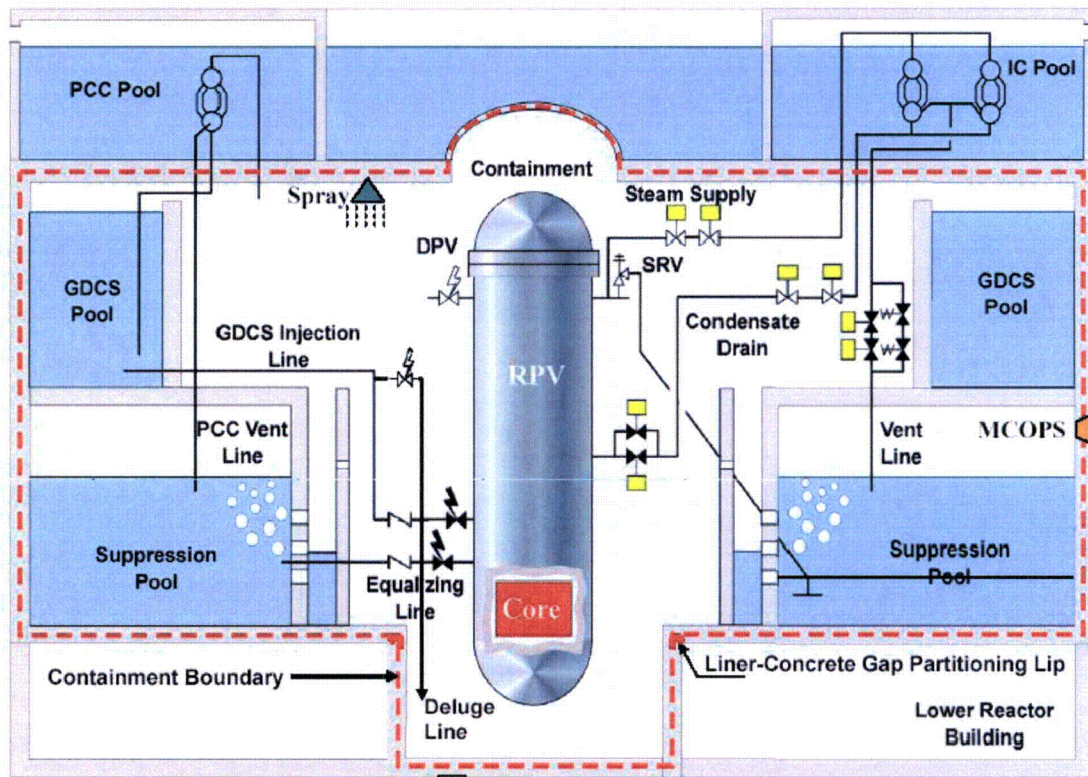
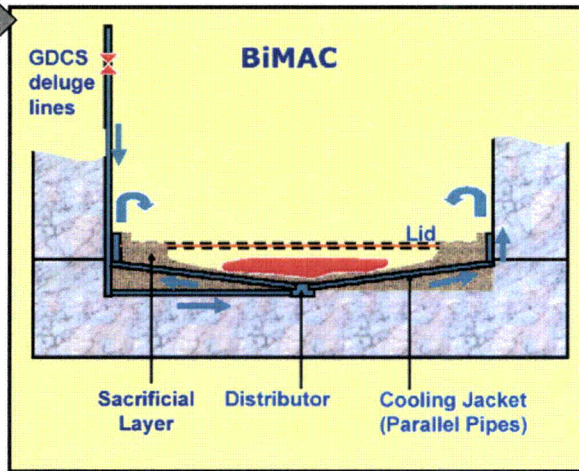


Figure A.1. Illustration of the ESBWR design features aimed for ensuring containment integrity under severe accident conditions. From top down: (i) PCCS pool and heat exchangers, operated on DW-to-WW pressure difference provide passive containment cooling,; (ii) IC pool and heat exchangers provide decay heat removal from RPV; (iii) GDCS (three pools, four divisions) with ADS (DPV, SRV) make up the ECCS; LDW deluge lines feeding off the GDCS supply the BiMAC for long-term coolability; (iv) Manual COPS (MCOPS) provides venting from wetwell, through 2" and 12" vents, in a controlled manner; (v) Basemat-Internal Melt Arrest and Coolability (BiMAC) device (shown in the bottom insert). It is initially fed by water flow from squib-valve-operated (along with some other type of valve for diversity—not shown in the figure) LDW deluge lines, while in the long term it is supplied by natural circulation, through downcomers (at the edges of LDW, not shown in the insert).



References to Chapter A

GE-NE (2005a), ESBWR Certification Probabilistic Safety Assessment. NEDC-33201P. August 2005.

GE-NE (2005b), ESBWR Design Control Document. 26A6642BZ Rev.00. August 2005.

Theofanous, T.G., Liu, C., Additon, S., Angelini, S., Kymalainen O., and Salmassi, T. (1996), "In-Vessel Coolability and Retention of a Core Melt," DOE/ID-10460, Vols. 1 and 2, October 1996. Also in

Theofanous, T.G., Liu, C., Additon, S., Angelini, S., Kymalainen O., and Salmassi, T. "In-Vessel Coolability and Retention of a Core Melt," *Nuclear Engineering & Design*, 169 (1997) 1–48.

Theofanous T.G., and Syri, S., "The Coolability Limits of a Reactor Pressure Vessel Lower Head," *Nuclear Engineering & Design* 169 (1997) 59–76.

Theofanous, T.G. and Dinh, T.N., "Basemat-Internal Melt Arrest and Coolability (BiMAC) device". Patent Application. Tcl/GE Document. GE Nuclear Energy. San Jose, March 30, 2005.

B. ROAAM-Based Treatment of Containment Threats; Interfaces to Levels 1&2 PRA

The Risk Oriented Accident Analysis Methodology (ROAAM) was developed for the purpose of resolving “issues” that proved hard to address in a purely probabilistic (PRA) framework (Theofanous, 1996). This purpose was met mainly due to a methodological emphasis on deterministic principles (key physics) along with an overall conservative mentality of treatment. Accordingly, principal ingredients of ROAAM include: (a) identification, separate treatment, and maintenance of this separation (to the end results), of Aleatory and Epistemic uncertainties; (b) identification and bounding/conservative treatment of Intangibles and Splinters; that is of epistemic uncertainties (in parameters and scenarios respectively) that are beyond the reach of any reasonably verifiable quantification; and (c) the use of external experts in a review, rather than in a primary quantification capacity (Theofanous, 2003).

Under the auspices of the US NRC, so-resolved issues include: “Mark-I Liner Attack” (Theofanous et al, 1991), “Direct Containment Heating for PWR’s” (Pilch, Yan and Theofanous, 1994), and, in a preliminary rendition, “Alpha Mode Failure for PWR’s” (Theofanous et al, 1987). Under support from the US DOE’s ARSAP program, the innovative In-Vessel Retention (IVR) technology for Westinghouse’s AP600 and AP1000 designs was developed and assessed (Theofanous et al 1996; Theofanous et al., 1998; Scobel, Theofanous and Sorrell, 1998), as was an early version of severe accident treatment for GE’s SBWR (Theofanous, 1993). The present treatment for ESBWR is based on the same philosophy of approach, same overall methodology, and it is leveraged on ideas, data, and tools developed during all this past work.

The principal consideration in addressing ex-vessel behavior is whether the lower head fails with the RPV being at high or low pressure (HP vs. LP). The demarcation is defined by the capacity of the resulting (superheated steam) blowdown to disperse previously ejected debris into the upper drywell (UDW), and conservatively we will take this here to be at 1 MPa (see Chapter 1). Thus, as a simplified overview, we have the frame in which two potential containment threatening events will manifest themselves: direct containment heating (DCH) for HP scenarios, and ex-vessel explosions (EVE) for LP sequences. Since both cases lead to large quantities of core debris relocated on the LDW floor, corium-concrete interactions, non-condensable gas generation, and base-mat melt penetration (BMP); that is, long term coolability is an all-pervasive issue.

A quantitative perspective on these matters, as derived from the Level I PRA, is shown in Figure B.1. The intent is to illustrate how the CDF is attributed to various kinds of SA sequences, along with the kind of containment integrity considerations appropriate to each case. First we note that, by far, the main contributors to CDF are the Class I (LP) accidents. Class II represents accidents in which core damage could occur in the very long term (>72 hours), and are recoverable by manual actions. These accidents are treated

in Level-2/3 PRA. In Class IV we have ATWS scenarios, 71% of which are recoverable at a point of core damage that is small enough to be stabilizable inside the RPV, 27% revert to LP with low water level in the LDW, 1% to HP with spray available, and another 1% lead to Containment Bypass (Class V) scenarios. The latter along with the Class-V-initiated scenarios (< 1%), and the 71% of ATWS, lead to systems-dependent source terms, and as such they are addressed in the Level-2/3 PRA.

Now turning to the related containment threats, we see that DCH is only relevant to Class III accidents, while EVE pertains only to Class I. Of the HP sequences, 78% have no sprays available. This (~1% of the CDF) will constitute the limiting condition for potential violation of UDW liner leak tightness under DCH (thermal loads). Of the LP sequences only ~1% have sufficient water in the LDW to be of concern for EVE. This (~1% of the CDF) will constitute the limiting condition for pedestal, and BiMAC failure under steam explosion loads. Finally, and as illustrated in the figure, the BMP is an all-encompassing issue; accordingly it is central to our severe accident management strategy (Theofanous and Dinh, 2005).

We will show that under conditions consistent with In-Vessel accident evolutions and Level 1 results, the margins to containment failure by all three mechanisms are very comfortable. In particular, we can expect no corium-concrete interactions, and thus we have no risk-significant concerns for long-term pressurization of the containment atmosphere due to non-condensable gas generation. With the PCCS working, similarly, there are no risk-significant concerns for containment over-pressurization and development of leakage flow paths.

On the other hand containment isolation failure must be addressed, and in addition as noted above, we must address the impact of PCCS and the IC systems failure (to remove decay heat) on containment integrity. These are systems-effects driven (i.e. they depend on the long term availability of water to replenish that lost to vaporization) and as such they are treated in the Level 2 PRA.

An overall framing of issues considered here in terms of Containment Phenomena Event Trees (CPET's) is given in Figures B.2 and B.3. Quantification of these trees, on the basis of results found in Chapters 1-3, is summarized in Chapter 4, which then feeds to the Level 2 PRA (GE-NE, 2005a).

The following remarks on these trees provide some pertinent clarifications.

1. As noted already ex-vessel explosions in the ESBWR are only relevant to LP scenarios. The potential severity of the EVE's is parameterized by the depth of the water pool in the LDW, and the probability split among the three classes of events shown in the CPET is obtained from Level 1 results. In the low water case the questions of pedestal, and BiMAC, damage do not arise. For melt release into deep water pools the uncertainties are too great for a ROAAM quantification, thus both are assumed to fail (see Chapters 2 and 4).

2. Natural depressurization can occur due to thermal loading of the MSL/SRV lines, in which case we transfer to the LP tree as indicated. As discussed in Chapter 1 uncertainties do not allow for a reliable quantification, thus this node of the tree is taken to be a splinter.
3. Except for the energetic containment failure events by EVE, or DCH, all other outcomes transfer to the CSET's of the Level 2 PRA addressing long-term containment over-pressurization by loss of decay heat removal.
4. Debris coolability is addressed in both the LP and HP trees. Success criteria is decomposed into BiMAC supply, a systems question, and BiMAC function, a physics question. Due to the outstanding importance of ensuring LDW flooding soon after the melt exits the RPV, the systems question is addressed in two diverse ways: (a) an active system whose overall unreliability is set to less than 10^{-3} and (b) a passive deluge system operated by means of releasing bottled-nitrogen pressure by a melt-induced mechanism that responds to a high LDW temperature environment.

In each case, in addressing a failure, the ROAAM treatment consists of five basic steps:

- A. Identification of the Key Physics.** This includes the definition of all principal mechanisms, their potential interactions, and order of magnitude estimations that we use in defining an optimal approach for quantifying how loads (thermal and/or mechanical) compare to fragilities (failure behaviors).
- B. Definition of a Probabilistic Framework.** This is to define the model(s) for the overall mechanics of quantifying loads, fragilities, and probabilities of failure. In particular this shows the types of uncertainties involved and the manner in which these uncertainties are bounded in the quantification.
- C. Quantification of Loads.** This goes into the technical details of quantifying loads with the intent of enveloping uncertainties. Also covered are the bases for the models used, and evidence of their verification/validation status.
- D. Quantification of Fragilities.** This addresses failure criteria, and in particular the intent is to provide a solid quantification of failure incipience (conservatively), and at the other end, of gross failure.
- E. Quantification of Failure Probabilities.** Here we transpose loads against fragilities and we evaluate potential for failure.

Finally, according to established ROAAM procedures, GE contracted 2 SA experts to conduct an independent review of the work reported herein. In addition, and according to own procedures, GE received 4 internal "verification" reports. These reports and the author's responses are reproduced in the Addendum.

V, 71% of IV, and RR
Treated in L-3 PRA
RR Residual Risk

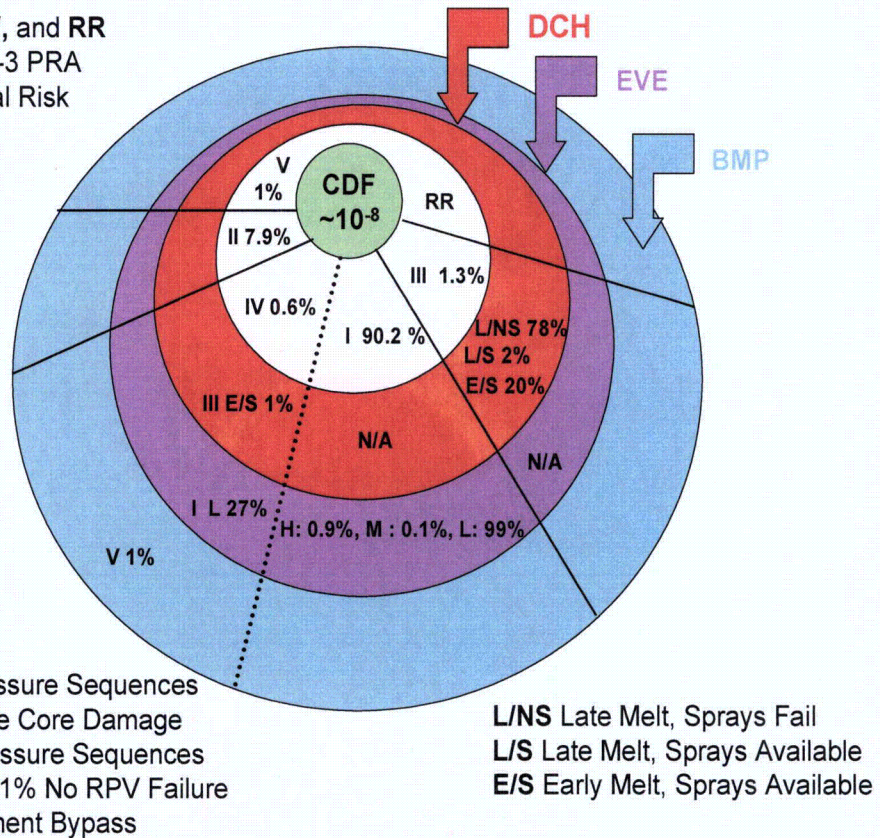


Figure B.1. The complexion of severe accidents in ESBWR.

Class II can be ignored—these sequences do not fail the core until after 72 hours and are recoverable with manual actions. L, M and H denote low, medium and high water levels in Lower Drywell, as they are of importance for EVE treatment. See also Figures B.2 and B.3. The EVE is not applicable to Class III because the LDW has only a small amount of condensate in all such sequences. The DCH is not applicable to Class I. The BMP is of concern to all severe accident sequences.

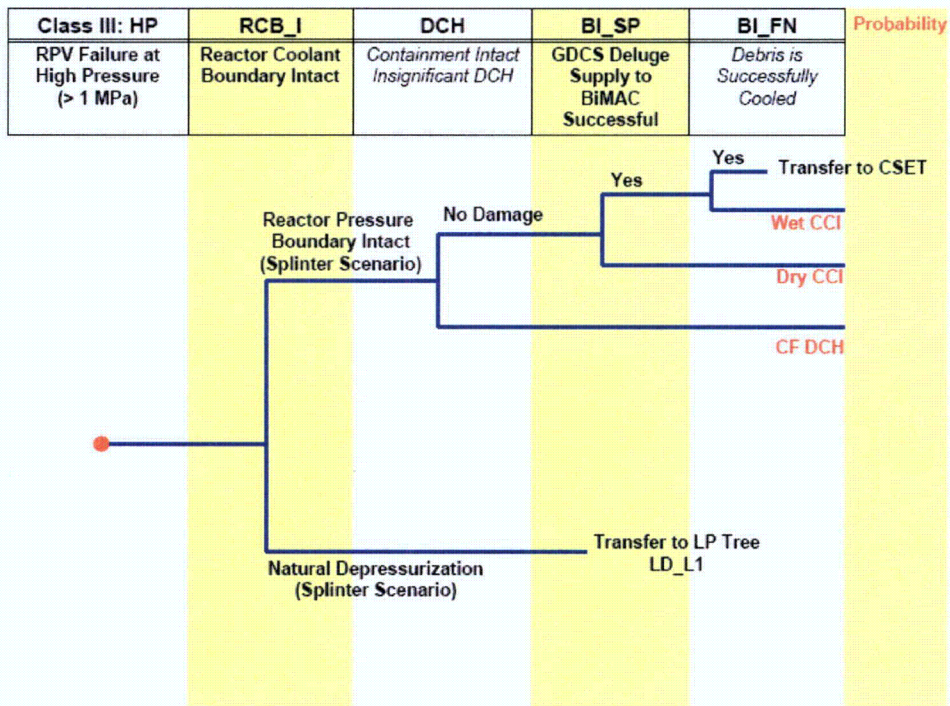


Figure B.2. CPET 1. Key events in ex-vessel evolution of high-pressure sequences.

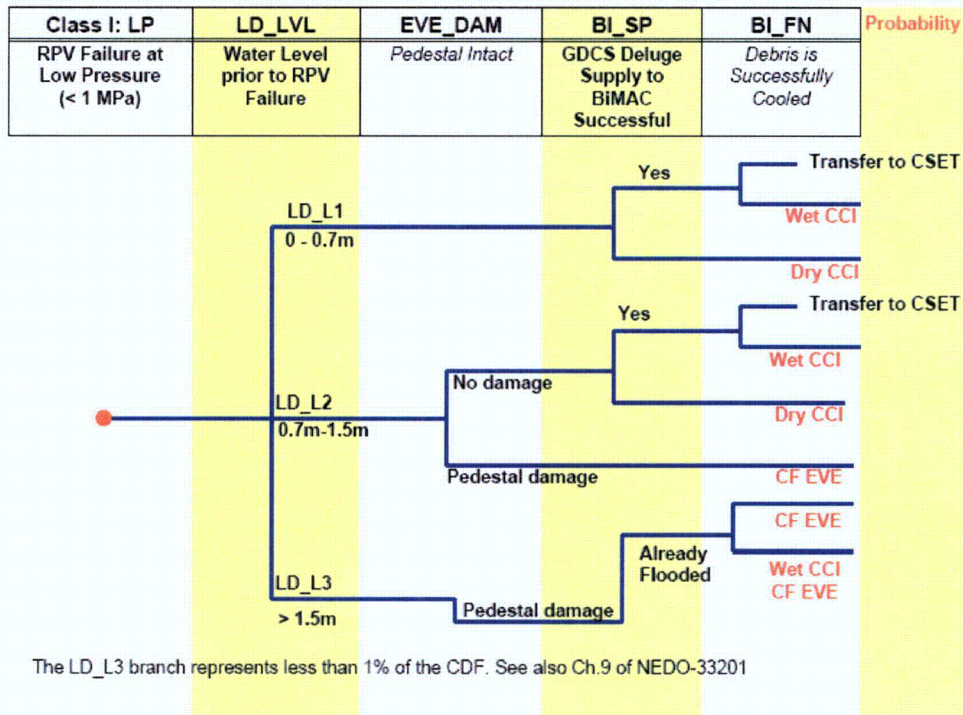


Figure B.3. CPET 2. Key events in ex-vessel evolution of low-pressure sequences.

References to Chapter B

GE-NE (2005a), ESBWR Certification Probabilistic Safety Assessment. NEDC-33201P. August 2005.

GE-NE (2005b), ESBWR Design Control Document. 26A6642BZ Rev.00. August 2005.

Pilch, M.M., Yan, H. and Theofanous, T.G. (1994), "The Probability of Containment Failure by Direct Containment Heating in Zion," NUREG/CR-6075, SAND93-1535, December 1994. Also in

Pilch, M.M., Yan, H. and Theofanous, T.G. , "The Probability of Containment Failure by Direct Containment Heating in Zion," *Nuclear Engineering & Design*, 164 (1996) 1–36.

Scobel, J.H., Theofanous, T.G., and Sorrell, S.W. (1998), "Application of the Risk Oriented Accident Analysis Methodology (ROAAM) to Severe Accident Management in the AP600 Advanced Light Water Reactor," *Reliability Engineering and Safety Systems*, 62 (1998) 51-58.

Theofanous, T.G., Amarasooriya, W.H., Najafi, B., Abolfadl, M.A., Lucas, G.E. and Rumble, E. (1989) "An Assessment of Steam-Explosion-Induced Containment Failure," NUREG/CR-5030, February 1989. Also in:

Theofanous, T.G., Najafi, B., and Rumble, E. (1987), "An Assessment of Steam-Explosion-Induced Containment Failure. Part I: Probabilistic Aspects," *Nuclear Science and Engineering*, 97, 259-281 (1987). M.A. Abolfadl and T.G. Theofanous, "An Assessment of Steam-Explosion-Induced Containment Failure. Part II: Premixing Limits," *Nuclear Science and Engineering*, 97, 282-295 (1987). W. H. Amarasooriya and T.G. Theofanous, "An Assessment of Steam-Explosion-Induced Containment Failure. Part III: Expansion and Energy Partition," *Nuclear Science and Engineering*, 97, 296-315 (1987). G.E. Lucas, W.H. Amarasooriya and T.G. Theofanous, "An Assessment of Steam-Explosion-Induced Containment Failure. Part IV: Impact Mechanics, Dissipation and Vessel Head Failure," *Nuclear Science and Engineering*, 97, 316-326 (1987).

Theofanous, T.G., Amarasooriya, W.H., Yan, H., and Ratnam, U. (1991), "The Probability of Liner Failure in a Mark-I Containment," NUREG/CR-5423, August 1991. Also in:

Theofanous, T.G., Yan, H. and Eltawila, F. (1993), "The Probability of Liner Failure in a Mark-I Containment, Part I: Probabilistic Framework and Results," *Nuclear Technology* 101 No. 3, 299-331, 1993. T.G. Theofanous and H. Yan, "The Probability of Liner Failure in a Mark-I Containment, Part II: Melt Release

and Spreading Phenomena,” *Nuclear Technology* 101 No. 3, 332-353, 1993. 49.
W.H. Amarasooriya, H. Yan, U. Ratnam and T.G. Theofanous, “The Probability of Liner Failure in a Mark-I Containment, Part III: Corium-Concrete Interactions and Liner Attack Phenomena,” *Nuclear Technology* 101 No. 3, 354-384, 1993.

Theofanous, T.G., Yan, H./UCSB; M.Z. Podowski, C.S. Cho/RPI; D.A. Powers, T.J. Heames/SNL; J.J. Sienicki, C.C. Chu, B.W. Spencer/ANL; J.C. Castro, Y.R. Rashid, R.A. Dameron, J.S. Maxwell, D.A. Powers/ANATECH (1993), “The Probability of Mark-I Containment Failure by Melt-Attack of the Liner,” NUREG/CR-6025, November 1993

Theofanous, T.G. (1993) “Ex-Vessel Coolability for the SBWR”, Report to DOE/ARSAP (ANL). August 5, 1993.

Theofanous, T.G. (1996), “On the Proper Formulation of Safety Goals and Assessment of Safety Margins for Rare and High-Consequence Hazards,” *Reliability Engineering & Systems Safety*, 54 (1996) 243–257.

Theofanous, T.G. (2003), “Risk Assessment and Management,” Ch.19 in Vol.1 in “*Comprehensive Structural Integrity*”, 10-Volume Handbook, Eds. I. Milne, R.O. Ritchie, B. Karihaloo, Elsevier.

Theofanous, T.G., Liu, C., Additon, S., Angelini, S., Kymalainen O., and Salmassi, T. (1996), “In-Vessel Coolability and Retention of a Core Melt,” DOE/ID-10460, Vols. 1 and 2, October 1996. Also in:

Theofanous, T.G., Liu, C., Additon, S., Angelini, S., Kymalainen O., and Salmassi, T. “In-Vessel Coolability and Retention of a Core Melt,” *Nuclear Engineering & Design*, 169 (1997) 1–48.

Theofanous T.G., and Syri, S., “The Coolability Limits of a Reactor Pressure Vessel Lower Head,” *Nuclear Engineering & Design* 169 (1997) 59–76.

Theofanous, T.G. and Dinh, T.N., “Basemat-Internal Melt Arrest and Coolability (BiMAC) device”. Patent Application. Tcl/GE Document. GE Nuclear Energy. San Jose, March 30, 2005.

1. Containment Performance Against Direct Containment Heating (DCH)

1.1. Overall Considerations

The set of potential accidents that lead to DCH consists of those involving core degradation and vessel failure at high primary system pressure. A necessary condition for this is that a minimum of 2 out of the 4 isolation condensers have failed due to either water depletion on the secondary side, or due to failure to open the condensate return valves that keep these IC's isolated during normal operation. In addition, all 8 of the squib activated, reactor depressurization valves, the DPV's, and all 10 of the Safety Relief Valves, the ADS SRV's, must fail to operate. The probability of such combinations of events is assessed at $\sim 2.8 \cdot 10^{-9}$ per year, and accordingly, for the ESBWR, such events must be thought of as *remote and speculative; that is, they could, without further ado, be left in the category of residual risks* (Theofanous, 1996, Scobel, Theofanous, and Sorrell, 1998). This is also reflected by the Level-1 PRA results that show HP accidents to constitute $\sim 1\%$ of the CDF. Moreover, as in PWR HP scenarios (Pilch, Yan, and Theofanous, 1994), natural convection, and forced flow due to SRV lifting, could be sufficient to thermally load the relief lines to failure, thus producing "natural depressurization", and transition to Low Pressure (LP) scenario (prior to lower head breach by the relocated molten core debris). Still, due to its potentially severe consequences, we chose to examine the likelihood for energetic containment failure due to DCH, and we will show that such a failure is *physically unreasonable*.

The key ingredient towards such a conclusion is that $\sim 14 \text{ m}^2$ of vent area, connecting to the enormous condensation potential of the suppression pool, makes it virtually impossible to pressurize the drywell volume. Just as in a LOCA-action of this venting, the timing of "vent clearing" is of essence, and we will pay special attention to modeling it with a high degree of fidelity.

Further, we also examine the potential for liner failure due to the associated high temperatures in the drywell. For the UDW liner this type of failure too was found to be *physically unreasonable*, while for the LDW, due to the immediate proximity and contact with large quantities of melt (given a HPME), local failures, although highly unlikely, cannot be excluded. As explained in the next section, the consequences of such a possibility would be limited due to a standard design feature which compartmentalizes the liner and isolates the gap space of the LDW from that of the UDW so as to clearly eliminate any flow paths to the outside.

1.2. ESBWR Design

An overall illustration of the ESBWR drywell, with highlights on features that impact DCH loading is given in Figure 1.2.1. Detailed representations are also provided as follows: (a) the lower drywell geometry, in Figure 1.2.2, (b) the vent geometry, in Figure 1.2.3, (c) the pathway around the RPV including reflective insulation, in Figure 1.2.4, (d) the BiMAC device, in Figure 1.2.5. The RPV itself is shown in Figures 1.2.6 and 1.2.7, which also contain the key details of interest here, including the penetration welds on the lower head (Figure 1.2.6), and the MSL, SRV, DPV, and IC lines connecting off the RPV upper plenum (Figure 1.2.7). The relevance of each of these features can be summarized as follows:

(a) Initially the vents are covered with water, so the DW volume must be considered closed for as long as it would take to force this water out under the action of DCH (addition of gaseous mass and energy) on the UDW atmosphere. For pressurization levels of interest to DW integrity, this vent-clearing time is something under 1 s. As described in Section 1.4.1, and Appendix B, LOCA being a design-basis event, the data, models and prediction of vent-clearing are on the firmest of grounds.

(b) The pathway that connects the LDW to the UDW is an annular space around the RPV with a characteristic dimension of ~ 2 m. As illustrated, in the LDW region this path is partially occupied by the reflective insulation that surrounds the RPV. Assuming that this rather weak structure will provide minimal resistance to the flow, we will, conservatively, ignore its presence. In the UDW region, the path is between the shield wall and the suppression pool wall. At the level of the suppression pool bottom, the path between LDW and UDW is narrowed by 8 massive blocks on which the RPV is supported. The connecting airspace at its narrowest consists of 8 passages, each of 1.7 m^2 area; that is 13.6 m^2 of total flow area, or a constriction by $\sim 70\%$ of the total annular flow path area.

(c) The role of the BiMAC cover plate, in addition to providing a base for workers to walk on, is to trap debris released during high pressure melt ejection, and to provide some degree of separation from the high velocity gas flow during the subsequent blowdown phase. Essentially complete separation, and elimination of DCH, could be achieved if such a plate could be suspended anywhere inside the LDW, allowing the melt to ablate through, but deflecting the majority of the gas flow (our CFD calculations indicate more than 90%) in the upward direction — see inset in Figure 1.2.5 — but supporting this structure (against the gas-dynamic loads) would be problematic. Employing it as a BiMAC cover, while not as effective, makes the concept practical, as the gas-dynamic loads on either side of this plate come quickly to near equilibrium. It is emphasized that this “trapping” is **not essential to the demonstration** that DCH is not a risk-significant containment failure mechanism in ESBWR. Rather it is provided as a due-diligence measure, to minimize (but not eliminate) the intensity of the dispersal event itself, and if effective in this role, to reduce the chance of LDW liner failure, which otherwise could not be excluded.

(d) Finally referring to Figure 1.2.7, the intent is to show the in-vessel natural convection flow paths, basically redistributing heat during the oxidation and degradation phases of a

severe accident to the upper vessel internals, and through the top portions of the upper plenum into the various lines that lead to the SRV's, DPV's, and the IC's. The thermal connection to the former one is by forced convection, through the MSL (due to SRV actuation), while for the two latter ones is by natural convection.

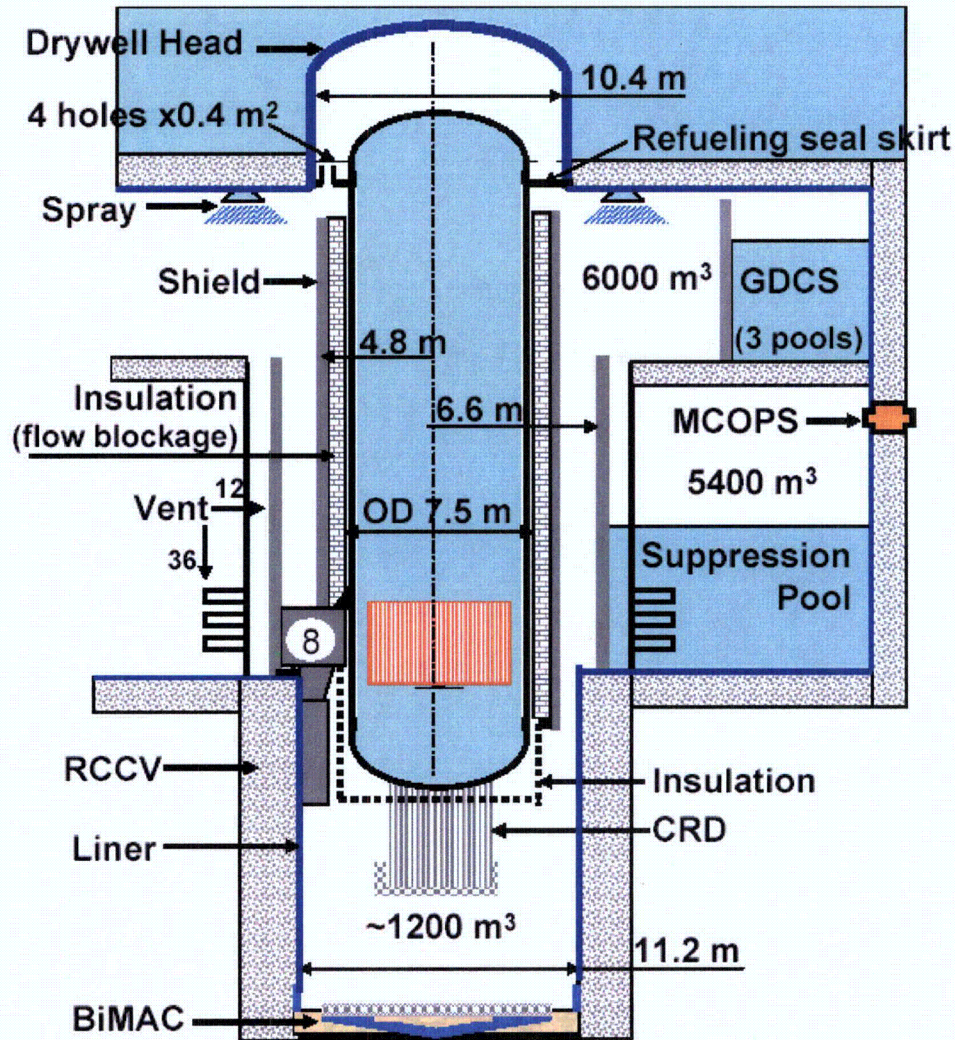


Figure 1.2.1. An overall illustration of the ESBWR drywell, with highlights on features and scales (volumes) that impact steam/gas flow, melt dispersal and DCH loading. Dimensions and arrangement of important volumes of LDW, UDW and annular airspaces connecting LDW to UDW, and vents to suppression pools are provided to scale. The spray would provide cooling to the drywell atmosphere after a DCH event, however, it is not necessary for reaching the conclusions in this report.

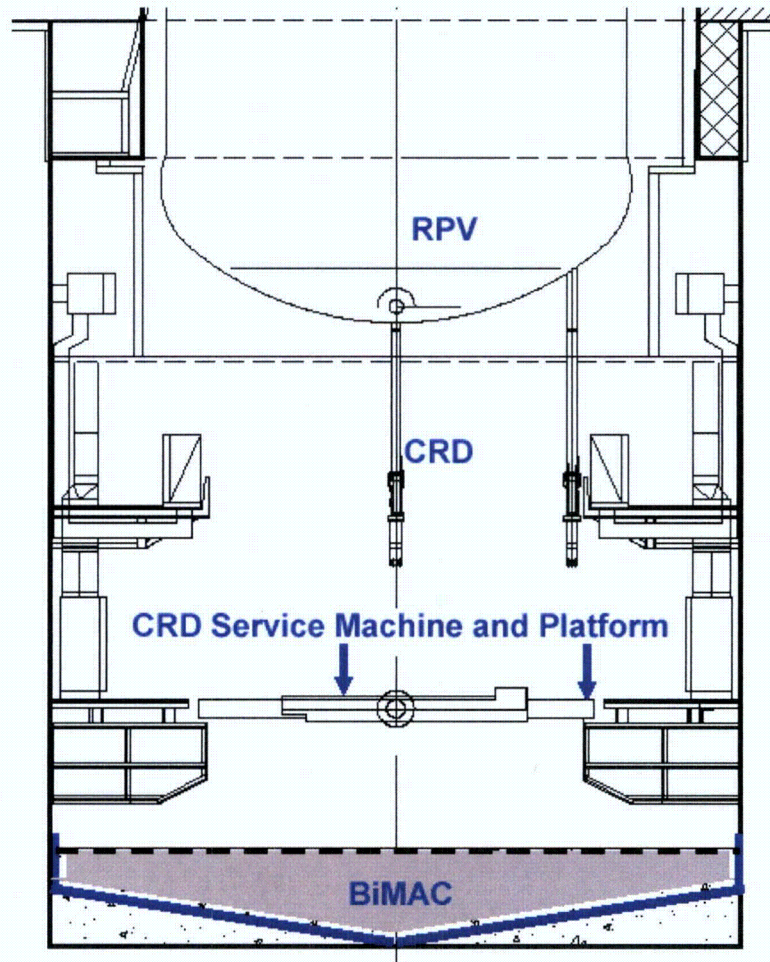


Figure 1.2.2. The ESBWR lower drywell (detail). The ascending flow of steam and entrained melt along the pedestal wall permeate through CRD service platform and peripheral standing platforms, into the annular space between the vessel and the LDW pedestal wall. The BiMAC is embedded in the layer of concrete (1.5 m height) and is covered by a 0.2 m thick layer of refractory material (ceramic Zirconia).

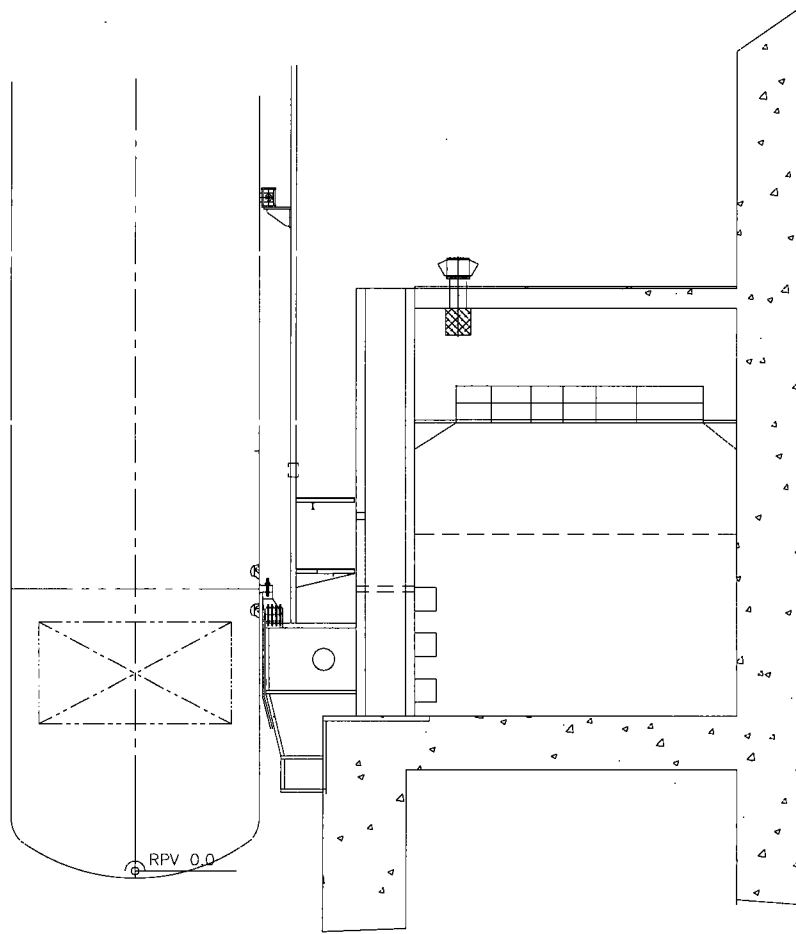


Figure 1.2.3. Suppression pool and vent geometry (details). There are 12 vertical vents that each feeds a column of three horizontal vents, for a total flow area of $\sim 14 \text{ m}^2$. Each horizontal vent diameter is 0.7 m providing a 0.385 m^2 flow area.

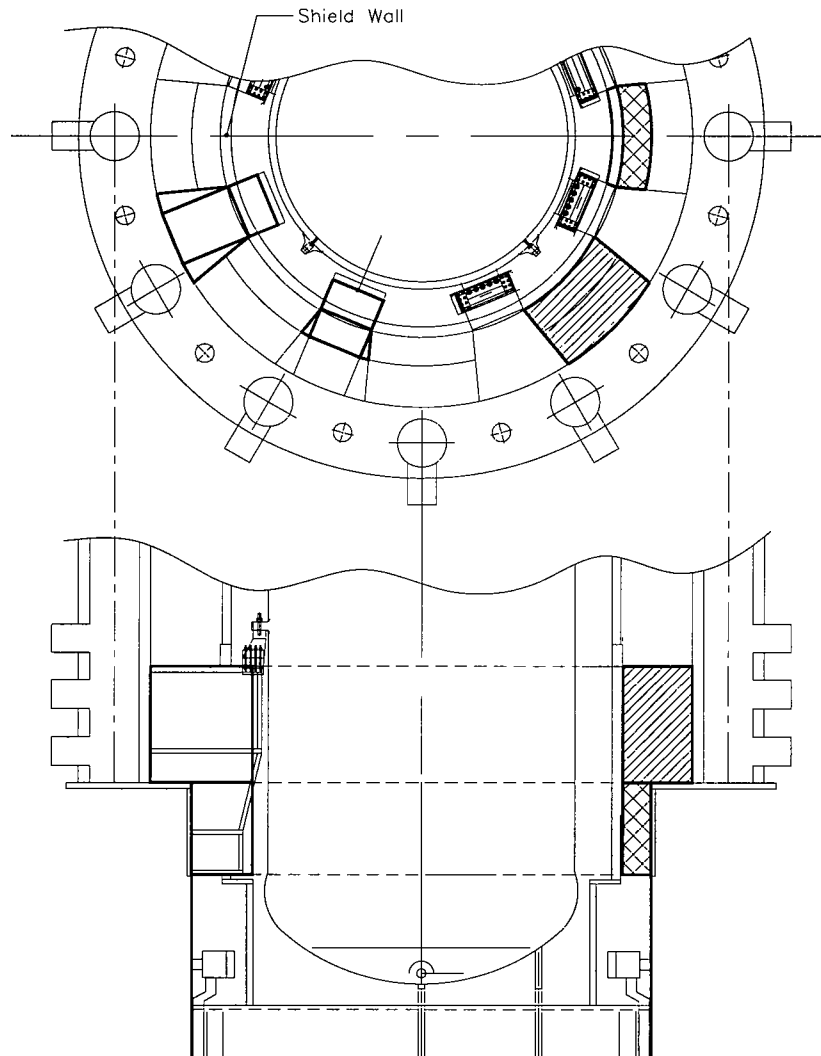


Figure 1.2.4. The pathway around the RPV, including reflective insulation and connecting airspace between LDW and UDW . There are 8 blocks on which the RPV is supported. The annular passage (shown by cross-hatched areas) between the shield and the concrete wall is open for air flow. The annular space between the RPV and the shield is filled with insulation materials and presents a flow blockage.

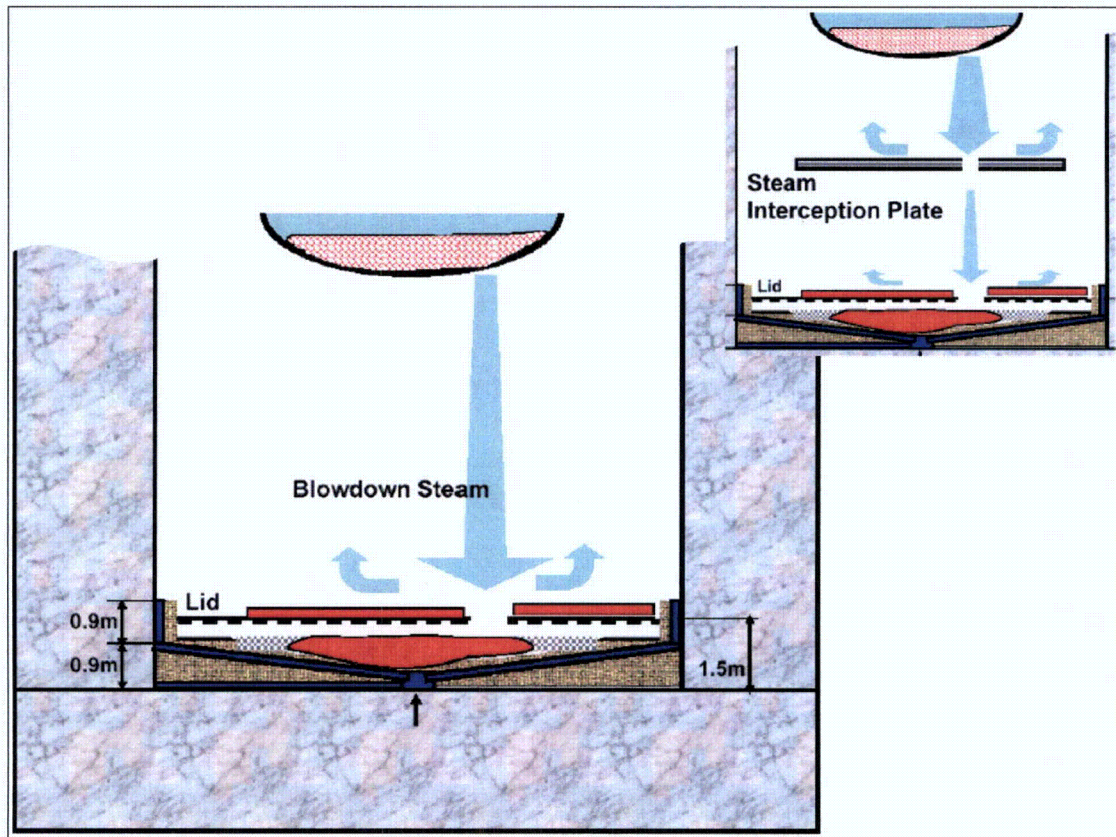


Figure 1.2.5. The BiMAC device and its incorporation in the ESBWR Lower Drywell. The SIP (Steam Interception Plate) concept is shown in the insert.

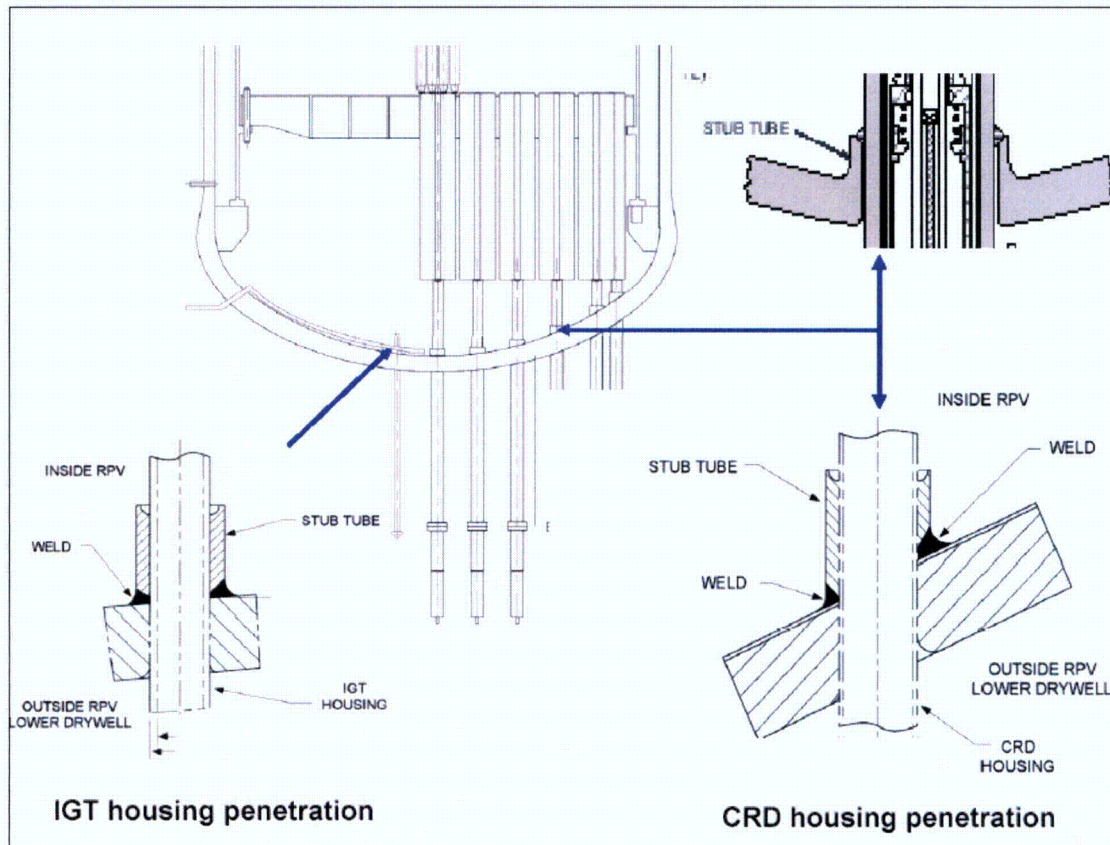


Figure 1.2.6. The RPV geometry (lower part), including the penetrations and penetration welds on the lower head. The CRD and IGT are supported on the vessel lower head by the weld between the penetration housing and the in-vessel stub tube. The weld elevation is 15 cm from the vessel inner surface. Upon core melt relocation to the lower plenum, a number of CRD and IGT become submerged in the core debris or core melt pool. This can result in vessel failure due to thermal attack on the penetration, failure of the stub-tube-to-penetration weld, and ejection of the penetration.

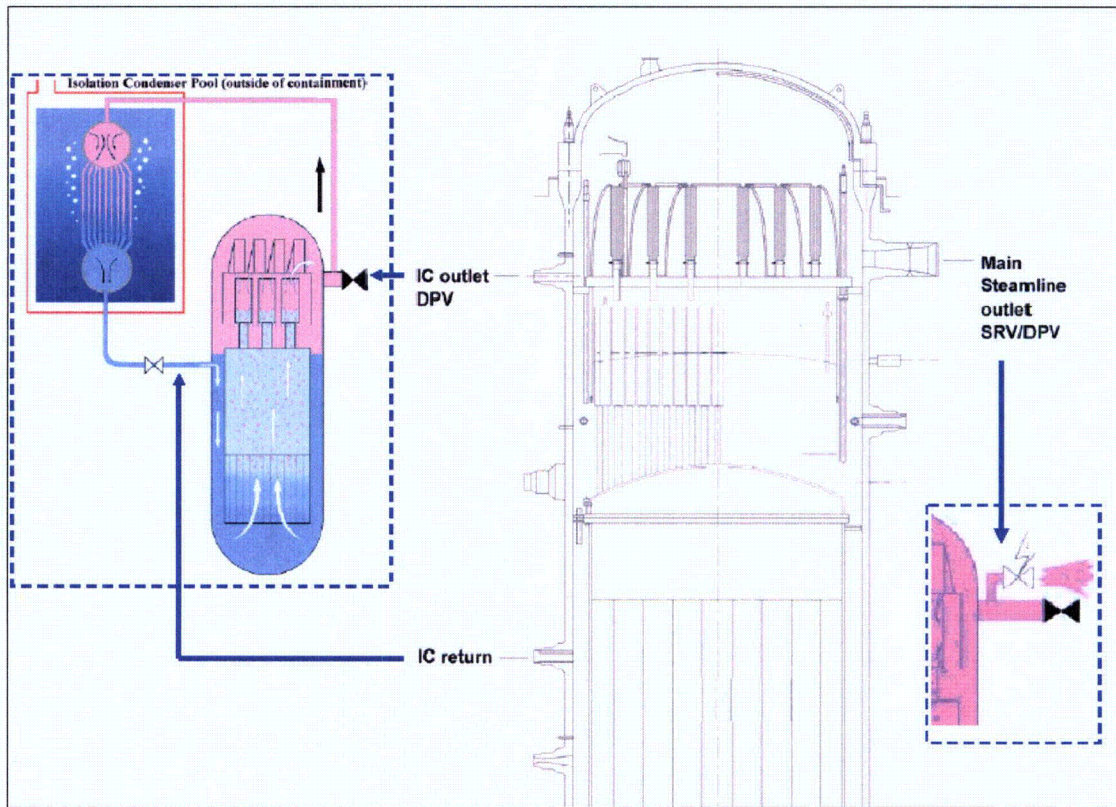


Figure 1.2.7. The RPV upper part with SRV, DPV, and IC lines off the RPV.

Intermittent flow of hot gases through SRVs (and into the Main Steam line) would thermally load the lines that constitute the relief path. The thermal connection to the IC lines is by natural convection, and thus weak compared to that of the SRV/MS lines. Also shown, in areas above the core and in the upper plenum, are structures which present heat sinks for hot gas/steam that would emanate from a degraded core.

1.3 Previous Work

Direct containment heating has been considered to be a major containment integrity issue in PWR's, and this drove very extensive research efforts during the late 80's and early 1990's. These efforts culminated with issue resolution in a ROAAM framework as documented in Pilch, Yan, and Theofanous (1996), and Pilch and Allen (1996). Reviews on the subject have been presented by Pilch et al (1997), and by Pilch and Henry (OECD, 1996). The latter considered also the BWR setting and recognized the significant load-mitigating role of venting into the WW heat sink.

The principal ingredient in quantifying DCH loads in this previous work was the realization that oxidation of the reactive components in the melt, and energy transfer to the containment are limited by the entrainment/dispersal process occurring over a time scale that restricts contact to only a fraction of the available (in the RPV) steam. Within this time scale the melt-steam contact was found to be so intense as to be describable by a thermochemical-mechanical equilibrium process. The principal experimental data came from the Integral Effects Tests (IET) (Allen et al., 1994; Binder et al., 1994), conducted for the US NRC with comprehensive review and input on scaling to reactor conditions from a group of experts. The interpretation and application to reactor predictions were made by means of the CLCH model (Yan and Theofanous, 1996) and the two-cell equilibrium model (Pilch, 1996). For PWR's the containment heat sinks played no significant role, and combustion of hydrogen produced in the DCH process had to be addressed. Also, for the PWR's the spontaneous depressurization scenario played an important role in the overall issue resolution scheme. In the ESBWR we need not be concerned about combustion in the containment atmosphere, and we will take no credit for spontaneous depressurization.

These developments were not available in the singular prior licensing assessment of DCH for a BWR. Done for the ABWR (GE, 1987;1994), it was assumed that 20% of core (molten materials) was dispersed (and equilibrated with the atmosphere) inside the 8,000 m³ UDW volume within 2 seconds, and the calculations produced over-pressurization that exceeded the structural capacity of the DW. This unrealistically conservative result was one of three reasons cited by the US NRC (1994) for judging that conditional (given a core melt) containment failure probability for ABWR could be as high as 10%.

1.4 Present Assessment

1.4.1 Key Physics in DCH

Direct containment heating can be expected when high velocity steam happens to impinge upon melt already released into a containment compartment, thus creating regions of fine scale mixing, large interfacial area for heat transfer, and oxidation of metallic components in the melt. The so-heated steam, flowing at very high volumetric flow rates, then provides a mass-and-energy source that can pressurize and heat the receiving atmosphere. Concurrently, the finely atomized melt is carried against gravity into the receiving volume(s), where the steam velocities are highly reduced, and the particles are allowed to fall (de-

entrain). In ESBWR the mixing occurs in the LDW, while the main receiving volume, in which de-entrainment occurs, is the UDW—these correspond to the reactor cavity and the sub-compartment(s) of Large Dry Containments (LDC) in PWR's respectively. In distinction to LDC's, in the ESBWR, as in all BWR's, the receiving volume, rather than being closed, is vented to another volume, the WW, which contains a large and effective heat sink. The key physics that drive all these phenomena, and that need to be quantified in predicting a realistic outcome, are as follows:

(a) Natural Depressurization and RPV Lower Head Breach. Natural depressurization, and thus transition to a LP scenario, would occur if any of the MS, SRV, DPV, or IC lines were to fail (due to thermal loading by gas natural convection) prior to lower head breach (by melt attack). The heat source is the melting/oxidizing reactor core. The heat transfer medium is the steam (and hydrogen) trapped inside the RPV at high pressure, and thus at high density. The process is by natural convection. It is set up between the core region and the cooler upper internal structures whose heat capacity defines the heat-up rates of the gases in the upper plenum. The flow of these gases into the MS, and SRV lines would be convective, as the SRV's lift periodically to relieve pressure, and thus the material temperatures reached would be close to that of the hot gases. As we will see below, the time scale for the melt material to reach the lower plenum in large quantities is ~1 hour, and in this time period gas temperatures reach up to ~1,000 K. This indicates conditions in the neighborhood of creep rupture (Smith, 1971, Reddy and Ayers, 1982) of the lines involved. In competition with this is a set of complicated processes in the lower plenum that lead up to lower head failure. These include quench and reheating of the relocated core debris, melt attack of lower head penetration welds and RPV failure by ejection of the penetration equipment involved, gradual re-melting of the core debris, and ultimately, if for some reason penetration failures did not occur, heating and creep rupture of the lower head material itself.

(b) Melt Ejection, Vessel Wall Ablation, and BiMAC Refractory Cover Ablation: Due to negligible resistance by the LDW atmosphere, the melt jet would remain essentially coherent until it hits the LDW floor [but see Addendum 3.5Add at the end of Chapter 3], and the BiMAC cover plate, which would then be penetrated essentially instantaneously to allow free access to the sacrificial refractory layer that covers and protects the top of the BiMAC pipes. The vessel wall would ablate due to heat transfer from the superheated melt. So would the refractory material if melt temperature exceeds its melting point. These processes are well understood and this understanding is supported by experiments. Results depend on the melt composition and superheat and will be treated in a bounding fashion. Similarly, the amount of melt mass involved in the ejection process, and the mass fractions of Zirconium and Iron in it, are treated in a bounding fashion.

(c) Steam Blowdown: The steam inside the reactor vessel would expand adiabatically during blowdown, and the steam discharge rate is defined by choked flow at the vessel breach area(s). Both processes can be accurately simulated by means of simple thermodynamics (ideal gas equation of state, adiabatic expansion) and Computational Fluid Dynamics (CFD) simulations respectively. Figure 1.4.1.1 shows the gas-dynamic pressures established in the LDW during a typical blowdown from a full-pressure RPV (safety valve set-point). As illustrated, the discharge flow accelerates to form a supersonic jet, with key

characteristics of flow area expansion by a factor of ~ 10 , and a loss of stagnation pressure due to repeated spontaneous/internal shock and expansion wave formation by $\sim 75\%$ to 90% . This jet, upon impinging the floor, and then again upon impinging the sidewalls, yields wall jets, which remain largely coherent and maintain velocities of hundreds of meters per second. An idea of the energy involved and of the overall flow pattern developed in the LDW can be obtained from snapshots of the velocity distributions from steam-only flow (no melt) in CFD simulations (Figure 1.4.1.2). Importantly, rough treatments that smear the flow out over the whole LDW cross-sectional area, such as those made in a few old attempts to define entrainment limits, would seem to be in error. Rather, momentum flux localization is the essential mechanism that determines melt atomization, and entrainment potential in DCH events for such a geometry.

(d) Interfacial Instability, Breakup, Entrainment, and Carry-over of Melt Exposed to the Gas Stream Inside the LDW. Liquids exposed to high velocity gas streams atomize and become dispersed. The mode and magnitude of the interfacial instability responsible for this behavior depends on the Weber number which is the ratio of the destabilizing momentum flux of the gas (ρv^2) to the stabilizing surface tension force (σ/R). For corium melts, the surface tension is about 10 times that of water, so the stability limit will be (for the same momentum flux) at a length scale that is ~ 10 times that of water. For example at a gas velocity of 300 m/s and atmospheric density of 1 kg/m^3 , the stable droplet size for water is ~ 10 microns, while for corium it is ~ 100 microns. This stability limit is captured by a critical Weber number of ~ 10 . Thus even a relatively small drop of 10 mm will experience an initial We number of 10^3 and a breakup pattern such as that illustrated in Figure 1.4.1.3, except that the mist shown would be at length scales of ~ 100 rather than ~ 10 microns.

Melt particles of 100 microns size can be suspended by air/steam velocities of as low as ~ 5 m/s. This is to be seen in the perspective of the jetting velocities seen in Figure 1.4.1.2, and some ~ 10 's of m/s exiting the lower drywell under typical high pressure steam blowdown rates. In addition, macroscopic motions are induced by pressure forces that accelerate bigger masses of liquid up the pedestal walls, in the manner illustrated (for a geometrically-scaled ESBWR geometry) in Figure 1.4.1.4. There is no question that any exposed melt inside the LDW will be atomized and dispersed into the UDW. Much of it would then be carried into the suppression pool, while some fraction would de-entrain and deposit on the UDW walls or fall on the floor, in a highly dispersed state. As discussed in Section 1.4.3, we can estimate the dispersal rates in terms of the DCH-scale as determined from scaled experiments (the IET series of tests).

(e) Entrainment of Melt Captured inside the BiMAC. The geometry of concern is illustrated in Figure 1.4.1.5. While the pressure established inside the BiMAC is the same as the stagnation pressure on the top of the cover plate, due to high frequency flow fluctuations, these pressures are unsteady, and as we found in scoping experiments, a net circulation pattern is established that continuously brings liquid into the immediate vicinity of the opening from where it is entrained to the outside in a highly atomized form. The velocities in this region can be as high as 600 m/s, and the mass loading on the flow is rather low (that is, we have a metering effect, defined by the internal circulation rate of the melt, on release and dispersal due to the BiMAC), so the Weber numbers may approach 10^4

and the length scales of atomization may be as low as 10 micron. Such particles could be carried around by gas flows as low as 2 m/s.

The influence of water (preexisting in the LDW) in any of the above does not need to be considered because the only HP scenario that can lead to flooded LDW is the SBLOCA with loss of DPV/SRV action and CRD water supply — a core damage frequency of $\sim 7 \times 10^{-13}$ or 0.01% of the total CDF.

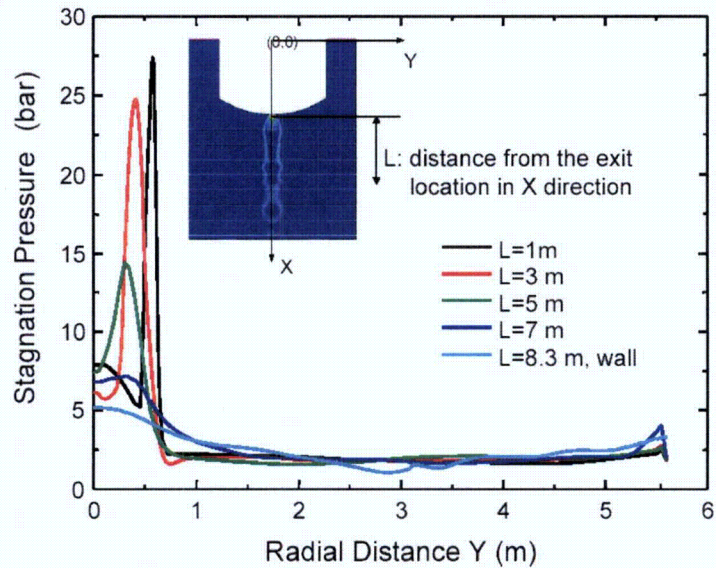


Figure 1.4.1.1. The stagnation pressures ($P_S + \rho V^2/2$) in the LDW ($t \sim 188$ ms) during a typical blowdown from a fully pressurized RPV through a 0.40 m diameter hole.

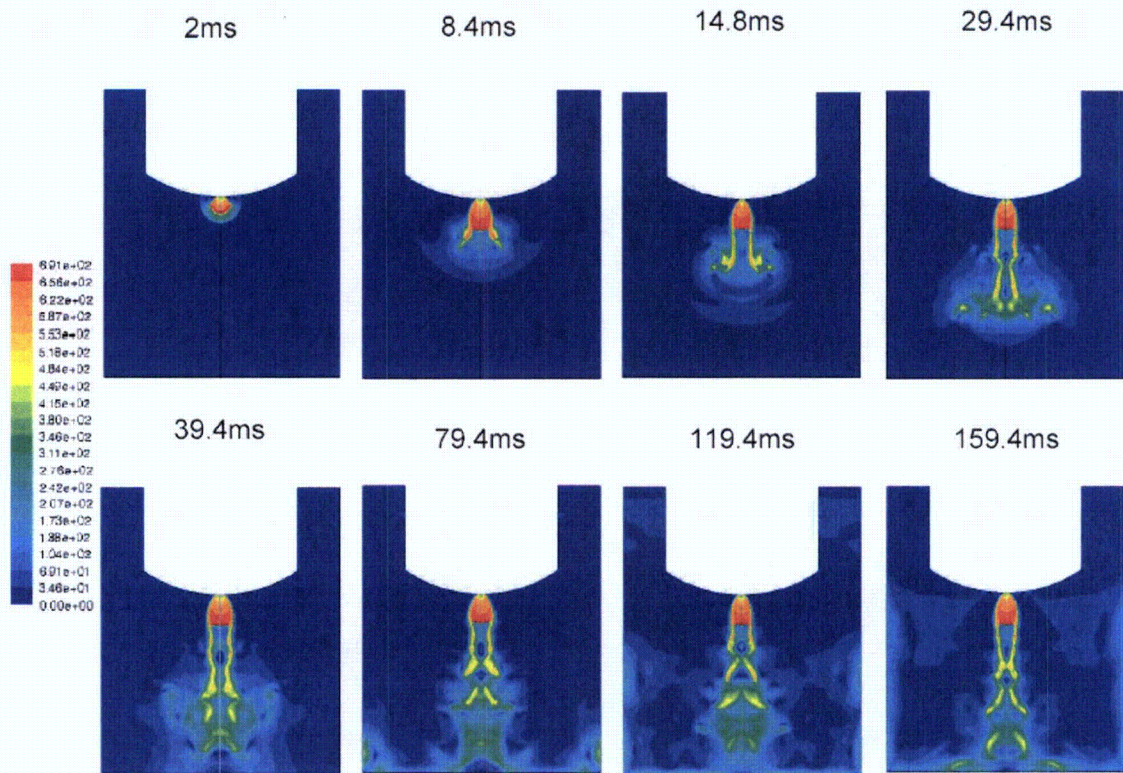


Figure 1.4.1.2. Velocity distributions in the LDW from steam-only flow (no melt) in CFD simulations. The velocity scale is shown on the left. The maximum value ~ 700 m/s.

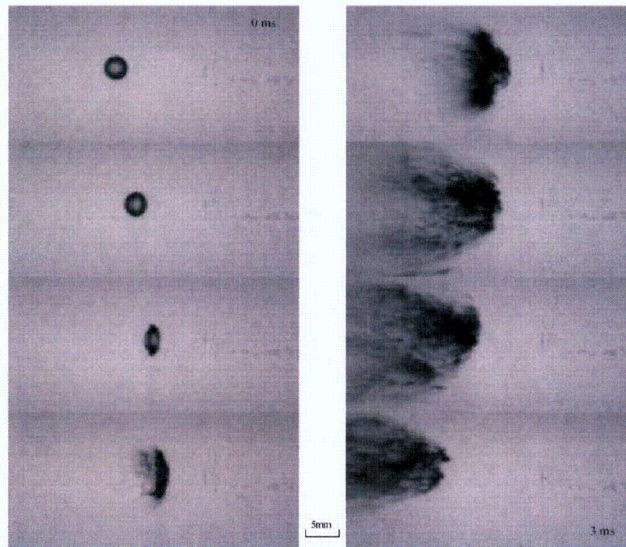


Figure 1.4.1.3.a. Water drop breakup at $We \sim 10^3$.

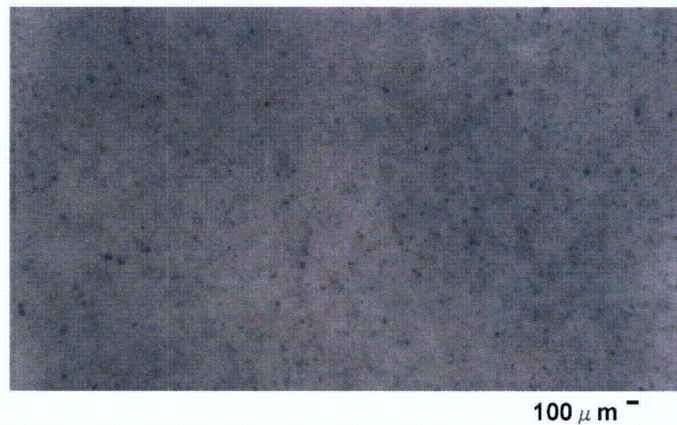


Figure 1.4.1.3.b. Close up image of fragments from a breakup at $We \sim 10^3$.

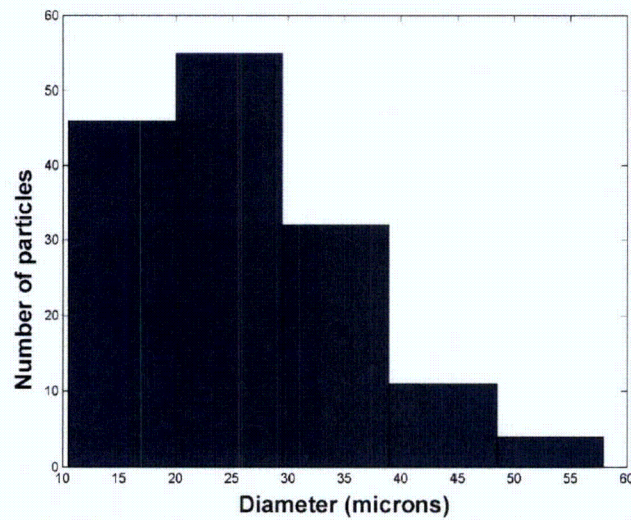


Figure 1.4.1.3.c. Droplet size distribution in Figure 1.4.1.3.b.

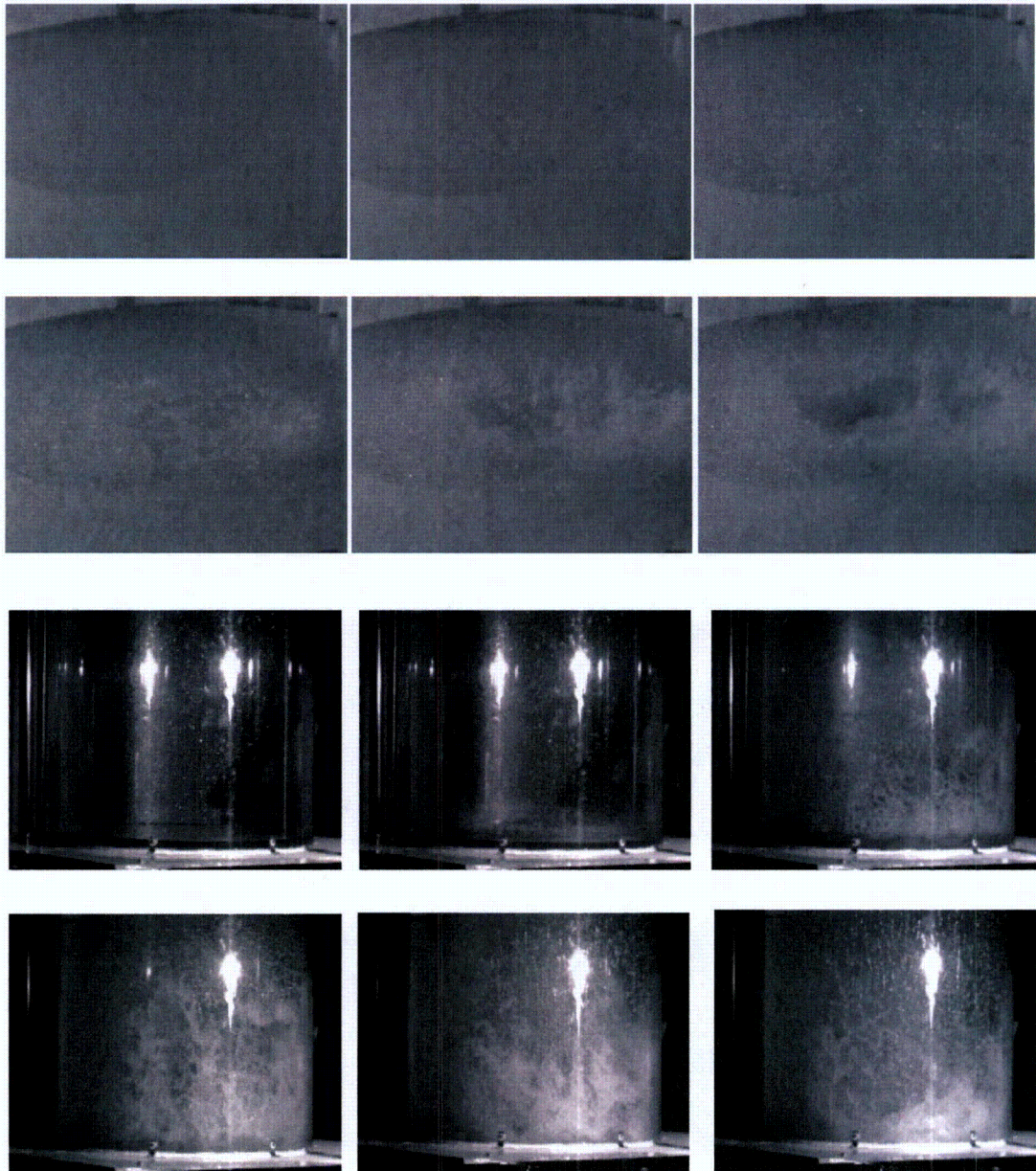


Figure 1.4.1.4. Visualization of liquid flow and entrainment during gas blowdown from 1 MPa pressure into an 1/10 scale model of the ESBWR LDW.

Upper 6 frames: Close-up view of the gas jet interacting with liquid layer resting on the vessel bottom plate. One can see the general pattern of interfacial instabilities, liquid atomization, and entrainment.

Lower 6 frames: Far view of the liquid dispersal and carry-over with the gas flow. The blowdown gas impinges upon the liquid, then spreads radially towards the cylinder boundary, and ascends as wall jets along the pedestal wall, carrying the liquid with it.

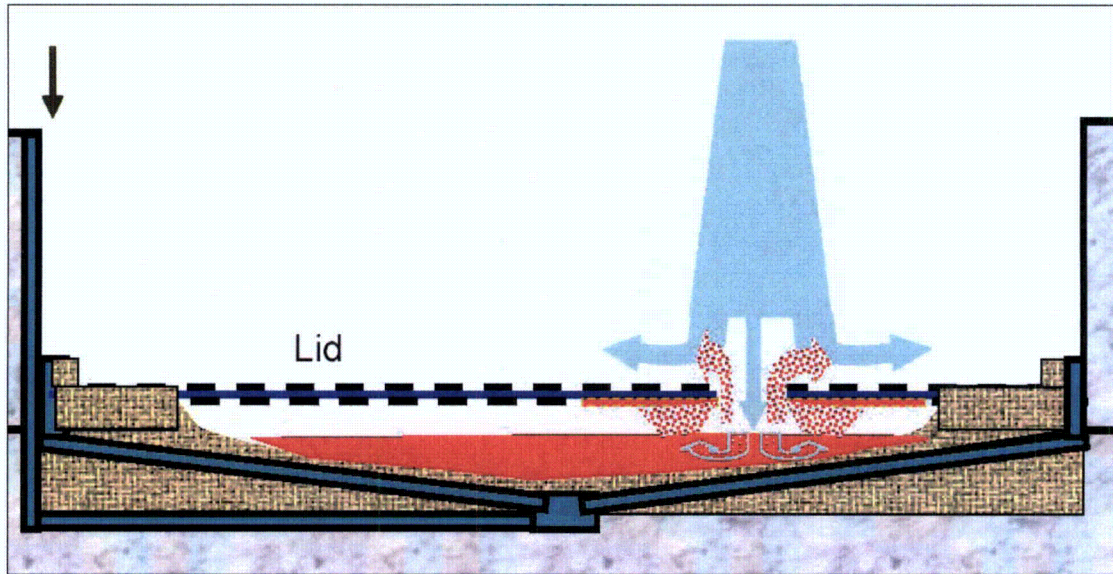


Figure 1.4.1.5. Conceptual visualization of melt entrapment in BiMAC and subsequent gradual entrainment (blowdown steam in blue and melt/debris in red).

1.4.2 Probabilistic Framework

First we address spontaneous depressurization. The precipitous loss of strength of the RCS wall/piping material at temperatures above 700 K is illustrated in Figure 1.4.2.2. The relevant stress levels in various piping components are listed in Table 1.4.2.1, and shown also in Figure 1.4.2.2. We can see that all these piping components are at risk of failure once they reach temperatures over ~1,000 K, and that due to the stress levels involved such a failure would be far more likely to occur in the MSL. In fact such temperature levels are known to be typical of the heat-up found in high pressure scenarios. For example, as noted already, MAAP calculations for the ESBWR show peak temperatures of ~900 K (GE-NE, 2005a). Moreover, in the DCH issue-resolution work for PWR's (Pilch et al, 1996), calculations with SCDAP/RELAP (at 8 MPa) show temperature levels reaching up to 1,700 K.

Table 1.4.2.1. Stress levels in piping components vulnerable to heating-up during core degradation at high pressure (evaluated for $P_{RCS} \sim 8$ MPa).

Component	Diameter D, m	Thickness δ , m	Hoop Stress, MPa $S = P_{RCS} \cdot D / 2\delta$
SRV Inlet Line	0.170	0.050	13.6
IC Inlet Line	0.450	0.080	22.5
MSL (before SRV)	0.700	0.037	75.7

We can see that for the MSL we are clearly in the creep rupture region. However, considering the uncertainties involved in calculating these temperatures, and the sensitivity of material properties in this temperature region, we believe that this aspect of HP scenario transition to LP should be treated as a splinter at this time. In practical terms this means that we take no credit for spontaneous depressurization. However we do note that high pressure sequences that lead to high pressure melt ejection may not be physically possible for the ESBWR.

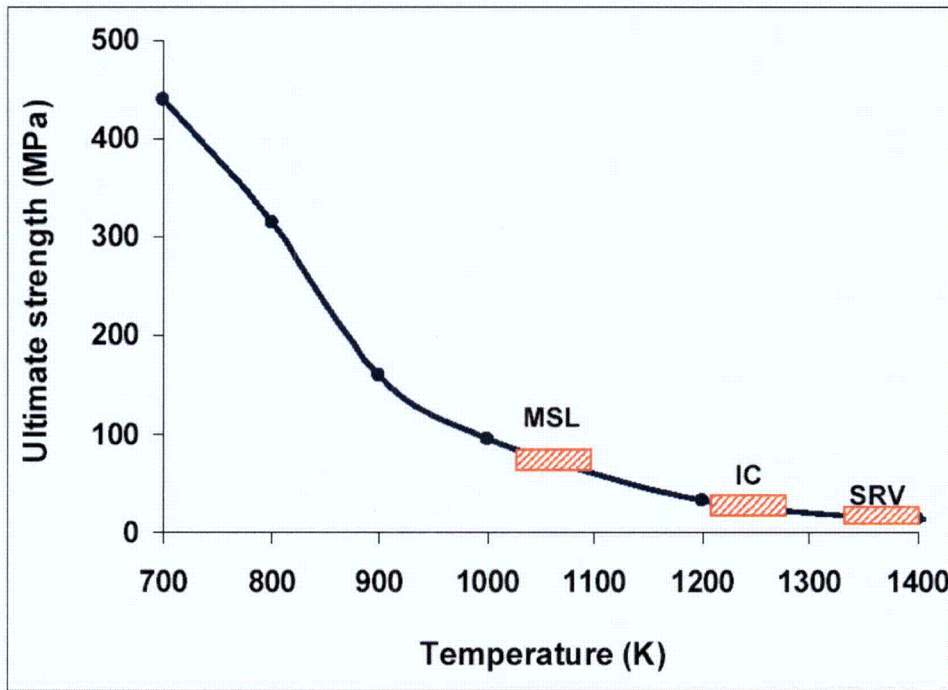


Figure 1.4.2.2. Ultimate strength of steel in the high temperature range. Also shown are the relevant temperature levels for creep rupture of the MS, IC, and SRV lines. Steel properties a summarized in J.L. Rempe, G.L. Thinnes and C.M. Allison (1990), "Light Water Reactor Lower Head failure Analysis", NUREG/CR-5642, US NRC.

Turning now to DCH loads, our principal concern is to address energetic failure due to DW over-pressurization. Our approach evolved, as we came to understand and appreciate the interesting dynamics of such a system, gradually and through various kinds of calculations. As it turns out there are three different kinds of pressurization regimes that are possible to realize, depending primarily on the size of the vessel breach area. One regime was found in trying to illustrate the case of pressurization levels approaching the failure pressure of the containment (1.2 MPa –see section 1.4.4) given an arbitrarily large breach area (>1 m in diameter). As expected this case involves extremely fast dynamics that tie closely to the clearing and the flow capacity of the vents. The second regime obtains for break areas at the upper end of credible creep ruptures (~0.55 m in diameter) as determined in the PWR DCH issue-resolution documents (Pilch, Yan, and Theofanous, 1996, and Pilch and Allen, 1996). This regime exhibits intermediate dynamics, with pressurization levels reaching up

to only half of the 1.2 MPa needed for approach to failure. Finally the third regime, found for break areas that correspond to a single penetration failure (after ablation to ~0.2 to 0.3 m in diameter), is quasi static, exhibiting comparatively low pressurization levels that depend mainly on the amounts of Zirconium available to react. The hypothetical case (first regime) is considered in this section as a way of providing perspectives on the bounding load calculations, including the other two regimes, which are presented in the next section. These calculations will also yield a way for bounding the UDW atmosphere temperatures as needed for the less important, yet still interesting question of creep-induced liner failure.

A hypothetical case that yields the first regime (see Section 1.4.3 for the mathematical model used in capturing them) is illustrated in Figure 1.4.2.3. The condition represented is for 300 ton of melt, containing 60 tons of Zirconium (20% content in the melt), it being dispersed by the blowdown from a vessel breach equivalent to a hole 1 m in diameter. The melt entrainment time is taken as 1 s, the blowdown time constant is ~1 s, thus implying a DCH-scale of ~1. This means there are no significant mitigative effects due to melt-steam incoherence. The peak pressure that develops in the LDW is due to the rapid energy supply by the DCH phenomenon, taken at an extreme manifestation here for purposes of illustration. At around 0.2 s, the pressurization due to this energy supply rate is compensated by mass/energy loss to the UDW, leading to a drop in pressure, till at ~0.4 s the balance again shifts in favor of supply, thus yielding a second pressure rise transient. By this time the LDW and UDW behave in tandem, until the end of melt dispersal, at which time the peak pressure of ~1.2 MPa is reached. Vent clearing occurs in the 0.4 to 0.6 s time interval, and the effect is seen to moderate the rate of pressure rise. Throughout this extremely fast transient the WW pressure has been hardly affected, while the magnitude of the second pressure peak is controlled by the flow capacity of the vents. Further in Figure 1.4.2.3 we see that the end of dispersal is followed by a rapid cooldown period, as the expanded, “cool” steam washes away the hot gases from the LDW. Increasing the DCH time scale to 2 or 3, that is melt entrainment times of 2 or 3 s respectively, has no significant effect on all these features of the transient. This is because the DCH contact process is already saturated (Yan and Theofanous, 1996), and the maximum possible extent of oxidation has taken place. From this bounding (in RPV pressure and amounts of melt and Zirconium) condition, the only way to effect a higher dynamic pressure would be by increasing the breach area even further, but this is already 4 times the upper bound considered credible in creep rupture scenarios for PWR’s (Pilch, Yan, and Theofanous, 1996, and Pilch and Allen, 1996), and more than ~10 times that created from a single penetration failure due to ablation from a 300-ton melt (see Section 1.4.3). Further, in the case considered above we use the total quantity of Zirconium in the core, which for the ESBWR is 76 tons, minus the 16 tons taken to have been already reacted to produce a containment pressure of 0.25 MPa consistently with that assumed to be initially present.

Thus it is clear that overpressure failure of the ESBWR DW due to DCH is physically unreasonable. Moreover, it is clear that this conclusion is robust in that it does not depend on a host of (intangibile) parameters that previous (PWR) assessments were found to depend on; such as, the total quantity of the melt involved and its Zirconium content, the breach area, and combustion in the receiving atmosphere (see Figure 1.4.2.4).

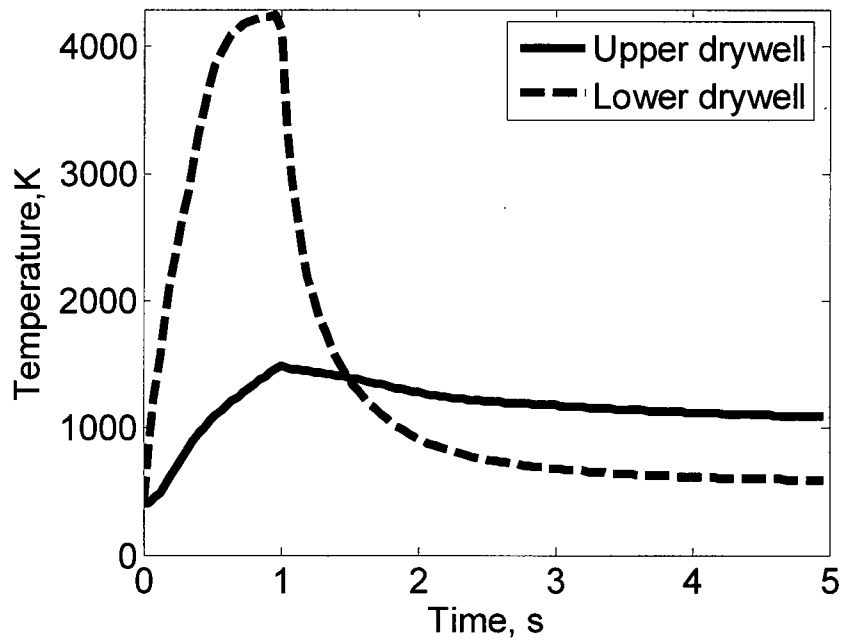
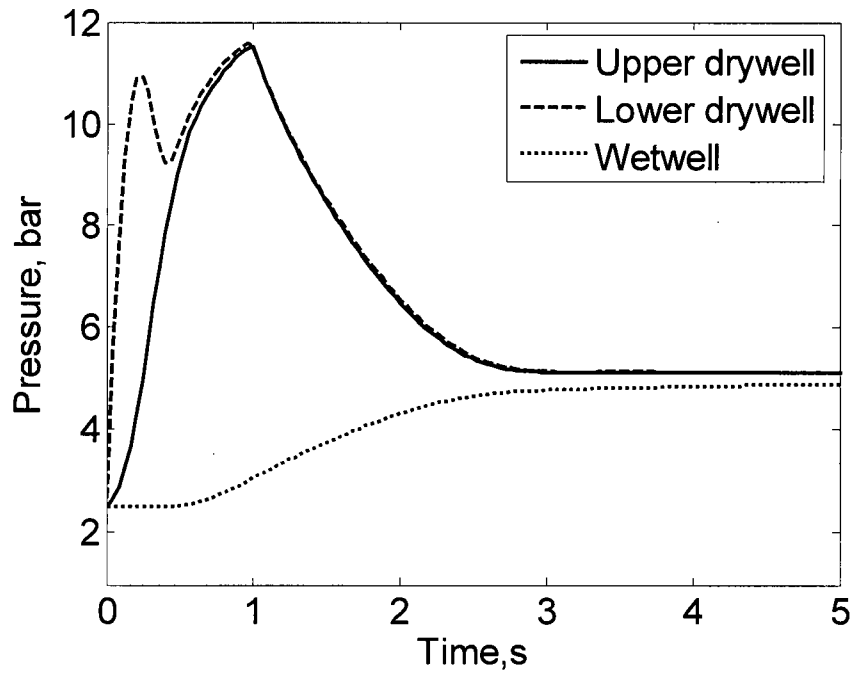


Figure 1.4.2.3. Drywell pressure (top), and temperature (bottom) in a strictly hypothetical scenario selected to illustrate the effect of vent clearing, and subsequent gas venting, at conditions that approach containment-integrity-challenging levels.

So what remains is to consider the effects of elevated temperatures of the DW atmosphere on liner (and penetration seals) integrity. Clearly this is only relevant to the sequences for which DW sprays are not available, and as noted already (see Figure B.1) these amount to 0.78% of the 1.3%, or ~1% of the CDF. The evaluation is done in the next section, and again we aim for a conservative treatment. Interestingly, in the DCH evaluations for PWR's peak temperatures reached only ~600 K, and they were never an issue—here in a much smaller DW volume, even though it is open, the DCH temperatures can reach considerably higher levels, even in the absence of combustion.

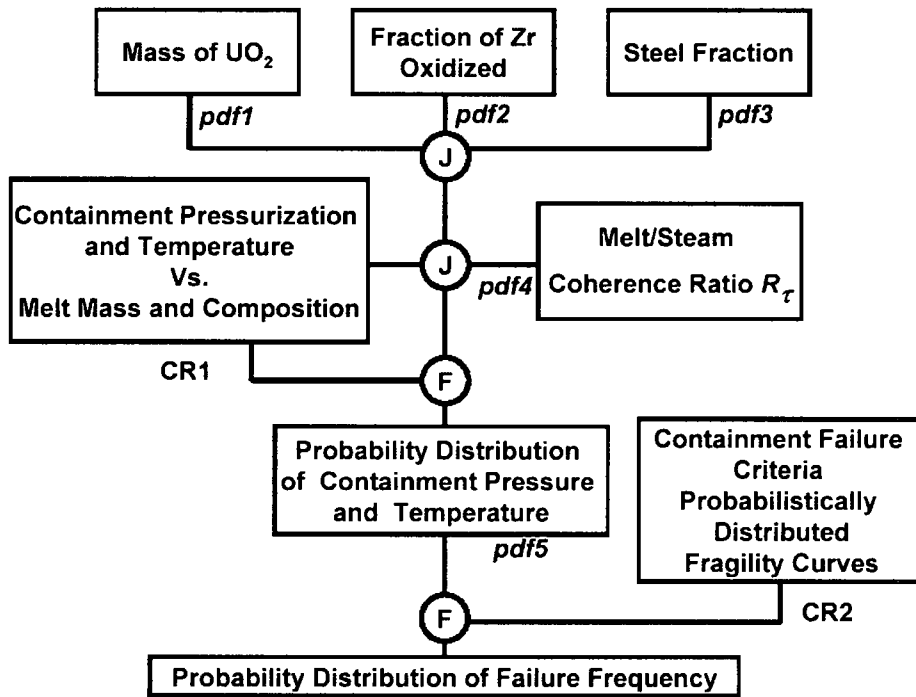


Figure 1.4.2.4. Probabilistic framework utilized in the PWR DCH issue resolution. (Theofanous, 1996; Pilch, Yan, Theofanous, 1996).

1.4.3 Quantification of DCH Loads

As noted already, we use the CLCH model (Yan and Theofanous, 1993) adapted for present purposes by a rendering that captures the full transient, in an open system, and its coupling to vent-clearing. The equations, simple mass and energy balances, over the communicating LDW, UDW, and WW volumes, are summarized in Table 1.4.3.1. This model was verified by comparison to final pressures/temperatures calculated for the original closed system configuration of the original model, as well as sample IET test results that included the complete transients (see Figure 1.4.3.1, and Appendix A).

The vent-clearing model reflects a simple accounting of water inertia, including the added mass effect, in the suppression pool, as it is being accelerated, under the action of the UDW pressure, into the WW. The equations are summarized in Table 1.4.3.2. Corium properties, metal-steam reactions and related energies are treated in the same way as in the previous work leading to resolution of DCH issue for PWRs (Pilch, Yan and Theofanous, 1996). As seen in Figure 1.4.3.2 and Table 1.4.3.3 (see also Appendix B), the model captures quantitatively the behavior as found in the full-scale, Pressure Suppression Test Facility (PSTF) experiments conducted in support of the LOCA-Loads program by GE (1974).

Finally, in the WW model, the heat losses from the gas stream passing through the suppression pool, which in a DCH event would be highly agitated and grossly dispersed, are accounted through parameters used to reflect the condensation and heat transfer (non-condensable) efficiencies.

Ablation of the initial penetration opening, and of the sacrificial refractory layer on top of the BiMAC during HPME was estimated according to well established models and procedures. The former case involves parallel flow and for it we use the model of Pilch (1994) as done by Pilch, Yan, and Theofanous (1996). The latter case involves impinging flow and for this we use the model of Saito (1991) as done by Theofanous et al (1996). The results for hole ablation are very similar to those obtained previously, yielding final diameters of 0.2 m and 0.3 m for 100 and 300 tons of melt involved in the expulsion process respectively. In terms of area, this is rather weakly dependent on the number of assumed simultaneous penetration failures, as this is compensated by the shorter duration of the HPME. The evaluation of refractory ablation is presented in Chapter 3 (on BMP).

In estimating DCH, in PWR's the principal ingredient in the original model was the DCH-scale (Yan and Theofanous, 1996), and this is used as such in the present application as well. In previous assessments, this quantity was quantified as an intangible parameter, with a most probable value given by Eq.1.4.3.1, and a probability distribution around this value assumed to be normal with a standard variation of 12.5% (roughly, and conservatively, based on the quality of agreement with the IET data).

$$R_{\tau} = \tau_m / \tau_s = 0.2V_{cav}^{1/3} T_{RCS,0}^{1/2} / P_{RCS,0} / \tau_s \quad (1.4.3.1)$$

$P_{RCS,0}$ is the primary system pressure prior to HPME (in MPa), τ_s is the characteristic blowdown time (given in Table 1.4.3.1), and τ_m is the melt entrainment time.

Table 1.4.3.1. The Transient CLCH Model (for nomenclature see Table 1.5.1)

Vessel:

$$\frac{P_{RCS}}{P_{RCS,0}} = \left\{ 1 + \frac{\gamma-1}{2} \Gamma \frac{t}{\tau_s} \right\}^{2\gamma/(\gamma-1)}$$

$$\dot{m}_{blowdown} = \eta A_b \rho_{s,0} a_{s,0} \Gamma \left\{ 1 + \frac{\gamma-1}{2} \Gamma \frac{t}{\tau_s} \right\}^{(\gamma+1)/(1-\gamma)}$$

$$\frac{T_{RCS}}{T_{RCS,0}} = \left(\frac{P_{RCS}}{P_{RCS,0}} \right)^{(\gamma-1)/\gamma}$$

where $a_{s,0} = (\gamma R T_{RCS,0})^{1/2}$, $\Gamma = \left[\frac{2}{\gamma+1} \right]^{(\gamma+1)/2(\gamma-1)}$ and $\tau_s = \frac{V_{RCS}}{\eta A_b a_{s,0}}$

Lower Drywell:

$$\dot{m}_m = \begin{cases} \frac{m_{m,0}}{\tau_m} & t \leq \tau_m \\ 0 & t > \tau_m \end{cases}$$

$$T_{mix} = \frac{\dot{m}_{blowdown} C_{p,s} T_{RCS} + \dot{m}_m C_{p,m} T_m + \dot{m}_{ox} Q_{ox}}{\dot{m}_{blowdown} C_{p,s} + \dot{m}_m C_{p,m}}$$

$$\dot{m}_{ox} = M_m \min\left(\frac{\dot{m}_m}{M_m}, \frac{\dot{m}_{blowdown}}{v M_v}\right)$$

$$\dot{m}_{conv} = f(p_{LDW}, p_{UDW}, T_{LDW}, T_{UDW}, A_{connect})$$

$$T_{conv} = \begin{cases} T_{LDW} & \text{if } \dot{m}_{conv} > 0 \\ T_{UDW} & \text{if } \dot{m}_{conv} < 0 \end{cases}$$

$$\frac{d(m_{LDW} C_{v,LDW} T_{LDW})}{dt} = \dot{m}_{blowdown} C_{p,s} T_{mix} - \dot{m}_{conv} C_{p,s} T_{conv}$$

$$\frac{dm_{LDW}}{dt} = \dot{m}_{blowdown} - \dot{m}_{conv}$$

Upper Drywell:

$$\frac{d(m_{UDW} C_{v,UDW} T_{UDW})}{dt} = \dot{m}_{conv} C_{p,s} T_{conv} - \dot{m}_{vent} C_{p,s} T_{UDW}$$

$$\frac{dm_{UDW}}{dt} = \dot{m}_{conv} - \dot{m}_{vent}$$

Table 1.4.3.1. The Transient CLCH Model (continued)

Wetwell:

$$\dot{m}_{H_2,WW} = f_{H_2}^{UDW} \dot{m}_{WW}$$

$$\dot{m}_{N_2,WW} = f_{N_2}^{UDW} \dot{m}_{WW}$$

$$\dot{m}_{H_2O,WW} = (1 - f_{H_2O}^{condense}) f_{H_2O}^{UDW} \dot{m}_{WW}$$

$$\frac{dm_{WW}}{dt} = \dot{m}_{H_2,WW} + \dot{m}_{N_2,WW} + \dot{m}_{H_2O,WW}$$

$$\frac{d(m_{WW} C_{v,WW} T_{WW})}{dt} = (\dot{m}_{H_2,WW} C_{p,H_2} + \dot{m}_{N_2,WW} C_{p,N_2} + \dot{m}_{H_2O,WW} C_{p,H_2O}) T_{WW}^{condense}$$

$$T_{WW}^{condense} = T_{UDW} (1 - \psi_{WW}) + T_{WW} \psi_{WW}$$

$$P_{WW} = \frac{m_{WW}}{M_{WW}} \frac{RT_{WW}}{V_{WW}}$$

Table 1.4.3.2. The Vent Model.

<p>Vertical Vent:</p> $\left\{ \frac{A_v}{nA_h} (L + D_h) + (H - z) \right\} \rho \frac{du}{dt} = P - (P_0 + \rho gz) - \frac{1}{2n^2} \left(\frac{A_v}{A_h} \right)^2 \rho u^2 (1 + C_{d,junc}); \quad u = \frac{dz}{dt}$ <p>(n is the number of vents yet to be cleared).</p> <p>Horizontal Vents:</p> <p>For $z > Z_i$: $(L + D_h) \rho \frac{du_h}{dt} = P - (P_0 + \rho gz) - \frac{1}{2} \rho u_h^2; \quad u_h = \frac{dx}{dt}$</p> <p>Venting Rate:</p> $\dot{m}_{vent} = \sum_i \delta_i f(P_{UDW}, P_{SP} + \rho_w g Z_{i,h}, T_{UDW}, T_{SP}, A_i)$ $\delta_i = \begin{cases} 0 & \text{if } x_i \leq L \\ 1 & \text{if } x_i > L \end{cases}$ $\dot{m}_{SP} = \dot{m}_{vent} \eta_{nc,UDW}$ <p>For details of the vent model derivation and nomenclature, see Appendix B.</p>

Table B.3.1 Summary of Various Predictions against the Experimental Data.

Test Series	Description	Data	TRACG	Present
5703-01	a. Short-term peak pressure (kPa)	193	200	205
	b. Vent clearing time (s)			
	- Top vent	0.86	0.85	1.18
	- Middle vent	1.15	1.15	1.48
	- Bottom vent	DNC	DNC	DNC
5703-02	a. Short-term peak pressure (kPa)	200	227.5	230
	b. Vent clearing time (s)			
	- Top vent	1.14	1.05	1.42
	- Middle vent	1.52	1.35	1.68
	- Bottom vent	DNC	DNC	DNC
5703-03	a. Short-term peak pressure (kPa)	252	289.6	293
	b. Vent clearing time (s)			
	- Top vent	0.99	0.85	1.16
	- Middle vent	1.19	1.05	1.35
	- Bottom vent	1.60	1.30	1.93

DNC denotes vent "do not clear".

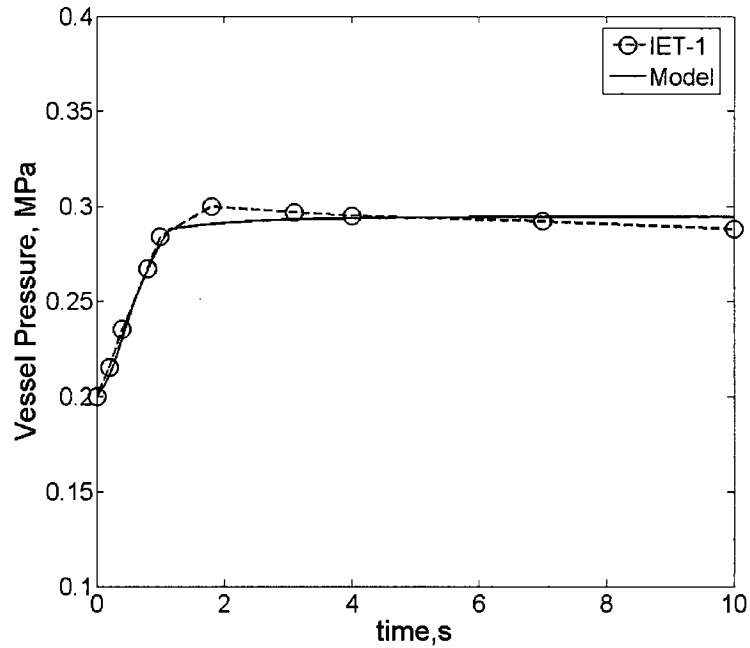


Figure 1.4.3.1. Prediction of DCH pressure in SNL IET-1 test.

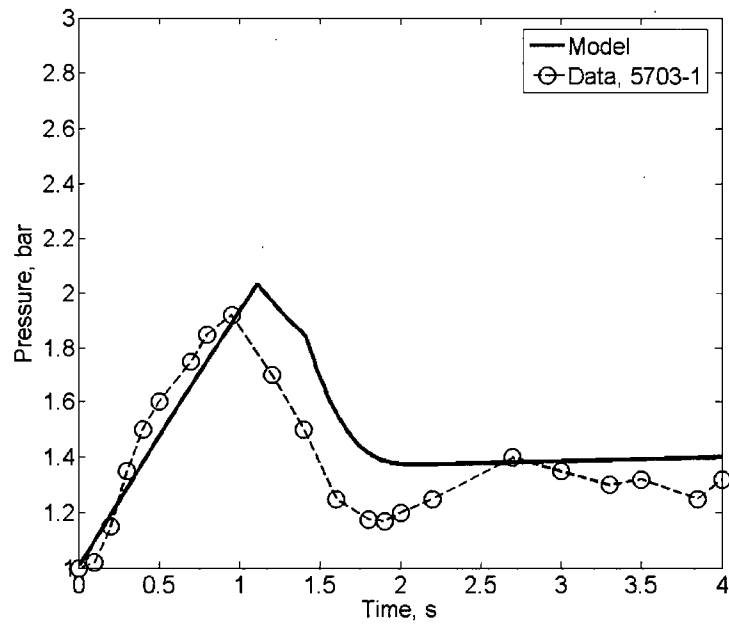


Figure 1.4.3.2. Prediction of drywell pressure in PSTF Test 5703-1.

Table 1.4.3.4. Geometry and Initial Conditions in Reactor Calculations.

Compartment	Parameter	Definition	Value
Primary System	V_{RCS}, m^3	Volume of RCS	500
	P_{RCS}^0, MPa	Pressure of RCS at blowdown	8
	T_{RCS}^0, K	Temperature of RCS at blowdown	800, 1500
	D_s, m	Vessel breach size (diameter)	0.2, 0.3, 0.5
Upper Drywell	V_{UDW}	Volume of upper drywell	6016 m ³
	P_{UDW}^0	Initial pressure of upper compartment	0.25 MPa
	T_{UDW}^0	Initial temperature of upper compartment	300 K
	$A_{connect}$	Area connecting upper and lower compartment through convection	14 m ²
Lower Drywell	V_{LDW}	Volume of lower compartment	1190 m ³
	P_{LDW}^0	Initial pressure of lower compartment	0.25 MPa
	T_{LDW}^0	Initial temperature of lower compartment	300 K
Wetwell	A_{pool}	Total area connecting the upper compartment to the suppression pool	16 m ²
	D_{vent}	Diameter of horizontal vent	0.7 m
		Number of rows of horizontal vents	3
		Distance between top and middle vents	1.37 m
		Distance between middle and bottom vents	1.37 m
	H, m	Height of water for clearing vent	Max. 5.45
	V_{ww}, m^3	Wetwell (free) volume	5400
Corium	$m_m^0, tons$	Initial corium mass in the lower drywell	50, 100, 300
	f_{Zr}	Mass fraction of metal Zr in corium	20%
	T_m^0, K	Initial corium temperature	2800
	$\Delta T_{m,sol}^0, K$	Initial superheat of molten corium	300

Table 1.4.3.5. Summary of Parameters and Variables used in Reactor Calculations.

Parameter	Parameter Definition	Reactor Case							
		A	B	C	D	E	F	G	H
m_m^0 (tons)	Initial mass of corium in the lower drywell	50	50	100	100	300	300	300	300
D_s , m	RPV hole size for steam blowdown	0.2	0.2	0.2	0.2	0.3	0.3	0.5	0.5
T_{RCS}^0 (K)	Initial temperature in the primary system	800	800	800	1500	800	800	800	800
τ_m (s)	Mixing time between melt and blowdown steam	7.8	3.6	10	10	7.8	10	3	6

Note: A set of common parameters used in reactor calculations (A-H cases) includes:
 Φ - Fraction of metal in entrained melt participating in steam-metal oxidation during blowdown; $\Phi = 0.5$
 α - Fraction of blowdown steam interacting with melt; $\alpha = 1$.
 $f_{H_2O}^{condense}$ - Efficiency of steam condensation in the suppression pool; $f_{H_2O}^{condense} = 1$.
 ψ_{WW} - Effectiveness of gas-coolant heat transfer in the suppression pool; $\psi_{WW} = 0.5$.

Table 1.4.3.6. Summary of Results of Reactor Calculations.

Parameter	Parameter Definition	Reactor Case							
		A	B	C	D	E	F	G	H
τ_s (s)	Blowdown time scale	28.7	28.7	28.7	28.7	12.8	12.8	4.6	4.6
$R = \tau_m / \tau_s$	DCH scale	0.27	0.14	0.35	0.35	0.61	0.78	0.65	1.3
P_1 (bar)	First (before vent clearing) pressure peak	3.35	3.3	3.3	3.1	4.0	4.0	4.7	4.7
P_2 (bar)	Second pressure peak	3.2	3.1	3.5	3.0	4.2	4.8	6.0	6.0
P_∞ (bar)	Long-term pressure	3.3	2.8	3.5	3.2	4.5	5.1	4.3	6.5
T_{STAB} (K)	Stabilized temperature	600	500	750	800	900	1000	1000	1200

Applied here as an example, at ESBWR conditions (800 K, 8 MPa, and 1,320 m³ LDW volume), Equation 1.4.3.1 yields $\tau_m = 7.8$ s. For 1 m break considered in the previous section, the blowdown time constant is $\tau_s = 1.1$ s, and thus the appropriate (for reference) DCH-scale value would then be ~ 7 . This means the blowdown would provide for full participation of steam in the DCH process (no incoherence). On the other hand, for a more reasonable break size, say the one noted as bounding the creep rupture type of vessel breach (0.5 m), the blowdown time constant would be 4.4 s, and the same melt entrainment time would produce a DCH scale of ~ 2 , that is still in the full utilization regime. Mitigation due to incoherence occurs only for penetration-type failures (0.2 to 0.3 m breaks), which yield quite long blowdown times and DCH scale values of 0.3 and 0.65 respectively. Thus immediately we can see that larger breaks involve not only stronger dynamics but also greater utilization of the steam in producing DCH loads.

These trends can be seen in a more tangible manner in the results of a series of calculations run for this purpose, as well as for the purpose of demonstrating upper bounds on pressurization and the margins to failure still available. The reactor data used in these calculations are summarized in Table 1.4.3.4, and the model parameter choices made to scope out the range of behavior are given in Table 1.4.3.5. As noted already the intent in choice of break areas is to span the range from an upper bound creep-type breach (cases G and H) to the more realistic penetration-type failures. Further we explore the sensitivity to the quantity of the melt involved, all the way to the maximum amount possible (300 tons), and also to the melt ejection time with parametric choices selected around the predicted value of 7.8 s. The sensitivity to the initial steam temperature is negligible, and in any case we use a conservatively low value of 800 K (the loads decrease with increasing steam temperature). All key results are summarized in Table 1.4.3.6, which will be used in the discussion that follows, along with Figures 1.4.3.4 to 1.4.3.11 depicting the calculated pressure transients, and Figure 1.4.3.12 depicting the temperatures obtained for the various cases.

Starting from the two large breach area cases (G and H), we see the same basic features as in the arbitrary-bounding case considered in the previous section, except that they are less accentuated. Now, rather than a peak in pressure of the LDW we have an inflection point, but the LDW and UDW pressures again equalize, and again there is a rapid cool-down following the melt entrainment period. However, there is also an essential difference in the dynamics of these two cases. The one with the rapid dispersal (case G), exhibits a peak pressure in the early, highly dynamic domain that does not involve, yet, the WW. The other (case H), with a more appropriate dispersal time, exhibits a double peak, the first being very similar to that of case G, while the second being of a quasi-static nature, and involving fully the WW volume. The two peaks are, quite coincidentally, of similar magnitudes (0.6 vs. 0.66 MPa). Now with reference to Table 1.4.3.6, we see that the DCH scales for these two cases are 0.65 and 1.3. This means that case G is steam-limited (note a final pressure of only 0.43 MPa), while case H is already close to the asymptotic regime of Yan and Theofanous (1996) — any further increases of the melt entrainment time would not lead to increased pressure levels beyond the 0.65 MPa found here. This quasi-static regime is also seen to dominate cases E and F. Here the DCH scale is less than 1, indicating the process is steam-starved. Indeed, the somewhat greater final pressure in F is due to differences in the amount of this steam limitation (DCH scale values of ~ 0.6 and ~ 0.8). This quasi-static

behavior, and effects of melt-steam incoherence, become more dramatic, as the breach area is further reduced, and the DCH scale, as a consequence gets even smaller (0.14 to 0.35) – cases A to D. These effects are also apparent in the UDW temperatures, reducing from a maximum value of ~1,200 for the near asymptotic case (H), down to 500K, as the DCH scale reduces from 1.3 down to 0.14.

As we will see in the next section these temperature levels would be of no concern to liner integrity, however, we do note that the LDW is subject, albeit for very short periods of time, to levels that can reach 4,000 K. In addition, in a postulated HPME and dispersal event, one would expect that melt, perhaps in significant quantities would contact the LDW liner. Both processes can induce local failures, and there is no way to know how likely this would be, except that (a) the situation could be possibly avoided if there is natural depressurization (the splinter discussed in Section 1.4.2), and (b) the melt might be effectively captured by the BiMAC device. Since both remedies are speculative, the potential for failure is acknowledged in the CPET's (see Chapter 4) and the Level-3 PRA.

See also Addendum to this Section at the end of Chapter 1.

Case A.

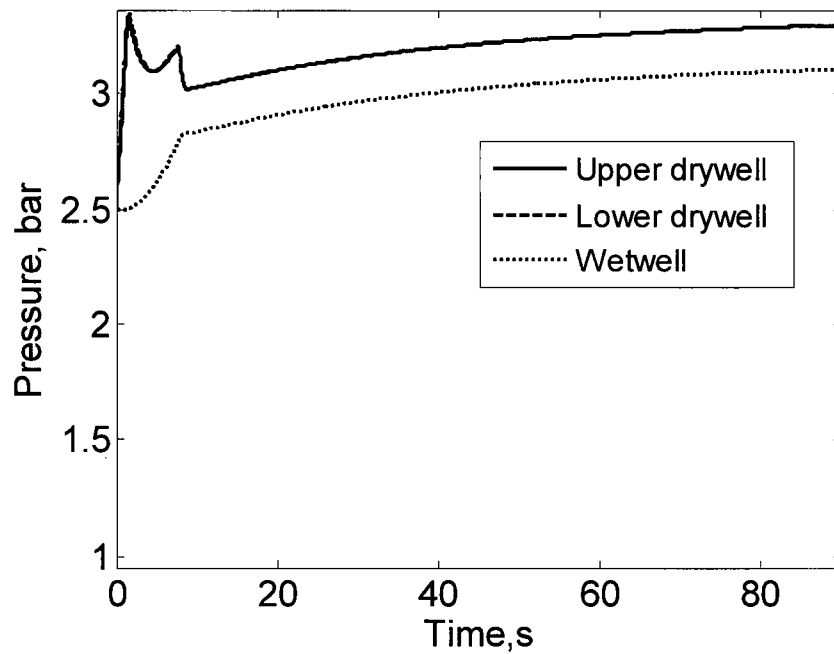
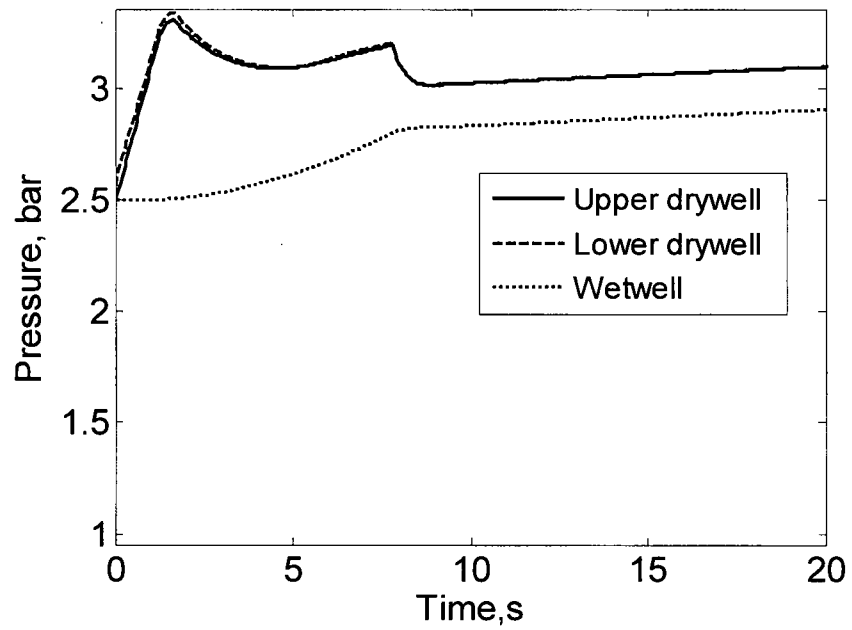


Figure 1.4.3.3. Predictions of pressures of in the DW and WW for Case A (pressures in the UDW and LDW follow each other closely, and are hardly distinguishable).

Case B.

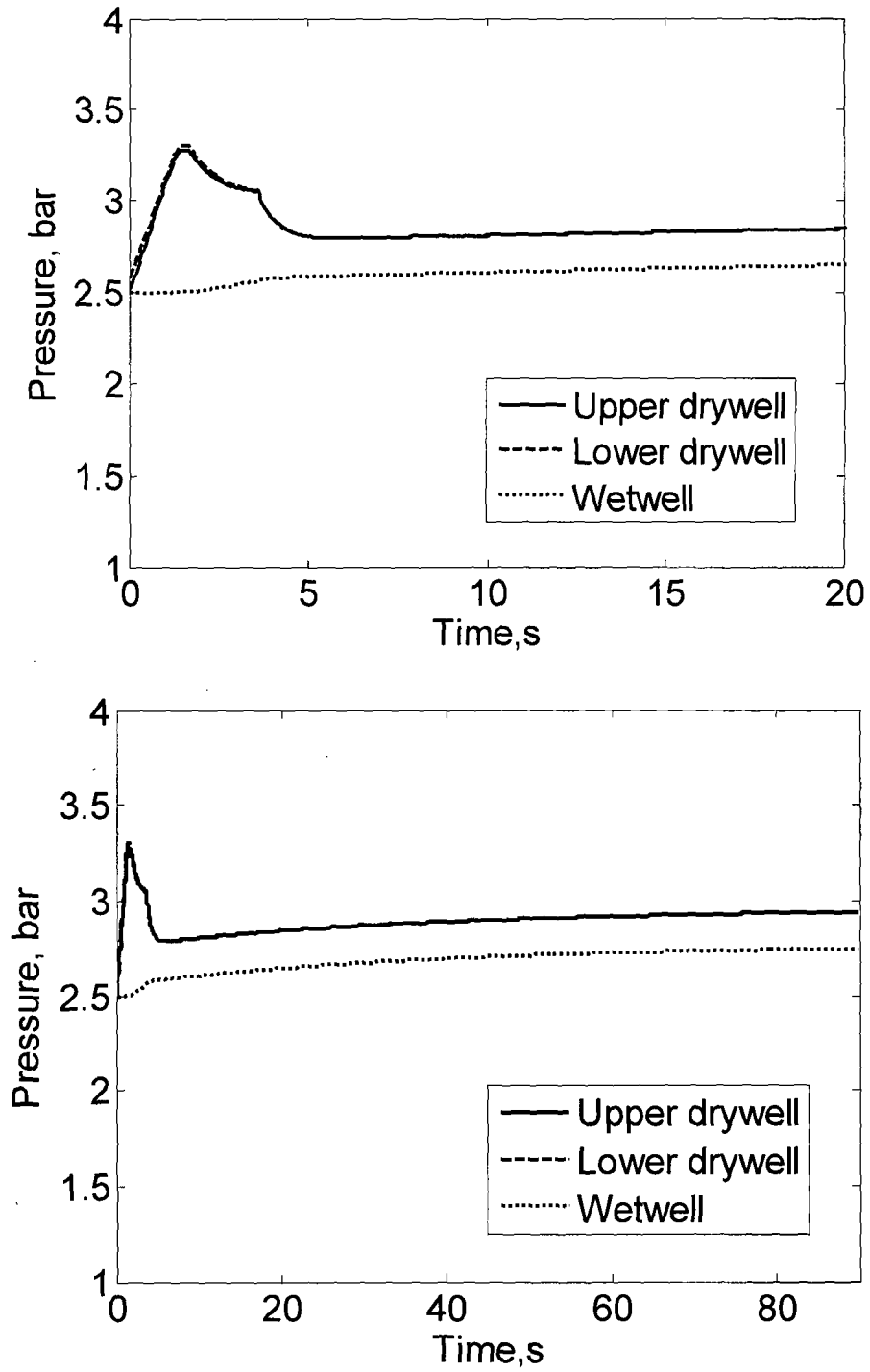


Figure 1.4.3.4 Predictions of pressures of in the DW and WW for Case B.

Case C.

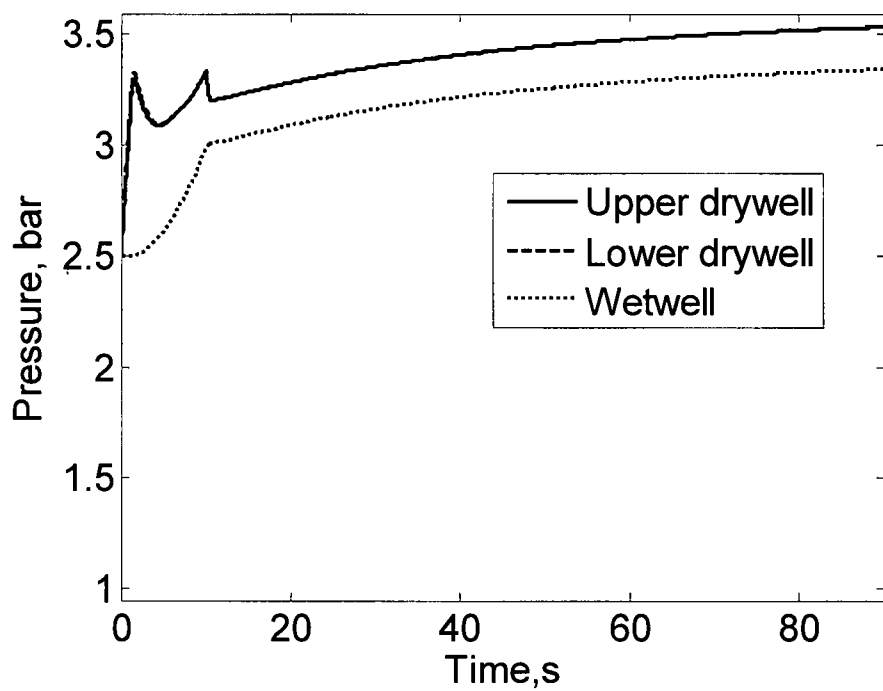
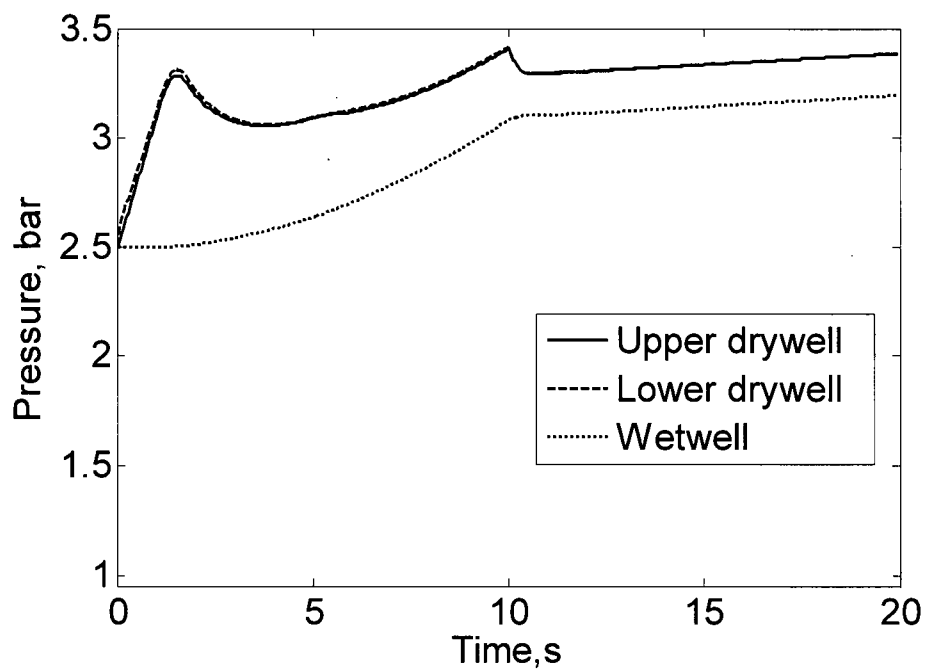


Figure 1.4.3.5. Predictions of pressures of in the DW and WW for Case C.

Case D.

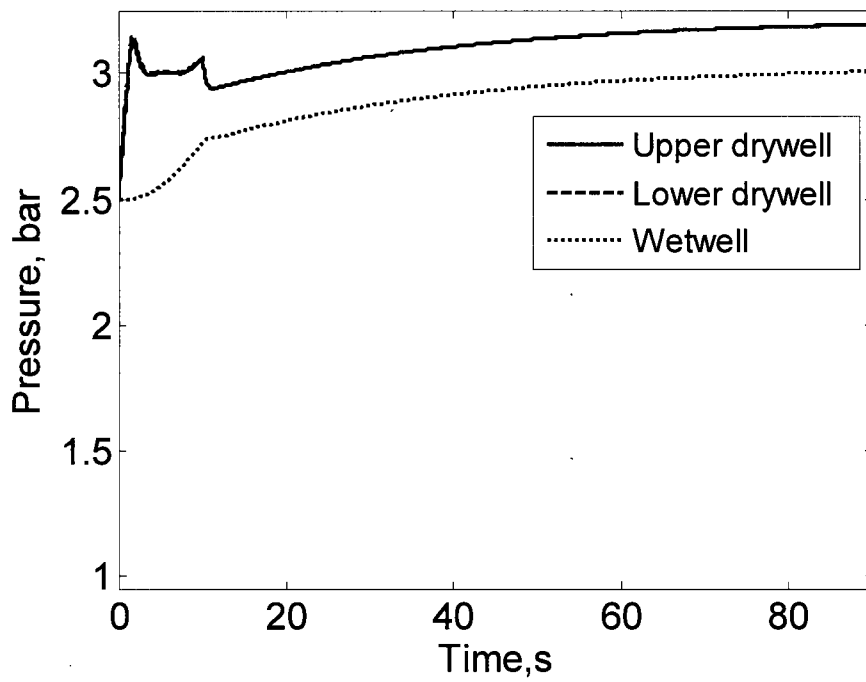
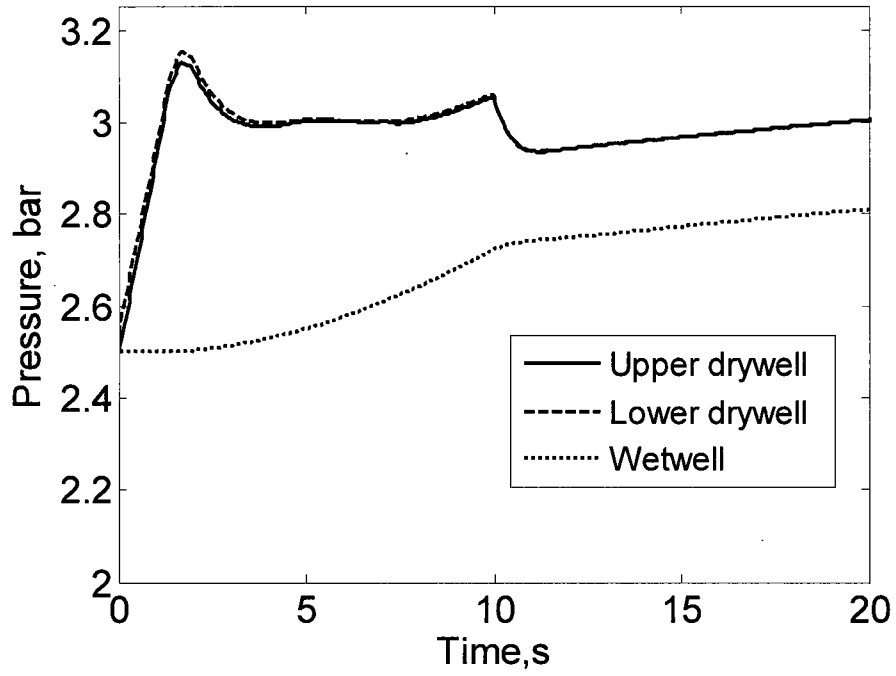


Figure 1.4.3.6. Predictions of pressures of in the DW and WW for Case D.

Case E

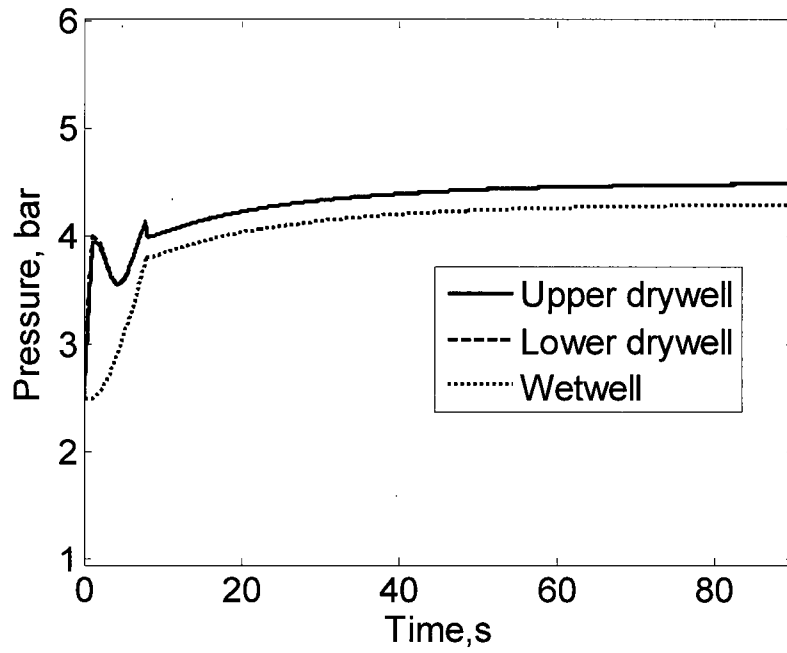
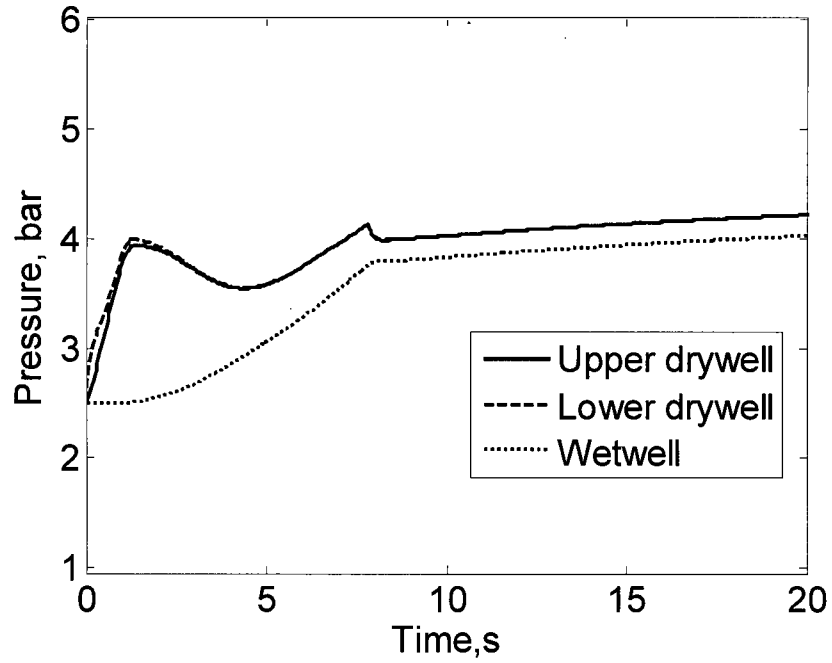


Figure 1.4.3.7. Predictions of pressures of in the DW and WW for Case E.

Case F

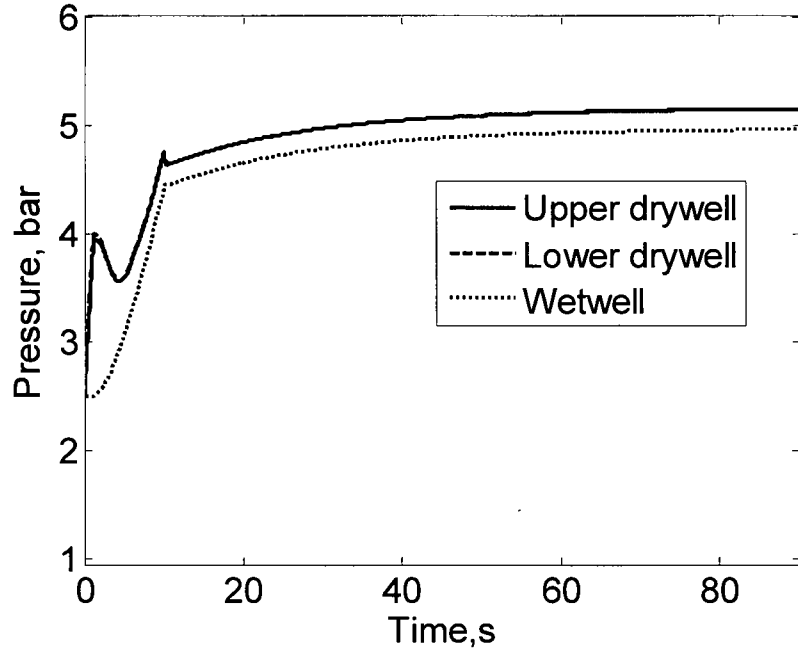
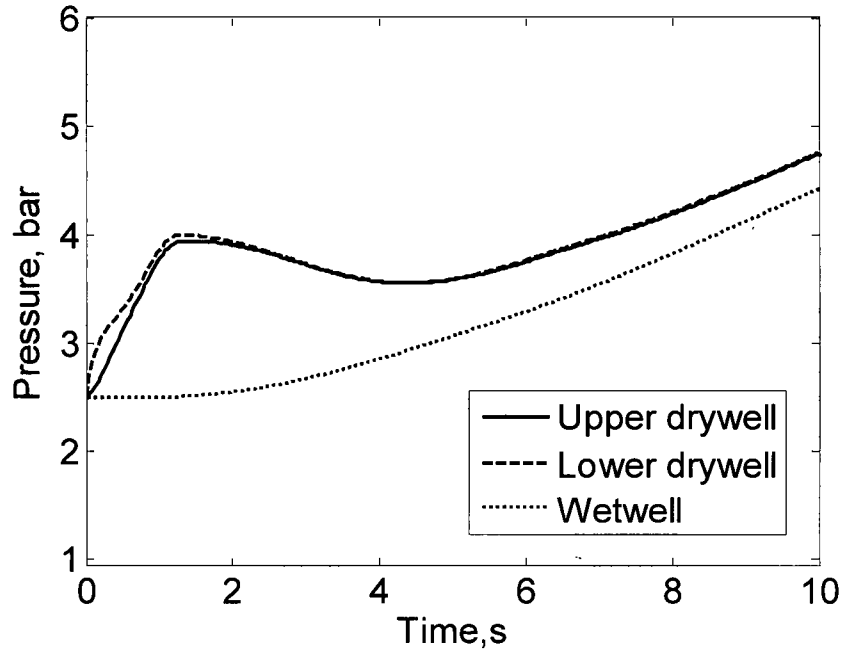


Figure 1.4.3.8. Predictions of pressures of in the DW and WW for Case F.

Case G

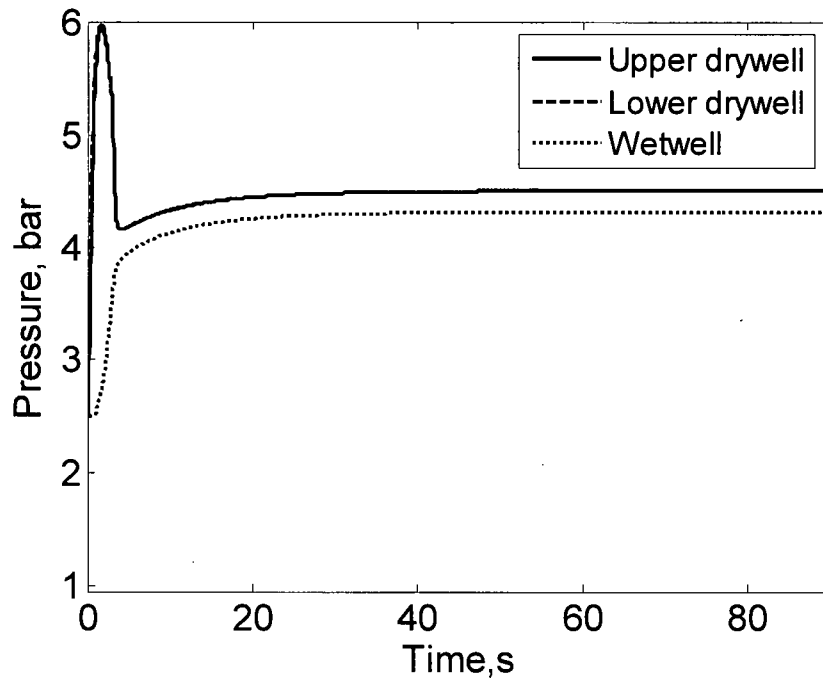
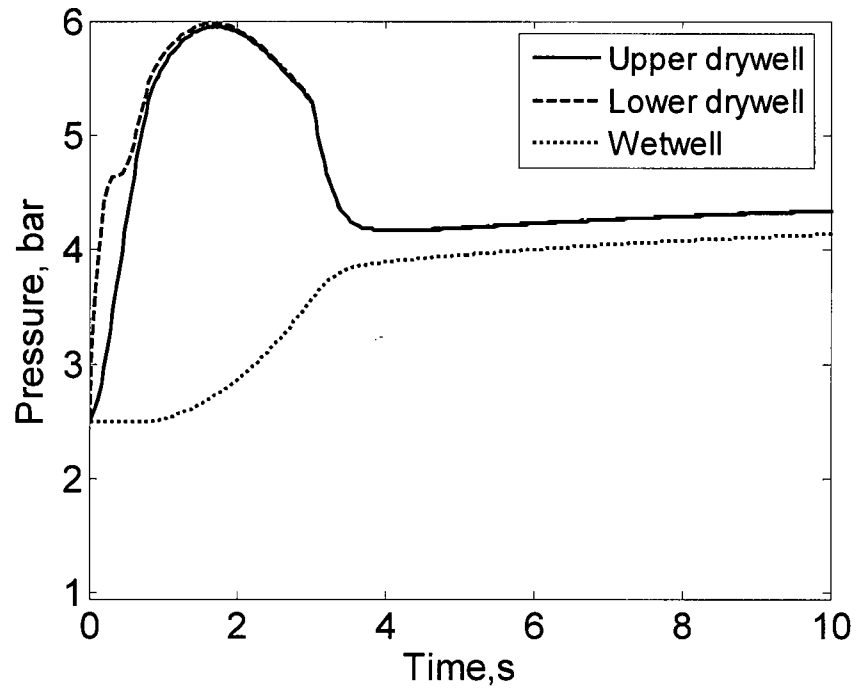


Figure 1.4.3.9. Predictions of pressures of in the DW and WW for Case G.

Case H

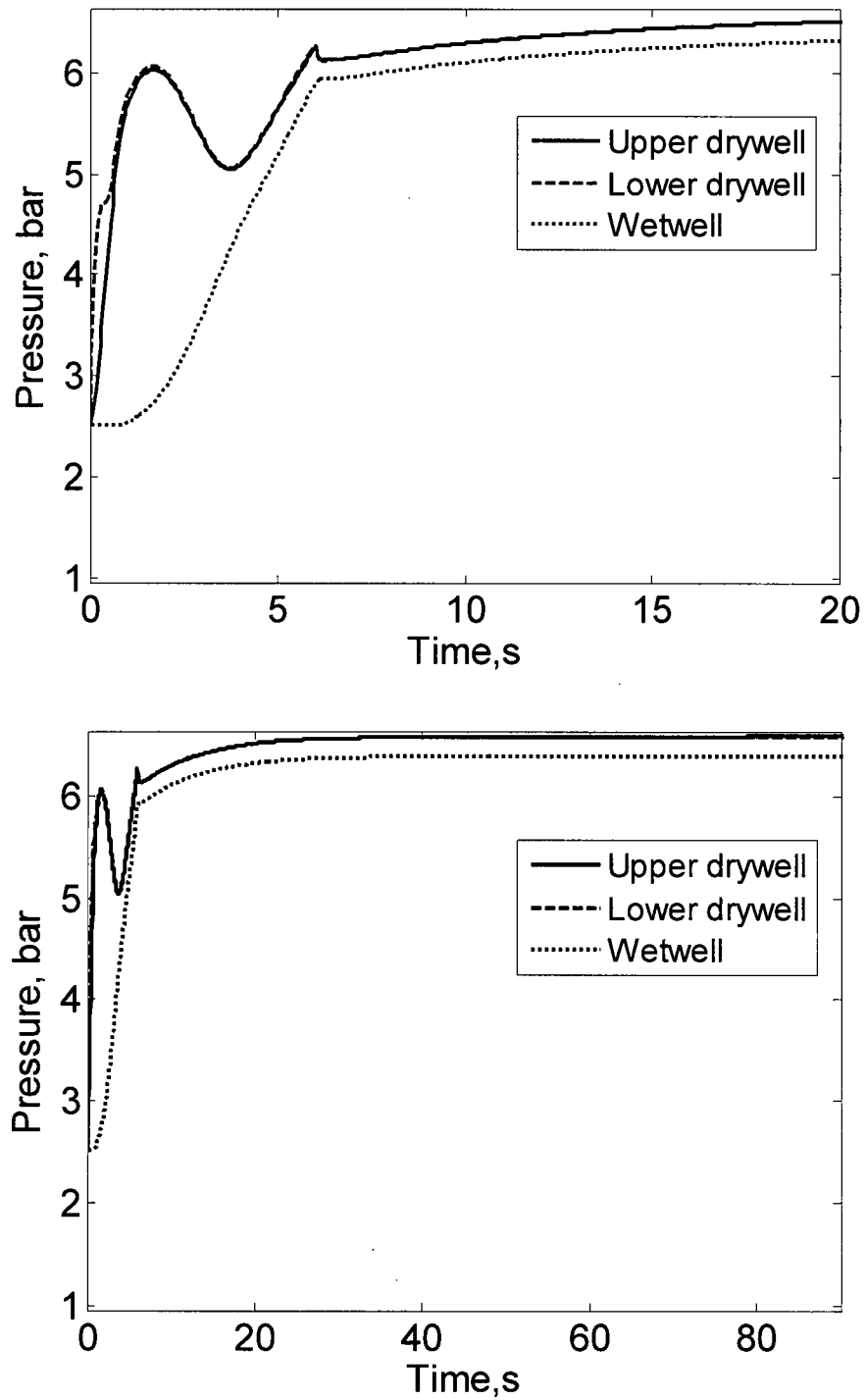


Figure 1.4.3.10. Predictions of pressures of in the DW and WW for Case H.

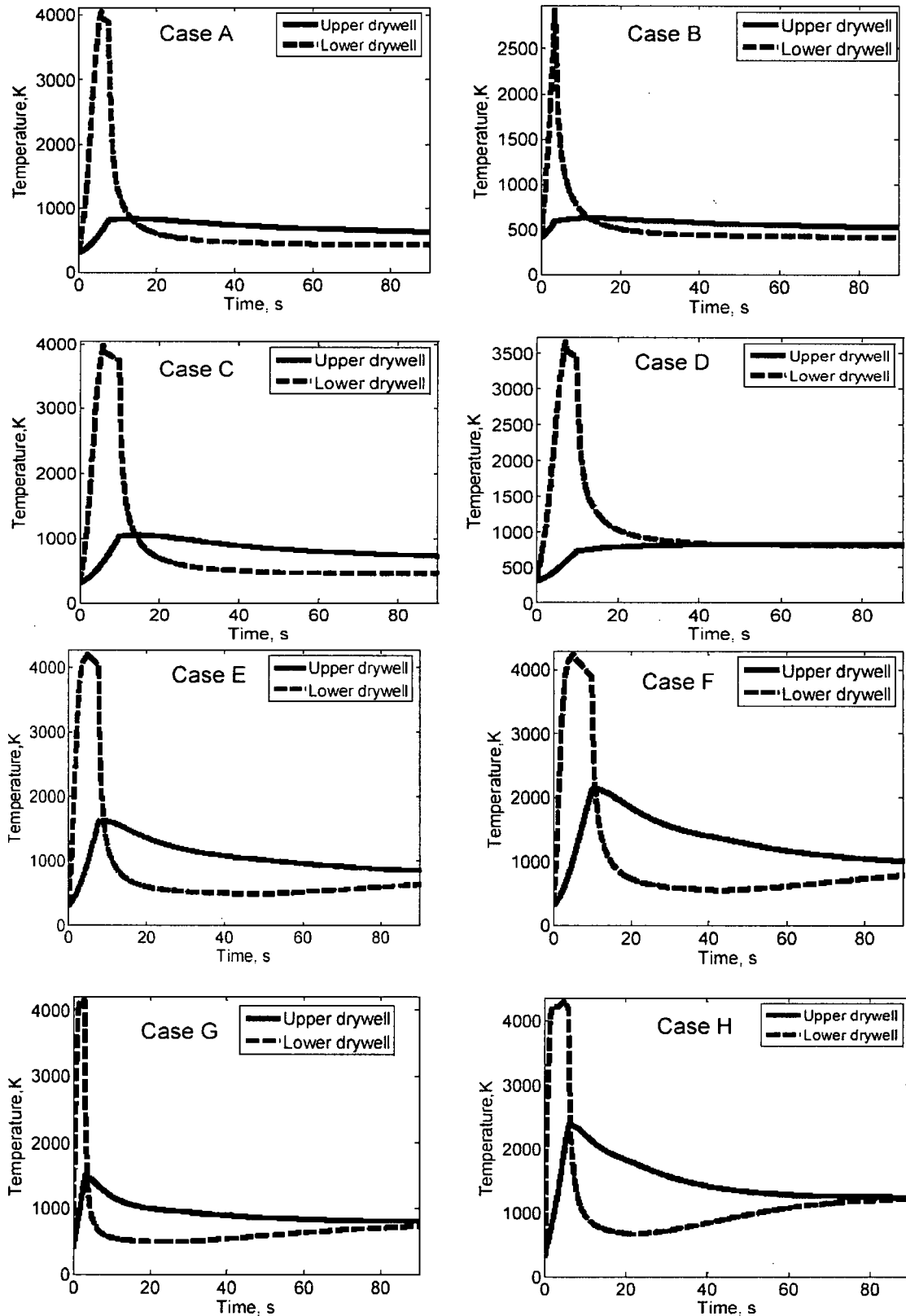


Figure 1.4.3.11. Predictions of gas temperatures in the LDW and UDW.

1.4.4. Quantification of Fragility to DCH

The ultimate capacity of the ESBWR containment structures, as documented in Chapter 8 of NEDC-33201, is summarized in Table 1.4.4.1. For DCH pressure loads, only the low temperature entries in this table are relevant. As we can see, the limiting component is the (torispherical steel) DW Head, estimated to be subject to incipient failure at a pressure level of ~1.2 MPa. The complete fragility, plotted from data supplied in the same document is shown in Figure 1.4.4.1.

Table 1.4.4.1 Ultimate Pressure Capabilities (evaluated at the 97% confidence level) of the ESBWR Containment.

Structural Component	Ultimate Pressure Capability MPa (gauge)		
	Ambient	~500 K	~800 K
Wetwell	4.33	3.90	1.94
Upper Drywell	4.80	4.32	1.89
Lower Drywell (Pedestal)	2.85	2.57	1.16
Suppression Pool Slab	1.47	NA	NA
Basemat	3.63	3.26	
Drywell Head	1.49	1.20	1.13

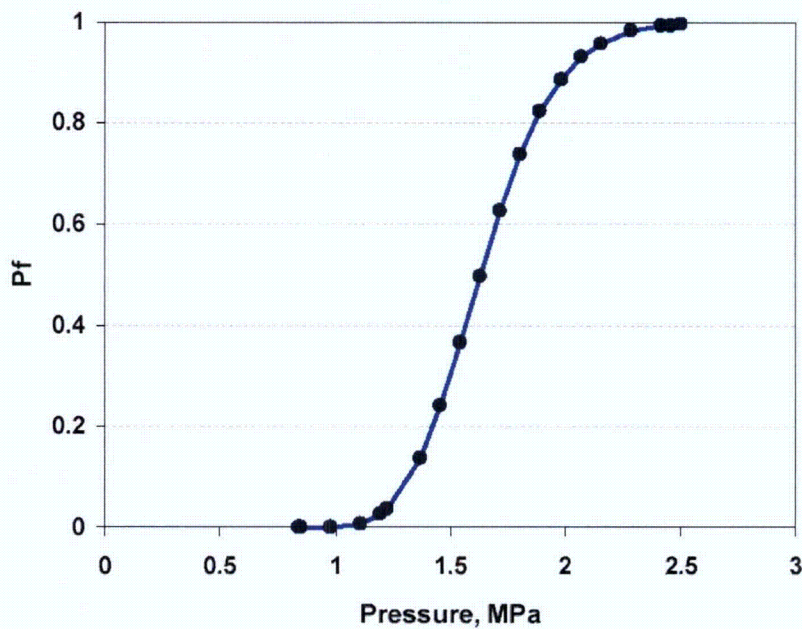


Figure 1.4.4.1 The drywell head fragility to internal pressure loads (from data in Chapter 8 of NEDC-33201).

Consideration of thermal expansion loads inducing liner buckling at the knuckle joint of the torispherical to the cylindrical sections of the TDH, and at the liner anchors, did not lead to concerns about liner failure at temperatures of up to 800 K. Further calculations were carried out using DYNA3D (2005) for temperatures reaching up to 1650 K. The temperature-dependent material properties utilized in these calculations are shown in Figure 1.4.4.2. A piece of liner in-between a neighboring set of anchors was considered and the presence of concrete backing was taken into account. The results as shown in Figure 1.4.4.3 indicate that creep is effective in releasing localized stresses, and that liner integrity is assured for temperatures up to near melting.

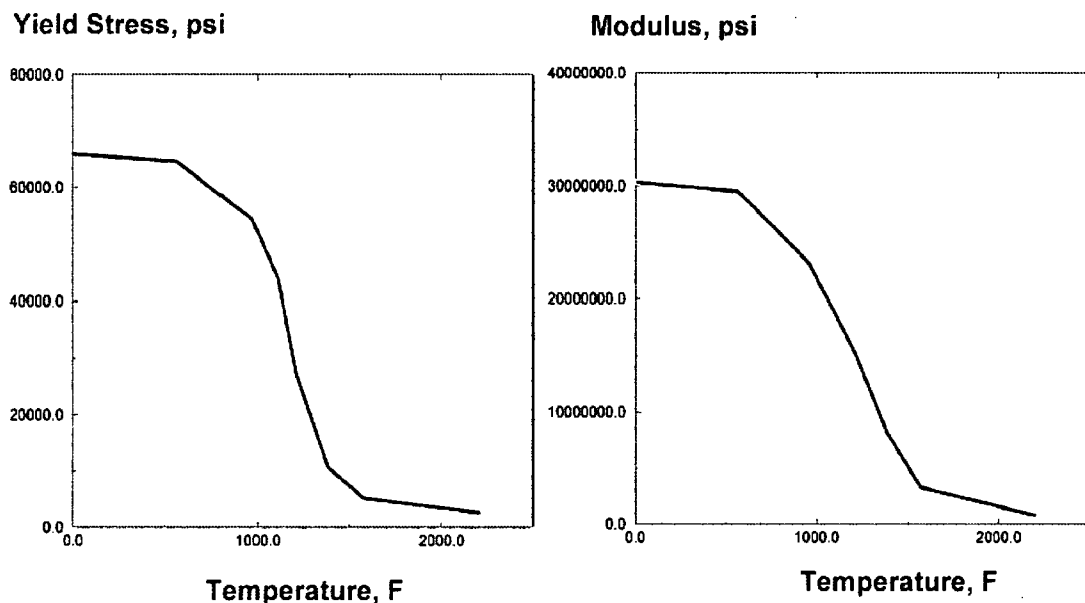


Figure 1.4.4.2 Temperature-dependent steel properties utilized in the finite element calculations of liner subjected to DCH thermal loads. (from Rashid, 1997).

Finally we address the UDW Head, and its sealing to the cylindrical top portion of the UDW. First we note that during normal operation this head is immersed in a water pool, and thus it remains cold during the whole duration of a HP meltdown sequence, even as the RPV heats up, and is in irradiative heat exchange with it. Bounding estimates of this process yield internal DW Head temperatures of less than 450 K, which is well within the range depicted in Table 1.4.4.1. This external cooling would be effective also in the long term, and quite sufficient in accommodating the thermal loads from the hot UDW atmosphere as it may develop during a DCH event. In fact, as shown in Figure 1.4.4.4, the access of these hot gases to the UDW is so extremely limited that any further heat transfer consideration in this regard would be rather superfluous.

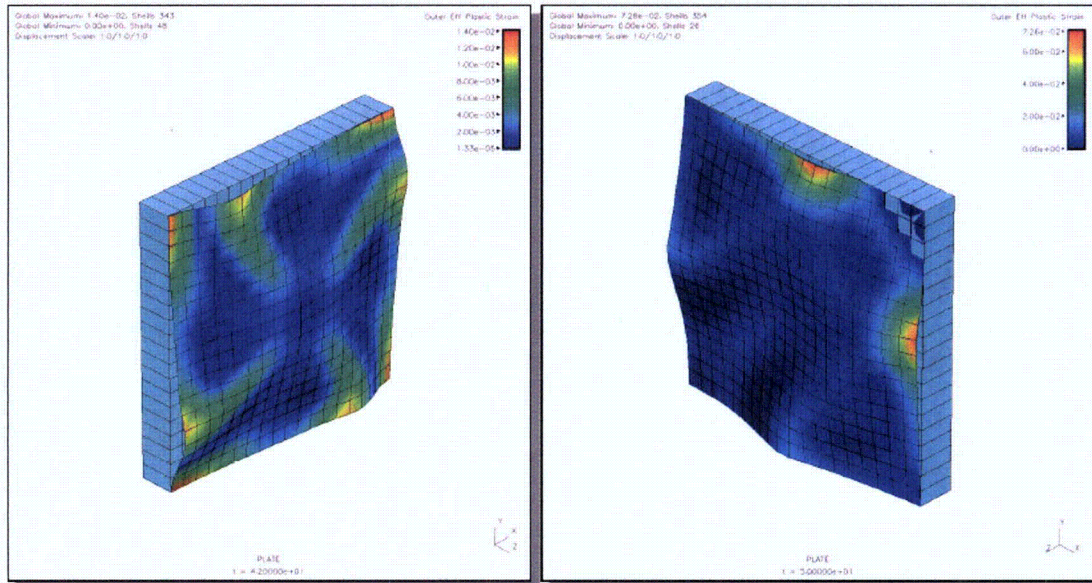


Figure 1.4.4.3 Effective plastic strains in a piece of liner in-between anchors at temperatures of 1400 K (left) and 1650 K (right). Maximum values calculated for the two cases are 1.4% and 7.26% respectively.

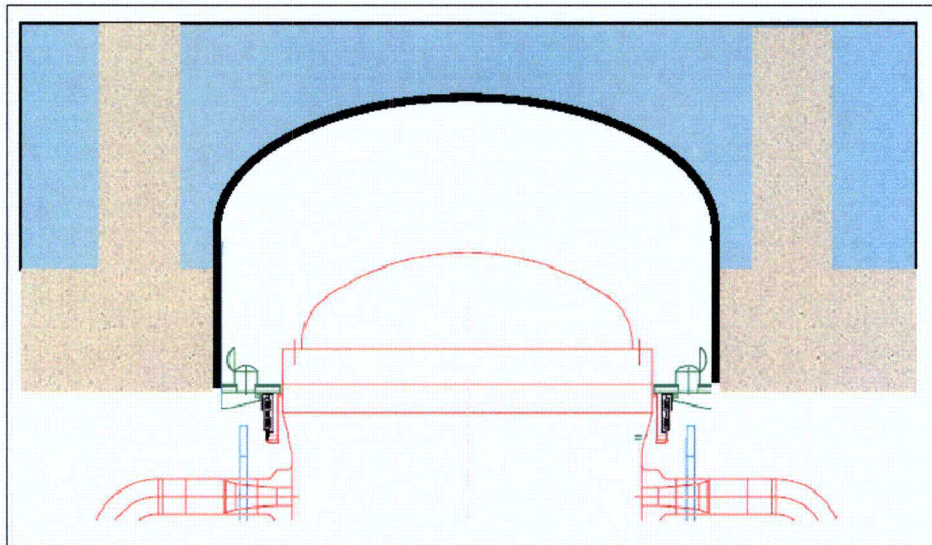


Figure 1.4.4.4. The upper drywell compartment (10.4 m diameter) contained between the UDW Head (in black) and the RPV Head (in red) is separated from the UDW's remaining volume by a refueling seal skirt (in green) with 4 access holes (each of 0.4 m² area) which are open during normal operation. Also shown is the water pool (blue) on top.

1.4.5. Prediction of Failure Probability due to DCH

Taken together the results of the previous two sections show that overpressure (catastrophic) failure of the ESBWR containment due to DCH is physically unreasonable. This conclusion covers all Class III accidents; that is, 1.3% of the CDF. The margins to failure, as shown by the bounding estimates of loads (upper bound) and fragility (lower bound) in Figure 1.4.5.1 are great indeed.

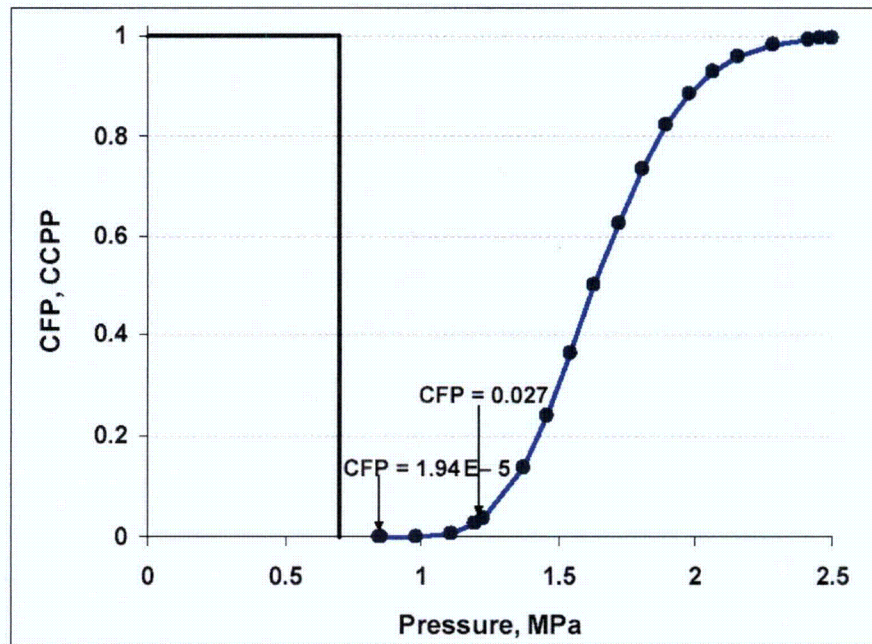


Figure 1.4.5.1 The margins to catastrophic failure in a DCH event, bounded at both ends. **CFP** is the ESBWR containment drywell head's cumulative failure probability. **CCPP** is the complementary cumulative pressure (load) probability due to DCH. The later is shown by an upper bound of 0.7 MPa which is case G, adjusted for an initial containment pressure of 0.4 MPa which is the maximum found in analyses of the core-degradation period in the Level II PRA analyses.

Thermally induced failure of the UDW Head and/or its seals is also physically unreasonable for all Class III accidents, as explained in the previous section.

Thermally induced failure of the liner, including the penetration areas, is relevant to Class III accidents in which DW spray is assumed to be not available, and these sequences amount to ~1% of the CDF. We find that even in these cases, strains due to thermal stresses are rather modest (< 8%) in relation to what might be considered necessary for cracking or tearing, even at temperatures approaching the melting point of the material. Bounding calculations of DCH-induced UDW temperatures indicate that the relevant temperature levels are ~1,000 K, which is considerably below the near-melting temperatures (over 1650 K) that could cause failure.

However, these calculations also show short periods of potentially very high temperatures in the LDW atmosphere (up to 4000 K). This, and the presence of potentially large quantities of melt in the LDW, indicate that the LDW liner could be subject to local failures, a condition that is noted in our HP CPET and is accounted for in Level-3 PRA.

1.5 Summary and Conclusions for DCH

The above results show that the ESBWR containment can withstand bounding DCH pressure loads and that catastrophic containment failure due to DCH is physically unreasonable.

Principal ingredients to such a conclusion can be recapitulated as follows:

1. The UDW atmosphere can vent into the WW through a large vent area and an effective heat sink,
2. The DW head is (externally) immersed in water, and essentially isolated, from the UDW atmosphere,
3. The containment steel liner is structurally backed by reinforced concrete, which cannot be structurally challenged by DCH.

Moreover, it is important to note that we have identified a splinter scenario for creep failure of the main steam line due to it being heated in the range of ~1,000 K. Such a failure would yield natural depressurization, and avoidance of HP melt ejection altogether. The so-made transition to a LP scenario would make available the GDCS for safety injection, thus possibly arresting the meltdown process.

We also show that UDW liner failure due to thermal loads is physically unreasonable, while for the LDW liner such failures cannot be excluded. However the ESBWR liner and the air-gap behind it are compartmentalized, providing a significant degree of isolation from such local failures, and thus providing a major interference to the flow path to the outside of containment. This is reflected in the HP CPET (Chapter 4), and the Level-3 PRA .

Table 1.5.1: Nomenclature to Chapter 1 (DCH)

a_{s0}	sound speed of steam
A_b	area of vessel breach
$A_{connect}$	area connecting LDW and UDW
C_p	specific heat at constant pressure
C_v	specific heat at constant volume
H	height of vertical vents
L	length of horizontal vents
m	mass
\dot{m}	mass flow rate
M	molecular mass
P	pressure
Q_{ox}	heat generated by oxidation of 1kg melt
t	time
T	temperature
V	volume
x_i	position of water slug in horizontal vent i
z	position of water slug in vertical vents
$Z_{i,h}$	vertical elevation of horizontal vent row i

Greek letters

β	virtual mass coefficient
η	discharge coefficient
η_{nc}	fraction of non-condensable gas
ρ	density
τ_m, τ_e	melt entrainment time during DCH
τ_s	blowdown time
ν	stoichiometric coefficient of oxidation reaction
Ψ_{WW}	effectiveness of gas-coolant heat transfer in SP

Subscripts

<i>conv</i>	convective transport between LDW and UDW
<i>LDW</i>	lower drywell
<i>m</i>	melt
<i>Mix</i>	melt-blowdown steam mixture
<i>RCS</i>	reactor coolant system
<i>UDW</i>	upper drywell
<i>WW</i>	wetwell
<i>v</i>	vapor
<i>0</i>	initial

1.6 References for Chapter 1 (DCH)

Allen, M.D., Pilch, M. M., Blanchat, T. K., Griffith, R. O., and Nichols, R. T. (1994), "Experiments to Investigate Direct Containment Heating Phenomena with Scaled Models of the Zion Nuclear Power Plant in the SURTSEY Test Facility," *NUREG/CR-6044, SAND93-1049*, Sandia National Laboratory, May 1994. Also in: The Integral Effects Test (IET-1) in the Surtsey Test Facility. 1991 Water Reactor Safety meeting; 28-30 Oct 1991; Washington, DC (SAND-91-2613C).

Binder, J. L., McUmbler, L. M., and Spencer, B. W. (1994), "Direct Containment Heating Integral Effects Tests at 1/40 Scale in Zion Nuclear Power Plant Geometry," *NUREG/CR-6168, ANL-94/18*, Argonne National Laboratory, September 1994.

DYNA3D (2004). Code Manual. Lawrence Livermore National Laboratory.

GE (1974). Mark III Confirmatory Test Program, Phase I - Large Scale Demonstration Tests, Test Series 5701 through 5703, NEDM-13377, October 1974.

GE (1987; 1994) General Electric. Standard Safety Analysis Report (SSAR) for ABWR (1994 Final Submission version).

GE-NE (2005a), ESBWR Certification Probabilistic Safety Assessment. NEDC-33201P. August 2005.

GE-NE (2005b), ESBWR Design Control Document. 26A6642BZ Rev.00. August 2005.

NRC (1994) U.S. Nuclear Regulatory Commission. "Final safety evaluation report related to the certification of the advanced boiling water reactor design",". NUREG-1503.

OECD/NEA/CSNI (1996). High pressure melt ejection (HPME) and direct containment heating (DCH): state-of-the-art report, 1996.. NEA/CSNI/R(96)25. OCDE/GD(96)194. Report prepared by Fauske and Associates Inc., Sandia National Laboratory in collaboration with NEA Group of Experts. 330p.

Pilch, M.M., Yan, H. and Theofanous, T.G. (1996), "The Probability of Containment Failure by Direct Containment Heating in Zion," *Nuclear Engineering & Design*, 164 (1996) 1-36.

Pilch, M.M. and Allen, M. D. (1996) "Closure of the direct containment heating issue for Zion", *Nuclear Engineering & Design*, 164, pp.37-60.

Pilch, M.M. (1994), Continued Enlargement of the Initial failure Site in the Reactor Pressure Vessel. Appendix J in NUREG/CR-6075, SAND93-1535. Also, *Nuclear Engineering and Design*, 164 (1996).

Pilch, M.M. (1996) "A Two-Cell Equilibrium Model for Predicting Direct Containment Heating", *Nuclear Engineering & Design*, 164, pp.61-94.

Pilch, M.M., Allen, M.D. and Williams, D.C. (1997) "Heat Transfer during Direct Containment Heating", V.29: Heat Transfer in Nuclear Reactor Safety. Elsevier, 1997.

Rashid, Y.R. (1997), "Creep Considerations of the Lower Head", *Nuclear Engineering & Design*, 169, 101-108.

Reddy, G.P. and Ayers, D.J. (1982), "High-Temperature Elastic-Plastic and Creep Properties for SA533 Grade B Class I and SA508 Materials", EPRI NP-2763, Electric Power Research Institute.

Scobel, J.H., Theofanous, T.G., and Sorrell, S.W. (1998), "Application of the Risk Oriented Accident Analysis Methodology (ROAAM) to Severe Accident Management in the AP600 Advanced Light Water Reactor," *Reliability Engineering and Safety Systems*, 62 (1998) 51-58.

Smith, G.V. (1971), "Evaluation of the Elevated Temperature Tensile and Creep Rupture Properties of C-Mo, Mn-Mo, and Mn-Mo-Ni Steels", Metal Properties Council, American Society for Testing and Materials, ASTM Data Series Publication DS47.

Theofanous, T.G. (1996), "On the Proper Formulation of Safety Goals and Assessment of Safety Margins for Rare and High-Consequence Hazards," *Reliability Engineering & Systems Safety*, 54 (1996) 243-257.

Yan, H. and Theofanous, T.G., (1993), "The Prediction of Direct Containment Heating," ANS Proceedings 1993 National Heat Transfer Conference, Atlanta, GA, Aug. 8-11, 1993, 294-309.

Yan, H. and Theofanous, T.G. (1996) "The Prediction of Direct Containment Heating," *Nuclear Engineering & Design*, 164 (1996) 95-116.

References in Addendum 1.4.3Add

Theofanous, T. G. Amarasooriya, W.H. Yan H. and Ratnam , U. (1991) "The Probability of Liner Failure in a Mark-I Containment," NUREG/CR-5423.

Theofanous T.G. et al. (1993) "The Probability of Mark-I Containment Failure by Melt-Attack of the Liner," NUREG/CR-6025.

1.4.3 Quantification of DCH loads (Addendum of July 31, 2006)

Subsequently to publication of this report, and as a result of internal audit checks, we found that due to miscommunication between this effort and other parts of systems design within the GE team, some of the basic inputs used in our evaluation of DCH loads had to be revised. The revised Table 1.4.3.4 is given as Table 1.4.3.4R. The purpose of this addendum is to supplement the previous quantification of DCH loads, using a completely verified set of reactor and containment design-related inputs. In addition we take this opportunity to more explicitly relate the various sets of melt release conditions assumed in the calculations to respectively-consistent melt relocation, and RPV failure scenarios.

The design-related input revisions are as follows:

- (a) The volume of RCS ($1,000 \text{ m}^3$) was taken as that of the SBWR (500 m^3), and the error was not caught in the original data audit because the ESBWR source (design) document was not available at the time.
- (b) Following a more detailed accounting of entities that occupy space in the wet-well, its free volume needed to be decreased from $5,400 \text{ m}^3$ to $5,000 \text{ m}^3$.
- (c) A typo in Table 1.4.3.4, showing the vent area as 16 m^2 is corrected to 13.6 m^2 .

Scenario-related input revisions are summarized in the following. As determined in the “Mark I liner attack”, ROAAM study (Theofanous et al, 1991, 1993), and confirmed by subsequent works, in BWRs, lower head failure is expected to occur in one of two possible, bifurcating scenarios. There is no way to assign relative probabilities to these, and thus in ROAAM we treat them both, independently, as “splinter scenarios.

- a) Scenario I involves a sudden release of a significant fraction of the core (~10 to 30 %) into the lower plenum, this initial release being followed by gradual relocation of the remaining core mass at rates that are basically determined by the rate of melting. For DCH the significance of such a release (~ 4 to 12 m^3) is that it would create the potential for immediate failure of one or more of the lower head penetrations (specifically by melting the welds on the instrument tube stubs), thus leading to an immediate high pressure melt ejection. Besides the melt quantity involved, this ejection would include the ~ 80 m^3 of water found at that time in the lower plenum, and, subject to two-phase choking, this ejection would last for 2 to 3 minutes—a time scale that is long enough to allow a great deal of thermal interactions at relatively low velocities, and thus a significant amount of quenching of the largely oxidic core debris, on the LDW floor, prior to it being subjected to the gaseous blow-down that would follow. Viewed in the light of the results presented originally (Table 1.4.3.6) it is rather obvious that Scenario I is not a significant DCH threat to containment integrity. Moreover, it should be quite clear that Scenario I would not lead to as significant temperature increases in the UDW, as found in the absence of water, perhaps not even in the LDW.
- b) Scenario II involves gradual releases from the core region, ready quench inside the lower plenum, and negligible potential for early failure of lower head penetration welds. Thus we expect that failure would require a dry-out and reheat cycle, and that it would occur much later, with essentially all the core debris found in the lower

plenum. Failure would occur via melt attack by the superheated metallic components, mainly steel and Fe-Zr eutectics, while the oxidic contents are still mostly in solid state. Considering that total quantities present, ~50 tons of metallic Zirconium and ~80 tons of steel, and the large thermal gradients due to relocation, quenching, composition, and convection history effects, bounding estimates of metallic mass available for release upon failure may be taken as 30% of the above quantities; that is 15 tons of Zirconium and 25 tons of steel, in total 40 tons of metallic melt. Thus for a consistent, but bounding set of high pressure melt ejection conditions, the values in Table 1.4.3.5Ra were used for DCH load quantification.

- c) In addition to the above, scenario-based definition, and for further perspectives on some of the cases shown previously in Table 1.4.3.5, calculations with a new set of release conditions, as found in Table 1.4.3.5Rb, and marked **arbitrary-parametrics** were carried out.

Since all basic behaviors and trends are as found and discussed in the first edition, results are summarized only in terms of peak pressures as shown in Table 1.4.3.6R. These results clearly verify and support our previous position on DCH loads, and thus our previous assessment of containment failure probability.

Table 1.4.3.4R. Geometry and Initial Conditions Used in Reactor Calculations.
(Previous values in Table 1.4.3.4, when different, are shown in parentheses)

Compartment	Parameter	Definition	Value
Primary System	V_{RCS} , m ³	Volume of RCS	950 (500)
	P_{RCS}^0 , MPa	Pressure of RCS at blowdown	8.5 (8.0)
	T_{RCS}^0 , K	Temperature of RCS at blowdown	800
	fH ₂ :fN ₂ :fH ₂ O	Gas molar composition (%)	0:0:100
Upper Drywell (UDW)	V_{UDW} , m ³	Volume of upper drywell	6016
	P_{UDW}^0 , MPa	Initial pressure of UDW	0.25
	T_{UDW}^0 , K	Initial temperature of UDW	420 (300)
	fH ₂ :fN ₂ :fH ₂ O	Gas molar composition (%)	25:65:10 (0:0:100)
	$A_{connect}$, m ²	Area connecting upper and lower compartment through convection	14
Lower Drywell (LDW)	V_{LDW} , m ³	Volume of lower compartment	1,190
	P_{LDW}^0 , MPa	Initial pressure of LDW	0.25
	T_{LDW}^0 , K	Initial temperature LDW	390 (300)
	fH ₂ :fN ₂ :fH ₂ O	Gas molar composition (%)	10;80;10 (0:100:0)
Wetwell	A_{pool} , m ²	Total area connecting the upper compartment to the suppression pool	13.6
	D_{vent} , m	Diameter of horizontal vent	0.7
		Number of rows of horizontal vents	3
		Distance between vent rows	1.37
	H , m	Height of water for clearing vent	5.45
	V_{WW} , m ³	Wetwell (free) volume	5,000 (5,400)
	P_{WW}^0 , MPa	Initial pressure of UDW	0.25
	T_{WW}^0 , K	Gas temperature in wetwell	370 (300)
	fH ₂ :fN ₂ :fH ₂ O	Gas molar composition (%)	50:35:15 (0:100:0)

**Table 1.4.3.5Ra. Release Conditions and Variables used
in Reactor Scenario-Based Bounding Calculations.**

Parameter	Parameter Definition	Bounding Case		
		A	B	C
m_m^0 (tons)	Initial mass of corium in the lower drywell (Scenario II, metallic melt)	40	50	50
D_s , m	RPV hole size for steam blowdown	0.2	0.2	0.3
T_{MELT}^0 (K)	Initial temperature	2300	2200	2200
τ_m (s)	Mixing time between melt and blowdown steam	10	15	10

**Table 1.4.3.5Rb. Release Conditions and Variables used
in Arbitrary-Parametric Calculations.**

Parameter	Parameter Definition	Arbitrary Case				
		V	W	X	Y	Z
m_m^0 (tons)	Initial mass of corium in the lower drywell (oxidic/metallic melt*)	100	100	100	300	300
T_{MELT}^0 (K)	Initial temperature	2400	2400	3000	2400	2400
D_s , m	RPV hole size for steam blowdown	0.2	0.3	0.3	0.3	0.5
τ_m (s)	Mixing time between melt and blow-down steam	20	10	10	12	8

* - In arbitrary-parametric calculations, the fraction of Zr is selected to reflect the material composition in full core, accounted for Zr oxidation prior to DCH ($f_{Zr} = 0.15$).

Note: A set of common parameters used in all of these calculations includes:

- Φ - Fraction of metal in entrained melt participating in steam-metal oxidation during blowdown; $\Phi = 0.5$
- α - Fraction of blowdown steam interacting with melt; $\alpha = 1.0$.
- Ψ_{WW} - Effectiveness of gas-coolant heat transfer in the suppression pool; $\Psi_{WW} = 0.9$.
- $f_{H_2O}^{condense}$ - Efficiency of steam condensation in the suppression pool; $f_{H_2O}^{condense} = 1$.

Table 1.4.3.6R. Summary of Results of Reactor Calculations.

Parameter	Parameter Definition	Bounding Case			Arbitrary Case				
		A	B	C	V	W	X	Y	Z
P_1 (bar)	First (before vent clearing) pressure peak	3.2	3.2	4.0	3.3	4.2	4.5	4.2	6.5
P_2 (bar)	Second pressure peak	5.0	5.8	6.8	7.0	7.3	8.0	7.7	10.1
P_∞ (bar)	Long-term pressure	5.7	6.3	7.7	7.4	8.1	8.6	8.5	10.8
T_{STAB} (K)	Stabilized temperature	750	850	800	1000	900	980	1000	1050

2. Containment and BiMAC-Device Performance Against Ex-Vessel Steam Explosions (EVE)

2.1. Overall considerations

Ex-Vessel Steam Explosions are energetic fuel-coolant interactions that are triggered from melt-coolant mixtures that are developed as the melt released from the RPV falls into, and traverses the depth of a water pool below. Metallic melts such as those expected here for low pressure scenarios are especially prone to such energetic behavior. The result is pressure pulses that may reach the kbar range. They are not quite sufficient to generate self-sharpening shock waves in water, but are potentially capable, when large quantities of melt are involved together with highly subcooled water, of loading major structures to failure. Failure is characterized by the impulse—the time-integral of the pressure acting on the surface of the structure (see Section 2.4.4).

While in-vessel explosions (IVE) are essentially of exclusive interest to PWR's, ex-vessel explosions (EVE) are of primary interest to BWR's. One reason is that in BWR's the initial release can be mostly metallic. Another reason is that LDW designs have traditionally employed very large-height geometries, which, when flooded, form deep water pools below the reactor vessel. Still another reason is that in BWR's the structural damage of the reactor pedestal can be much more serious to containment integrity than that of reactor cavities in PWR's.

From another perspective, these large geometries in BWR's have been thought of as a means to assuring long-term coolability for core-on-the-floor scenarios. The idea in this case is that deep flooding would provide sufficient travel distance for the melt to fragment and quench, thus forming a coolable debris bed on the LDW floor. Currently the Swedish-built BWR's operate under this premise. However, the efficacy of this coolability concept can be questioned, while at the same time the thus-generated threat to the structural integrity of the reactor pedestal has been raised (Theofanous et al, 1995, Almström et al, 1999).

In the ABWR SSAR (1994), while the term "steam explosion" is used, the actual calculations only reflect a mild steam spike with a peak pressure of 1 MPa. For the SBWR on the other hand, the EVE threat was appreciated, and a massive obstacle, the "corium shield" (a 4-inch-thick cylindrical steel piece surrounding the open LDW space), was incorporated to protect the reactor pedestal from such explosive loads. Such a shield is not necessary in the ESBWR design.

In the ESBWR, besides the pedestal we also need to be concerned about the "worthiness" of the BiMAC structure against such explosive events. We will show that this too can be build to withstand major explosive events, as is the pedestal. However, given the

uncertainties involved in mode of RPV failure, and in the simulation of 3D melt-water mixing and explosion in large geometries (deep, sub-cooled water pools in particular), we will **not** attempt to demonstrate that failure is physically unreasonable under all conceivable scenarios. Rather our management approach is based on limiting such scenarios so that at most we have to deal with shallow, saturated water pools. This turned out to be possible because of the simple design of the primary coolant system, and it was achieved by means of containment layout changes as described in the next section.

The simple idea is that there can be no explosions in the absence of water, and it is possible to show that this can be achieved in 99% of the Class I (that is LP) sequences. Water needs to be added to the LDW soon after the first ex-vessel melt relocation, this is done by means of a deluge system, and a complementary aspect of this approach is ensuring that this does not occur prematurely. As explained in detail in Chapter 3, a maximum unreliability of this LDW deluge system was placed at 0.1%.

This basic approach to the EVE threat is further buttressed by three additional elements:

- (a) Reiterating analyses that show shallow, saturated water pools to yield highly voided premixtures that resist triggering and escalation to detonation,
- (b) Showing that the pedestal can stand very strong energetic events involving melt pour rates of up to ~1 ton/s into sub-cooled water pools of depths up to 5 m,
- (c) Showing that the BiMAC can withstand perhaps not all, but a significant fraction of such arbitrarily severe conditions (relative to the cases of interest).

In regards to item (a), the basic ideas have been expressed previously by Henry and Fauske, 1981, Theofanous et al., 1987, and were further confirmed by others, including all experimental evidence available to-date. In regards to item (b), the basic idea is explosion venting as articulated and shown by the results in the first consideration of explosive load delivery in open pool systems (Yuen and Theofanous, 1995). Venting is an effect that produces a smaller impulse to distant structures by reducing both the time for the pressure wave unloading at the pool surface, as well as the amplitude of the wave that propagates radially outwards

The technology used in our assessment is based mostly on work done under DOE's ARSAP program, as summarized in Section 2.3, and on some follow up work done for the US NRC in the 1998-2003 time frame.

2.2. ESBWR Design

Regarding potential damage from EVE's, the relevant structures are the reactor pedestal, a 2.5 m reinforced concrete wall as illustrated in Figure 2.2.1, and the BiMAC device, a layer of thick-walled steel pipes that are well embedded into reinforced concrete in a way that they are supported in all directions as shown in Figure 2.2.2. The structural details of both are given in Section 2.4.4.

Failure of the reactor pedestal, along with the steel liner on it, would constitute violation of the containment boundary. While the load-bearing capacity of this structure is 2.85 MPa, explosive-level pressures acting on a millisecond time scales can produce sufficient extent of concrete cracking, along with liner stretching and tearing, to compromise leak-tightness of the containment. Failure of the BiMAC device on the other hand is defined as crushing (or locally collapsing) of the pipes so that they cannot perform their heat removal function — channeling the so-generated two-phase mixture from the bottom onto the top of the debris mass. Such failure would raise the possibility of continuing corium-concrete interactions, basemat penetration, and containment pressurization by the so-generated non-condensable gases.

As noted already the principal element of our approach on EVE is to address the quantities (and subcooling) of water in the LDW, just prior to melt exiting the RPV. It is at this time that the relocation can be potentially massive, and thus of energetic concern. In particular:

- (a) As a result of our early interactions with Level-1 PRA personnel and the ESBWR designers, modifications in the containment layout were made so as to prevent subcooled water, from entering the LDW through the UDW; in particular this covered the re-routing of GDCS overflow, and to prevent overflow of the suppression pool water to the LDW,
- (b) A BiMAC device activation system was defined (see Chapter 3) by integrating environmental signals (high temperatures) with valving action on the LDW deluge lines (feeding off the GDCS pools) so that premature flooding is to be reliably prevented.

Item (b), as discussed in Chapter 3 (on BMP), is based on a BiMAC design that makes it function immediately upon opening up the deluge lines. Thus there is no need to pre-flood the LDW.

In regards to building in additional margins, and with the pedestal already designed quite robustly to satisfy other structural considerations (load-bearing capacity under seismic conditions), our considerations focused on having a structurally robust BiMAC as well. As the structural response calculations in Section 2.4.4 show this was achieved to a significant degree by the choice of pipe diameter and wall thickness, and the embedded mutually supporting configuration.

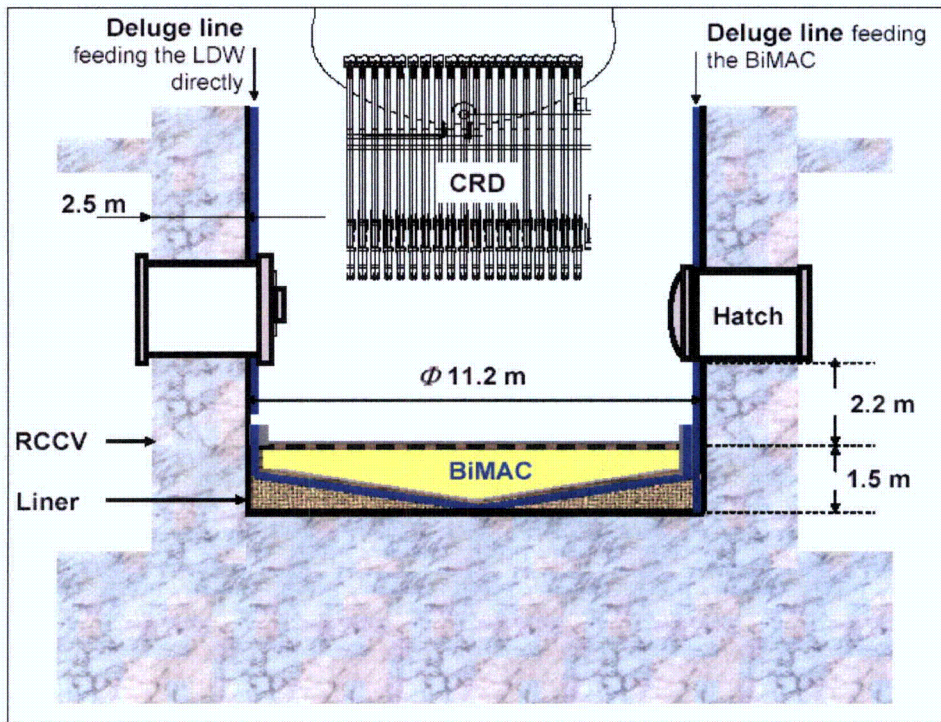


Figure 2.2.1 The overall LDW geometry relevant to EVE's, including the structural composition, and steel liner.

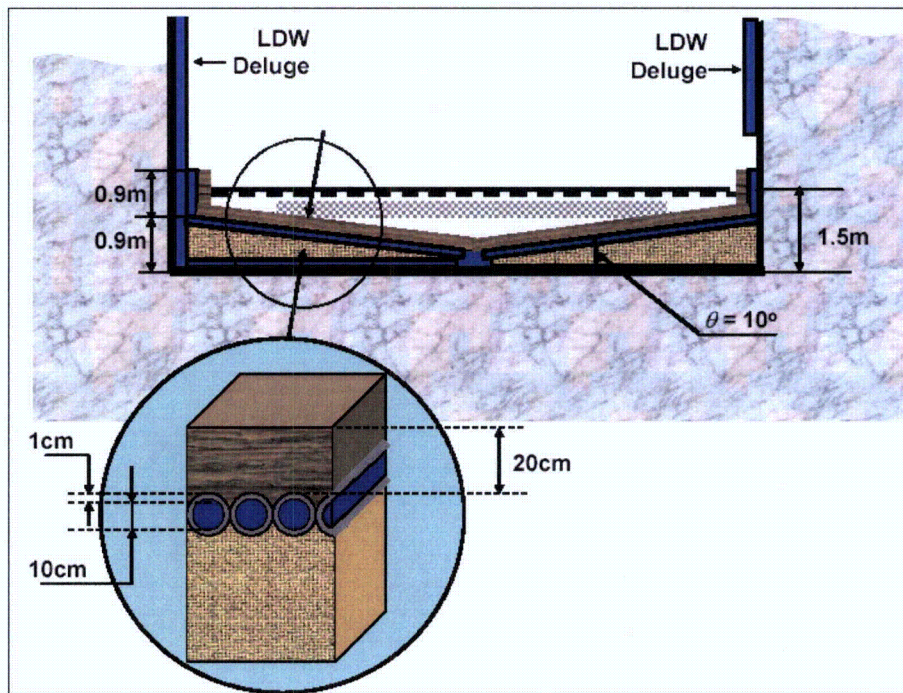


Figure 2.2.2 The BiMAC device in the pedestal region, and key dimensions of the geometry. The pipes are 10 cm in diameter (4") and 1 cm thick (schedule 80). The inset shows detail arrangement of BiMAC pipes embedded within the concrete, with a 0.2 m thick refractory layer on top.

2.3. Previous Work

The Steam Explosions Review Group (SERG) convened by the US NRC, in both of its meetings, focused on the alpha mode containment failure (SERG-1, 1985; SERG-2, 1995)—an energetic steam explosion in the lower plenum of the RPV, leading to the generation of internal and then external missiles that penetrate the containment shell. Thus only in-vessel steam explosions for PWR's were considered in detail. For BWR's, the lower plenum design, largely and densely occupied by control rod guide tubes, was considered to be generically prohibitive of the large scale events required for α -failure. Other licensing-related work for in-vessel steam explosions is the ROAAM-based consideration of α -failure in Sizewell B (Turland et al, 1994) and of lower head integrity for the AP600 (Theofanous et al, 1999c).

Major milestones in understanding the physics of steam explosions, and in the development of computational and modeling technology for simulating energetics, have been summarized previously by Theofanous et al (1987), Amarasooriya and Theofanous (1991), Theofanous et al (1994, 1995), Fletcher and Theofanous (1997), Theofanous and Yuen (1995), and Theofanous et al (1999abc). The key idea in modeling energetics is that of "microinteractions" (Yuen and Theofanous, 1999). The computer codes PM-ALPHA (Yuen and Theofanous, 1995) and ESPROSE.m (Yuen and Theofanous, 1995), for premixing and propagation respectively, are still the state-of-the-art (CFD simulation) tools. Verification and validation of these codes (Theofanous et al, 1999a, Theofanous et al, 1999b) has been documented and reviewed extensively (full ROAAM review) during the AP600 Design Certification effort. These codes are now also used by US NRC consultants during licensing reviews such as for ex-vessel explosions in the AP1000 (Westinghouse, 2002, Khatib-Rabar and Ismaeli, 2005).

There is no previous work on fragility to impulsive loads of a structure such as the BiMAC. Previous assessments of thick reinforced concrete walls, done only in a very crude manner (Rashid, Theofanous, and Foadian, 1995), indicates that an impulse magnitude of ~ 100 kPa.s could begin to inflict significant damage (cracking) on a reinforced concrete wall (pedestal) that is 1.5 m thick. At such levels of explosion impulse, cracking was found to be significantly reduced for a 7,000 psi concrete, and to be virtually eliminated for a 10,000 psi concrete. However, such improved grades of concrete are more expensive than the "normal" 5,000 psi grade considered for ESBWR.

We note in passing that the pedestal fragility in the ABWR safety analysis (ABWR SSAR, GE, 1994) was (stated to be) based on an approach similar to that applied for the Grand Gulf Mark III assessment of NUGEG-1150 (1990) — an approach based on energy absorption of a 6-cm-thick liner, that produced a failure impulse of 24 kPa.s. The ABWR result was expressed in terms of a peak pressure of "at least 0.85 MPa", this was then translated to a steam explosion involving 9.5% of the ABWR core (~ 22 tons), and on this basis it was concluded that "This failure mechanism need not be considered further in the containment event trees or the uncertainty analysis".

2.4. Present Assessment

2.4.1. Key Physics

In an open system, such as the LDW of the ESBWR, the susceptibility of a pre-mixture to triggering decreases as the volume fraction of steam (the void fraction) in it increases; thus subcooled water pools are considerably more prone to energetic behavior in comparison to saturated pools. On the other hand, the energetics of an explosion increases along with the total quantity of melt found in the pre-mixture at the time of triggering; thus explosions in deep pools can be more damaging in comparison to those in shallow pools. Both of these features, the subcooling and the depth, couple with a host of other parameters (melt mass break-up, momentum exchanges between melt and coolant, phase changes of coolant, etc) in a highly dynamic set of phenomena, to produce, for any particular mixing realization, an evolution of pre-mixtures, each one with a particular susceptibility to triggering and efficiency in thermal-to-mechanical energy conversion. As in our previous assessments done for licensing purposes (Theofanous et al, 1999c), both triggering and efficiency are treated here in a bounding fashion; that is, triggering is assumed to occur at the time of most favorable (least voided) premixture, and key limitations to energetics, such as fuel freezing during premixing, and non-equilibrium in the micro-interactions are not accounted for. So, in assessing EVE loads, we rely on well-qualified mechanisms and tools to account for pressure wave unloading/venting phenomena applied to idealized/efficient (to the extent that the Thermodynamics allow; this is where premixture voiding comes into play) explosions.

Current understanding of structural integrity under impulsive loading derives from work with high explosives (HE), acting mostly within a gaseous medium. In comparison to these explosions, in EVE's the pressure pulses would be of much lower amplitudes and of a much longer duration. Still, with a structure whose natural frequency is much longer than the pulse width, it is the delivered impulse that characterizes damage, and existing HE-derived tools, such as the DYNA3D code used in this work (Noble et al, 2005), can be expected to be well applicable. Again conservatively, in this application, we ignore the dissipative effects (and so-reduced actual loading) due to fluid-structure interaction. That is, pressure pulses obtained from explosion calculations carried out in a rigid wall geometry, are then applied to the structural calculation.

As concrete is highly resistant to compression but rather weak in tension, the mode of failure for the reactor pedestal is concrete cracking, separation from the rebar net, spallation at the "free end", and rebar-yielding that result in displacements sufficient to both, begin to lose load-bearing capacity as well as strain the liner to failure. In other words, to lose containment integrity, both the liner must be strained to failure (typically ~30% effective plastic strain) and the wall must be damaged enough to not be able to support leak tightness. Reinforcement, sometimes pre-tensioned, is employed to balance load-bearing performance in this respect. However, at the kbar range of pressures of interest here, this load-bearing is to reduce the extent, rather than eliminate cracking, and in any case it is not considered in this assessment. For the BiMAC, the same mechanisms are superposed to yield deformation of the steel pipes, and eventually plastic yielding that when it is of sufficient extent leads to collapse, and thus failure of BiMAC function.

2.4.2. Probabilistic Framework

According to our emphasis in eliminating melt-down sequences that involve deep, subcooled water pools in the LDW, our quantification approach is largely based on the Integrated ROAAM; that is, accounting for aspects of the design that prohibit such large-scale contact scenarios. In this task our work has interacted with Level I PRA and in the end it has been informed by the results obtained thereby. The rest of our task is to demonstrate some significant margins, both for the Pedestal and the BiMAC, even in many scenarios that are postulated to not meet the criteria of “shallow, saturated pools”, and this will be done rather roughly, as we feel this is consistent with the demonstration needs in this case.

In treating the EVE threat we need only consider Class I accidents. They amount to ~90% of the CDF, and of these the proportions with High ($H > 1.5$ m), Medium ($0.7 < H < 1.5$), and Low ($H < 0.7$) water pool depths (on the LDW floor, at the time of vessel breach) are 0.9%, 0.1%, and 99% respectively. Adjusting these proportions for the 0.6% of the Class IV accidents that revert to Class I with Low water pool levels is not significant. This in combination with the extremely low CDF, satisfies the Integrated ROAAM criteria for ignoring scenarios that are remote and speculative.

The 1.5 m demarcation for the “deep” water pool was selected in consideration of the position of the hatch door, combined with a collective judgment in which we aimed to leave out ranges of conditions that we do not feel could be reasonably captured by current capabilities and experience. On the other hand it should be noted that this choice is not critical to our conclusions—we found that those rare sequences that exceed the low height category ($H < 0.7$ m) tend to produce fully-flooded LDW conditions (which are also subcooled), while the low level category results from condensation processes thus yielding saturated pools.

As noted above saturated premixtures become highly voided, and are highly resistant to supporting the escalation of spontaneous triggers towards detonations. Moreover, even if any explosions were to be developed, they would be rather inefficient, and of low energetics. One task in the next section is to illustrate this behavior for shallow/saturated pools. Our other task is to contrast this behavior with that of subcooled/deep pools, and provide some perspectives on the level of energetics that could possibly result in the latter case. This then together with the perspectives on structural failure provided in Section 1.4.4 will yield an understanding of the resilience of these structures to hypothetical energetic events from EVE's.

2.4.3. Quantification of Loads

Steam explosion calculations were carried out with the PM-ALPHA.L-3D, and ESPROSE.m codes for water pool depths of 1, 2 and 5 m with 100 K subcooling. The 2 m deep case was also considered with saturated water. In all cases the pour rate was set at 720 kg/s, which was based on a penetration failure and gravity draining aided by 0.2 MPa overpressure. In the premixing calculation the melt enters the domain over an area of $\sim 0.03 \text{ m}^2$, with a velocity of 13 m/s, and a volume fraction of 22%.

The premixing calculations were run in 3D, while for the explosion, in order to capture the wave dynamics at a sufficient resolution, the calculations were run in 2D axi-symmetric geometry. Grid-convergence studies were made to confirm that this is indeed the case. The proximity of the explosion to the sidewall (off-center pours) was investigated by using domains of 4 m in diameter. The positions for which dynamic loads are given are summarized in Figure 2.4.3.1.

All parameters in these computations were selected in a conservative fashion, and consistently with experience from previous such assessments (i.e., Theofanous et al, 1996). In particular, for the key explosion parameters β and γ (β is the fragmentation model parameter, and γ is the thermal enhancement factor that is used to account for the effect of pressure on microinteractions) we have used values of 9 and 4-2-1 (that is, a value reducing from 4 to 2 to 1 as local pressures increase from ambient to 1 kbar), consistently with the interpretation of the highly energetic KROTOS tests (Theofanous et al, 1999b).

The premixing results are summarized in Figures 2.4.3.2 (a) to (d). In all cases there is the characteristic opening up due to the initial plunging (see also Appendix C), however the subsequent evolutions are quite different between the saturated and subcooled cases. In particular in (a) we see that at $t=0.48 \text{ s}$ there is an attempt to collapse, however further boiling leads to arrest and further expansion, while in all subcooled cases we see that this closing is actually completed to significant degree, thus leading to potentially energetic premixtures. Moreover we note that the collapse itself could provide the trigger needed to produce an explosion precisely at this opportune, from a premixing standpoint, time. One-to-one comparison is given in Figure 2.4.3.2 (d) to further illustrate the differences in voiding patterns.

As expected the highly voided premixtures in the saturated pool case could not be made to escalate even with rather energetic triggers. All other cases produced explosions, and the results are summarized in Figures 2.4.3.3 (a) to (d) in terms of the pressure transients and the resulting impulses on the bottom and the sidewalls. We can see that with one exception typical primary impulses on the bottom are $\sim 100 \text{ kPa s}$, while on the side they increase with pool depth from ~ 40 to 150 kPa s . Also we can see the effect of venting, as in the deeper pools there is a second pulse due to side wall reflections that remain strong. These second pulses are of course not relevant to the open geometry of the LDW for pool depths of 1 or 2 meters.

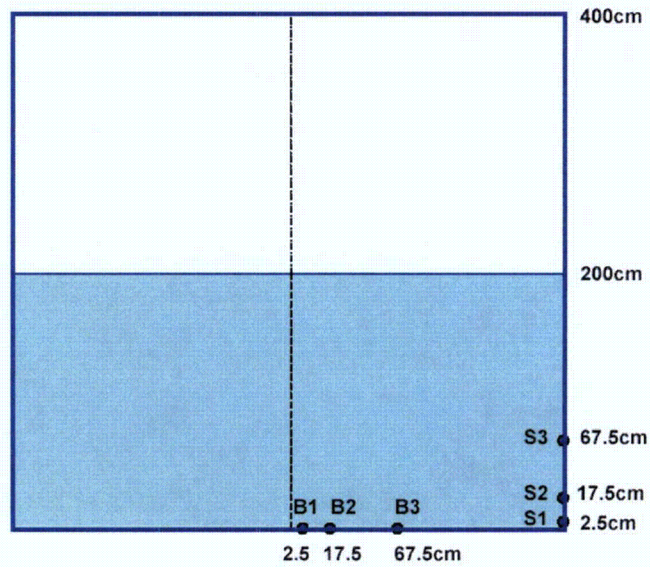


Figure 2.4.3.1 The computational domain of a cylindrical cavity utilized in the ESPROSE.m calculation for the 2 m deep water pool case. B1, B2 and B3 are locations on bottom wall (basemat) and S1, S2 and S3 are locations on the sidewall (pedestal), where pressures and impulses are provided in subsequent figures. These locations remain the same for all pool dimensions considered.

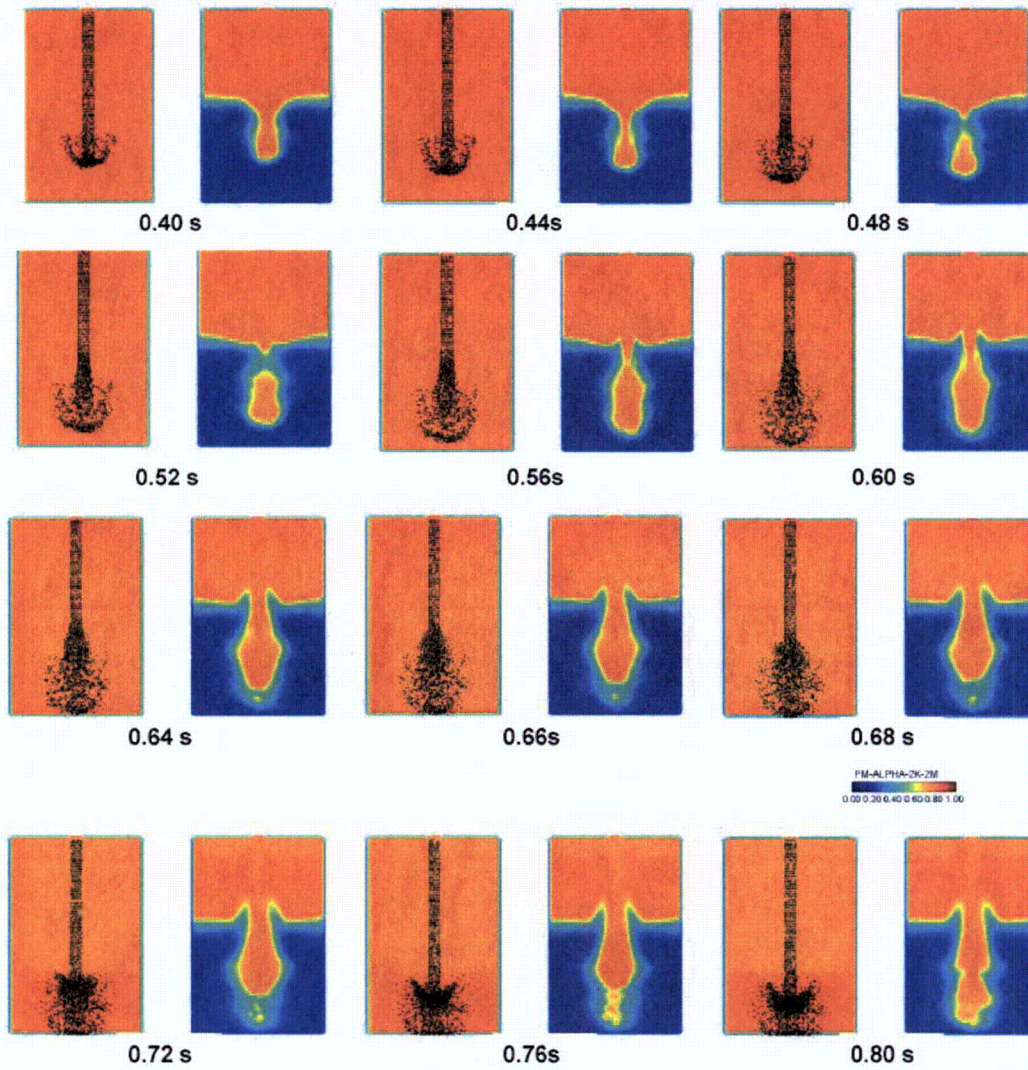


Figure 2.4.3.2a. Evolution of premixtures in a 2-meter-deep pool, 2 K subcooling. Melt (left) and void fraction (right) distributions.

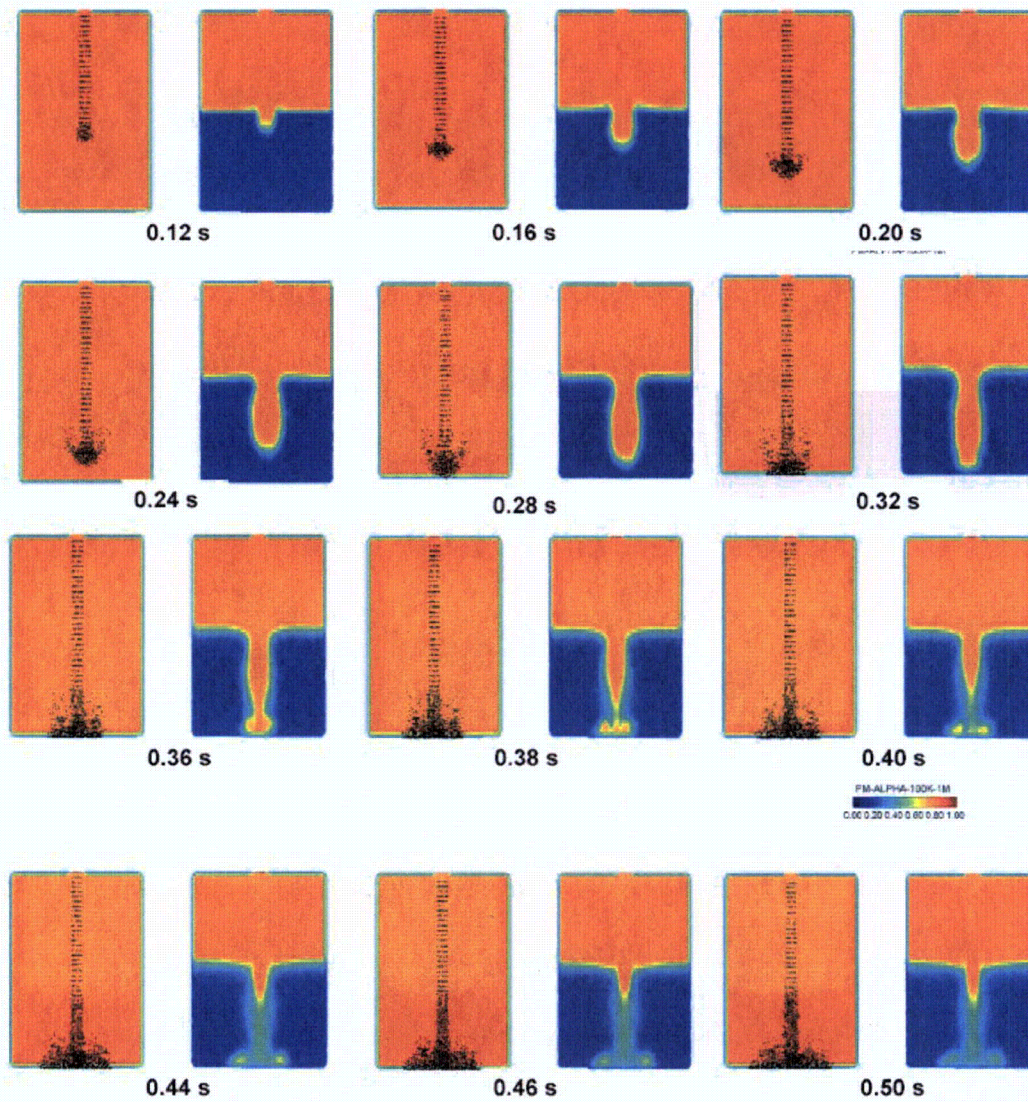


Figure 2.4.3.2b. Evolution of premixtures in an 1m-deep pool, with 100 K subcooling. Melt (left) and void fraction (right) distributions.

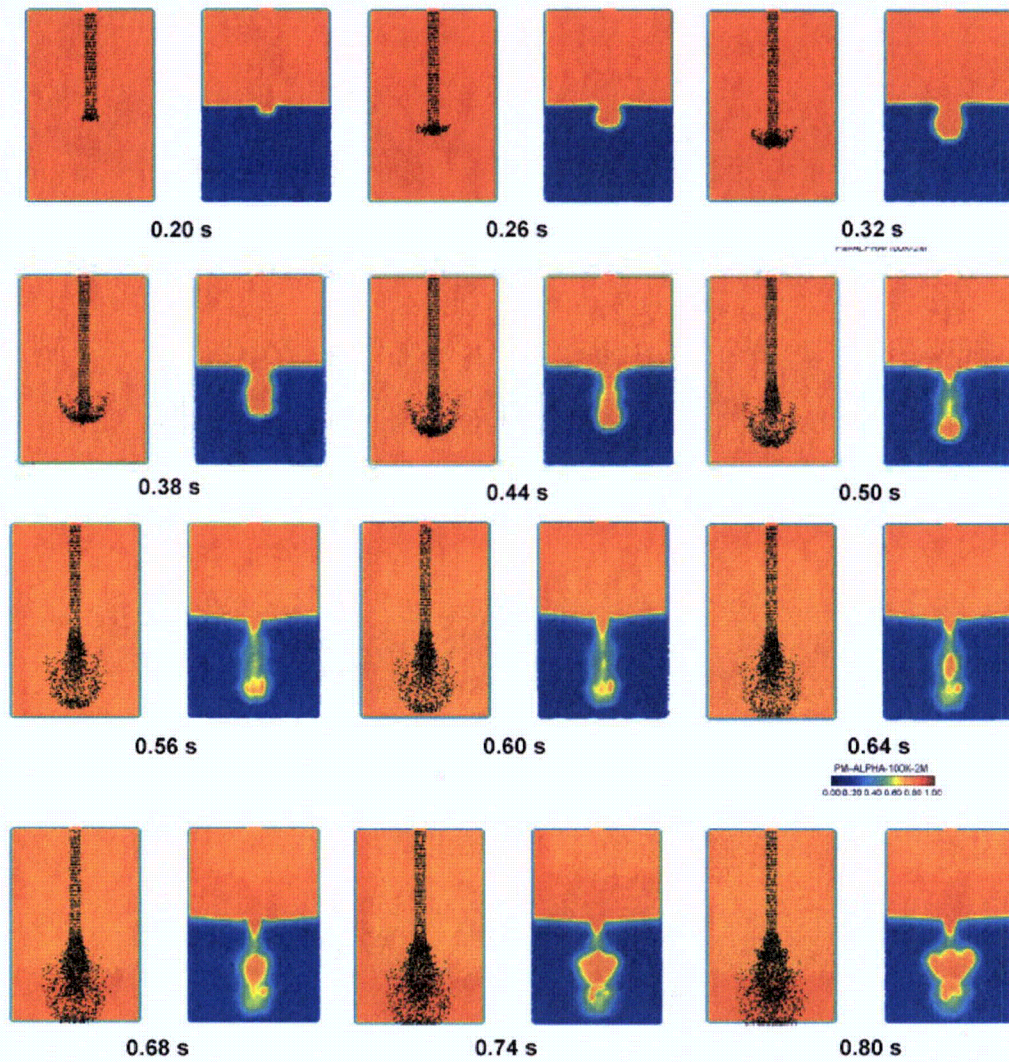


Figure 2.4.3.2c. Evolution of premixtures in a 2-meter-deep pool, with 100 K subcooling. Melt (left) and void fraction (right) distribution.

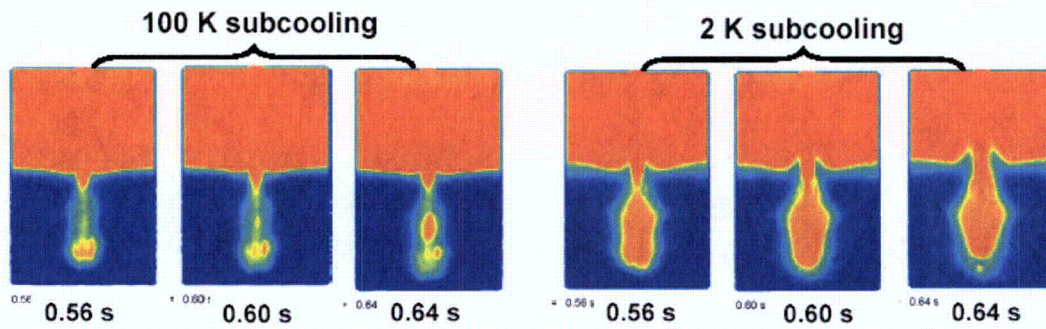


Figure 2.4.3.2d. Comparison of premixing patterns in 2m-deep pools, with 100K and 2 K subcooling.

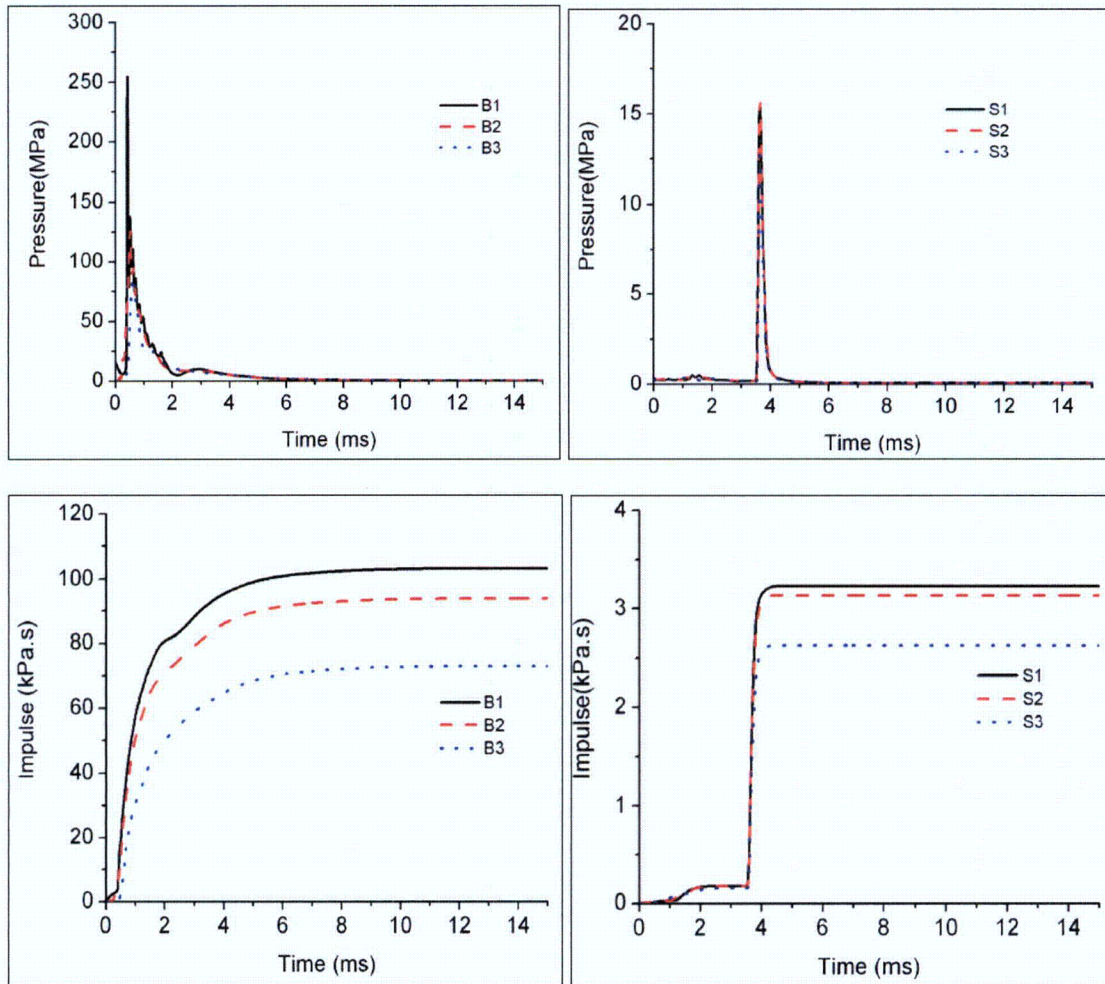


Figure 2.4.3.4 (a). Pressures and impulses on the floor (B) and pedestal (S) from an explosion in 1 m deep, subcooled pool. Trigger time: 0.28s. The resulting impulse on the pedestal is insignificant, due to the effect of explosion venting.

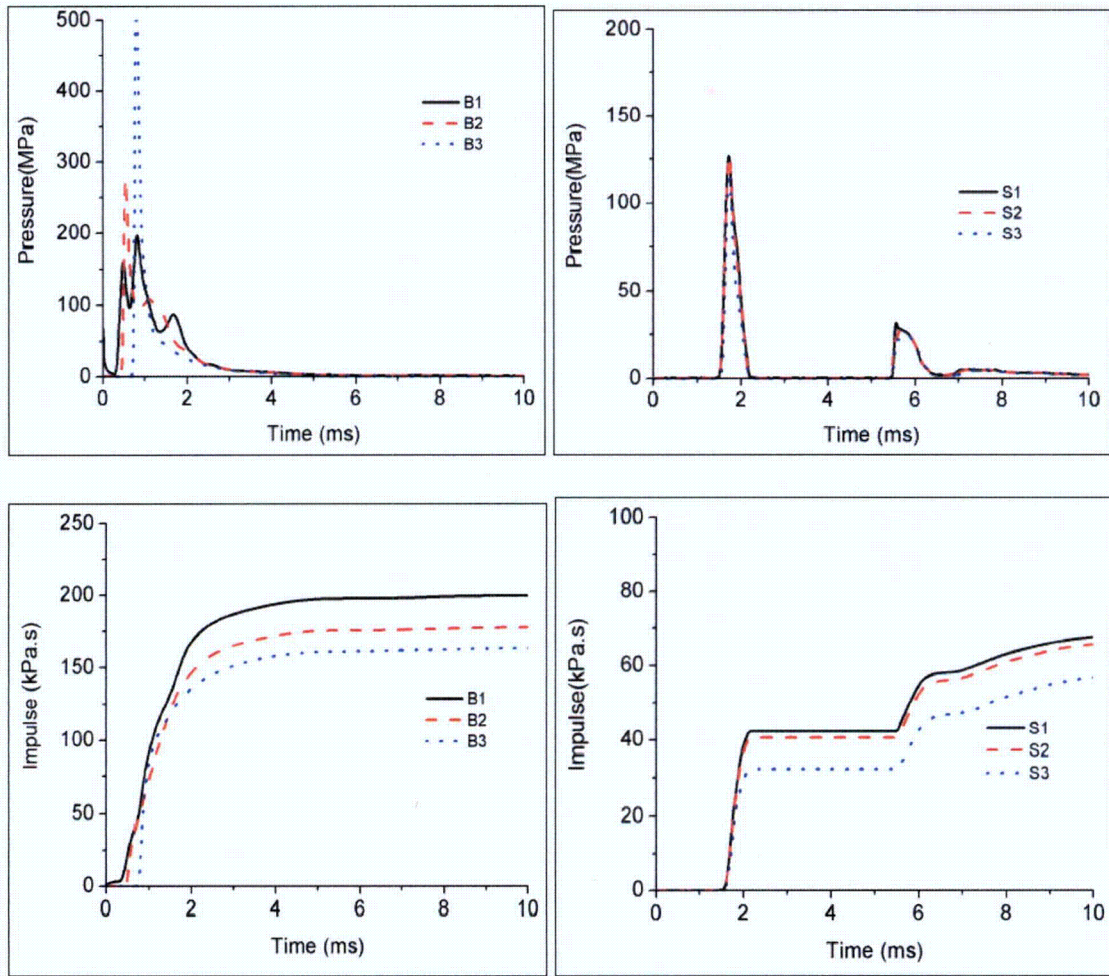


Figure 2.4.3.3 (b). Pressures and impulses on the floor (B) and pedestal (S) from an explosion in 1 m deep, subcooled pool. Trigger time: 0.47s. No explosion developed when trigger energy of 20 kJ was used. A higher trigger energy (50 kJ) was needed for explosion to develop.

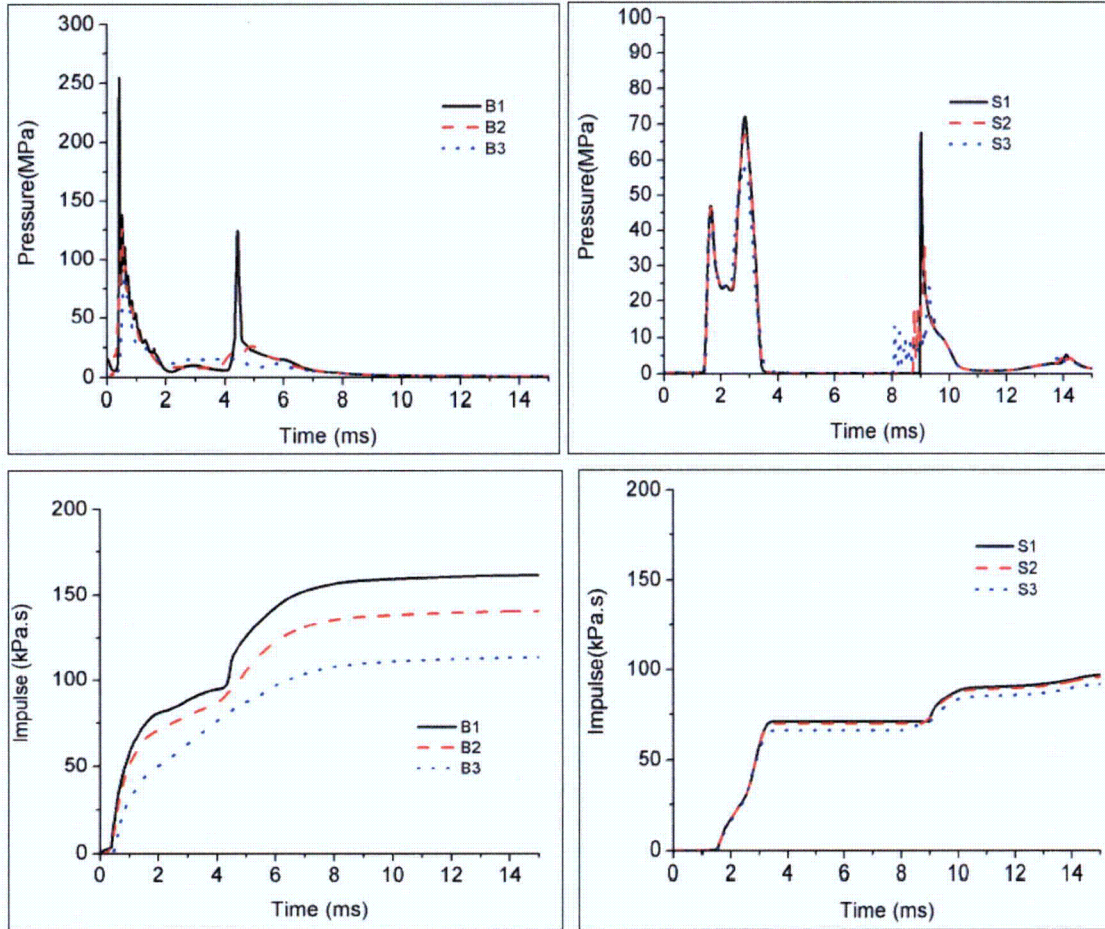


Figure 2.4.3.5. Pressures and impulses on the floor (B) and pedestal (S) from an explosion in 2 m deep, subcooled pool. Trigger time: 0.63s. Trigger energy was 20 kJ. The second pressure pulse is from the convergence of reflections off the side walls, and would not be present in an open LDW pool, even if the explosion was 2 m away from a side wall.

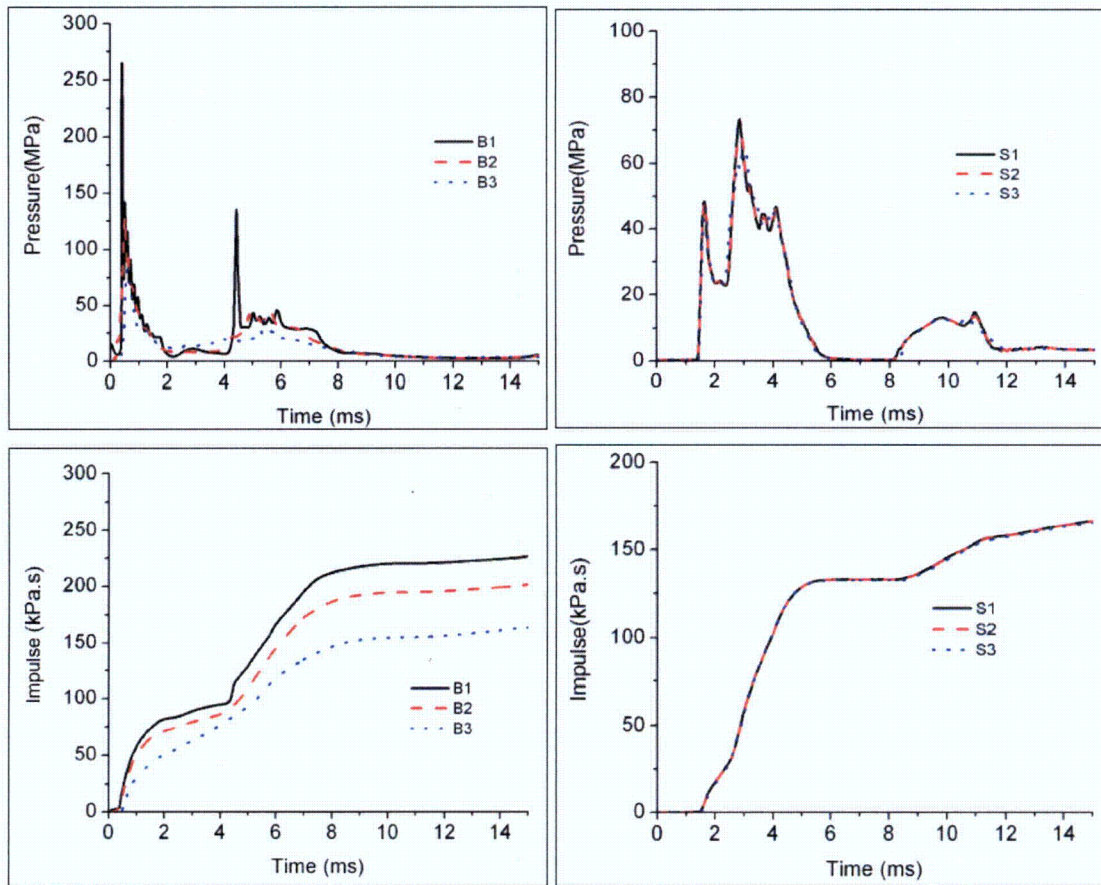
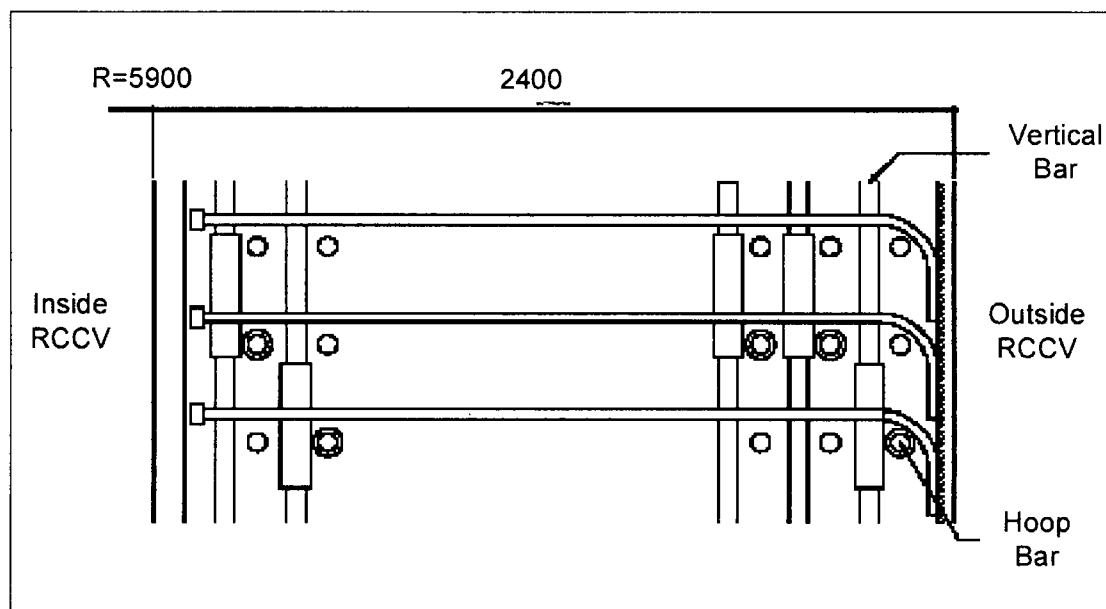


Figure 2.4.3.6. Pressures and impulses on the floor (B) and pedestal (S) from an explosion in 5 m deep, subcooled pool. Trigger time: 0.63s. Same remark on reflected wave convergence applies to the second pulse as in previous figure, although the larger inertia constraint here would still support some of this type of reflection even in 10 m diameter pool.

2.4.4. Quantification of Fragility

The detailed structural makeup of the pedestal is shown in Figure 2.4.4.1. It was assumed that a standard, 5,000 psi concrete mix will be used. This rebar-concrete material assembly, including the liner, was represented by the DYNA3D model shown in Figure 2.4.4.2 (DYNA3D Manual). Further details on the concrete model, the so-called K&C model (Karagozian and Case) can be found in Malvar et al (1997), and verification/validation of DYNA3D performance on problems of this type has just been released (Noble et al, 2005).

Calculations were carried out both with and without the 6.4 mm steel liner, it being in contact with the inside surface of the concrete. The dynamic load was applied over the whole circumference to a height of 2.5 m. This is to conservatively envelope the two classes of lower pool depths defined above. The applied impulses were varied by adjusting the peak amplitude and time-duration of a triangular pressure pulse.



		Arrangement	Rebar ratio (%)
Hoop	Outside	3 - # 18 @ 300	1.08
	Inside	2 - # 18 @ 300	0.72
Vertical	Outside	3 - # 18 @ 1.8°	1.51
	Inside	2 - # 18 @ 1.8°	1.01
Shear		# 9 @ 300x300	0.72

Figure 2.4.4.1 Structural definition of the reactor pedestal (2.4 m thick) used in the DYNA3D model.

Three results selected around the condition of failure are shown in Figure 2.4.4.3. The peak pressures utilized in these calculation are in the 1.3 to 2 kbar range, and pulse widths

were of 3 and 6 ms. At the low end, the impulse is ~200 kPa s, and at the high end it is 600 kPa s. The calculated strains show that at the upper end (600 kPa s) there is incipient liner failure. At the same time the concrete seems to have suffered sufficient damage that it can be considered near the end of its load-bearing capacity. On the other hand, the intermediate case — 2 kbar peak pressure, 3 ms pulse, 300 kPa.s impulse — is seen to hold up quite well, and so is the lowest impulse case at 200 kPa.s. Further results testing the sensitivity to concrete model (an earlier version in the DYNA3D code), are summarized in Figures 2.4.4.4a-f. It is clear that there is a significant benefit from the improved model, and that the previous, general “understanding” that failure can be expected at ~100 kPa.s, at least for the ESBWR, needs to be revised upwards to ~0.5 MPa.s.

See also Addendum (2.4.4 RR Add) to this Section at the end of Chapter 2.

The BiMAC device, Figure 2.2.2, was modeled conservatively in a quasi 1D fashion; that is, the load was assumed to be applied over the whole floor area, which allows vertical planes of symmetry through any two adjacent pipes (steel A36), and thus a great detail in the DYNA3D representation, as illustrated in Figure 2.4.4.5. Calculations were carried out with the same type of impulse loadings as done for the reactor pedestal. The results leading up to crushing of the pipes are shown in Figure 2.4.4.6. Note that at around 200 kPa.s, a thin portion of the pipes yields significantly, however, the remaining material remains basically intact, while the pipe cross-sectional area is still largely intact. We take this as the level of incipient failure by crushing.

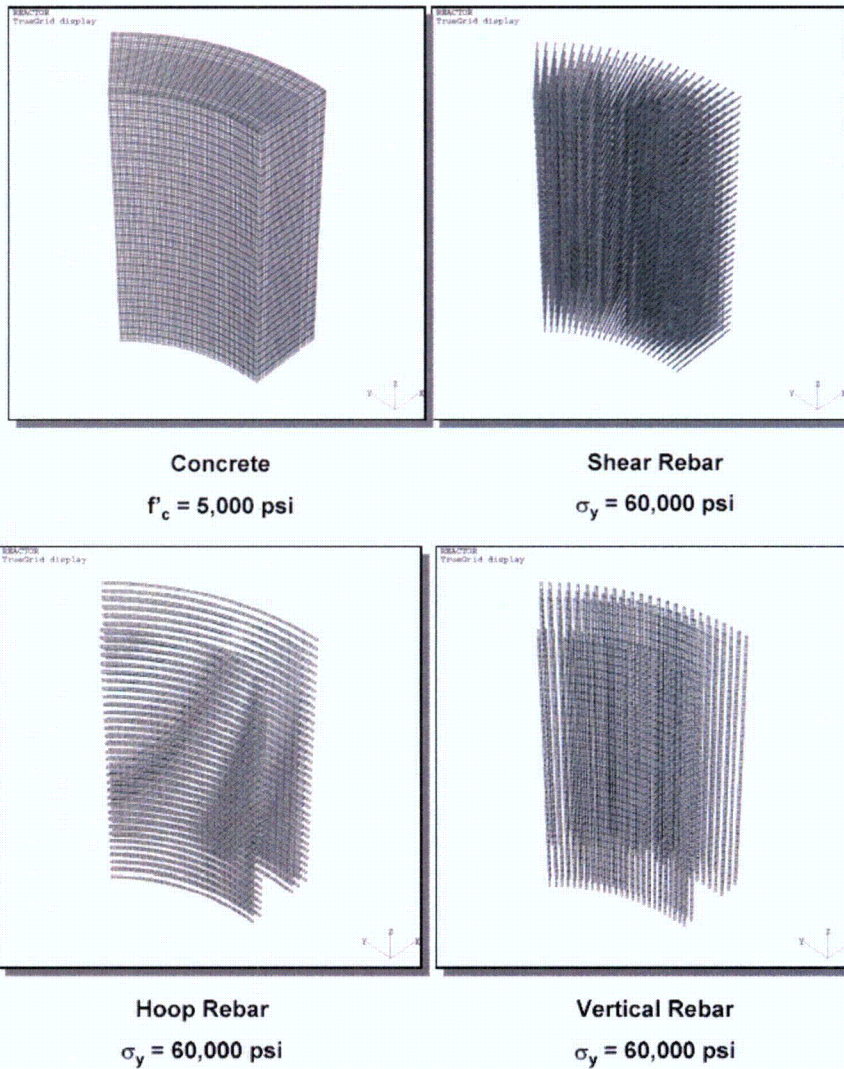


Figure 2.4.4.2 The DYNA3D model used in the fragility calculations. A 6-m vertical wall was azimuthally cut to a 45° segment by planes of symmetry as shown. The discretization involved 0.5 million hexahedral elements. Also shown are the radial (shear), hoop, and vertical rebar positions, all included in the model. Calculations were also run with the steel liner (6 mm) in place (not shown in figure).

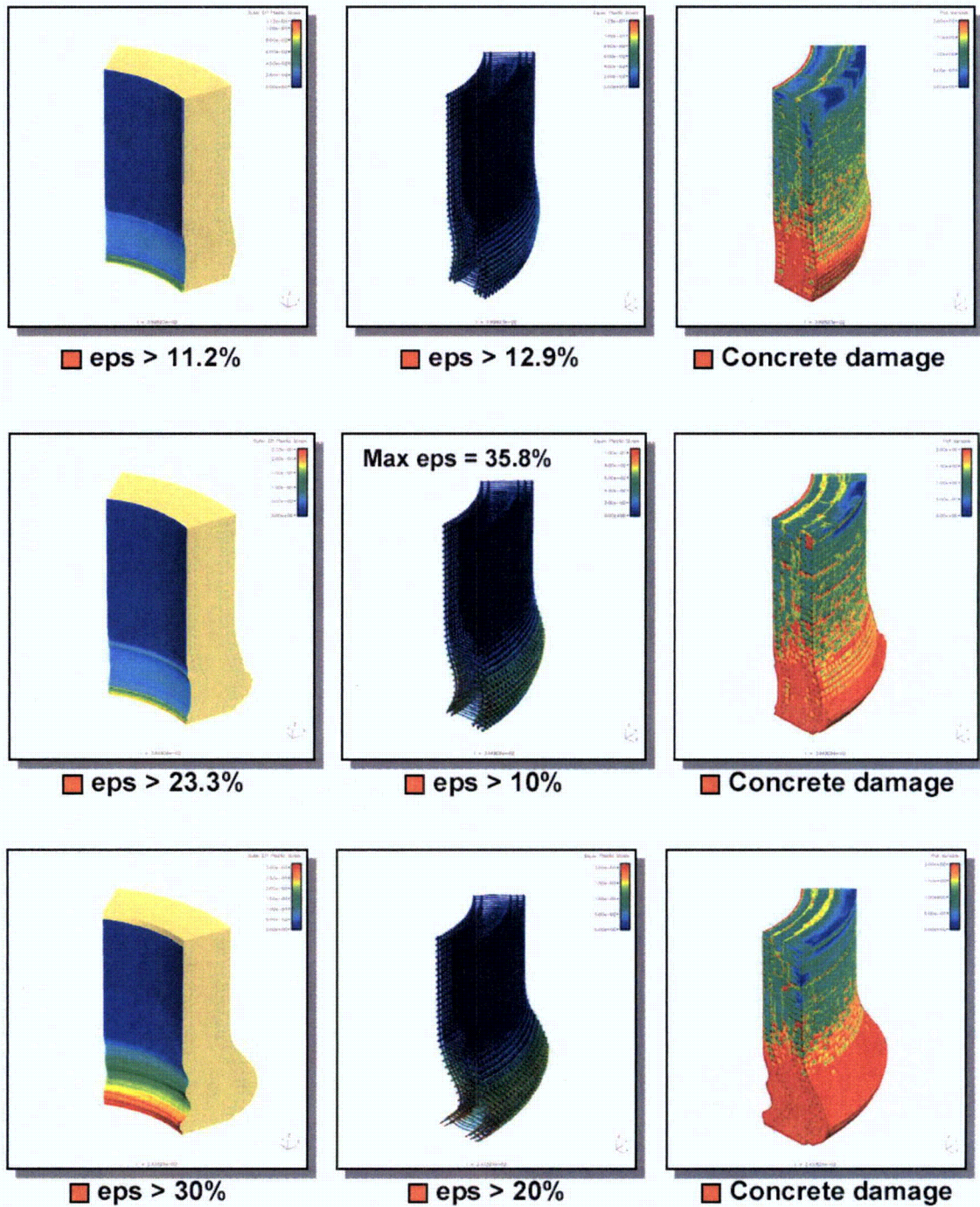
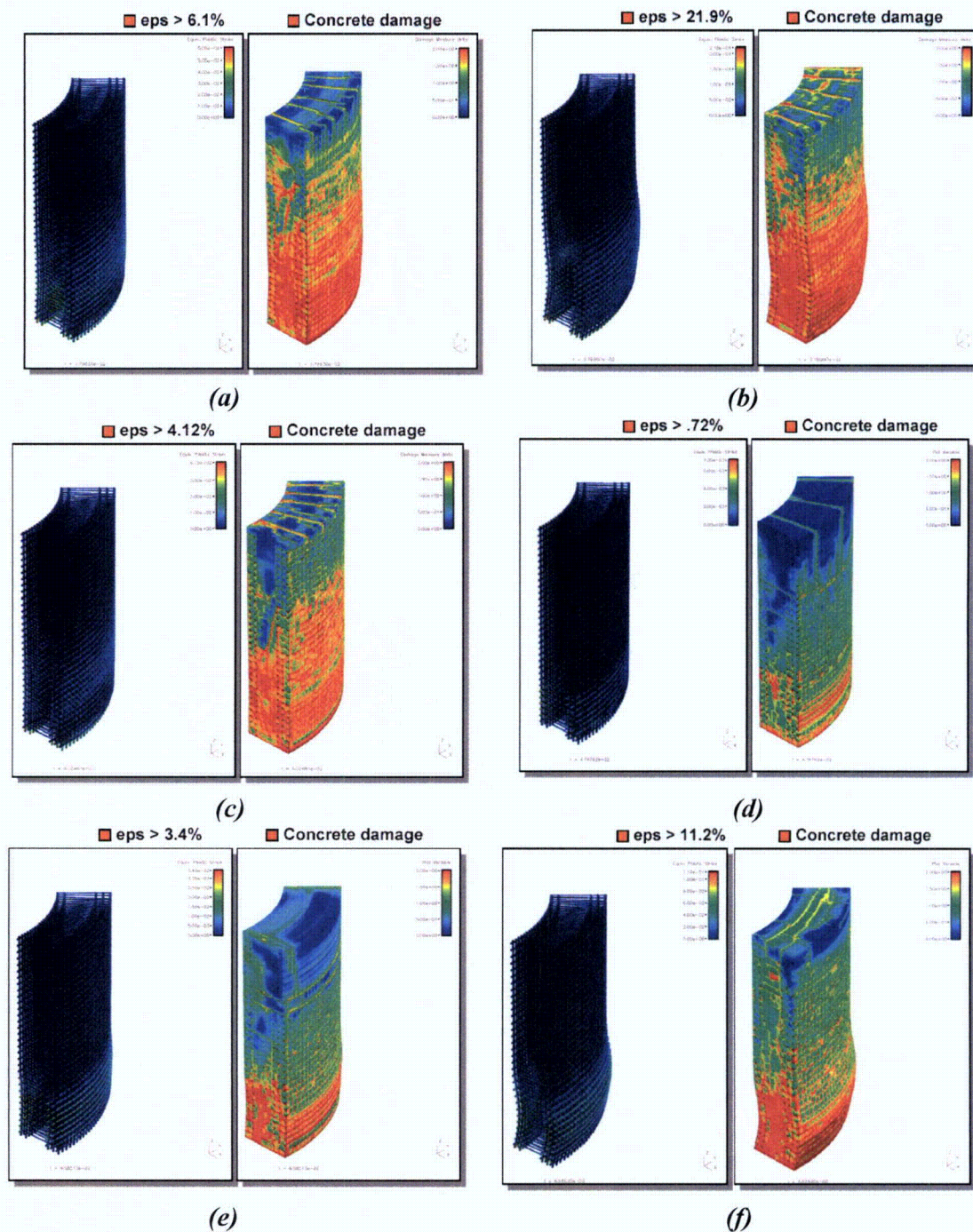


Figure 2.4.4.3 Results of three load cases in DYNA3D, with the Old (standard) K&C concrete model. Top row 1.36 kbar, 3 ms pulse (200 kPa.s), middle row 2 kbar, 3 ms pulse (300 kPa.s), bottom row 2 kbar, 6 ms pulse (600 kPa.s). Left column: liner effective plastic strain. Central column: rebar strain. Right column: concrete damage.



Figures 2.4.4.4. Results of four load cases, calculated with the standard (SKC) and improved K&C (IKC) concrete models in DYNA3D code.
 (a) 1.36 kbar, 3 ms pulse (200 kPa.s) (IKC); (b) 1.36 kbar, 6 ms pulse (400 kPa.s) (IKC);
 (c) 0.68 kbar, 6 ms pulse (200 kPa.s) (IKC); (d) 0.34kbar, 3 ms pulse (50 kPa.s) (SKC);
 (e) 0.68 kbar, 3 ms pulse (100 kPa.s) (SKC); (f) 1.36 kbar, 3 ms pulse (200 kPa.s) (SKC);
 [several typos in the caption of this figure discovered by the authors have been corrected].

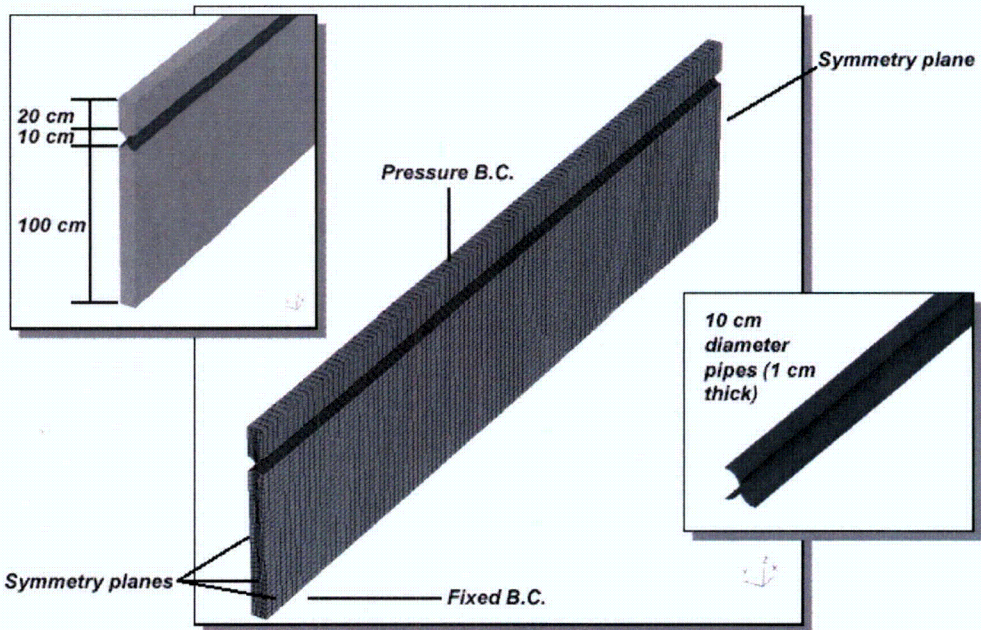


Figure 2.4.4.5. The DYNA3D representation of the BiMAC device . There are 40,000 hexahedral elements and 2,000 shell elements (for the pipe material).

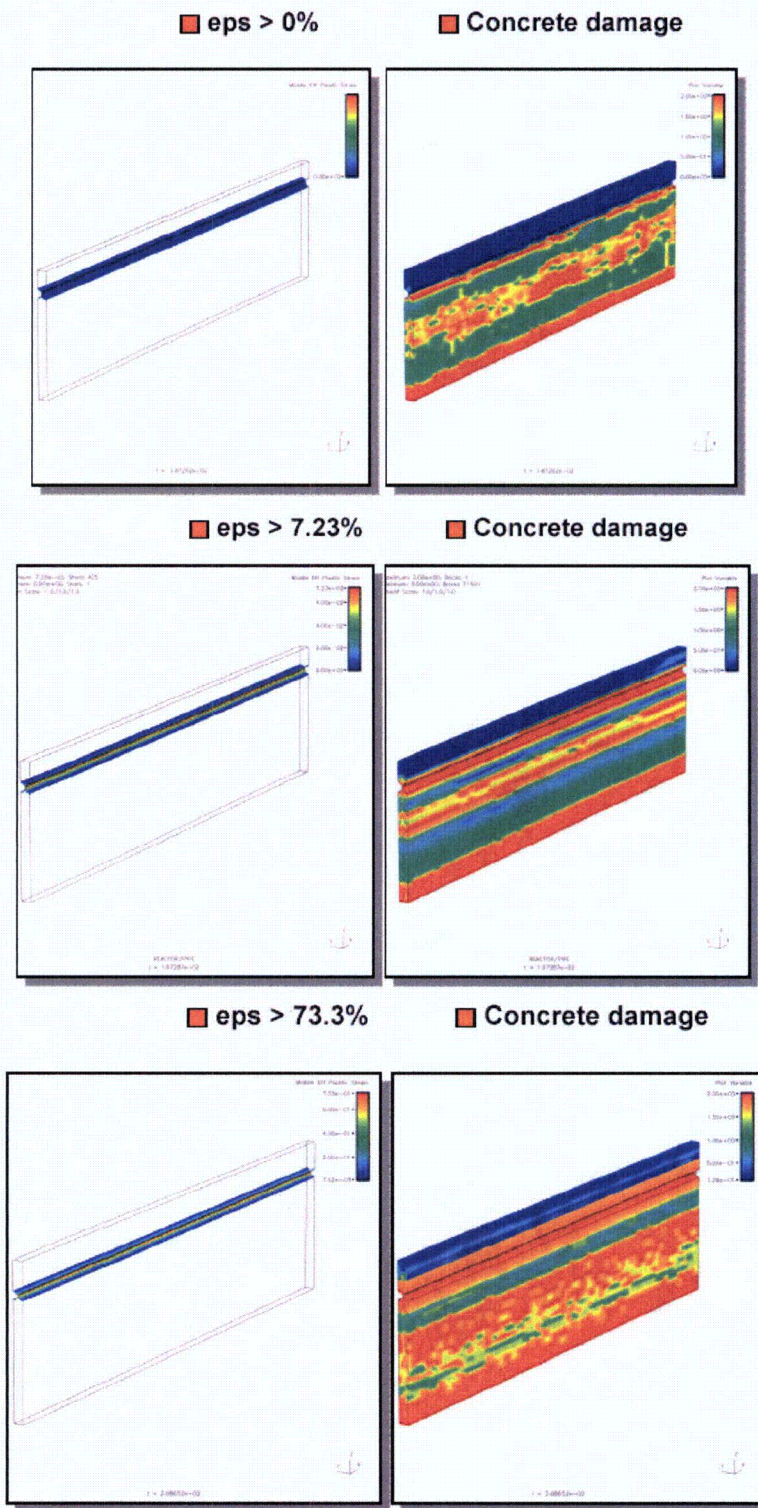


Figure 2.4.4.6. Strain of the pipe, and extent of concrete damage calculated by DYN3D. Top to bottom the impulses were 50, 100, and 200 kPa s respectively.

2.4.5. Prediction of Failure Probability

The results of the previous two sections on pedestal loads and fragility are juxtaposed in Figure 2.4.5.1. The loads from 1 and 2 m deep, highly sub-cooled pools are taken to bound loads from shallow, saturated pools. There is a huge margin in this bound, and as the figure shows there is an extra huge margin to failure even given this bounding of loads. Thus we conclude that in 99% of the Class I severe accidents in ESBWR, pedestal failure by an EVE is physically unreasonable. This covers ~99% of the CDF too.

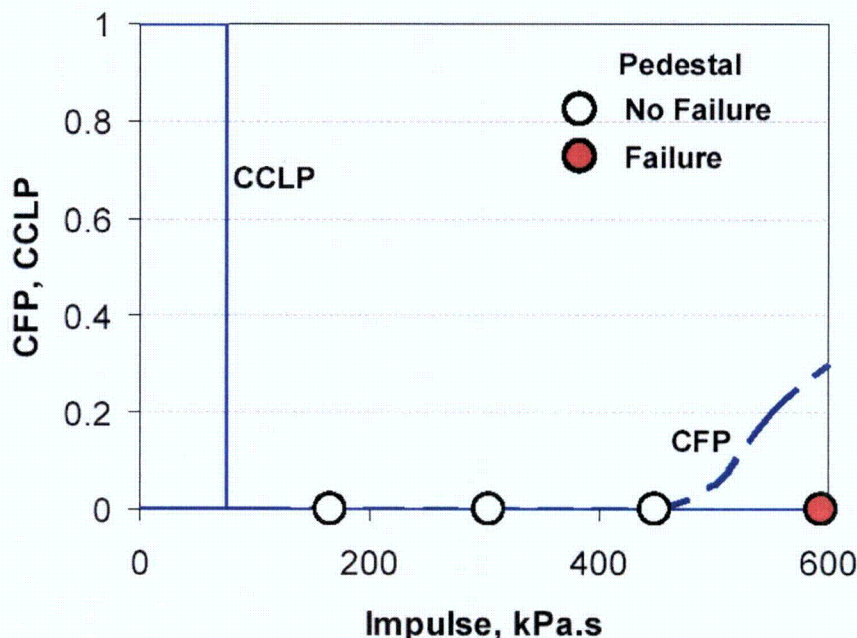


Figure 2.4.5.1. Cumulative Failure Probability (CFP) and Complementary Cumulative Load Probability (CCLP) for the pedestal.

The remaining 1% refers to Class I with deep ($H \gg 1.5$ m), sub-cooled water pools. For such pools, although not considered in any detail here, an appropriately conservative position would be that “integrity of both the liner and the concrete structure could be possibly compromised”.

Similarly the results for the structural integrity of the BiMAC can be visualized with the help of Figure 2.4.5.2. Failure incipience is shown at impulses of somewhere between 100 and 200 kPa.s. Two load types are indicated. The realistic one is for the low level (LL) case which would yield negligible energetics. The high level (HL) case is to schematically illustrate a bounding load appropriate for 1-2 meter deep, sub-cooled water pools that were analyzed. We can see that for 99% of the Class I severe accident scenarios BiMAC failure by an EVE would be physically unreasonable. We also see that BiMAC is structurally so strong as to allow significant margins to failure even in many EVE’s postulated to occur in deeper and sub-cooled pools.

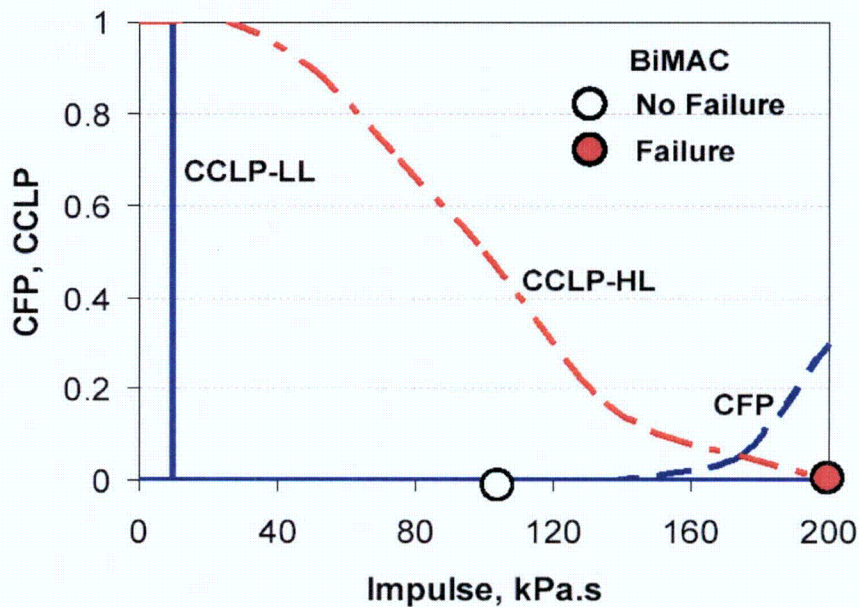


Figure 2.4.5.2. Cumulative Failure Probability (CFP) and Complementary Cumulative Load Probability (CCLP) for the BiMAC pipes for case with low water level (LL) and high water level (HL).

2.5. Summary and Conclusions for EVE

The above results show that for all but 1% of the CDF, that is accidents involving deep, subcooled water pools, violation of the ESBWR containment leak-tightness, and of the BiMAC function, due to ex-vessel steam explosions are physically unreasonable.

Principal ingredients to such a conclusion can be recapitulated as follows:

1. An accident management strategy, and related hardware features that prohibit large amounts of cold water from entering the LDW prior to RPV breach,
2. The physical fact that premixtures in saturated water pools become highly voided and thus unable to support the escalation of natural triggers to thermal detonations,
3. Reactor pedestal and BiMAC structural designs that are capable of resisting explosion load impulses of over ~ 500 kPa s and ~ 100 kPa s respectively.

References to Chapter 2 (EVE)

Almström, H., Sundel, T., Frid, W., Engelbrektson, A. (1999), "Significance of fluid-structure interaction phenomena for containment response to ex-vessel steam explosions", *Nuclear Engineering and Design*, v.189, pp.405–422.

Amarasooriya, W.H. and Theofanous, T.G. (1991), "Premixing of Steam Explosions: A Three-Fluid Model," *Nuclear Engineering & Design* 126, 23-39.

DYNA3D (2004). Code Manual. Lawrence Livermore National Laboratory.

GE (1987; 1994) General Electric. Standard Safety Analysis Report (SSAR) for ABWR (1994 Final Submission version).

Henry, R.E. and Fauske, H.K. (1981), "Required Initial Conditions for Energetic Steam Explosion", ASME HTD v.19, pp.99-108.

Esmaili, H. and Khatib-Rahbar, M. (2005), Analysis of likelihood of lower head failure and ex-vessel fuel coolant interaction energetics for AP1000. *Nuclear Engineering and Design*, 235 (15), July 2005, pp. 1583-1605.

Fletcher, D.F. and Theofanous, T.G. (1997) "Heat Transfer and Fluid Dynamic Aspects of Explosive Melt-Water Interactions," *Advances in Heat Transfer*, 29, 129-213.

Malvar, L.J. , Crawford, J.E. , Wesevich, J.W. , Simons. D. (1997) "A Plasticity Concrete Material Model for DYNA3D". *Int. J. Impact Engineering* Vol. 19, Nos. 9-10, pp. 847-873, 1997

Noble, C.J. et al (2005). "Concrete Model Description and Summary of Benchmark Studies for Blast Effects and Simulation". UCRL-215024, Lawrence Livermore National Laboratory (July, 2005).

NRC (1994). U.S. Nuclear Regulatory Commission. "Final safety evaluation report related to the certification of the advanced boiling water reactor design",. NUREG-1503.

NUREG–1150 (1990). Severe Accident Risks: An assessment for five U.S. nuclear power plants. Technical Report NUREG–1150, U.S. Nuclear Regulatory Commission.

Rashid, Y.R., Theofanous, T.G., and Foadian, H. (1995), Failure Assessment of Reactor Vessel Support Structure Subjected to Ex-Vessel Explosion Loads, 1995 ASME/JSME Pressure Vessel and Piping Conference, Honolulu, Hawaii, July23-27, 1995. Also published in a *Trans. of the ASME, Journal of Pressure Vessel Technology* (1997).

SERG (1985) Review of the current understanding of the potential for containment failure from in-vessel steam explosions, NUREG-1116, U.S. NRC (1985).

SERG-2 (1995) Proceedings of the Second Steam Explosion Review Group (SERG-2) Workshop, NUREG-1524, ed., S. Basu and T. Ginsberg, August 1996. (Follow-on international FCI research summarized in Proceedings of the OECD/CSNI Specialists Meeting on Fuel-Coolant Interactions, NEA/CSNI/R(97)26, ed., M. Akiyama, N. Yamano and J. Sugimoto, January 1998.)

Theofanous, T.G., Najafi, B., and Rumble, E. (1987), "An Assessment of Steam-Explosion-Induced Containment Failure. Part I: Probabilistic Aspects," *Nuclear Science and Engineering*, 97, 259-281 (1987). M.A. Abolfadl and T.G. Theofanous, "An Assessment of Steam-Explosion-Induced Containment Failure. Part II: Premixing Limits," *Nuclear Science and Engineering*, 97, 282-295 (1987). W. H. Amarasooriya and T.G. Theofanous, "An Assessment of Steam-Explosion-Induced Containment Failure. Part III: Expansion and Energy Partition," *Nuclear Science and Engineering*, 97, 296-315 (1987). G.E. Lucas, W.H. Amarasooriya and T.G. Theofanous, "An Assessment of Steam-Explosion-Induced Containment Failure. Part IV: Impact Mechanics, Dissipation and Vessel Head Failure," *Nuclear Science and Engineering*, 97, 316-326 (1987).

Theofanous, T.G. (1995) "The Study of Steam Explosions in Nuclear Systems," *Nuclear Engineering & Design* 155 (1995) 1-26. (Also see S. Angelini, E. Takara, W.W. Yuen and T.G. Theofanous, "Multiphase Transients in the Premixing of Steam Explosions," *Nuclear Engineering & Design*, 146, 83-95, 1994. W.W. Yuen, X. Chen and T.G. Theofanous, "On the Fundamental Microinteractions That Support the Propagation of Steam Explosions," *Nuclear Engineering & Design*, 146, 133-146, 1994.)

Theofanous, T.G., and Yuen, W.W. (1995) "The Probability of Alpha-Mode Containment Failure Updated," *Nuclear Engineering & Design* 155 (1995) 459-473.

Theofanous, T.G., Yuen, W.W., Zhao, H., Jansson, I., Frid, W. (1995). A study of ex-vessel steam explosions in Swedish BWRs. Proc. OECD Specialist Meeting on Selected Containment Severe Accident Management Strategies, Stockholm, Sweden, 13-15 June 1994, SKI Report 95:34, NEA:CSNI/R(95)3.

Theofanous, T.G. (1996), "On the Proper Formulation of Safety Goals and Assessment of Safety Margins for Rare and High-Consequence Hazards," *Reliability Engineering & Systems Safety*, 54 (1996) 243-257.

Theofanous, T.G., Yuen, W.W., and Angelini, S. (1999a), "The Verification Basis of the PM-ALPHA Code," *Nuclear Engineering & Design*, 189 (1999) 59-102. (Also T.G. Theofanous, W.W. Yuen and S. Angelini, "Premixing of Steam Explosions: PM-ALPHA Verification Studies," DOE/ID-10504, June 1998.)

Theofanous, T.G., Yuen, W.W., Freeman, K. and Chen, X. (1999b), "The Verification Basis of the ESPROSE.m Code," *Nuclear Engineering & Design*, 189 (1999) 103-138. (Also T.G. Theofanous, W.W. Yuen, K. Freeman and X. Chen, "Propagation of Steam Explosions: ESPROSE.m Verification Studies," DOE/ID-10503, June 1998.)

Theofanous, T.G., Yuen, W.W., Angelini, S., Sienicki, J.J., Freeman, K., Chen, X. and Salmassi, T. (1999c) "Lower Head Integrity Under Steam Explosion Loads," *Nuclear Engineering & Design*, 189 (1999) 7-57. (also T.G. Theofanous, W.W. Yuen, S. Angelini,

J.J. Sienicki, K. Freeman, X. Chen and T. Salmassi, "Lower Head Integrity Under In-Vessel Steam Explosion Loads," DOE/ID-10541, June 1998.)

Turland, B.D., Fletcher, D.F., and Hodges, K.I. (1994), "Quantification of the Probability and Containment Failure Caused by an In-Vessel Steam Explosion for the Sizewell B PWR", NUREG/CP-0127, 1994.

Westinghouse Electric Company (2002). The AP1000 Design Control Document.

Yuen, W.W. and Theofanous, T.G. (1995) "ESPROSE.m: A Computer Code for Addressing the Escalation/Propagation of Steam Explosions," DOE/ID-10501, April 1995.

Yuen, W.W. and Theofanous, T.G. (1995) "PM-ALPHA: A Computer Code for Addressing the Premixing of Steam Explosions," DOE/ID-10502, May 1995.

Yuen, W.W. and Theofanous, T.G. (1995) "The Prediction of 2D Thermal Detonations and Resulting Damage Potential", *Nuclear Engineering & Design*, **155** (1995) 289-309.

Yuen, W.W. and Theofanous, T.G. (1999) "On the Existence of Multiphase Thermal Detonations," *Int. Jl. Multiphase Flow*, 25 (1999) 1505-1519.

2.4.4 RR Add Quantification of Fragility (Addendum of Dec. 19, 2006)

This Addendum is to respond to reviewer's request for more legible structural analyses figures. Enlarged figures are hereby included, and the correspondence to the figures appearing in Section 2.4.4 is as follows:

Figure 2.4.3: (a) is Case 7, (b) -Case 8, (c) -Case 9, (d) - Case 4, (e) - Case 5, (f) - Case 6

Figure 2.4.4: Top, Middle Bottom easily identifiable by pressure pulse (same order).

Additional calculations were also performed with material (rebar) properties found in one of the reviewer's calculations and these are presented along with additional comments on fragility of the pedestal under ROAAM Review correspondence with Dr. J Rashid.

3. Containment and BiMAC Performance Against Basemat Melt Penetration (BMP)

3.1. Overall considerations

For all[†] currently operated LWR's, the severe accident management case is based on the so-called core-on-the-floor concept. The basic premise is that, provided there is sufficient floor area available for spreading and sufficient amount of water to cover the molten core debris, the debris will become quenched, and will remain coolable thereafter. Unfortunately, despite extensive commitment of resources, and rather protracted R&D efforts internationally, this idea remains little more than a speculation. While work appears to be continuing, operation of reactors is justified on the basis of analyses that are claimed to satisfy the so-called 24-hour rule. These analyses assume a split of decay power between the upwards (into water) and downwards (into concrete) directions, and predict that (a) basemat penetration will not occur for a minimum of 24 hours, and (b) containment will not fail by accumulation of so-generated non-condensable gases also for a minimum of 24 hours.

While ESBWR satisfies the basic conditions for this approach as intended, with a LDW floor area according to the EPRI URD guidelines for advanced reactors, and while our analyses, such as those described above, show that the 24-hour rule is satisfied with great margins (more than 72 hours), this core-on-the-floor approach was not considered appropriate here. Rather we have incorporated hardware and procedures that make the issue of corium-concrete interactions, along with the great uncertainties that arise in its consideration, mute.

The importance of assuring long term coolability has been also appreciated by other designers of advanced passive plants: the AP600 was provided with features that assure in-vessel retention and coolability as already shown to be the case for the Loviisa VVER-440, the AP1000 has followed the same approach, and the European Pressurized Reactor (EPR) design placed this line of defense ex-vessel, by means of a rather elaborate scheme for facilitating corium spreading and heat removal (Fisher, 2003). Further, the new Russian V-320 design of VVER-1000 plant in Tianwan, China has a very elaborate ex-vessel core catcher, which includes a basket made of Al_2O_3 - Fe_2O_3 -steel mixture and filled with a special material compound (Kukhtevich, 2001).

3.2. ESBWR Design

Inspired by, and leveraging on IVR technology developed during DOE's ARSAP program nearly a decade ago (Theofanous et al, 1996), we employ here a passively-cooled boundary that is impenetrable by the core debris in whatever configuration it could possibly exist on the LDW floor. For ex-vessel implementation this boundary is conveniently, and advantageously

[†] This does not include the VVER-440 at Loviisa, and the VVER-1000 at Tianwan (see below).

made by a series of side-by-side placed inclined pipes, forming a jacket which can be effectively and passively cooled by natural circulation when subjected to thermal loading on any portion(s) of it. Water is supplied to this device from the GDCS pools via a set of deluge lines (we call these the LDW deluge lines). The timing and flows are such that (a) cooling becomes available immediately upon actuation, and (b) the chance of flooding prematurely the LDW to an extent that opens up a vulnerability to steam explosions is very remote. The detection/activation system will be finalized at the COL stage the design, and the required unreliability (at a high confidence level) of it is now specified to 10^{-3} per demand. The jacket is buried inside the concrete basemat and would be called into action immediately upon the first melt arrival on the LDW floor.

The device, call Basemat Internal Melt Arrest and Coolability device (BiMAC) (Theofanous and Dinh, 2005), is illustrated in Figure 3.2.1. Important considerations in the design and implementation of this concept are as follows:

- (a) **Pipe inclination angle.** As we show further below, both the thermal load due to melt natural circulation (q_D), and the burnout heat flux (the CHF), increase with angle of inclination of the bottom boundary from a low value pertinent to a near horizontal orientation. This increase is much faster for the CHF in the region $0 < \theta < 20^\circ$, and there is a maximum separation from q_D at around the upper end of this range. Within a reasonable value of the overall vertical dimension of the BiMAC device, the whole LDW can be covered conveniently with pipes inclined at near the upper end of this range.
- (b) **Sacrificial refractory layer.** A refractory material is laid on top of the BiMAC pipes so as to protect against melt impingement during the initial (main) relocation event, and to allow some adequately short time for diagnosing that conditions are appropriate for flooding. This is to minimize the chance of inadvertent, early flooding. The material is selected to have high structural integrity, and high resistance to melting — such as is for ceramic Zirconia. As shown below, with this material, a layer thickness of 0.2 m is quite adequate to meet these design objectives.
- (c) **Cover plate.** As shown in Figure 3.2.1, we use a supported steel plate to cover the BiMAC. On the one hand this allows that the top is a floor as needed for normal operations, and that the BiMAC is basically “out of the way” until its function is needed. On the other hand the so-created cavity, with a total capacity of $\sim 90 \text{ m}^3$, is there to receive and trap all possible quantity of melt in a hypothetical ex-vessel severe accident evolution, including a high pressure melt ejection (see Chapter 1). For this purpose the top plate is stainless steel, 2 mm in thickness so as to be essentially instantaneously penetrable by a high-velocity melt jet. The plate is made to sit on top of normal floor grating, which itself is supported from below by steel columns as indicated schematically in the same figure (Further details on this simple support system are straightforward engineering tasks more pertinent to the COL stage of the plant design and review). Between the plate and the grating we have a layer of refractory material, like a mat of zirconium oxide, so as to protect the steel material from thermal loads from below during the $\sim 40 \text{ s}$ needed to the end of steam blowdown, yet not able to provide any structural resistance to melt penetration as

needed for the trapping function noted above. For low pressure sequences, this whole cover structure has no bearing on the outcome.

- (d) **The BiMAC cavity.** The space available below the BiMAC plate is sufficient to accommodate the full-core debris, while the whole space available, up to a height of the vertical segments of the BiMAC pipes, amounts to a volume of ~400% of the full-core debris. Thus there is no possibility for the melt to remain in contact with the LDW liner. Similarly, the two sumps, needed for detecting leakage flow during normal operation, are positioned and protected in the same manner as is the rest of the LDW liner (Figure 3.2.1d). There is complete floor coverage.
- (e) **The LDW deluge system.** According to the preliminary design, this system consists of three main lines that feed off the three GDCS pools, respectively, each then separating into a pair of lines. One from each pair of these lines connects to the BiMAC main header, the other discharges directly into the LDW from near the top (Figure 3.2.1). There are six valves, one for each line. Three of them (the ones that feed into the BiMAC) are operated off numerous thermocouples/conductivity probes that cover the LDW floor area to a sufficient degree to indicate melt arrival following RPV breach. The other three, the ones that fed directly into the LDW, are activated in a diverse/passive manner by the high LDW atmosphere temperatures reached upon melt release from the RPV. The lines are sized so that any three of them would be sufficient to ensure proper BiMAC functioning; that is, capable to operate in the natural circulation mode within 5 minutes from melt arrival on the floor. As noted above the required failure rate of the active portion of this system is not to exceed 10^{-3} per demand.

As described below, the BiMAC concept is based on fundamental analytical considerations built on top of separate-effects experiences on burnout heat fluxes in inverted geometries, and two-phase (boiling) pressure drop in inclined pipes. These provide reasonable confidence that the concept is sound. We expect that the BiMAC device design will be fully confirmed in confirmatory testing, which will also help in optimizing performance at the COL stage of licensing the ESBWR.

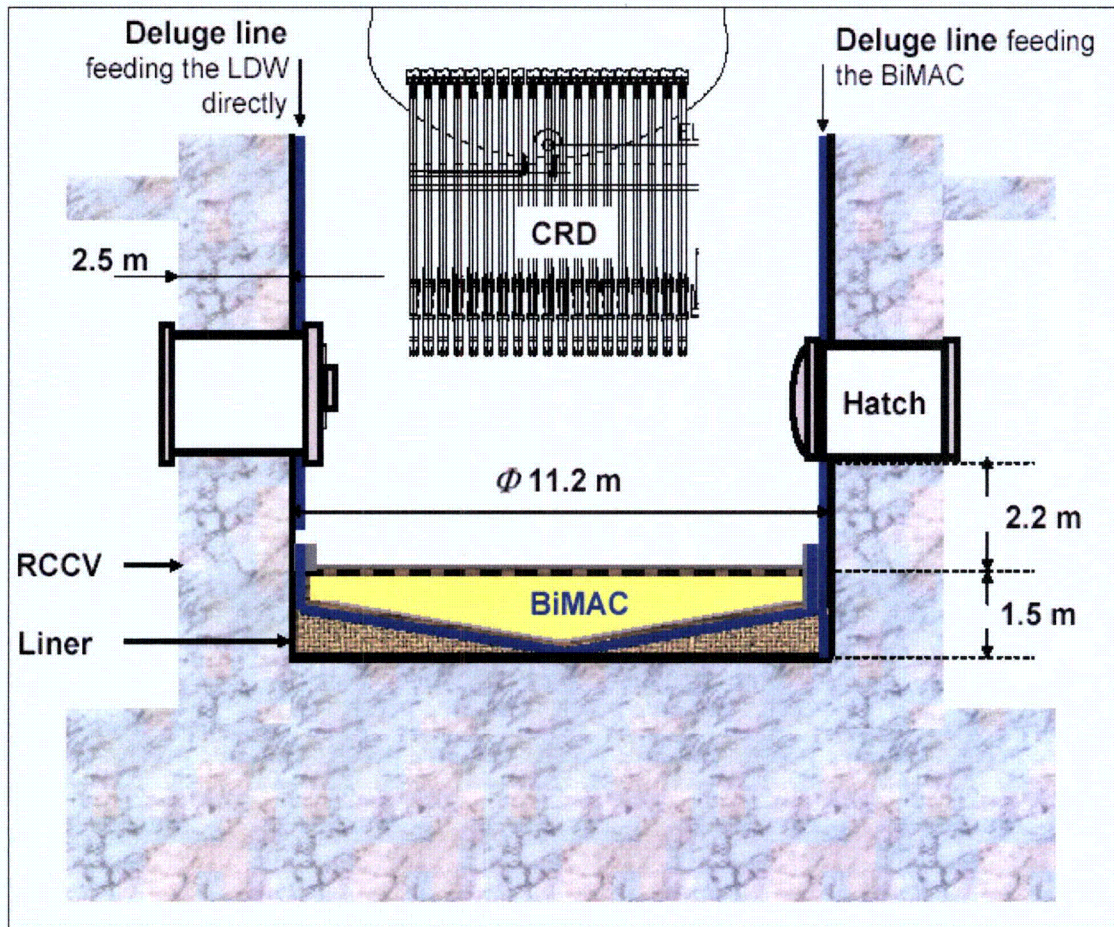


Figure 3.2.1a The BiMAC positioned inside the LDW. Initial cooling is provided by the flow into the BiMAC [Deluge line shown on the right]. The LDW is flooded independently by direct flow [Deluge line shown on the left].
 [Schematic, not to scale. See also Addendum 3.2 at the end of this chapter].

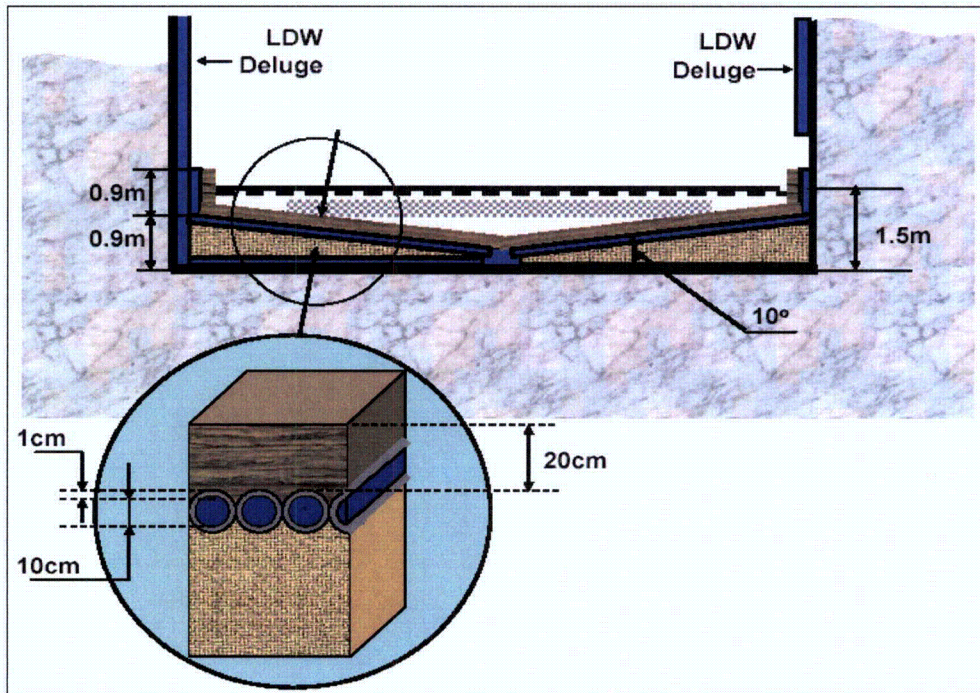


Figure 3.2.1b The BiMAC pipes and protective ceramic layer.

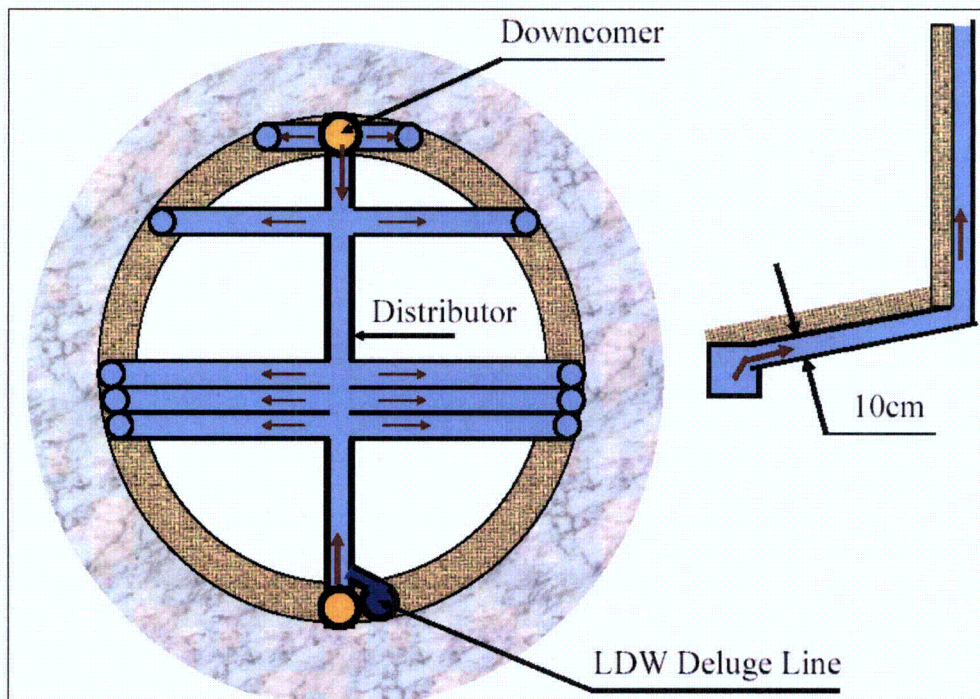


Figure 3.2.1c. Schematic arrangement of the BiMAC pipes to form a wedge-shaped jacket.. The distributor (the vertical blue line in the figure) serves as the main header. The downcomers (marked in yellow, connected to the distributor) and the pipes, including the vertical segments, serving as risers, form natural circulation loops that respond passively to the local cooling demand. [Not all pipes are shown, and the deluge lines are of appropriately larger diameter as discussed in Appendix E. In a flooded LDW condition the water level is above the top ends of the vertical pipes].

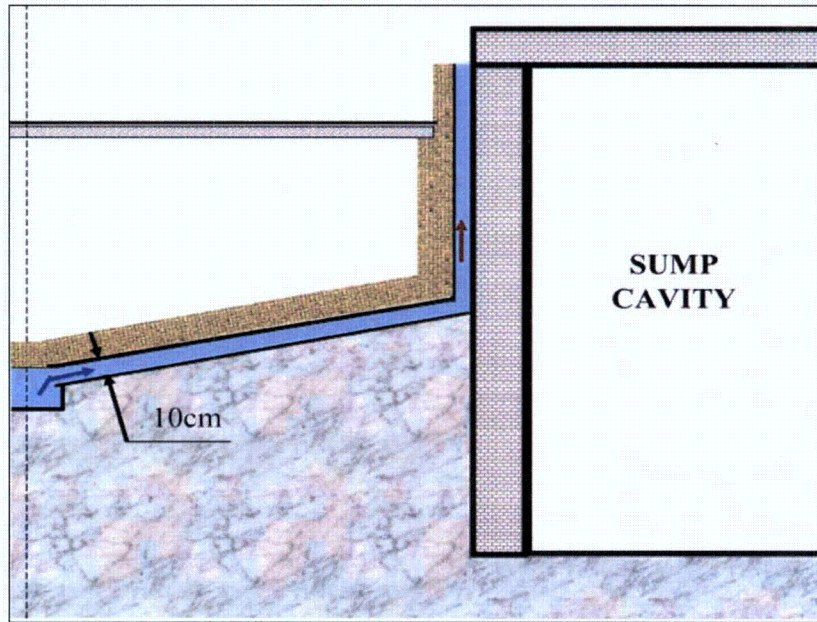


Figure 3.2.1d. Schematic representation of a sump and its protection (against melt attack) by the BiMAC cooling pipes. There are two sumps, shaped and positioned next to the pedestal wall [see Figure 3.2.1e] so that they offer no significant "target" to the melt stream exiting the vessel under most release scenarios. There is no other place for melt to go except into the BiMAC. [The sumps are to monitor leakage during normal operation. Not to scale].

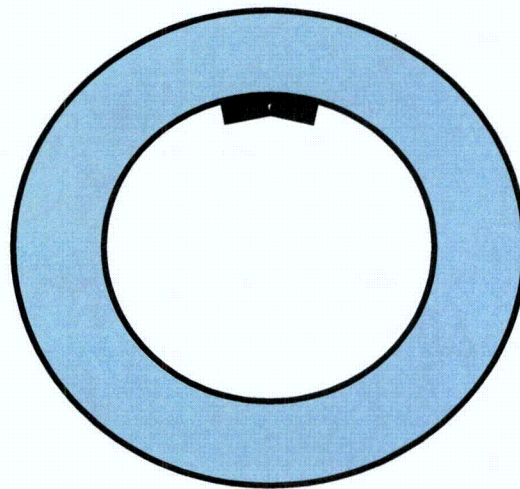


Figure 3.2.1e The two sump positions inside the reactor pedestal. Top view; to scale.

3.3. Previous Work

As noted already the BiMAC was inspired by the IVR coolability concept, and its design is based on basic technology developed during this earlier work done under DOE's ARSAP program. This technology includes the initial (Configuration I) ULPU tests that quantify CHF as a function of inclination (Theofanous and Syri, 1997), the ACOPO tests that quantify natural convection loads from volumetrically-heated pools (Theofanous and Angelini, 2000), and ROAAM that provides the organizing principle for the whole assessment (Theofanous et al, 1994, 1996). One major simplification at present is that the behavior is not susceptible to the so-called "focusing effect", a phenomenon that can arise in in-vessel situations when (if) there is an insufficient amount of molten steel to spread the heat over a large enough area of the side wall, together with the absence of water on top of the molten pool.

Since this early work, there has been an intense follow-up internationally on IVR, including a CSNI specialist's meeting (Garching, 1994), several test programs in France (SULTAN tests), Finland (COPO tests, VTT tests), Sweden (SIMECO, FOREVER tests), Korea (KAIST tests), and Russia (RASPLAV, MASCA tests). All this work is confirmatory of the work done by UCSB for the Loviisa, AP600 and AP1000.

In addition, and on fundamental grounds, since that time the mechanism of Boiling Crisis is understood better (Theofanous et al., 2002a, 2002b; Theofanous and Dinh, 2002, 2004). So is natural convection (Theofanous and Angelini, 2000; Dinh et al., 2004a, 2004b). The latter has been also greatly impacted by advances in CFD and computing power that allow rather detailed Direct Numerical Simulations (DNS) of such phenomena with [sufficient] reliability. We make use of this simulation capability for assessing the thermal loads in the present 2D wedge-shaped geometry.

3.4. Present Assessment

3.4.1. Key Physics

Successful functioning of the BiMAC device depends crucially on the condition that heat removal capability (by boiling) exceeds the thermal loading due to melt natural convection. Thus, quite simply, the key physics here concern processes that control the magnitude of these two outcomes. In addition, it must be shown that, at the end of the main melt relocation event, and associated ablation process, the BiMAC sacrificial layer is left with some material still protecting the steel pipes, and this needs to be done both for HP as well as for LP sequences.

- (a) **Thermal Loads.** Any amount of core debris that is not coolable, will form into a molten pool that, heated in volume, and rejecting heat to the outside through all its boundaries, would eventually reach a quasi-steady, maximum extend configuration. This means that such a molten pool would tend to spread, incorporating more and more debris and concrete material, until eventually all heat supplied to all of its boundaries from the inside is removed by conduction through the surrounding solid crusts and associated materials found on the outside. Thus at the top boundary, it being in contact with water, this balance between heat supply and rejection would define the thickness

of the solidified material that is assumed to exist, persist, and be impenetrable to water—for otherwise, the debris would be coolable on its own, without a need for BiMAC. At the bottom boundary, the melting would extend eventually to a degree that only a rather thin layer of remaining sacrificial material and solidified debris would separate the melt from the steel pipes below. Thus, all around on the inside, the molten pool would see the liquidus temperature, while it develops the amount of superheat needed for rejecting the decay power generated within. We are mainly interested on the thermal loads delivered to the lower, wedge-shaped boundary, and to any vertical boundaries for pools that are voluminous enough to create a submergence on the vertical pipe segments. Bounding estimates of these loads can be obtained by assuming a maximum extent pool involving the total amount of core-and-internals debris possible. From previous experience (for example Angelini and Theofanous, 1995) with such large, high Rayleigh number pools, we know that these loads are spatially non-uniform and that the magnitudes increase with angle of inclination of the lower boundary reaching a maximum at vertical boundaries. We also know that a key parameter, the up-to-down power split, is typically in a proportion within the 2 to 3 range. Thus on an average basis we have here, at the most, a downwards heat flux in the $\sim 100 \text{ kW/m}^2$ range, while due to the small angle of inclination we can expect, on fundamental grounds, that at local heat peaking would not exceed $\sim 300 \text{ kW/m}^2$. On the vertical boundary we can expect as much as 300 kW/m^2 on the average, which with local peaking would yield $\sim 500 \text{ kW/m}^2$ near the top. It should be noted that these order of magnitude results are provided here for some initial perspectives—results specific to the present geometry and conditions are presented in Section 3.4.3.

- (b) **Limits of Coolability.** These limits are defined by the burnout heat flux, or Critical Heat Flux (CHF), of water boiling on the inside of the inclined, and vertical BiMAC pipes. Previous experience in such geometries (Theofanous and Syri, 1997) shows that the CHF increases rapidly with angle of inclination, and that this increase is most rapid in the 0 to 20° interval, ranging from 300 kW/m^2 at the low end to 500 kW/m^2 at the upper end. More recent fundamental data show that burnout in nucleate boiling occurs due to dryout of extremely thin liquid films (tens of microns in thickness) and that surface wettability plays a key role in this dryout (Theofanous et al, 2002a-b). Engineering surfaces such as those of the steel pipes to be employed here were found to be very resilient to dryout. Still, assessment of CHF for any new situation is a matter of empirical determinations under the appropriate geometry and fluid flow conditions that are representative of the application. This was in particular the case for the AP600 and AP1000 (Theofanous et al, 1996, and Dinh et al, 2003), and this is the approach we take here. In addition, we need to be concerned about flow regimes, pressure drop, and flow stability, especially in regards to temporary dryouts, that could develop into irreversible burnouts.
- (c) **Sacrificial Material Ablation by Jet Impingement.** Heat transfer and related phase change processes during melt jet impinging on a solid slab have been studied extensively in the past and their mechanisms are well understood today (Theofanous et al., 1996). A key consideration is whether the instantaneous contact temperature between the melt and the substrate is below the freezing point of the melt—if so, crusts form upon contact and the thermal boundary condition is the melt liquidus; in other words melt superheat governs the rate of heat transfer. This, along with the jet velocity

and the thermo-physical properties, define the rate of heat transfer. These considerations lead to Zirconia as the material of choice for protecting the BiMAC pipes from melt impingement. By having a melting range (2950 - 3120 K), well above the temperature of any reasonably expected metallic melt, the possibility of ablation is completely eliminated. On the other hand, while this is not the case for oxidic jets, the superheats in this case are by comparison (to metallic melts) rather small, and this together with the low thermal conductivities of such melts limit the ablation rates to such low levels that good protection can be achieved without overburdening the device with an excessively thick protective layer.

3.4.2. Probabilistic Framework

The framework for the BMP assessment with BiMAC included in the design is straightforward (Fig.3.4.2.1) and similar to that of Theofanous et al (1996) developed for IVR. Here too there are thermal and mechanical (EVE) loads to be considered. The EVE threat is addressed in Chapter 2. The thermal loads include, as in the IVR case, melt-through by direct jet impingement, and by locally exceeding the burnout heat flux. In addition here we have to be concerned about global mechanisms, such as flow instabilities, that could potentially lead to local dry-outs (due to flow supply deficiencies). As noted above, for the impingement problem we have here the luxury (not available in IVR) of selecting the protective material (a refractory).

More specifically, the following additional remarks can be made:

- (a) Ablation of the protective ceramic layer needs to be addressed under both LP and HP scenarios. The definition of a local ablation depth as a failure criterion refers to a remaining thickness (after ablation), that would be considered structurally stable, consistently with the manner in which the ablation rate has been determined. This is taken as 50 mm.
- (b) The thermal load under melt jet impingement, and any amounts of ablation predicted as a result, is to consider both metallic and oxidic melts, at appropriate levels of superheats, and amounts of material potentially involved in the first, major, pour.
- (c) The thermal loading, is derived from melt natural convection within the BiMAC boundaries, and it informs both thermal failure modes, but in a different emphasis— for the local burnout we are interested in heat flux peaking, such as it occurs at the edges of the inclined portion of the pipes, while for the dryout, we are interested in overall heated channel behavior as driven by total power levels and numbers of channels involved (Section 3.4.3), that is by the average values of heat flux.
- (d) The local critical heat flux, at such power levels as found here, is due to a mechanism very similar to that in nucleate boiling, but at different length and time scales (Angellini et al, 1997, Theofanous et al, 1998, Theofanous et al 2002a,b).
- (e) The dryout condition is defined by a liquid content that may be insufficient to maintain wetting (due to the near-horizontal orientation) over the whole heated area of

the pipe wall—this can arise from strong evaporation along the channel, or from flow instability that involves temporal depletions of sufficient duration to result in dryout.

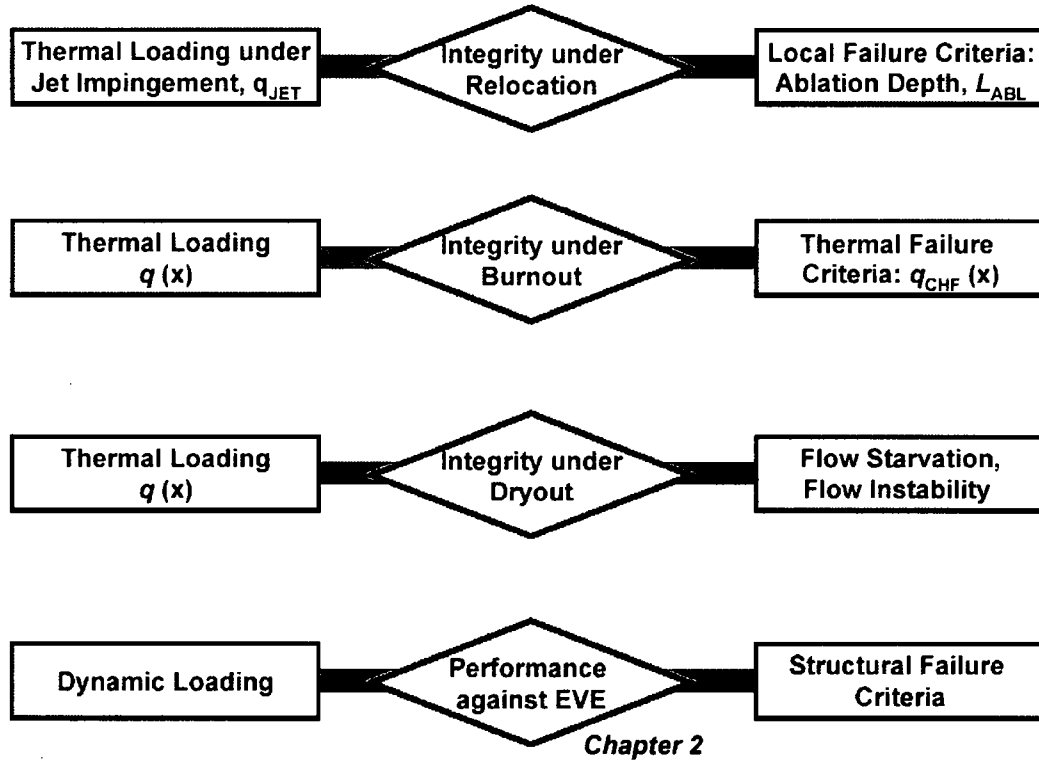


Figure 3.4.2.1. The scope of analysis carried out to address failure of BiMAC function. There are four potential failure modes, as named by the rombic boxes. In each case we also indicate the applicable loading and failure criteria.

3.4.3 Quantification of Loads

Thermal Loads due to Melt Natural Circulation. Significant thermal loads on the BiMAC can only arise from the portions of corium debris that remain in the molten state and are naturally convecting (heat) to the pool boundaries. These loads will depend on the pool configuration/geometry, and our task here is to bound these loads in a manner that does not depend on the details of vessel breach, melt disposition, and more generally ex-vessel behavior insofar as their effect on pool geometry is concerned. This is a basic requirement, which we feel is appropriate for this stage of accident management.

To begin with we note that:

- a. the setting is a fully submerged (in water) debris volume,
- b. there is no convecting (metallic) melt layer on top of the oxidic pool—that is absence of the “focusing effects” familiar from the IVR assessments,

- c. the initial pour, occurring at the time of lower head breach, would involve some fraction (probably significantly less than 1) of the vessel inventory, and will occur in essentially dry LDW space, thus spreading to all available space within the BiMAC space,
- d. subsequent discharges will be gradual, and occurring into a flooded LDW, thus being subject to quenching, as they lie on top of the debris found already on the LDW floor, and
- e. a major, if not all, fraction of the core debris that has been quenched, would be coolable, and thus absent from the molten pool energy balance.

In the following, the quantity of the fuel involved in a melt pool will be denoted by the fraction of the total amount possible (220 tons)—that is, a “50% pool” will be one containing 110 tons of molten fuel. The other key variable is decay power density. For simplicity this will be bounded by 1.2 MW/m^3 (that is, per cubic meter of fuel involved in the melt being considered), which is pertinent to the fastest evolving severe accident sequences in the ESBWR.

An overall view of the melt pool geometries (that is heights and degree to which the vertical boundaries of the BiMAC are submerged) and resulting average heat fluxes (using the 3:1, up-to-down power split discussed below) as functions of the total quantities of melt involved is given in Table 3.4.3.1. Clearly the relevant, yet extremely conservative, as explained just above, flux levels are at $\sim 100 \text{ kW/m}^2$ on the lower boundary, and $\sim 300 \text{ kW/m}^2$ on the side boundary of the BiMAC. These numbers will be used in assessing flow demand and stability requirements of the BiMAC in operation; that is the “Dry-out” question, and this is further pursued in Section 3.4.4. What remains to be done here is to determine the appropriate peaking factors to apply to these fluxes for the purpose of evaluating the Burnout question. We refer to these as horizontal and vertical peaking, as corresponding to the lower and vertical boundaries respectively.

For this purpose we make use of Computational Fluid Dynamics (CFD) simulations (see Appendix D). We considered two pool configurations as defined in Tables 3.4.3.2 and 3.4.3.3. Configuration I corresponds to a “central” BiMAC channel, that is a slice taken in a near-diametrical position, and melt depths that do not submerge the vertical pipes. Configuration II is chosen to correspond to a near-the-edge channel, that is a slice taken far-off the diametric position, and melt depths that submerge the vertical pipes to levels typical of bounding, full-inventory pools. In order to gain in spatial resolution all these calculations were carried in 2D. The effect of 3D convection was also explored for two conditions: Configuration I case C, and Configuration II case M. The thermo-physical quantities used are summarized in Table 3.4.3.4. Key numerical results can be found in Table 3.4.3.5. Detailed results are given in Figures 3.4.3.1 to 3.4.3.4. The following observations can be made on the basis of these results.

- (a) The 2D calculations yield conservative estimates of the up-to-down power split, as well as for the power peaking along the boundary. This is because in 2D turbulence is artificially restricted thus reducing mixing and turbulent energy transfer down the motion cascade. On this basis we take a split of 3, which is still conservative compared to the calculated value of 3.4. For peaking factors we chose to use , still conservatively, the results from the 2D calculations.

(b) Horizontal peaking seems to be insensitive to the pool depth in both configurations. For central channels all cases seem to be well represented by a peaking factor value of 1.25. For near-edge channels the peaking involves a narrow region with sharp rise up to a value of ~3. This is because of the descending, vertical boundary layer (see Figure 3.4.3.1b) which creates an “impact” region right around the point where the vertical and near-horizontal boundaries meet.

(c) Vertical peaking is rather mild, and it can be well bounded by a value of 1.4.

Applying these results to a full-inventory pool we obtain the following, extremely conservative (bounding) estimates:

For Central Channels: $q_{dn} = 100 \text{ kW/m}^2$, $q_{\max, dn} = 125 \text{ kW/m}^2$

For Near-Edge Channels: $q_{dn} = 100 \text{ kW/m}^2$, $q_{\max, dn} = 300 \text{ kW/m}^2$

For Vertical channels: $q_v = 320 \text{ kW/m}^2$, $q_{\max, v} = 450 \text{ kW/m}^2$

See also Addendum to this Section at the end of Chapter 3.

Table 3.4.3.1. BiMAC Capacity as a Function of Melt Pool Height, and Resulting Average Heat Fluxes. Total Decay Power taken at ~6 Hours into the Accident (36.4 MW)

H_melt, m	0.2	0.4	0.6	0.8	1.0
V_melt ^a , m ³	2.2	9.	20.5	35.8	53.8
Mass, tons	18	72.5	164	287	431
i_vertical ^b	51	47	41	29	1
V_sump, m ³	0.3	0.85	1.4	2	2.6
M_sacrificial layer, tons	7.6	15	21.7	27.3	30.7
Top Boundary, m ²	25	49	70.5	87.7	95.8
Bottom Boundary, m ²	25.4	49.7	71.5	88	97.3
Side Boundary, m ²	0	~0	0.8	2.1	5.1
	All melt assumed to be Fuel			All oxides + 20 tons of metal	All oxides + 160 tons of metal
Decay power, MW	1.5	8.6	21.5	36.4	36.4
Upward heat flux, kW/m ²	45	132	226	305	271
Downward heat flux, kW/m ²	15	43	74	100	89
Sideward heat flux, kW/m ²	-	-	300	320	350

a. V_melt – already accounts for volume taken by the sumps.

b. i_vertical - # of BiMAC pipes beyond which the pipes are subject to thermal load on the vertical part (at the center: # 1, at the far end: #51)

c. The total ESBWR vessel inventory is: 220 tons Fuel, 76 tons Zirconium, and 50 tons S-S. An oxidic pool would contain, besides the fraction of the fuel assumed, the fraction of Zr assumed to have oxidized (typically 30%, or 27 tons), some fraction of the steel inventory, and the amounts of refractory material assumed to have melted in.

d. The up-to-down power split was taken as 3:1, and side-fluxes, as per simulations, at ~300 kW/m².

**Table 3.4.3.2. Computational Domain of Melt Pool Configuration I
(Central Slice of the Wedge, without Vertical Section)**

Case	A	B	C
Melt pool's total height, H [m]	0.2	0.4	0.6
Horizontal span of the inclined boundary, L_C [m]	1.13	2.27	3.40
Height of vertical boundary, H_V [m]	0	0	0

**Table 3.4.3.3. Computational Domain of Melt Pool Configuration II
(Near-Edge Slice of the Wedge, with a Vertical Section)**

Case	M	N	O
Melt pool's total height, H [m]	0.6	0.6	0.4
Horizontal span of the inclined boundary, L_C [m]	1.13	2.27	1.13
Height of vertical boundary, H_V [m]	0.4	0.2	0.2

Table 3.4.3.4. Fluid Thermo-Physical Properties and Parameters Used

Properties and Parameters	Value
Density, ρ [kg/m ³]	8000
Thermal conductivity, k [W/m.K]	4
Heat capacity, C_p [kJ/kg.K]	300
Thermal diffusivity, α [m ² /s]	$1.67 \cdot 10^{-6}$
Thermal expansion coefficient, β [1/K]	0.002
Viscosity, μ [Pa.s]	0.01
Prandtle Number $Pr = \nu/\alpha$	0.75
Heat generation rate, q_{vol} [MW/m ³]	1
Angle of inclination, $^\circ$	10

Table 3.4.3.5. Summary of Power Split and Peaking Factor Results from the Direct Numerical Simulations (all fluxes in kW/m²).

Case No.	q_{up}	q_{dn}	q_s	q_{up}/q_{dn}	$q_{max}/q_{dn \text{ or } s}$
A	63	30	N/A	2.1	1.25
B	120	54	N/A	2.2	1.25
C	178	80	N/A	2.2	1.25
C-3D	238	68	N/A	3.5	1.2
M-3D	286	85	280	3.4	3.0 / 1.4
M	255	125	330	2.0	3.0 / 1.4
N	238	126	340	1.9	3.0 / 1.2
O	168	83	245	2.0	3.0 / 1.2

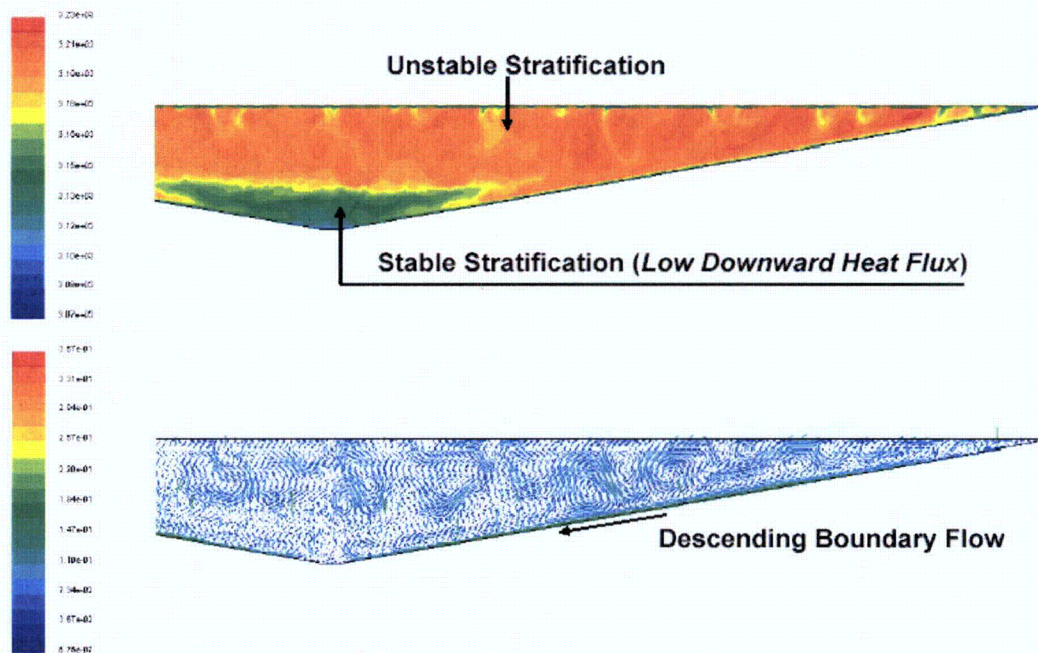


Figure 3.4.3.1a. Illustration: Temperature (top) and velocity (bottom) fields in Configuration I (Case C).

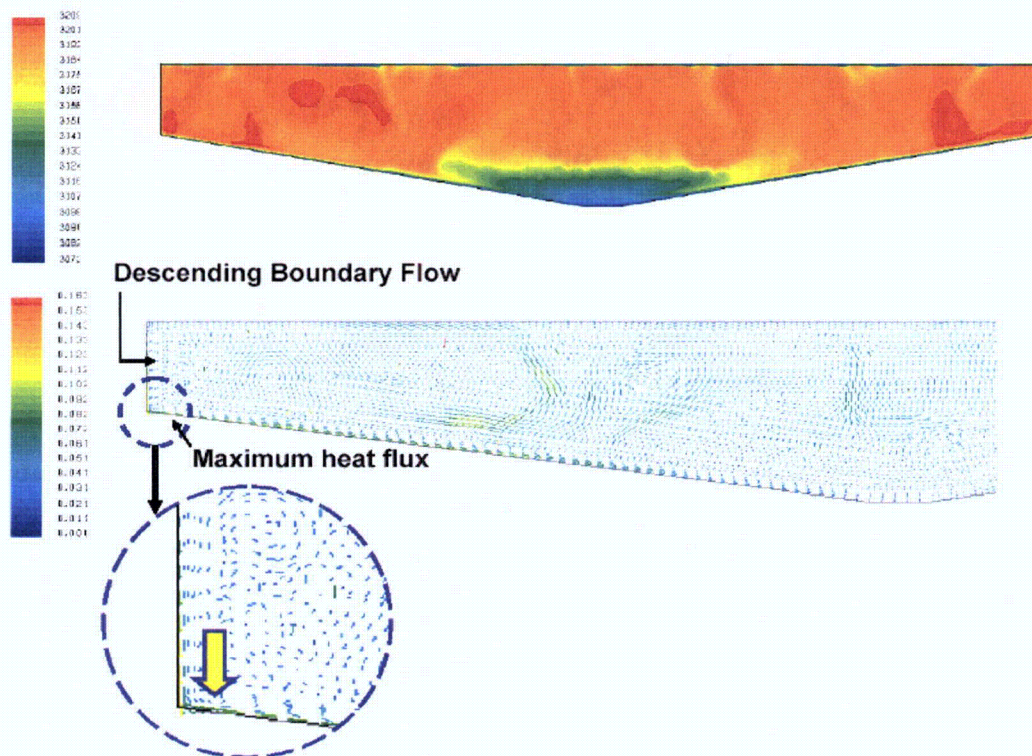


Figure 3.4.3.1b. Illustration: Temperature (top) and velocity (bottom) fields in Configuration II (Case O).

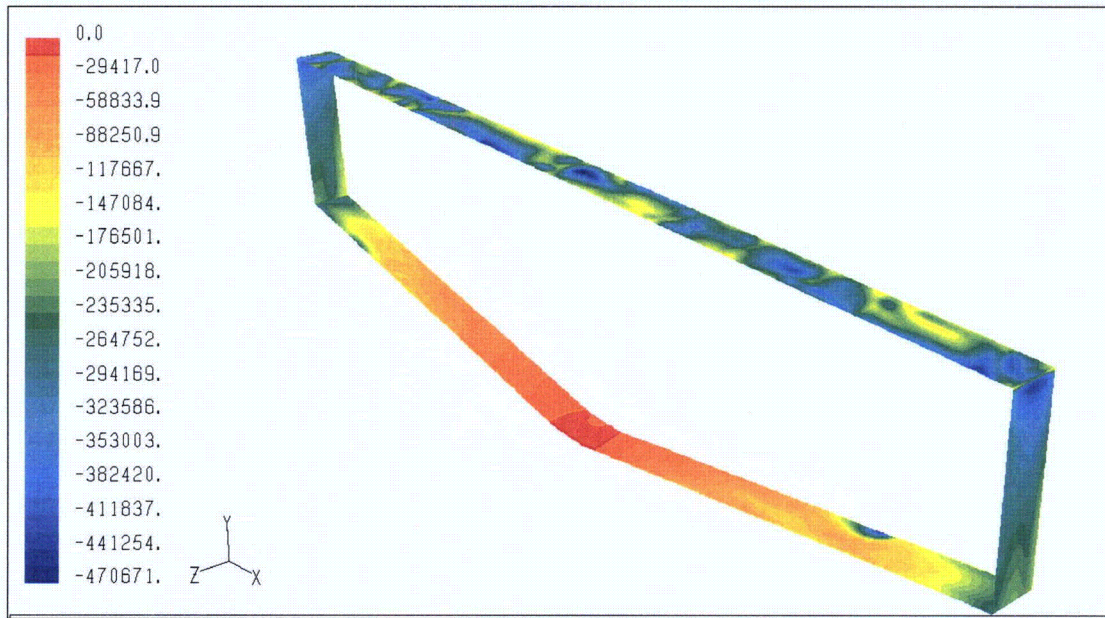


Figure 3.4.3.2. Instantaneous map of heat flux at the pool's boundaries from 3D simulation of Configuration II (Case M-3D) over a width of 0.2 m. Note the negative sign on the scale: the highest absolute heat flux is in dark blue, and the smallest is in red.

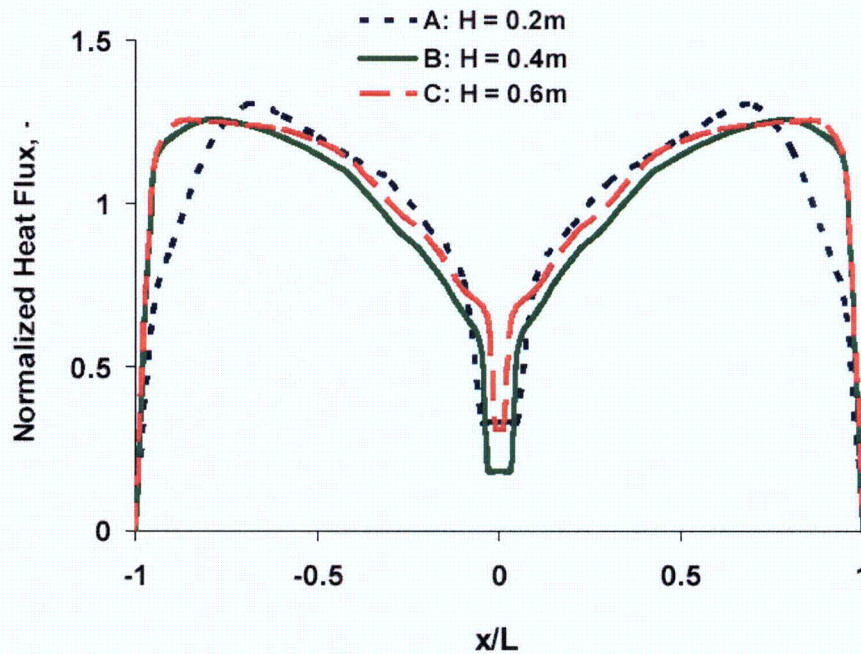


Figure 3.4.3.3. Configuration I results: Downward heat flux distributions along the inclined boundary (total length L).

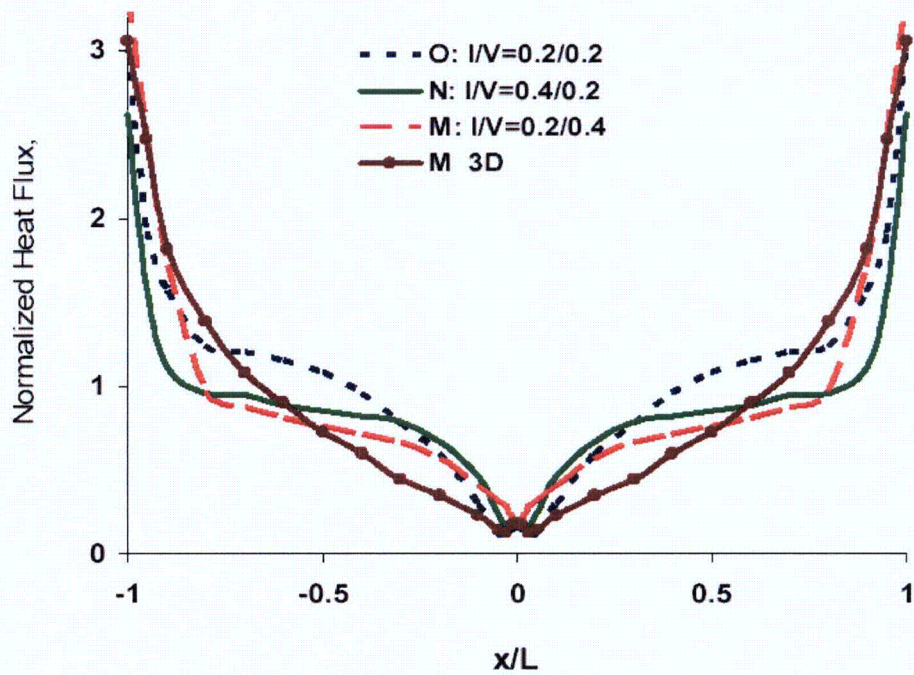


Figure 3.4.3.4. Configuration II results: Downward heat flux distributions along the inclined boundary. (I/V denote heights of the “inclined/vertical” sections of the pool boundaries respectively).

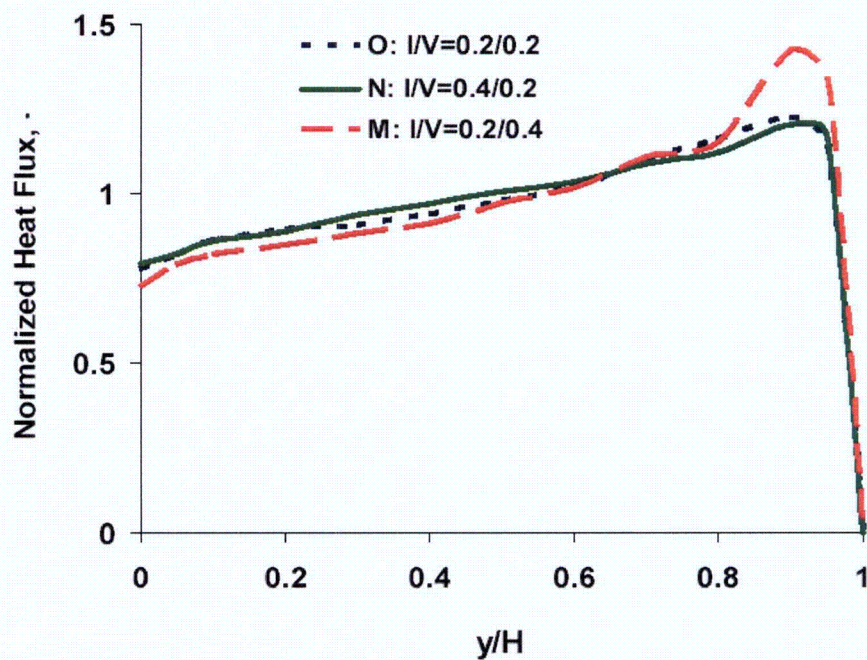


Figure 3.4.3.5. Configuration II results: Sideward heat flux distributions along the vertical pool boundaries of length H . (I/V denote heights of the “inclined/vertical” sections of the pool boundaries respectively).

Protective Layer Ablation under Melt-Jet Impingement

Zirconia[‡] is known to be highly stable in oxidizing atmospheres, and inert in contact with most metals at high temperatures, including molten steels and zirconium, so no chemical ablation of the refractory layer is expected if the discharge happens to be metallic. For metallic melts no thermal (melting) ablation is possible either because Zirconia melts at a temperature range (of 2950 - 3120 K) that is far above any conceivable metallic temperatures in the core debris. Thus we need only be concerned here with oxidic melts that are very highly superheated.

Pure oxidic materials, such as UO₂ or ZrO₂, have melting points of ~3,000 K, which is close to the Zirconia melting range, however, as these oxides interact with other materials, including control rod materials during the formation of the melt pool in the lower plenum, eutectic mixtures are formed (Asmolov, 2000) and melting temperatures as low as 2340 K can be expected. Consequently, given a few 100's K of superheat at the time of vessel breach, the relevant melt temperatures to assess protective layer performance are in the ~2,600 K range, and still well below what is needed to effect melt attack on the Zirconia.

We emphasize that this logic is meant to apply only in the short-term, impingement process that would occur during the first, major relocation event. In the longer term, if the debris is not coolable from above, a combination of melt superheating and eutectics formation should yield ceramic ablation to the extent needed to conduct the needed amount of heat flux into the boiling of water flowing inside the BiMAC.

Further perspective on the question of ablation by an oxidic melt can be gained by calculating the ablation rate for an assumed pure oxidic melt at a temperature of 3,100 K, that is a 100 K superheat. We employ the Saito (1989) correlation, as it has been independently verified by additional experiments, and further established on theoretical grounds (Dinh et al, 1997).

$$Nu = 0.0027 Re.Pr = 0.0027 Pe = 0.0027 U d/\alpha$$

Where U is the velocity, d is the jet diameter, and α is the thermal diffusivity, all referring to melt quantities. Thus the heat flux is found as,

$$q = \Delta T h = 0.0027 U \rho C \Delta T$$

where ρ , C, and ΔT are the melt density, heat capacity, and superheat respectively. The ablation rate is then found by dividing this heat flux into the heat capacitance (including the heat of fusion) of the Zirconia (1,700 kJ/kg, and 6,100 kg/m³).

Applied this for a HP scenario with d= 0.2 m, ΔT = 100 K, and U= 40 m/s, we obtain a heat flux of ~13 MW/m² which would give an ablation rate of 2.5 mm/s. such a pour involving 120 tons would last for ~30 s, and would produce a total ablation of ~8 cm. For LP scenarios lower jet velocities would be exactly compensated by longer pour times, yielding the same result, unless the superheat was different. For example a superheat of 200K, for the same-volume pour, would produce a total ablation depth of 16 cm.

[‡] ["Handbook of Industrial Refractories Technology : Principles, Types, Properties and Applications", Stephen C. Carniglia, Gordon L. Barna, April 1992.]

3.4.4. Quantification of Fragility

Fragility of BiMAC is considered here according to the decomposition shown in Figure 3.4.2.1; namely, failure due to (short-term) interactions between melt and BiMAC pipes during melt relocation, and failure due to long-term thermal loading (melt pool convective heat transfer). The latter, in turn, consists of two aspects: (i) natural circulation flow stability as potentially impacting the development of dry-outs, and (ii) local heat fluxes exceeding the burnout heat flux.

a) Structural Failure Criteria for an Ablated Zirconia Layer. Noting that the protective layer is well supported from below, and that such a ceramic layer when well-cast and cured is very tough, especially to compression, we believe any macroscopic thickness remaining (after ablation) would be sufficient to protect the BiMAC pipes. We will take a thickness of 50 mm to represent, conservatively, the failure threshold.

(b) Natural circulation of coolant flow in BiMAC. This failure mode is assessed by means of the two-phase flow model described in Appendix E. Of interest is to determine at what power level the natural circulation flow becomes susceptible to Ledineg instability; that is, at what power level the two-phase pressure drop causes a sufficient reduction on flow to yield a near-voided condition in the BiMAC channels. As shown in Appendix E, multi-channel flow demand on the BiMAC header can be satisfied by multiple down-comers, so that performance can be adequately matched by using a single channel for both the Downcomer and the Riser.

The basic trend in the results can be seen in Figures 3.4.4.1 and 3.4.4.2. They show flow rates and exit void fractions as functions of supplied heat flux. The latter is applied uniformly over the whole of the riser, which includes the inclined and the vertical portions of the boundary. The effect of non-uniform power supply was evaluated, within the limits that are reasonable in the BiMAC environment, and it was found to be negligible. We consider only a central channel, and saturated water at the inlet, which provide the most limiting conditions for present purposes.

In Figure 3.4.4.1 we note the broad maximum in flow rate obtained at heat fluxes around 100 kW/m^2 , the value that represents an upper bound of what would be possible in the LDW of the ESBWR. The decline in flow rates is due to two-phase pressure drop compensating at an increasing rate for the increased gravity head created by an increased channel voiding condition. In Figure 3.4.4.2 we can see this increase in voiding with heat flux. The increase is monotonic, and reaches up to an exit void fraction of $\sim 40\%$ found for a heat flux level of 100 kW/m^2 . The flow is stable throughout this range of possible conditions in that the rates of change of gravity head with increasing heat flux is higher than the change in demand due to increase in frictional pressure drop.

In regards to dryout due to water depletion, it is clear that a 40% exit void fraction would not place the channel at any such risk. In Figure 3.4.4.2 we show the 70% exit void fraction level as a potential demarcation of the water-deficient regime, and the figure further shows that the relevant heat flux level would then be $\sim 350 \text{ kW/m}^2$ —it is emphasized that this is for an average heat flux applied to the whole length of the longest, central channels of the BiMAC. Much higher fluxes would be needed for the middle or near-edge channels that are shorter and have vertical sections.

See also Addendum to this subsection at the end of Chapter 3.

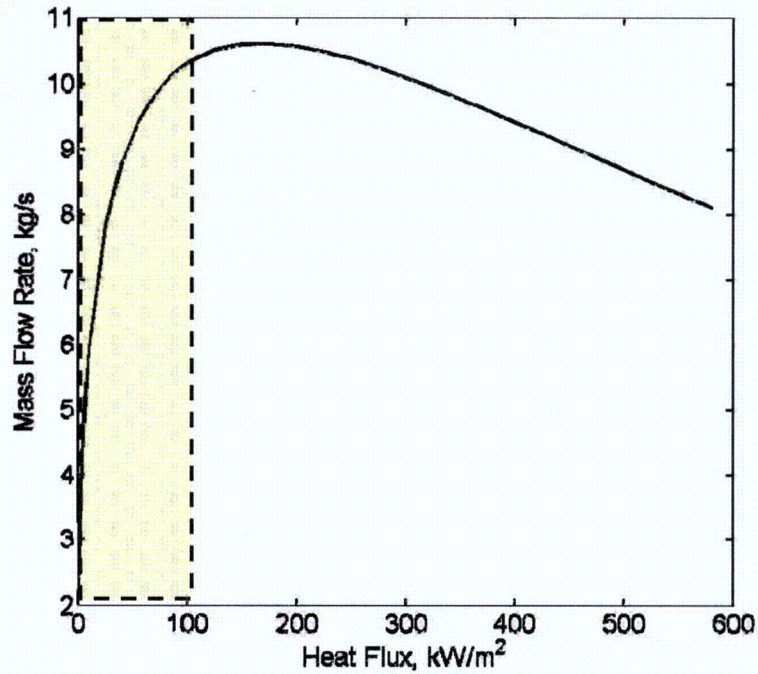


Figure 3.4.4.1. Predicted mass flow rate through a BiMAC channel, in natural convection, as function of applied heat flux (based on the pipe projected area). Shaded is the relevant range of heat fluxes.

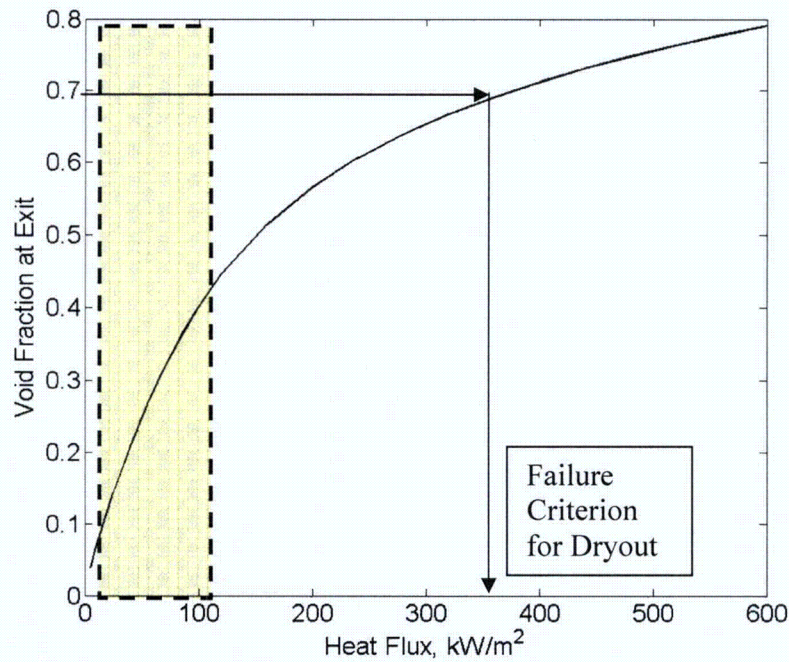


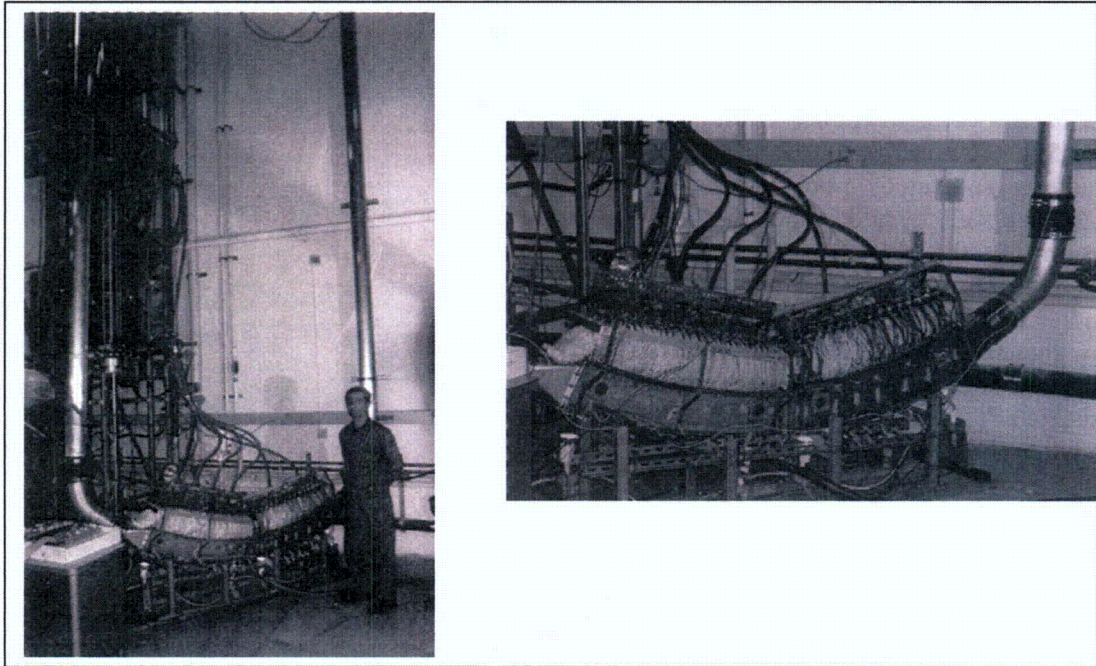
Figure 3.4.4.2. Predicted void fractions at the exit of a BiMAC channel, in natural convection, as function of applied heat flux (based on the pipe projected area). Shaded is the relevant range of heat fluxes.

(c). Limits to Coolability. For the pipes that make up the lower boundary of the BiMAC jacket we make use here of experiments made to support the IVR case for the AP600, and the Loviisa reactor in Finland (Theofanous et al 1996, 1994). These experiments were done in a series of several geometric configurations, and these evolved along the way as understanding was being developed. It turns out that the very first of the ULPU setups, the one known as Configuration I (C-I), were designed to address what at the time was the principal unknown, namely the inverted, near horizontal geometry at the pole of the lower head. It turns out that this design matches exactly the geometry of interest here (Figure 3.4.4.4). All the rest of the test program, performed over the period of some years, and spanning a total of five configurations, provides a further support of these first results, as well as of our effort to relate and interpret them for our purposes here. In particular, the emphasis in this program shifted with time to the more limiting (for the PWR IVR) near-vertical boundary, at the upper edge of the lower head. This is relevant here too, as it characterizes the Critical Heat Flux (CHF) on the pipes that make up the vertical boundary of the BiMAC. For this, the ULPU Configuration IV (Figure 3.4.4.5) is relevant. The pool boiling data from C-I are reproduced in Figure 3.4.4.6, and those from C-IV in Figure 3.4.4.7. In both C-I and C-IV the channel cross section was 10x15 cm, that is quite close to that of a BiMAC pipe.

In Figure 3.4.4.6 we can see that according to these data, and for the range of inclination angles θ of our interest ($\theta \sim 10\text{-}15^\circ$), the CHF is in the range of 450 to 550 kW/m². It should be noted that these test were conducted at pool boiling conditions (no net flow supplied) and rather low submergence, so we can expect they provide a conservative representation of BiMAC forced (initially) or natural (the rest of the time) convection environment.

In Figure 3.4.4.7 we can see that at near vertical orientation a CHF of 1 MW/m² is quite appropriate. Indeed, this estimate is robust as this would be also a typical lower bound of CHF from an upwards-facing flat plate (engineering surface) in water.

While as we see in the next section further enhancements are hardly needed, it may be worth pointing out that CHF enhancement technology has been advanced greatly over the past decade, and that we would plan to take advantage of them in the final design to be carried out at the COL stage. These advances are due to both improvements in basic understanding of high heat-flux boiling and burnout physics, as well as empirical development of innovative approaches, which make use of heater surface treatment and coolant chemistry to improve the coolability limit in boiling systems. In particular, we note that the C-I experiments were conducted with distilled water, whereas both reactor water and GDCS water are not distilled. In our recent work for the AP1000, we established a significant, beneficial effect of reactor (and containment) water chemistry on CHF (see Dinh, Tu and Theofanous, 2003; Tu, Dinh and Theofanous, 2003; Theofanous and Dinh, 2004).



ULPU 2000
Configuration C-1

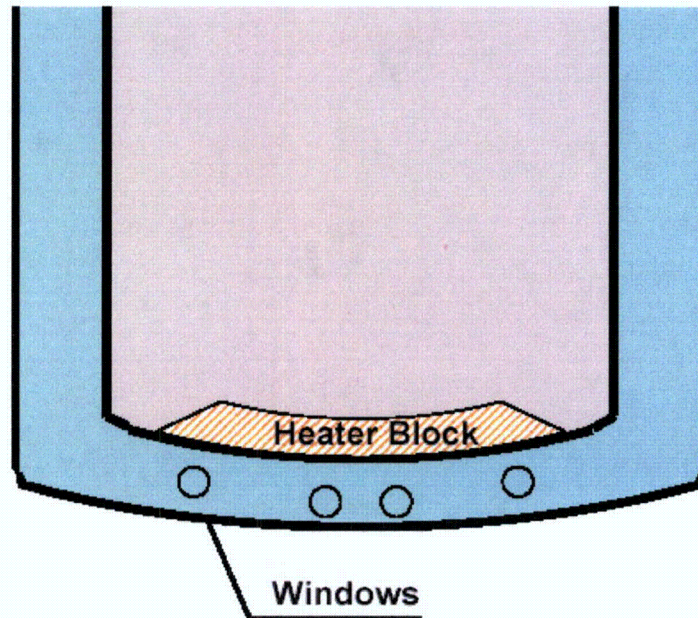


Figure 3.4.4.4. Pictures and schematic of the ULPU Configuration C-I: low-submergence, pool-boiling conditions. Similarity between C-I and BiMAC is rather straightforward.

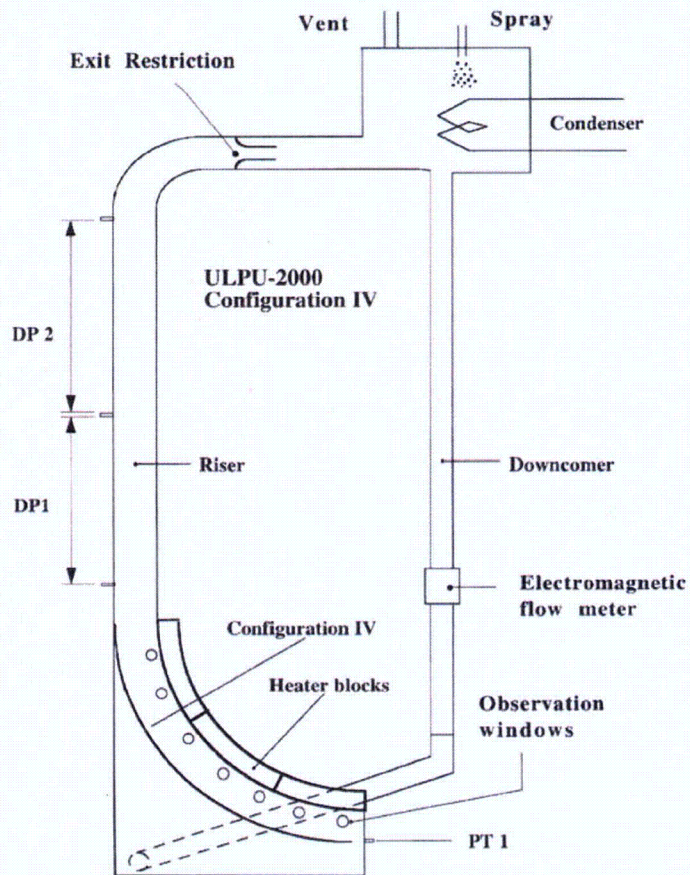
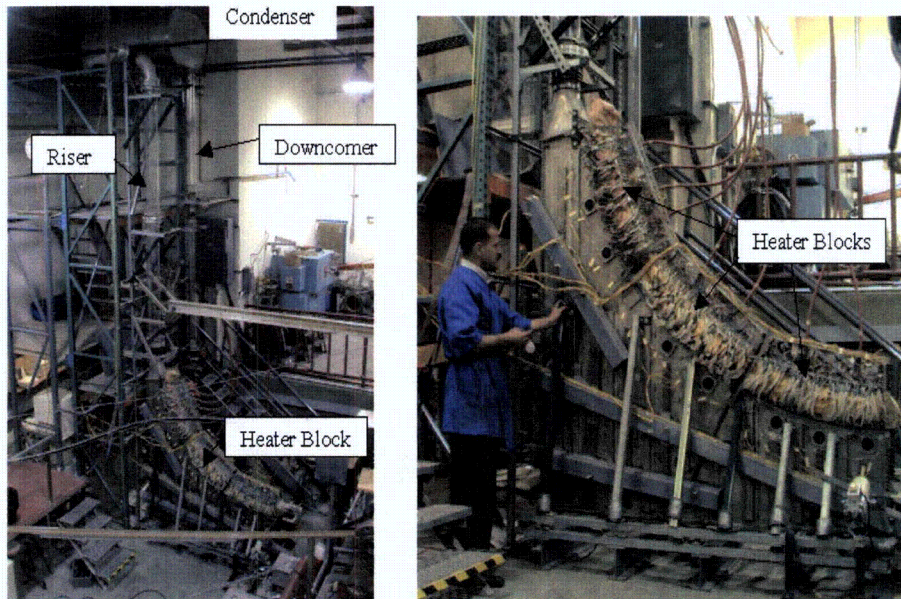


Figure 3.4.4.5 Pictures and schematic of the ULPU Configuration C-IV. The curved baffle shown creates a channel similar to a BiMAC in regards to the vertical segment of pipe. The pool boiling condition is defined by a water level near the exit of the curved portion of the flow channel.

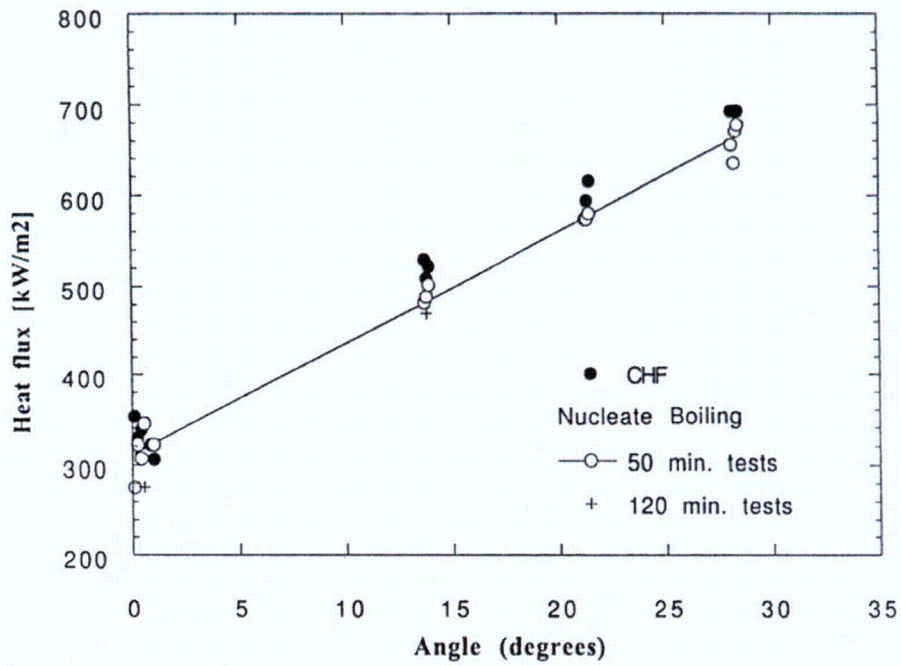


Figure 3.4.4.6. Critical Heat Flux measured in ULPU C-I (near horizontal, inverted geometry) under pool boiling conditions (Theofanous et al., 1994b).

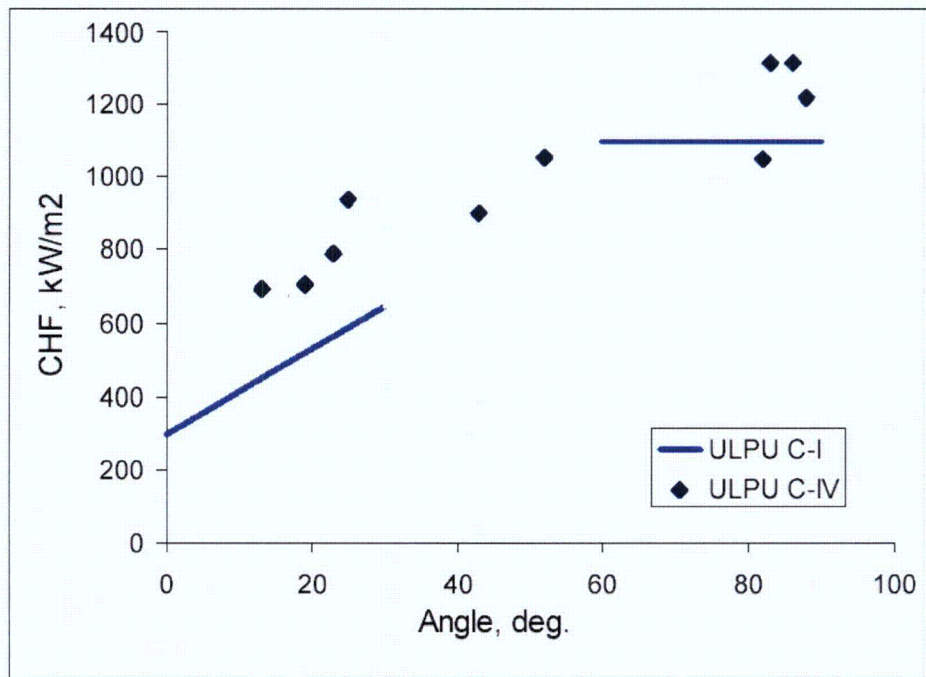


Figure 3.4.4.7. Critical Heat Flux measured in ULPU C-IV, under pool boiling conditions (Theofanous et al., 1994b; 1996).

3.4.5. Prediction of Failure Probability

Combining the results of the previous two sections we can now evaluate the likelihood of BiMAC device's failure to function for its intended purpose as follows:

- (a) The ceramic-refractory material of the protective layer is only susceptible (by ablation) to superheated oxidic melt impingement. Even then it would require a melt volume of ~500 tons to penetrate the 200 mm layer down to within 50 mm from the BiMAC pipes. Thus failure by melt impingement is physically unreasonable.
- (b) For the range of thermal loadings that are applicable to non-coolable melt-pool configurations in the LDW, two-phase natural circulation is seen to be quite sufficient in supplying the BiMAC pipes with a cooling stream that is stable, and of sufficiently high liquid (water) content to ensure a well-wetting condition every where. As shown in Figure 3.4.4.2, the available margin is over 300%. Thus, failure by dry-outs due to flow and water supply deficiencies is physically unreasonable.
- (c) As indicated in Figures 3.4.5.1 and 3.4.5.2, the (conservatively estimated) margins to local burnout are anywhere from 500% for a central channel, to 100% near the top of a vertical channel, to 60% near the edges of the inclined lower boundary of a near-edge channel. These margins, placed on the basis of bounding estimates both for thermal loads and burnout heat fluxes, dwarf any uncertainties due to the small geometric differences between BiMAC pipes and the ULPU test sections. Thus, failure due to local burnout is physically unreasonable.
- (d) Finally we note that the BiMAC cooling jacket protects also the two sumps found in the LDW floor in a way that prevents melt from entering them.

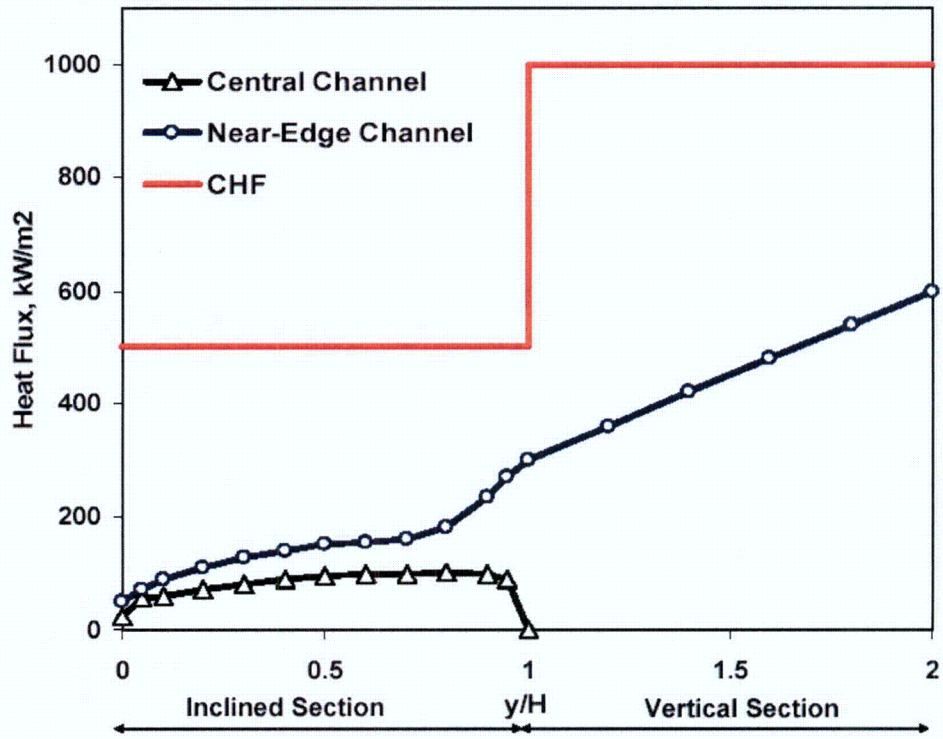


Figure 3.4.5.1. Local thermal loads and coolability limits in BiMAC at bounding conditions and estimations.

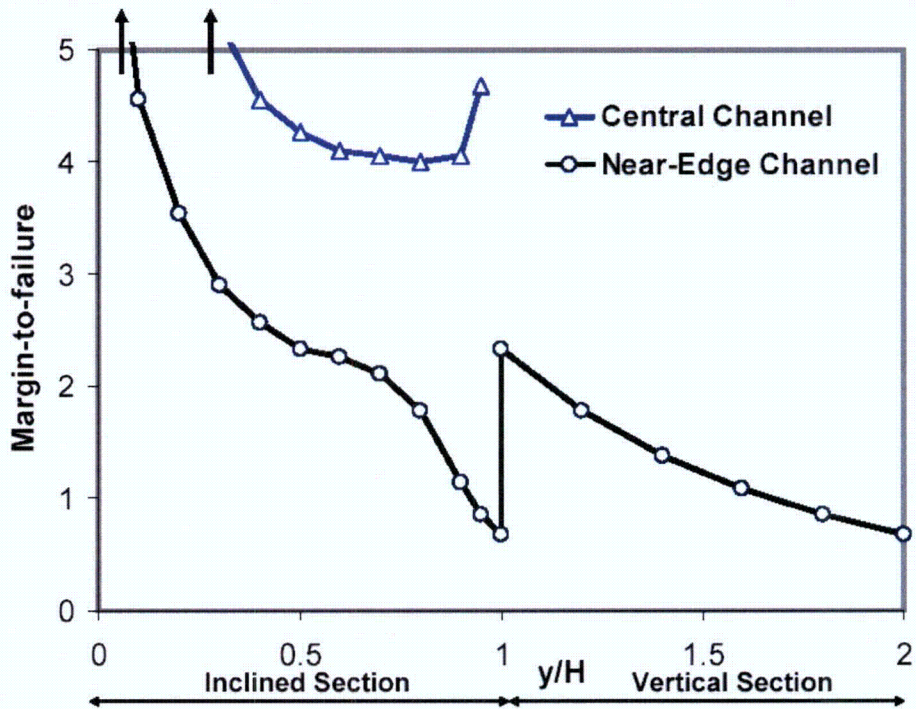


Figure 3.4.5.2 Margins to burnout in BiMAC. The margin is defined as $(q_{CHF}/q - 1)$ where q is the local bounding heat flux, and q_{CHF} is the local minimum bound of burnout flux.

3.5. Summary and Conclusions for BMP

We have shown that the BiMAC device is effective in containing all potential core melt releases from the RPV in a manner that assures long term coolability and stabilization of the resulting debris. In this way the concrete basemat penetration issue becomes mute, and so is containment over-pressurization by concrete decomposition gases.

The principal ingredients in this effective functioning of the device can be recapitulated as follows:

- (a) Choice of a refractory ceramic material as a protective layer, that eliminates ablation by superheated metallic jets, and a layer thickness chosen so as to provide ample margins to the ablation front reaching the BiMAC pipes even under the most extreme, large-volume-pours of superheated melts (for both for LP and HP scenarios),
- (b) Positioning and dimensioning of the cooling jacket (the BiMAC pipes) so that while resistant to significant dynamic loads (see Chapter 2), they allow for stable, low-pressure-loss, natural circulation that is not susceptible to local burnout due to thermal loads exceeding the critical heat flux, or to dry-outs due to flow and water deficient regimes,
- (c) Sizing and positioning the BiMAC in the LDW in such a way that all melt released from the vessel is captured (except of course of any melt dispersed to the UDW in HP scenarios) and contained within , and
- (d) Providing for an angle of inclination of the lower boundary that balances the various requirements, including operational space available, and good margins to local burnout.

Full-scale testing of BiMAC is needed for final confirmation and optimization of the design and it is planned to be carried out and be available for the COL stage of the licensing review..

See also Addendum to this Section at the end of Chapter 3.

References to Chapter 3 (BMP)

S. Angelini, Y. Buyevich and T.G. Theofanous, "The Mechanism and Prediction of Critical Heat Flux in Inverted Geometries," NURETH-8, Kyoto Japan, September 30-October 4, 1997, Vol. 1, 147-156.

Asmolov, V.V. (2000), "RASPLAV Project Major Activities and Results", RASPLAV Seminar, Program Review Meeting of OECD RASPLAV Project, November, 2000, Munich, Germany. Also in:

Asmolov, V.V., S.S. Abalin, A.V. Merzliakov, V.N. Zagryazkin, Ye.V. Astakhova, I.D. Daragan, V.D. Daragan, Ye.K. D'yakov, A.Yu. Kotov, A.S. Maskaev, Ye.M. Rakitskaja, V.M. Repnikov, V.Yu. Vishnevsky, V.V. Volko; A.G. Popkov, V.F. Strizhov, (2000) "RASPLAV Final report: Properties Studies: Methodology and Results". Kurchatov Institute, Moscow, 2000.

Dinh, T.N., and Nourgaliev, R.R. (1997). "Turbulence Modeling in Large Volumetrically Heated Liquid Pools", *Nuclear Engineering and Design*, **169**, 131-150, 1997. Also in

R.R. Nourgaliev, and T.N. Dinh, (1997). "The Investigation of Turbulence Characteristics in an Internally Heated Unstably Stratified Fluid Layers", *Nuclear Engineering and Design*, **178**:(1), 235-259, 1997.

R.R. Nourgaliev, T.N. Dinh, and B.R. Sehgal, (1997a). "Simulation and Analysis of Transient Cooldown Natural Convection Experiments", *International Journal of Nuclear Engineering and Design*, **178**:(1), pp.13-27, 1997a.

R.R. Nourgaliev, T.N. Dinh, and B.R. Sehgal, (1997b). "Effect of Fluid Prandtl Number on Heat Transfer Characteristics in Internally Heated Liquid Pools with Raleigh Numbers up to 10^{12} ", *Nuclear Engineering and Design*, **169**, 165-184, 1997b.

Dinh, T.N., and Theofanous, T.G, (2003). "Nucleation Phenomena in Boiling", *Multiphase Science and Technology*. **15**(1-4), pp.349-363, 2003.

Dinh, T.N., Tu, J.P., Salmassi, T., Theofanous, T.G, (2003). "Limits of Coolability in AP1000-Related ULPU-2400 Configuration V Facility," *International Topical Meeting on Nuclear Reactor Thermal Hydraulics*, Seoul, Korea, Oct., 2003.

Dinh, T.N., Tu, J.P. and Theofanous, T.G. (2004) "Hydrodynamic and Physico-Chemical Nature of Burnout in Pool Boiling", International Conference on Multiphase Flow, Yokohama, Japan, May 2004. Paper 296. 14p.

Dinh, T.N., Yang, Y.Z., Tu, J.P., Nourgaliev, R.R., and Theofanous, T.G. (2004a), "Rayleigh-Bénard Natural Convection Heat Transfer: Pattern Formation, Complexity and Predictability", *2004 International Congress on Advances in Nuclear Power Plants*, Pittsburgh, PA, June 13-17, 2004. Also in,

T.N. Dinh, J.P. Tu, Y.Z. Yang, R.R. Nourgaliev and T.G. Theofanous (2004b), "Characterization and Predictability of Transient Heat Transfer in an Unstably Stratified Layer during Power Startup", *37th AIAA Thermophysics Conference*, Portland, OR, June 27-30, 2004. AIAA-2004-2733.

Fischer, M., (2003). "Severe Accident Mitigation and Core Melt Retention in the European Pressurized Reactor (EPR)", *11th International Conference on Nuclear Engineering*, Tokyo, JAPAN, April 20-23, 2003, ICONE11-36196

Fluent (2004).Fluent 6.0 -- CFD Code Manual.

Garching (1998) OECD/CSNI/NEA Workshop on "In-vessel core debris retention and coolability", Garching, Germany, 3-6 March, 1998.

GE-NE (2005a), ESBWR Certification Probabilistic Safety Assessment. NEDC-33201P. August 2005.

GE-NE (2005b), ESBWR Design Control Document. 26A6642BZ Rev.00. August 2005.

Grenoble (1994) OECD/CSNI/NEA Workshop on Large Molten Pool Heat Transfer, Nuclear Research Centre, Grenoble, France, March 9-11, 1994.

Kukhtevich, I.V. , Bezlepkin, V.V, Leontiev, Yu. G., Strizhov, V., Proklov, V.B. (2001). "Severe Accident Management Measures for Tianwan NPP with VVER-1000, in "Implementation of Severe Accident Management Measures"", *Workshop Proceedings PSI-Villigen*, Switzerland, 10-13 September 2001. Nuclear Safety NEA/CSNI/R(2001)20 PSI Report Nr. 01-15, November 2001.

Kymäläinen, O., Tuomisto, H., Hongisto, O., and Theofanous, T.G. (1994). "Heat Flux Distribution from a Volumetrically Heated Pool with High Rayleigh Number," *Nuclear Engineering & Design*, 149, 401-408, 1994.

Kymäläinen, O., Tuomisto, H., , and Theofanous, T.G. (1997). "In-vessel Retention of Corium at the Loviisa Plant," *Nuclear Engineering & Design*, 169, pp109–130, 1997.

Saito M., et al (1989), "Melting Attack of Solid Plate by a High-Temperature Liquid Jet- of Crust Formation", *Nuclear Engineering & Design*, 121, p.11, 1990.

Scobel, J.H., Theofanous T.G., and Conway, L.E. (2002). "In-Vessel Retention of Molten Core Debris in the Westinghouse AP1000 Advanced Passive PWR," *Proceedings, ANS 2002 Annual Meeting*, International Congress on Advanced Nuclear Power Plants (ICAAP), Hollywood, FL, June 9-13, 2002.

Theofanous, T.G. , Liu, C., Angelini, S., Kymäläinen, O., Tuomisto, H., and Additon, S., (1994a). "Experience From the First Two Integrated Approaches to In-Vessel Retention Through External Cooling," *OECD/CSNI/NEA Workshop on Large Molten Pool Heat Transfer*, Nuclear Research Centre, Grenoble, France, March, 9–11, 1994.

Theofanous, T.G., Syri, S., Salmassi, T., Kymäläinen, O. and Tuomisto, H. (1994b). "Critical Heat Flux Through Curved, Downward Facing, Thick Walls," *Nuclear Engineering & Design*, 151, 247-258, 1994.

Theofanous, T.G., Syri, S., Salmassi, T., Kymäläinen, O. and Tuomisto, H (1994c). "Critical Heat Flux Through Curved, Downward Facing, Thick Walls," *OECD/CSNI/NEA Workshop on Large Molten Pool Heat Transfer*, Nuclear Research Centre, Grenoble, France, March, 9–11, 1994.

Theofanous, T.G., Liu, C., Additon, S., Angelini, S., Kymalainen O., and Salmassi, T. (1996), "In-Vessel Coolability and Retention of a Core Melt," DOE/ID-10460, Vols. 1 and 2, October 1996.

Theofanous, T.G., Liu, C., Additon, S., Angelini, S., Kymalainen O., and Salmassi, T. (1997) "In-Vessel Coolability and Retention of a Core Melt," *Nuclear Engineering & Design*, 169 (1997) 1–48.

Theofanous T.G., and Syri, S. (1997) "The Coolability Limits of a Reactor Pressure Vessel Lower Head," *Nuclear Engineering & Design* 169 (1997) 59–76.

Theofanous T. G., Tu J. P., Maenpaa, T. K. (1998) "The Mechanism and Prediction of Critical Heat Flux in Inverted Geometries" Third International Conference on Multiphase Flow, Lyon, France, June 8-12, 1998.

Theofanous, T. G. and Angelini, S. (2000). "Natural Convection for In-Vessel Retention at Prototypic Rayleigh Numbers," *Nuclear Engineering and Design*, 200, 1-9, 2000.

Theofanous, T.G., Tu, J.P., Dinh, A.T. and Dinh, T.N. (2002a). "The Boiling Crisis Phenomenon. Part I: Nucleation and Nucleate Boiling Heat Transfer", *Experimental Thermal and Fluid Science*, 26, 775-792, 2002.

Theofanous, T.G., Tu, J.P., Dinh, A.T. and Dinh, T.N. (2002b). "The Boiling Crisis Phenomenon. Part II: Dryout Dynamics and Burnout", *Experimental Thermal and Fluid Science* 26, 793-810, 2002.

Theofanous, T.G. and Dinh, T.N. (2003), "On the Prediction of Flow Patterns as a Principal Scientific Issue in Multifluid Flow", *Multiphase Science and Technology*. 15(1-4), pp.57-76, 2003.

Theofanous, T.G. and Dinh, T.N. (2004), "High Heat Flux Boiling and Burnout as Microphysical Phenomena: Mounting Evidence and Opportunities", accepted for *Multiphase Science and Technology*. 2005. Also *Keynote Paper*. Japan-US Seminar on Two-Phase Flow Dynamics. December 6-11, 2004. Nagahama. CD-ROM Proceedings.

Theofanous, T.G. and Dinh, T.N. (2005) "Basemat-Internal Melt Arrest and Coolability (BiMAC) device". Patent Application. TcI/GE Document. GE Nuclear Energy. San Jose, March 30, 2005.

Tu, J.P., Dinh, T.N., Theofanous, T.G. (2003). "Enhancing Resistance to Burnout via Coolant Chemistry," *10th International Topical Meeting on Nuclear Reactor Thermal Hydraulics*, Seoul, Korea, Oct., 2003.

3.4.3 Add Quantification of thermal loads (Addendum of July 31, 2006)

Due to the importance of the up-to-down power split in the maximum thermal loading estimate of BiMAC, additional calculations were made both in 2D and 3D, with refined nodalization (roughly a reduction of node size by a factor of 4) as indicated in Table 3.4.3.5Add. The numbers in parenthesis are the previous results as presented originally in Table 3.4.3.5. In addition we explored the effects of increasing the Prandtl number, and decreasing the Rayleigh number due to assumed variations in transport properties. All these variations were made on test case M, considering a central “slice” of the melt pool, 0.1 m in thickness (see Figure 3.4.3.2), with periodic or symmetry (zero gradient) boundary conditions on the side-surfaces of this slice.

As seen in Table 3.4.3.5Add, the effects of all these variations are minimal, and the results confirm that the value of flux ratio used in our assessment is appropriate, and robustly conservative.

The flux distributions are also consistent with our previous results, except for showing in somewhat accentuated degree (by ~20%) the highly localized corner-region heat flux increases discussed previously in Section 3.4.3. As we noted therein, these are somewhat of an artifice of the numerical simulations that do not take into account the effect of crusts at the pool boundaries.

Table 3.4.3.5 Add. Summary of power split results in refined-grid calculations of melt natural convection in a central BiMAC “slice”. The numbers in parenthesis are previous results found in Table 3.4.3.5.

<u>Case No.</u>	<u>Ra'</u>	<u>Pr</u>	<u>q_{up}/q_{dn}</u>	<u>Minimum Node size Δx- Δy- Δz (mm)</u>
<i>M-2D-FG</i>	$1.82 \cdot 10^{14}$	0.75	2.1 (2.0)	1-0.5
<i>M-3D-FG</i>	$1.82 \cdot 10^{14}$	0.75	3.3 (3.4)	1-0.5-2
<i>M-3D-FG-Pr</i>	$1.82 \cdot 10^{14}$	7.5	3.42	1-0.5-2
<i>M-3D-FG-Vi</i>	$1.82 \cdot 10^{13}$	0.75	3.61	1-0.5-2

3.4.4 (b) Add Quantification of fragility (Addendum of July 31, 2006)

Another perspective on the margins to failure due to this mechanism that can limit coolability can be gained by determining, in the fashion employed in Section 3.4.4 (b), the pipe diameter for which, at a heat flux level of 100 kw/m^2 , the change in flow due to increase in power level first becomes negative. As can be seen from Figures 3.4.4.1a to 3.4.4.2b, this condition is bracketed between pipe diameters of 5 and 7.5 cm.

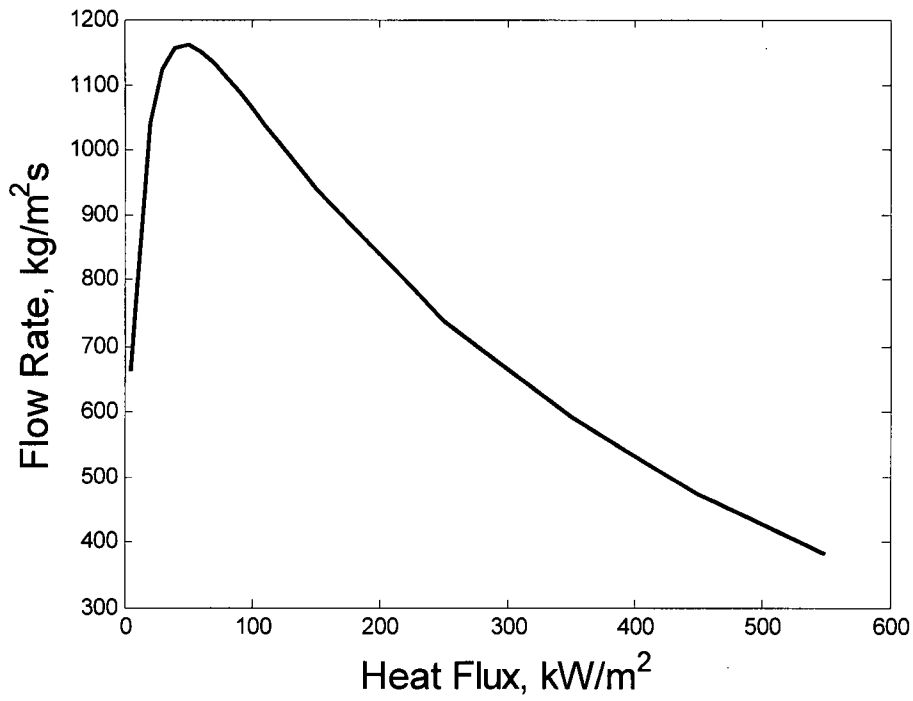


Figure 3.4.4.1a. Same as Figure 1.4.4.1 but with a pipe diameter of 5 cm.

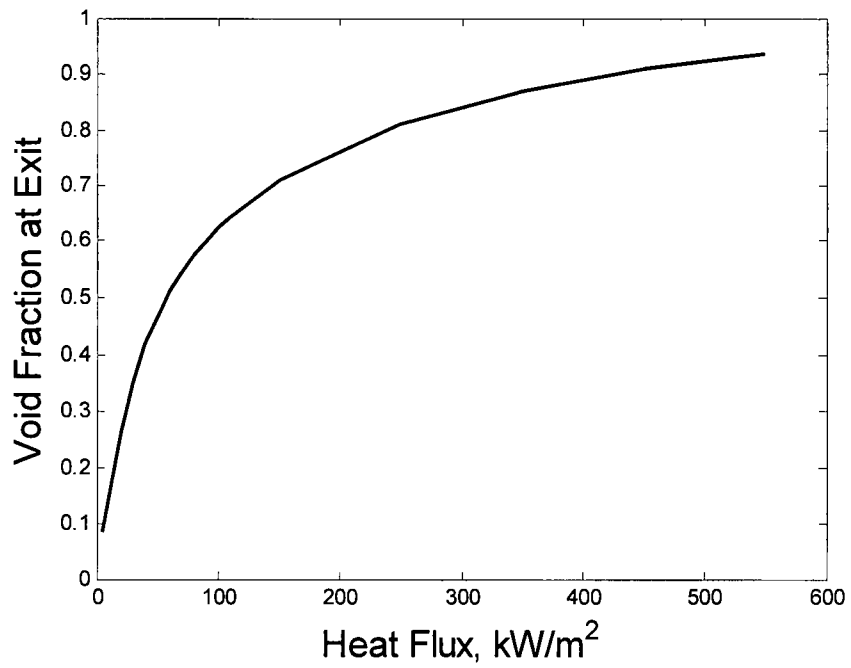


Figure 3.4.4.2a. Same as Figure 1.4.4.2 but with a pipe diameter of 5 cm.

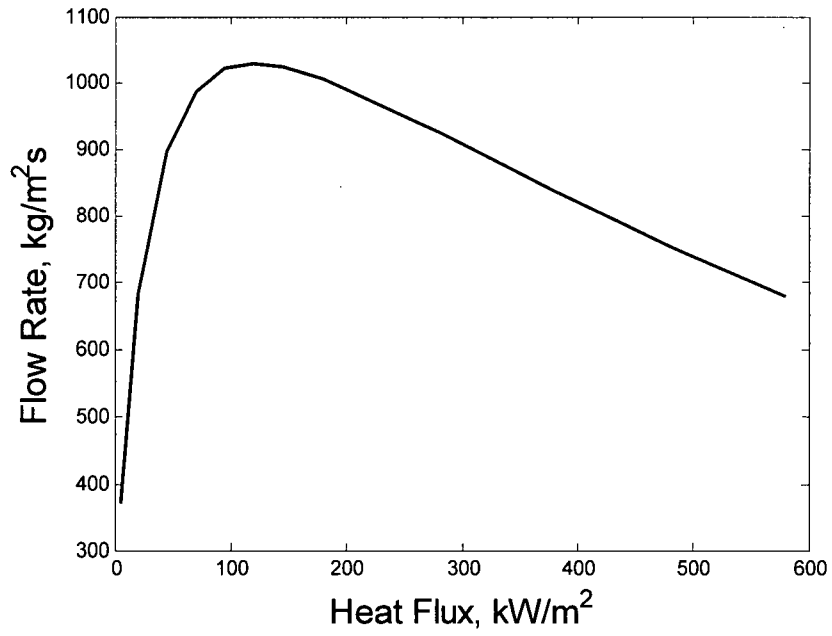


Figure 3.4.4.1b. Same as Figure 1.4.4.1 but with a pipe diameter of 7.5 cm.

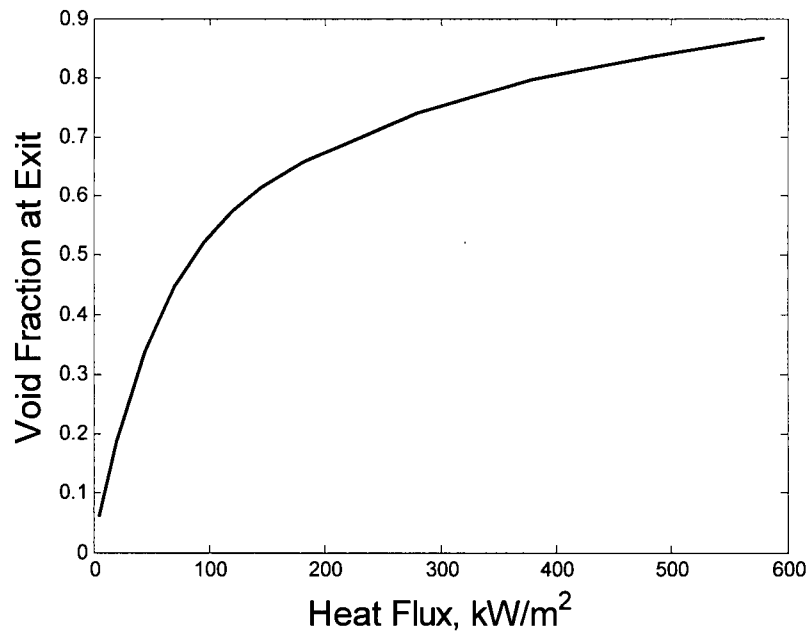


Figure 3.4.4.2b. Same as Figure 1.4.4.2 but with a pipe diameter of 7.5 cm.

3.5 Add Summary and Conclusions for BMP (Addendum of July 31, 2006)

In addition to the thermal load considerations detailed in this chapter, and the upcoming BiMAC experiments, the detailed design of BiMAC will involve considerations of external protection against mechanical loads, such as may be generated by falling, or ejected objects/debris following RPV failure. This addendum is to note that this design effort will be facilitated by relaxing the melt-retentive property originally envisioned for the BiMAC cover plate, and now found to be unnecessary.

In particular, rather than requiring that this cover plate be readily penetrable by impinging molten core material, we now prefer that it be materially substantial, thermally robust, and it be well supported from below in a manner that offers a naturally protective function.

In considering potential mechanical loads for the detailed design, we recognize that:

- a) Because in the ESBWR design the control rod drives (CRDs) are “hooked” to the lower core support plate, they cannot fall even if the welds that seal the lower head penetrations were to melt out (actually this hooking is to protect against rod ejection in case of such a failure under normal operation). Thus the only mechanism for failure is detachment of one or more instrument tubes. While not supported externally in a manner that would prevent their total detachment, these tubes have restraints that would impede their motion following such detachment, and these would have to be taken into account in defining the design criteria for the BiMAC cover plate. In addition this would have to include the protective function of the intervening CRD-maintenance platform.
- b) Because the CRD motors along with related supports form a massive and compact region at the lower ends of the CRDs, any jet(s) emanating from instrument tube penetration failures on the lower head would be disrupted and dispersed. This dissipation/defocusing of mechanical as well as thermal energy loads beneficially impacts the design requirements for protection of the BiMAC, including its ceramic sacrificial layer.
- c) This enhanced protection is consistent and of benefit in the reliability design of the BiMAC flooding deluge system, as it relaxes the timing requirements for activation, following the instant of initial RPV failure and melt release. Of further benefit in this regard is the appreciation that the initial release would be metallic and of rather limited quantity.

3.5 Add Further comments on mechanical loads (Addendum of May 7, 2007)

This is written in response to Dr. Henry’s suggestion for a more detailed consideration of the physics involved (along a ROAM framework) in mechanically loading the BiMAC due to detachment of lower head penetrating structures. While initially this was our intent too, further considerations of the coolability limits of BiMAC, such as those provided by Drs. H. Fauske and M. Fisher during the review process, suggest margins to failure that may allow a much lower angle of inclination of the BiMAC pipes. This, in addition to other considerations on thermal aspects, suggest that the final detailed design could be made to incorporate such large amounts of sacrificial material as to make the issue of mechanical impacts mute. Thus we would rather wait for the BiMAC coolability results before we finalize design in a manner consistent, and to the extent possible optimal in every respect including mechanical loads of the type raised in this review.

3.2Add ESBWR Design (Addendum of May 7, 2007)

This is in response to Prof. Griffith's request for further clarification of the BiMAC design concept. In addition to Figure A.1 in Chapter A, Figure 3.2.1aa shows the placement of the BiMAC inside the containment. A scaled 3D rendering of the BiMAC basic pipe structure is shown in Figure 3.2.1ca (1/4 symmetry). As noted throughout details such as angle of inclination, sacrificial material choice, and BiMAC cover (LDW floor), will be optimized on the basis of the BiMAC coolability experiments (currently in progress).

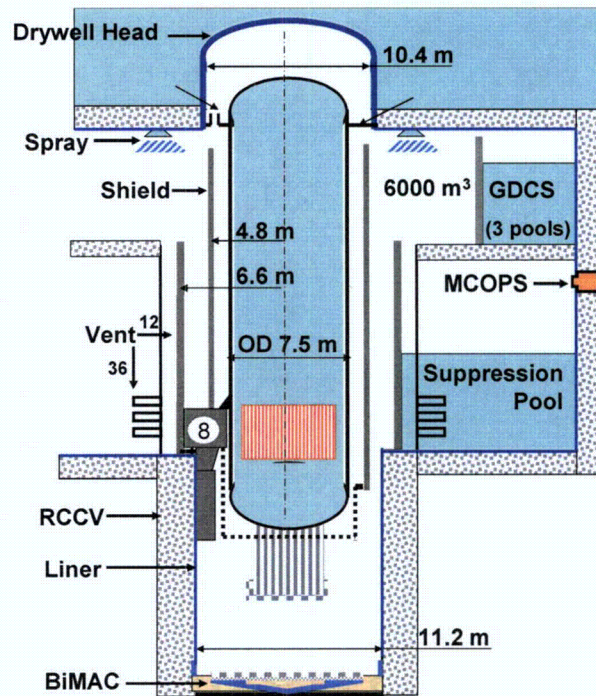


Figure 3.2.1aa. Same as Figure 3.2.1a, but in a different perspective.

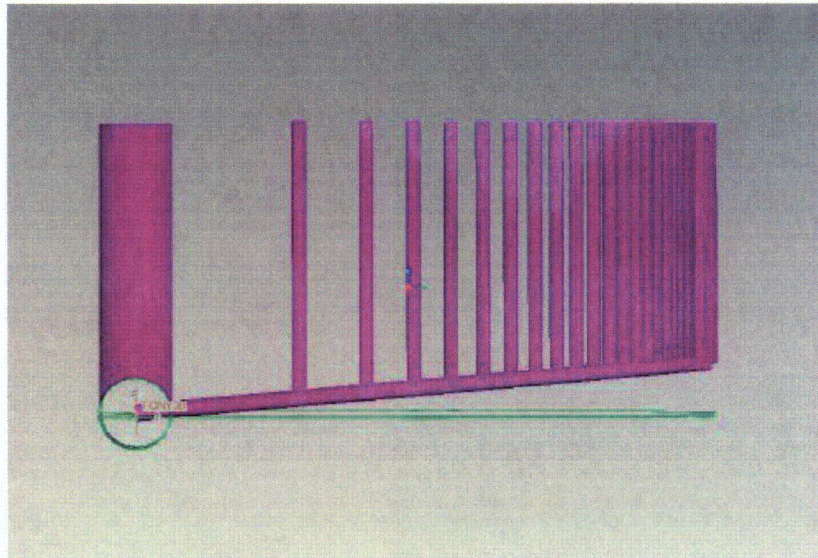


Figure 3.2.1ca. A scaled 3D rendering of Figure 3.2.1c, in $\frac{1}{4}$ symmetry. Perspective views of the BiMAC as rendered in the experimental facility design concept. Top: an oblique/down view. Bottom: a diametric/horizontal view. The facility represents an one-quarter equivalent at $\frac{1}{2}$ -linear scale.

THE END OF CHAPTER 3

4. Conclusions Summarized in the Form of CPETs.

The results of the previous three chapters are summarized in Figures 4.1 and 4.2. These are the final results taken up by the Level 2 PRA towards (a) assessing containment performance in terms of containment decay heat removal systems availability in the long term (the “Transfer to CSET” outcomes), and (b) defining release categories for use in Level 3 PRA (the “CF EVE” outcome”). As indicated, all other outcomes are Physically Unreasonable (PU) and not worthy of further pursuit in the main PRA frame. A few further words about these two kinds of outcomes may be in order.

In ROAAM we acknowledge that when the basis of evaluation is epistemic, probabilities are subjective, and quantification of such probabilities cannot be done, in substance, any other way but in terms of definitions that themselves are of subjective/epistemic character. Thus a numerical probability scale is used only for the purpose of propagating uncertainty, and we insist that the end results be only interpreted in terms of the same probability scale (see Table 4.1) applied in reverse. This kind of procedure was used in all previous applications of ROAAM (as enumerated in Chapter B), and such a qualitative interpretation of the end results was found to be appropriate and sufficient.

In the present case the situation is simpler and the results are even more robust in two ways: (a) for all potential containment threats, strongly bounding arguments could be made at a level of generality, and margins that obviated the need for propagation of uncertainty, and (b) according to the ROAAM “quality of evaluation” criteria (see Table 4.2), all assessments could be made in a manner that is independent of scenario details, thus yielding the most desirable, highest-confidence level, Grade A.

The CF EVE outcome (containment failure by ex-vessel steam explosion) is assumed in light of the large uncertainties that would have to be addressed if a claim was to be made to otherwise. While we feel that in the frame of ROAAM this could not be effectively accomplished, it may be worth pointing out that other levels of treatment have been proposed and accepted by the US NRC (ie the ABWR SSAR) argued that such a failure was not risk-significant. This line of argumentation and related parametric/sensitivity studies can be found in Chapter 9 of NEDO-33201. As indicated this outcome pertains to a deeply-flooded LDW and reflects less than 1% of the CDF. It is important to recall that this low incidence rate of such scenarios was engineered as part of the ESBWR SAM precisely for this reason.

Failure of deluge supply to BiMAC is taken as physically unreasonable on the basis of the specified very reliability of the active system, which is further backed up by a diverse and passive system.

Table 4.1. Definition of ROAAM Probability Levels (Theofanous, 1996)

Process Likelihood	Process Characteristic
1/10	Behavior is within known trends but obtainable only at the edge-of-spectrum parameters
1/100	Behavior cannot be positively excluded, but it is outside the spectrum of reason
1/1000	Behavior is physically unreasonable and violates well-known reality. Its occurrence can be argued against positively

Table 4.2. Definition of ROAAM Quality Grades (Theofanous, 1996)

Grade A	Framework characterized by a simple, limiting process, evaluated on basic physical laws, with appropriately bounding inputs. No scenario dependence.
Grade B	Framework involves a single complex process evaluated at a high confidence level. There may be slight scenario dependence compensated by appropriate quantification of intangibles.
Grade C	Framework involves sequence of processes. Significant scenario dependence compensated by appropriate choice of intangibles and splinter scenarios.

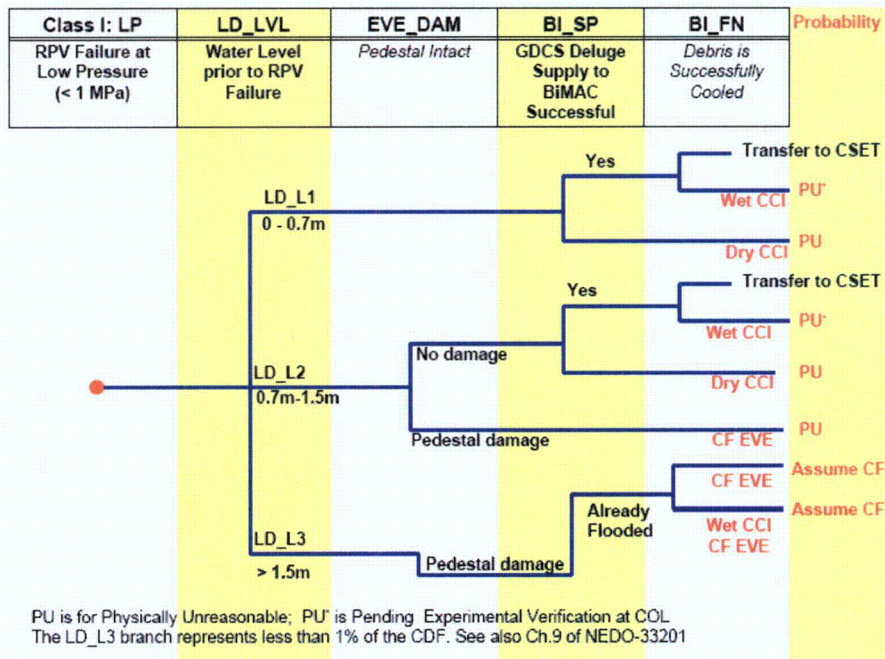


Figure 4.1. Class I accident CPET quantified in the manner described in the text.

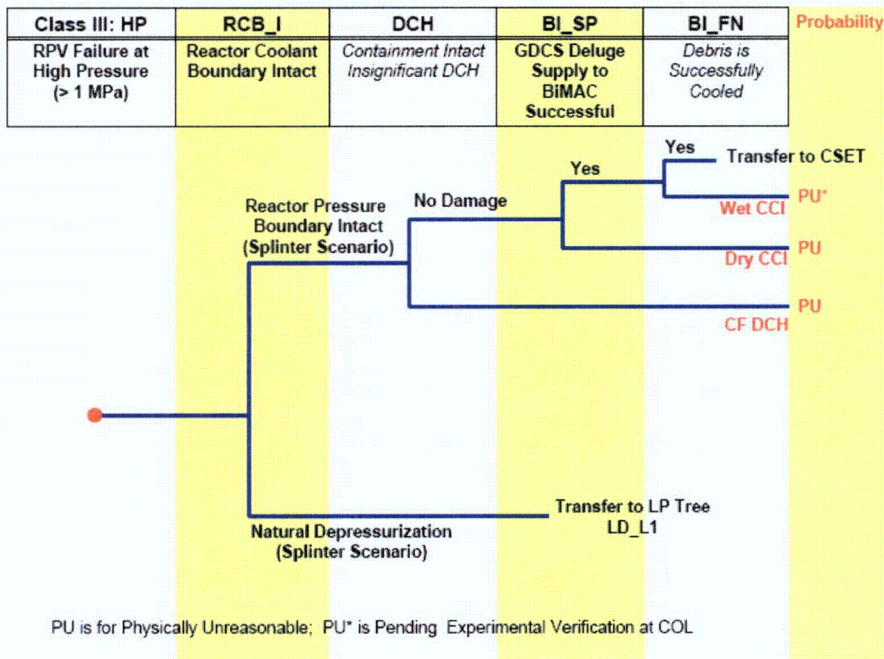


Figure 4.2 Class III accident CPET quantified in the manner described in the text.

**Table 4.3 Summary of Containment Threats and Mitigative Mechanisms
or Systems in Place for Responding to Them**

<i>Threat</i>	<i>Failure Mode</i>	<i>Mitigation</i>
DCH	<i>Energetic DW Failure</i>	<i>Pressure Suppression Vents Reinforced Concrete Support</i>
	<i>UDW Liner Thermal Failure</i>	<i>Liner Anchoring System</i>
	<i>LDW Liner Thermal Failure</i>	<i>Reinforced Concrete Barrier Gap Separation from UDW</i>
EVE	<i>Pedestal/Liner Failure</i>	<i>Dimensions and Reinforcement</i>
	<i>BiMAC Failure</i>	<i>Pipe Size and Thickness Pipes Embedded into Concrete</i>
BMP & CCI	<i>BiMAC Activation Failure</i>	<i>Sensing & Actuation Instrumentation Diverse/Passive Valve Action</i>
	<i>Local Burnout</i>	<i>Natural Circulation</i>
	<i>Water Depletion</i>	<i>Natural Circulation</i>
	<i>Local Melt-Through</i>	<i>Refractory Protective Layer</i>

References to Chapter 4

Theofanous, T.G. (1996), "On the Proper Formulation of Safety Goals and Assessment of Safety Margins for Rare and High-Consequence Hazards," *Reliability Engineering & Systems Safety*, 54 (1996) 243–257

Theofanous, T.G. (2003), "Risk Assessment and Management," Ch.19 in Vol.1 in "Comprehensive Structural Integrity", 10-Volume Handbook, Eds. I. Milne, R.O. Ritchie, B. Karahaloo, Elsevier.

Appendix A

Verification of the Transient CLCH Model

In this appendix, the transient CLCH model is verified with a sample of three experiments from the Integral Effects Tests (IET) series. This adds to the previous extensive validation of the original CLCH model that captured only the final state. The tests were scaled to typical PWR conditions, including the preservation (linearly scaled) of the key geometric features (see Figures A.1 and A.2), especially with respect to the cavity and the so-called intermediate compartment. The IET tests were conducted in counterparts at two scales: at 1/10-scale in the SURTSEY facility at Sandia National Laboratories (SNL) (Allen et al., 1994), and at 1/40-scale in the COREXIT facility at Argonne National Laboratory (ANL) (Binder et al., 1994). Two ANL tests (IET-1RR and IET-8) and one SNL test (IET-1) were selected for interpretation here—they were conducted in inert atmospheres as is appropriate to the present application.

The CLCH model reflects thermal/chemical equilibrium in the melt dispersal (flow) process, and separation of the melt out of this 'equilibrium stream' in the intermediate compartment. The "analysis domain" consists of two major compartments: the "vessel" which represents the containment in the plant geometry, and the "sub-compartment" which represents the intermediate volume (see a schematic representation in Figure A.3). By solving a system of mass and energy balance equations for these compartments, we can obtain the dynamics of pressurization in the "vessel". This extension of the model to capture the transient is straightforward, and the complete formulation can be found in Table 1.4.3.1 of Section 1.4.3 in the main body of the report.

The model implementation to these particular tests considered here was done in terms of the definition of conditions given in Table A.1. The parameters utilized are summarized in Table A.2. The melt entrainment time was obtained from the CLCH model correlation, and the oxidation efficiency too is from this previous work with CLCH. The ejection time quoted in Table A.2 is from the experimental data and reflects the transition period from melt ejection to pure steam blowdown. While unimportant in the previous applications of CLCH, it is important here in our interest to capture the complete transient. As seen in Figure A.4, the pure blowdown portion is predictable by a straightforward isentropic expansion. The blowdown rate used for the transition period was approximated in the manner as shown in the figure.

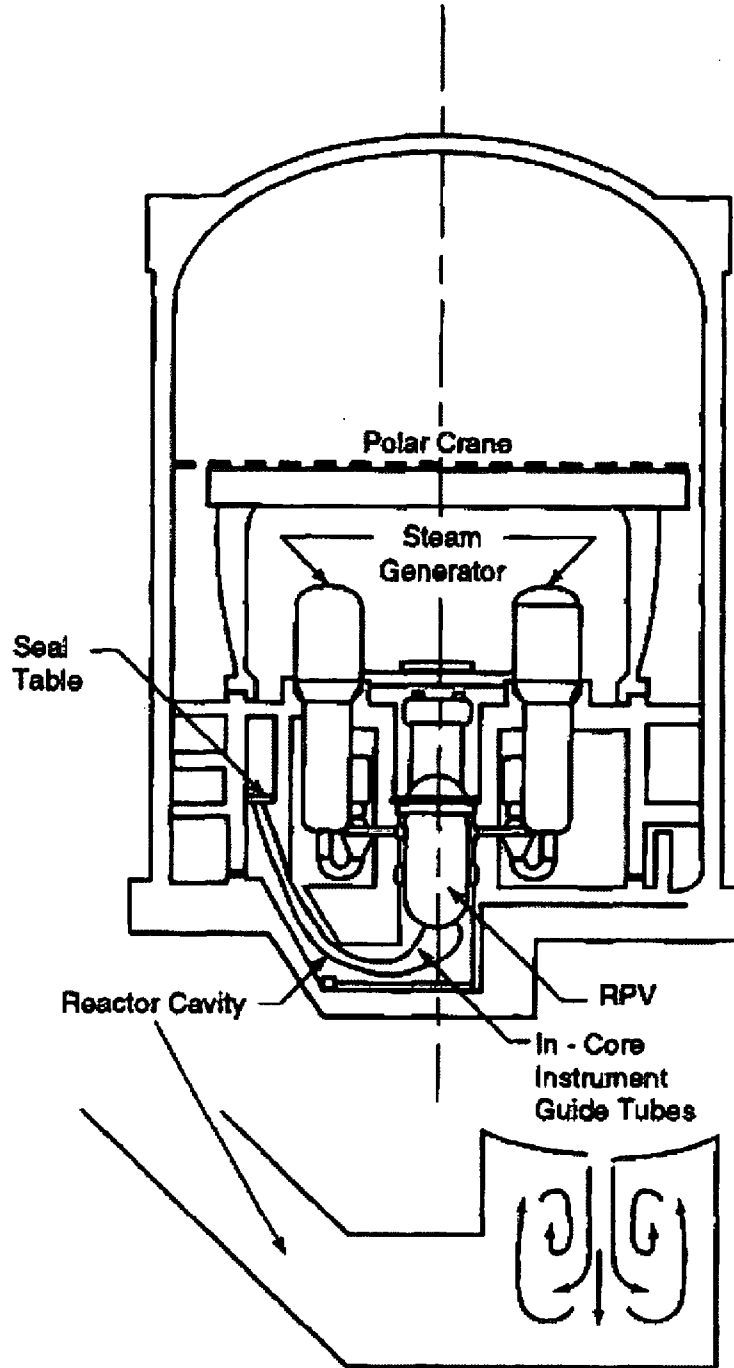


Figure A.1. The containment geometry considered in the IET tests and an illustration of the recirculation flow pattern in the cavity (adapted from Yan and Theofanous (1996)).

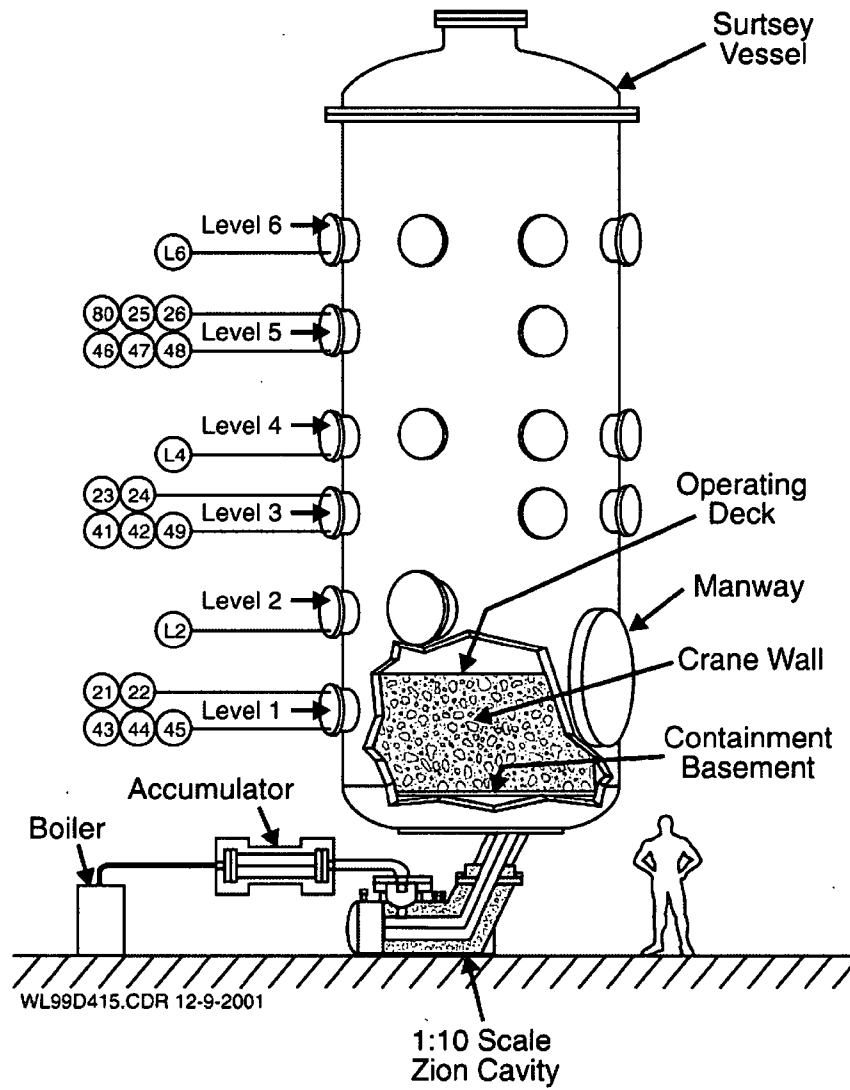


Figure A.2. The Surtsey Vessel, High-Pressure Melt Ejection System, and Sub-Compartment Structures Used in the IET Experiments (Allen, et al., 1994).

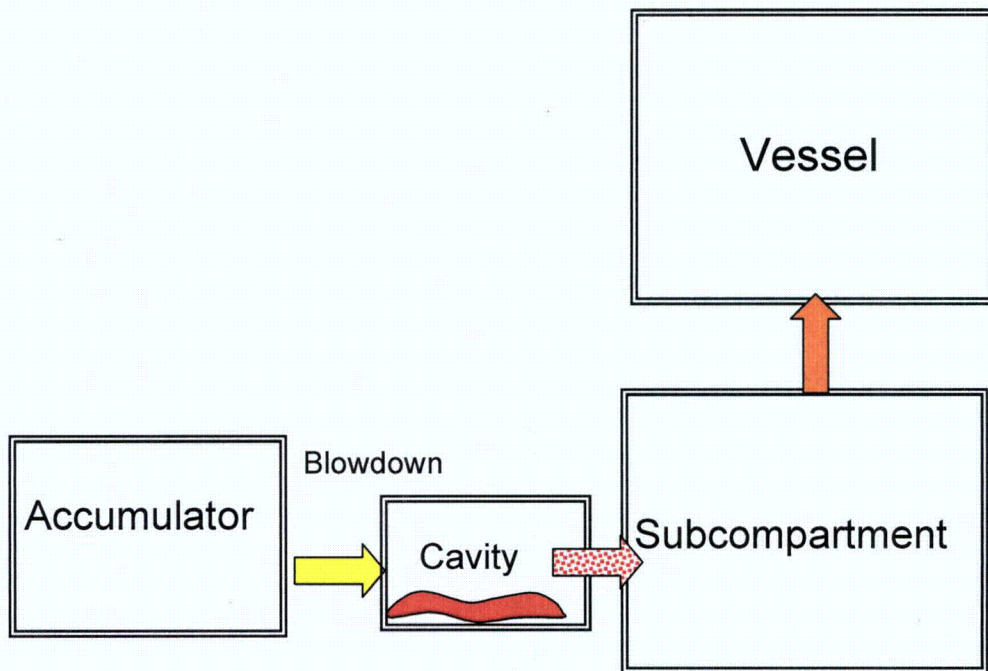


Figure A.3 Schematic of control volumes used in the implementation of the transient CLCH model to the interpretation of the IET tests.

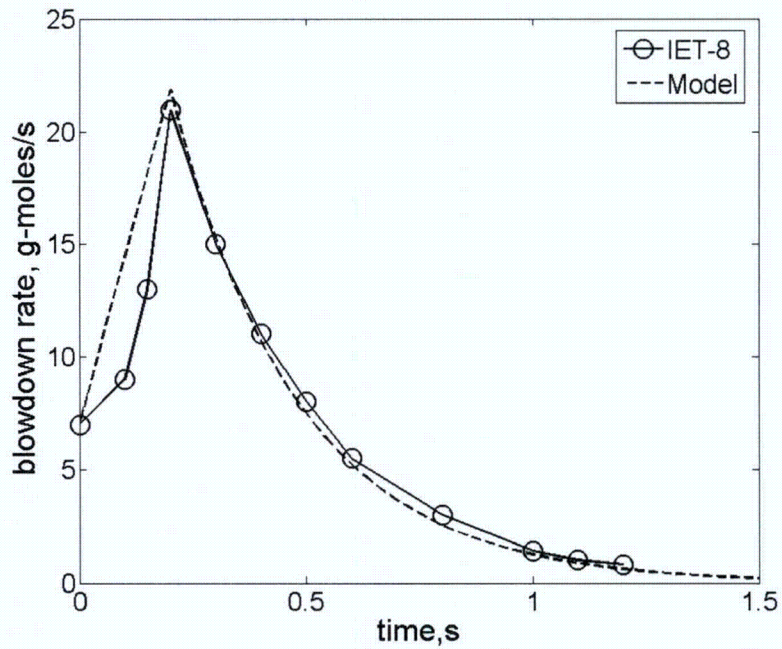


Figure A.4. The blowdown rates measured in IET-8 and the approximate representation of the transition period utilized in the interpretation. The same was used for IET-1RR

Table A.1. Parameters that Define the IET Tests Considered Here.

Parameters	Definitions	ANL IET-1RR	ANL IET-8	SNL IET-1
V_{RCS} (m ³)	Volume of accumulator (simulating RCS)	0.0061	0.0061	0.345
$V_{subcomp}$ (m ³)	Freeboard volume inside subcompartment structures	0.072	0.072	4.64
V_{dome} (m ³)	Volume of the dome (simulating the containment)	1.51	1.51	85.15
D_{hole} (cm)	Hole diameter	0.89	1.1	3.5
Initial containment gas conditions	% N ₂	99.90	37.4	99.90
	% O ₂	0.03	7.7	0.03
	% H ₂	0.00	3.9	0.00
	% H ₂ O	0.00	50.0	0.00
	% CO ₂	0.01	0.0	0.01
	Other	0.06	0.0	0.06
m_{corium} (kg)	Mass	0.71	0.71	43
T_{melt} (K)	Melt temperature	2550	2550	2550
Melt composition	% Fe	52	52	52
	% Cr	11	11	11
	% Al	3	3	3
	% Al ₂ O ₃	34	34	34
P_{RCS}^0 (MPa)	Initial pressure of accumulator	6.7	6.5	7.1
T_{RCS}^0 (K)	Initial temperature of accumulator	600	600	600

**Table A.2. Values of the Transient CLCH Model Parameters
Used in the Interpretation.**

Parameters	Definitions	ANL IET-1RR	ANL IET-8	SNL IET-1
$\tau_{ejection}$ (s)	Ejection time during which steam and melt are ejected together	0.2	0.2	0.4
τ_m (s)	Entrainment time	0.24	0.24	0.74
Φ	Oxidation efficiency	0.5	0.5	0.5

Results for the ANL IET-8 and IET-1RR Tests

The results are summarized in comparison to the experimental data in Figures A.5. We can see that both the pressurization rate and peak pressure reached are matched very well. The falloff of pressure at later times is due to heat losses which are not represented in the model. There are 5.0 g of hydrogen predicted to have been produced in comparison to the 4.8 g found in the experiment.

A parametric of the effect of the melt entrainment time on pressure, for a range around the predicted value of 0.24 s is shown in Figure A.5b. The effect on temperature is given in Figure A.5c. Consistently with the CLCH results presented originally, DCH loads increase as the DCH-scale (i.e. the melt entrainment time) increases—more of the stored steam is found in contact with the melt. Interestingly, in an open system such as the one of interest here, such an increase in DCH-scale would result in slower rates of pressurization, and thus lower peak pressures. The effect of the oxidation parameter (Φ) is examined in Figure A.5d. As expected the effect on pressure is minimal (one mole of steam produces one mole of hydrogen), and the small change seen is due to the different amounts of oxidation energy involved in each case.

The comparison to IET-1RR, as illustrated in Figure A.6 is very similar.

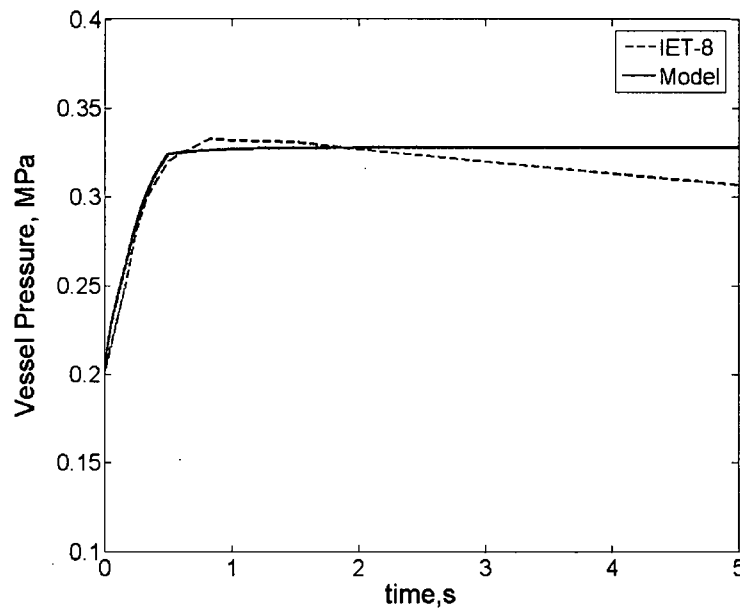


Figure A.5a. Prediction and measurement of the pressure transient in test IET-8.

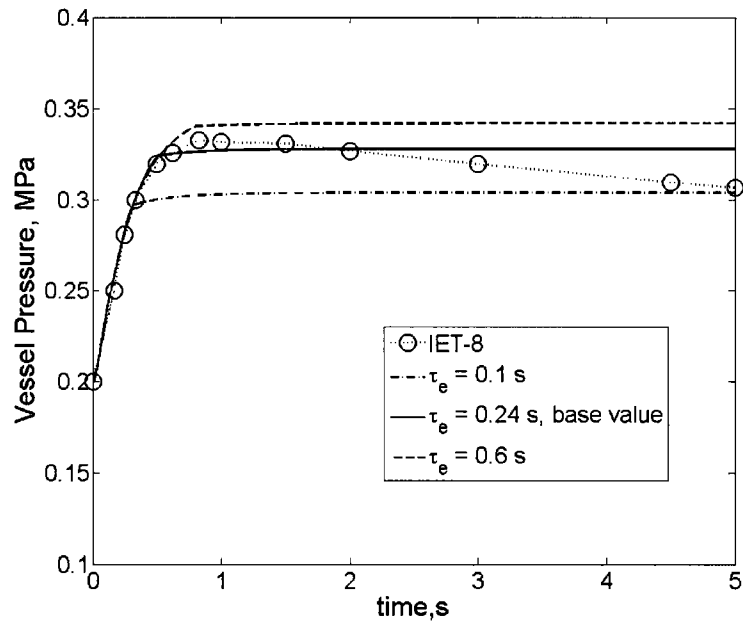


Figure A.5b. Sensitivity of predicted pressure transient on melt entrainment time.

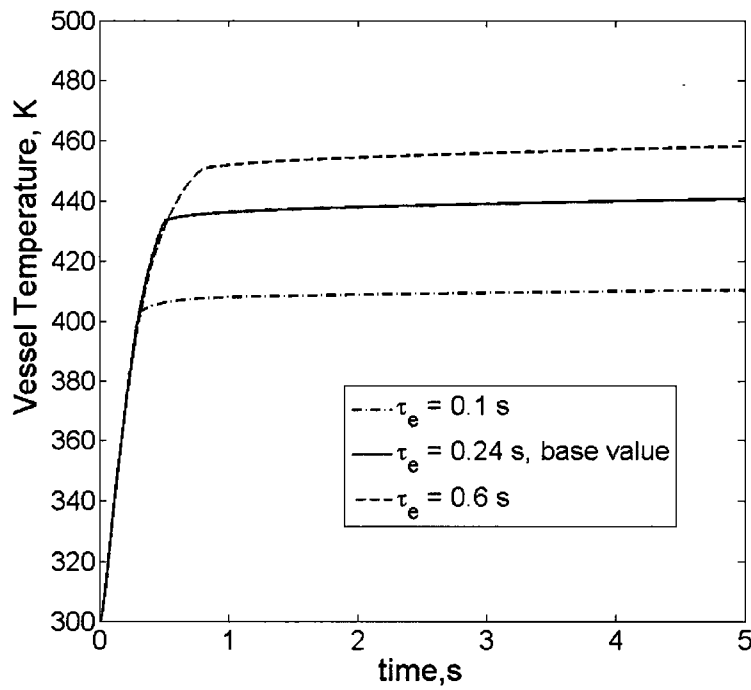


Figure A.5c Sensitivity of the temperature transient on melt the entrainment time.

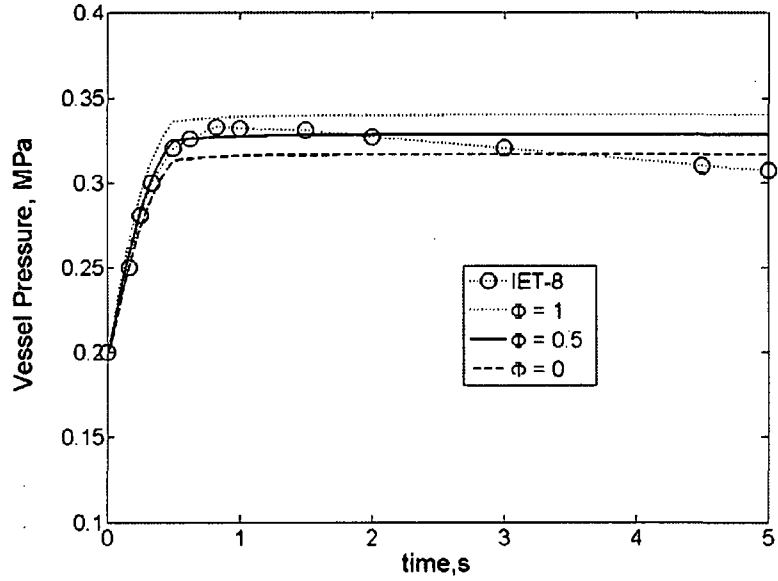


Figure A.5d. Sensitivity of pressure transient on the oxidation efficiency.

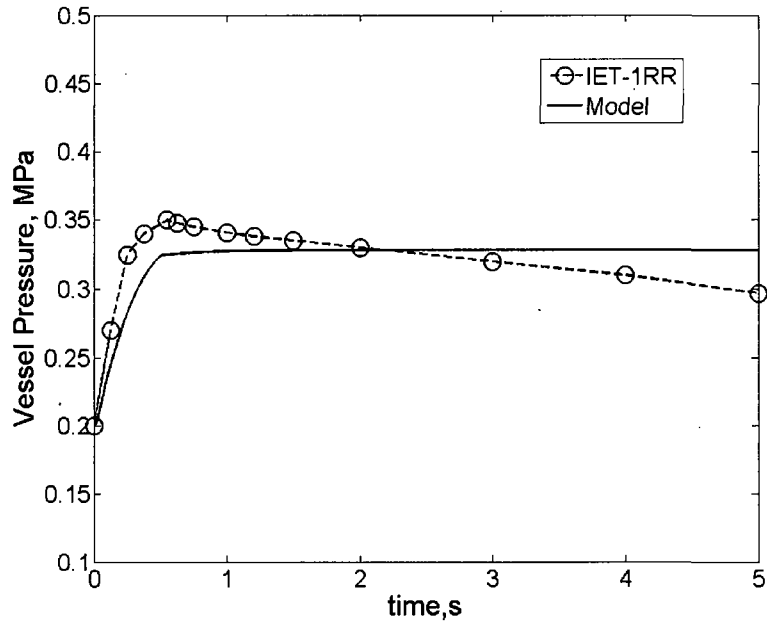


Figure A.6. Predicted and measured pressure transients in test IET-1RR.

Results for the SNL Test IET-1

Measured and predicted pressure transients are shown in Figure A.7a. Note that due to the much smaller surface to volume ratio in this test, the rate of pressure loss (cooldown) is much less in comparison to the ANL tests, and the long-term agreement is better. A total of 174 g of hydrogen produced in the calculation compare to 233 g found in the experiment.

The temperature transients are compared in Figure A.7b. As shown by the data, temperatures depend on position in the short term. We note that around the time of 2 s, the level 1 and 3 data are quite close to the subcompartment temperatures calculated in the model, and that by 3 s all calculated and measured temperatures (with the exception of that at the highest point, elevation 5 converge to a close-together range. The later decay in the data is due to losses which were not represented in the calculation.

A parametric on the melt entrainment time for a range around the predicted value of 0.74 s is shown in Figure A.7c. Again the larger the DCH-scale the higher the calculated loads, but note that this comes about through the turning over to an asymptote at different times, rather than through effecting the rate of pressure rise in the initial period.

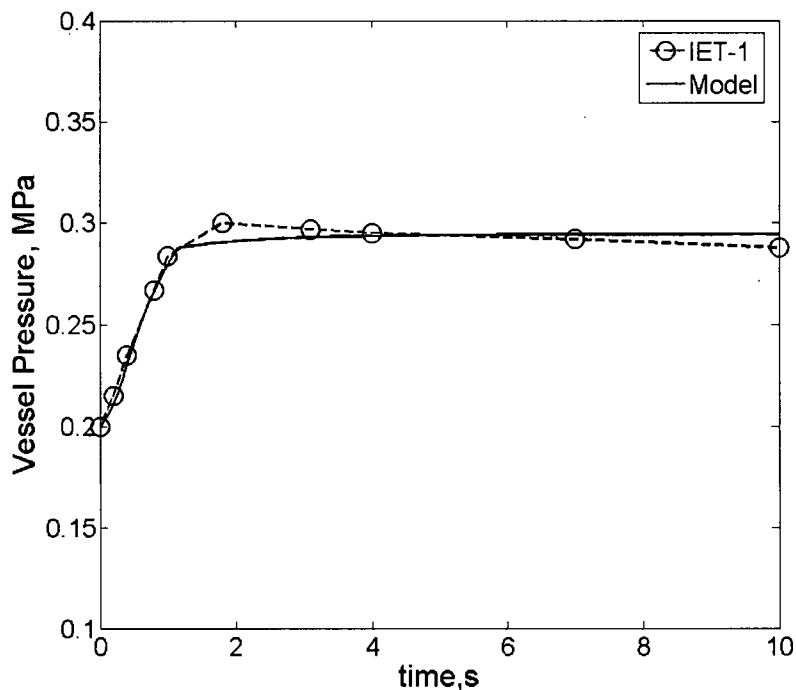


Figure A.7a. Measured and predicted pressure transients in test IET-1.

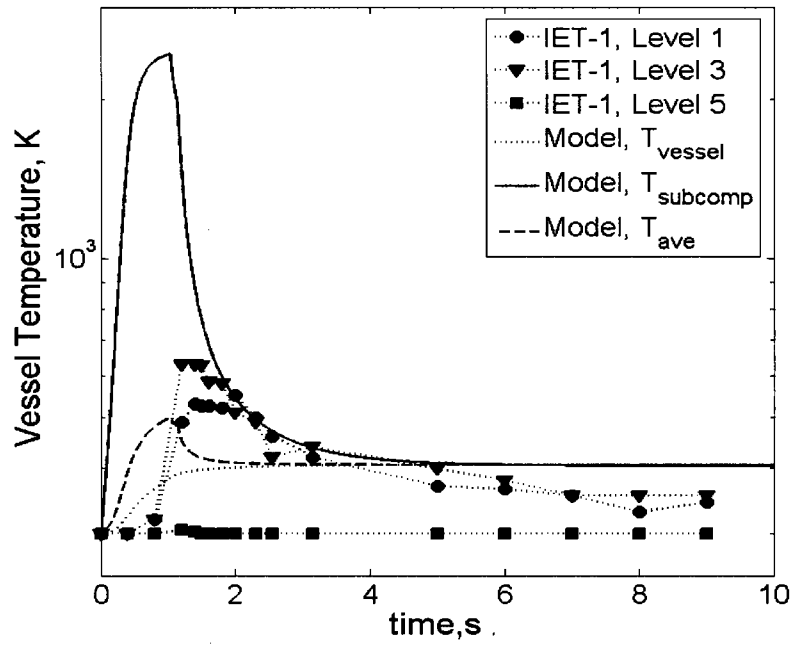


Figure A.7b. Predicted and measured temperatures transients in IET-1 test. The positions to which the various levels refer to are shown in Figure A.2.

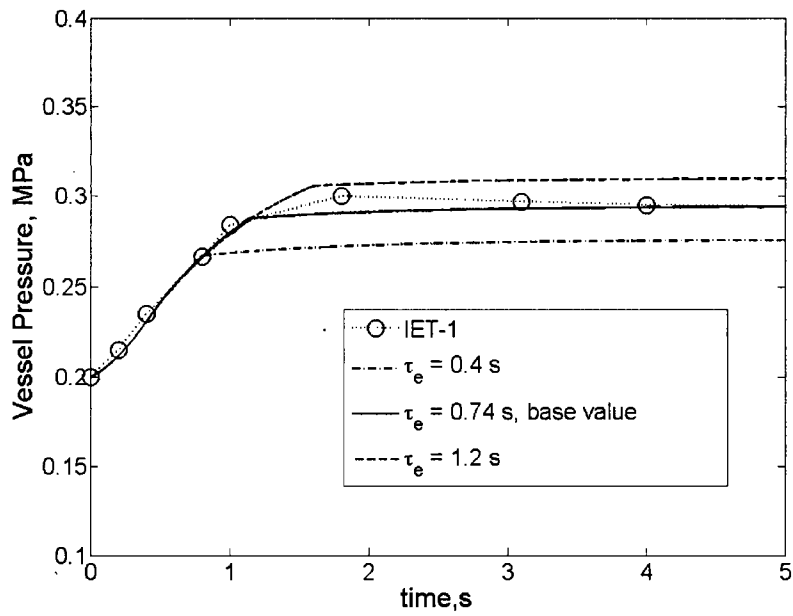


Figure A.7c. Sensitivity of pressure transient on the melt entrainment time.

References to Appendix A

Allen, M. D., Pilch, M. M., Blanchat, T. K., Griffith, R. O., and Nichols, R. T. (1994), "Experiments to Investigate Direct Containment Heating Phenomena with Scaled Models of the Zion Nuclear Power Plant in the SURTSEY Test Facility," *NUREG/CR-6044, SAND93-1049*, Sandia National Laboratory, May 1994. Also, The Integral Effects Test (IET-1) in the Surtsey Test Facility. 1991 Water Reactor Safety meeting; 28-30 Oct 1991; Washington, DC (SAND-91-2613C).

Binder, J. L., McUmbler, L. M., and Spencer, B. W. (1994), "Direct Containment Heating Integral Effects Tests at 1/40 Scale in Zion Nuclear Power Plant Geometry," *NUREG/CR-6168, ANL-94/18*, Argonne National Laboratory, September 1994.

Pilch, M.M. Yan, H. and Theofanous, T.G. (1994), "The Probability of Containment Failure by Direct Containment Heating in Zion," *NUREG/CR-6075, SAND93-1535*, December 1994. M.M. Pilch, H. Yan and T.G. Theofanous, "The Probability of Containment Failure by Direct Containment Heating in Zion," *Nuclear Engineering & Design*, 164 (1996) 1–36.

Yan, H. and Theofanous, T.G. (1993), "The Prediction of Direct Containment Heating," *ANS Proceedings 1993 National Heat Transfer Conference*, Atlanta, GA, Aug. 8-11, 1993, 294-309. Also H. Yan and T.G. Theofanous, "The Prediction of Direct Containment Heating," *Nuclear Engineering & Design*, 164 (1996) 95–116.

Appendix B

Validation of the Vent-Clearing Model for CLCH

B.1. Introduction

In this Appendix we use data from the (Full-Scale) Pressure Suppression Test Facility (PSTF) tests (GE, 1974) to validate our model for vent clearing. A sensitive measure of this is the peak pressure obtained in the drywell during such an event. The PSTF tests were carried out in support of the Mark III pressure suppression containment concept using the horizontal vent system design as is the case for the ESBWR. More recently, PSTF tests were used for qualification of the TRACG code (GE, 1996) developed and used by GE for safety analyses of the GE ABWR, SBWR, and ESBWR designs under LOCA conditions (GE, 2003).

The facility consists of three major components as illustrated in Figure B.1.1. These components are (1) an electrically heated pressure vessel to represent the RPV, (2) another pressure vessel to represent the drywell volume, and (3) a suppression pool and wetwell volume. Steam blowdown was initiated by means of a rupture disc.

The horizontal vent system configuration of the ESBWR design is similar to the vent system configuration tested in the PSTF Test Series 5703. In both the PSTF and the ESBWR, the three horizontal vents are 0.70m in diameter, and they have a vertical spacing (center to center) of 1.37m (GE, 1974; GE, 2003). Also in both the PSTF and the ESBWR the total flow area of the horizontal vents is equal to the flow area of the vertical vent that leads to them. Other key geometric parameters in the experiments are summarized in Table B.1.1. Two different break sizes were used: 63.5 mm and 92.0 mm. Top-vent submergence values were varied between 2.06 m and 3.37 m. The drywell was preheated to 93°C to minimize condensation effects. The main results are (i) vent clearing times and (ii) transient pressures in the drywell.

B.2. Model Formulation

Figure B.2.1 illustrates the vent system in the PSTF (and the ESBWR). The system consists of a vertical pipe and three horizontal pipes. Increasing of drywell pressure due to blowdown leads to depression of the water level in the vertical vent pipe, and, subsequently to vent clearing, to flow of gases and steam to the suppression pool. The blowdown rate as measured in the tests is given in Figure B.2.2.

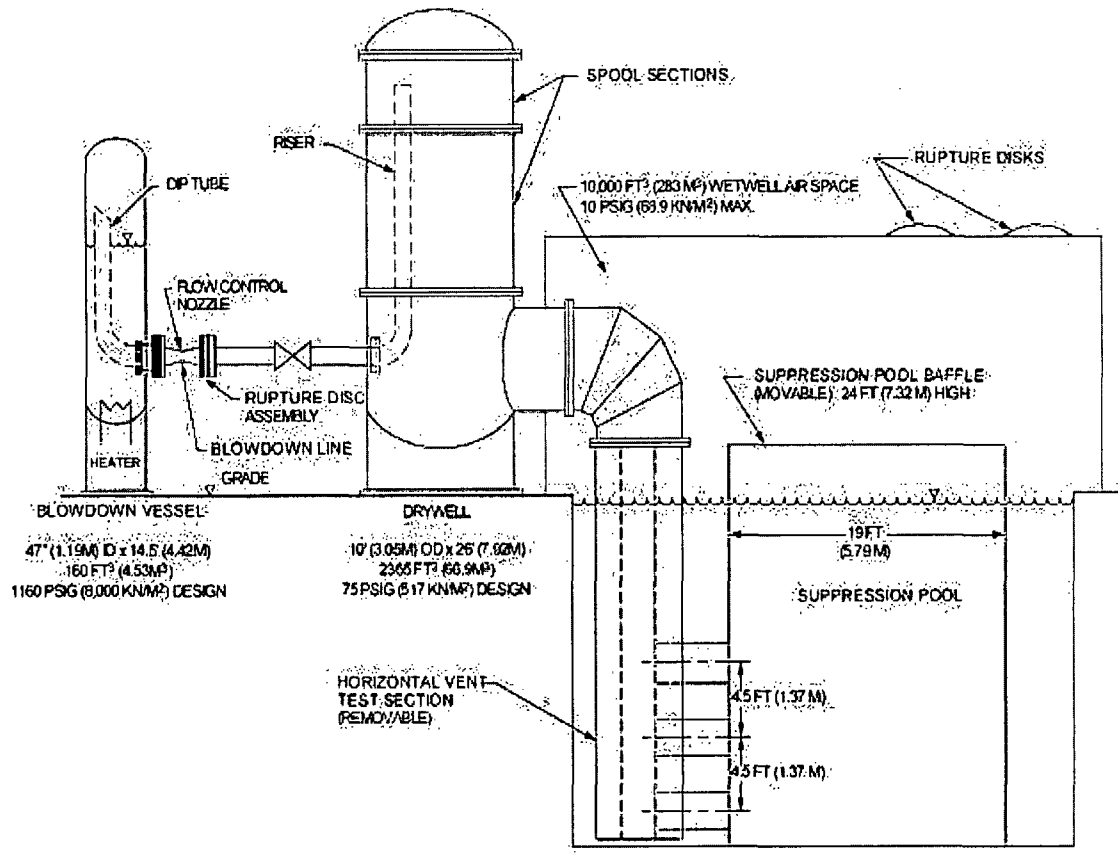


Figure B.1.1. Schematic of the PSTF (GE, 1974; GE, 2003).

Table B.1.1 Geometric Definition of the PSTF test series 5703.

Notation	Definitions	5703-1	5703-2	5703-3
	Number of horizontal vents	3	3	3
D_{hole} (mm)	Flow restrictor diameter	63.5	63.5	92.0
H_{top} (m)	Top vent submergence	2.06	3.33	3.37
D_{vent} (cm)	Horizontal vent diameter	0.7	0.7	0.7
	Vertical axial spacing (m)			
	• Top and Middle Vent	1.37	1.37	1.37
	• Middle and Bottom Vent	1.37	1.37	1.37
A_H (m ²)	Total area of horizontal vent	1.155	1.155	1.155
A_V (m ²)	Total area of vertical vent	1.131	1.131	1.131

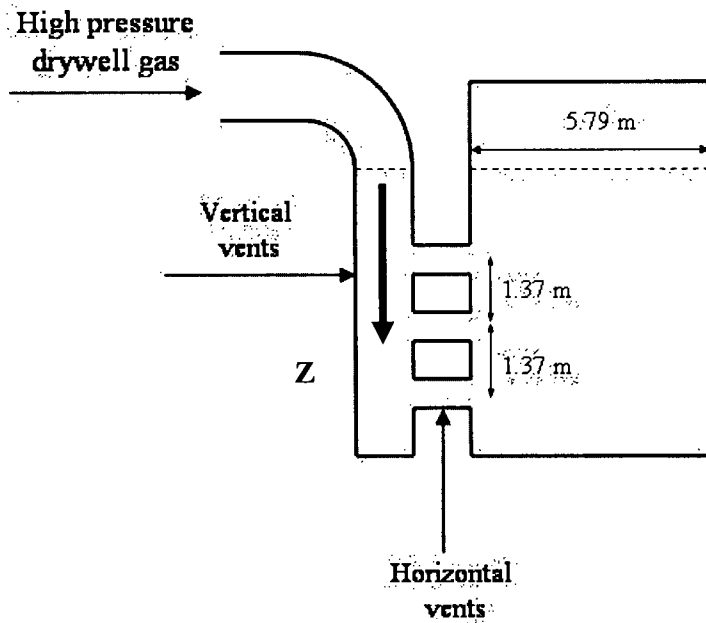


Figure B.2.1. The vent configuration in PSTF. The Z coordinate origin is at the initial water level position and directed downwards.

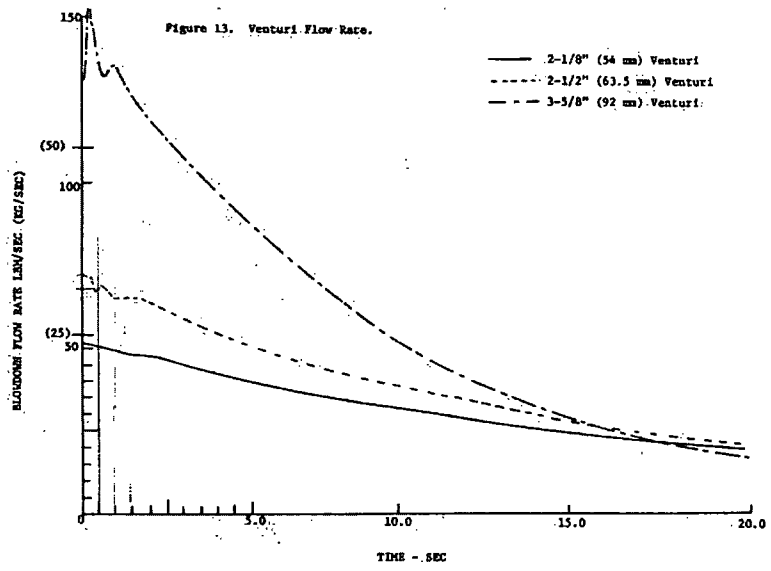


Figure B.2.2 Blowdown flow rates measured in three PSTF experiments (GE, 2003).

The mechanical energy balance, written for a control volume that encloses all the liquid in both the vertical and horizontal vents is:

$$\frac{d}{dt} \left\{ \frac{1}{2} m_v u_v^2 + \frac{n}{2} m_h u_h^2 + \frac{n}{2} m_a u_h^2 + \frac{1}{2} m_v g (H - z) \right\} = -\frac{n}{2} (\rho A_h u_h) u_h^2 - \rho g A_v u_v (H - \frac{1}{n} \sum Z_i) + P A_v u_v - \sum (P_0 + \rho g Z_i) A_h u_h - n \rho \frac{C_{d,junc}}{2} u_h^2 A_h u_h \quad (1)$$

where m is mass, u is velocity, A is flow area, subscripts v and h refer to vertical and horizontal vents respectively, P is pressure, ρ is density, g is acceleration of gravity, H is the initial water pool depth, Z_i is the submergence of vent i ($i = 1, 2$ or 3). n is the total number of vents that are not cleared yet. The $C_{d,junc}$ is a loss coefficient due to the 90° flow turn along with the flow area reduction by ~33%, which give a value of ~2. The masses in the vertical (m_v) and horizontal vents (m_h) and that due to the added mass (m_a) can be written in terms of z the distance from the original position of the interface of the water slug, L the length of the horizontal vents, and D_h the diameter of the horizontal vents as:

$$m_v = \rho L (H - z) A_v \quad m_h = \rho L A_h \quad m_a = \rho D_h A_h \quad (2, 3, 4)$$

Then, using the fact that the flow area of the vertical vent is three times the flow area of each of the horizontal vents, and after some simplification we have:

$$\{(H - z) + L + D_h\} \frac{du}{dt} = \frac{P - P_0}{\rho} - gz - 2u^2 \quad \text{and} \quad u = \frac{dz}{dt} \quad (5)$$

The general result, where n is the number of vents yet to be cleared, is

$$\left\{ \frac{A_v}{n A_h} (L + D_h) + (H - z) \right\} \rho \frac{du}{dt} = P - (P_0 + \rho g z) - \frac{1}{2 n^2} \left(\frac{A_v}{A_h} \right)^2 \rho u^2 (1 + C_{d,junc}) \quad (6)$$

When the water level in the vertical vent reaches the elevation of a horizontal vent, the final stage to clearing can be described similarly by,

$$\frac{d}{dt} \left\{ \frac{1}{2} m_h u_h^2 + \frac{1}{2} m_a u_h^2 \right\} = -\frac{1}{2} (\rho A_h u_h) u_h^2 + P A_h u_h - (P_0 + \rho g Z_i) A_h u_h \quad (7)$$

or

$$(L + D_h) \rho \frac{du_h}{dt} = P - (P_0 + \rho g z) - \frac{1}{2} \rho u_h^2 \quad \text{and} \quad u_h = \frac{dx}{dt} \quad (8)$$

where x is the length of the water slug in the horizontal vent.

Clearing of the horizontal vents is initiated if $z = Z_h$. After a horizontal vent is cleared (i.e. $x > L$), the vapor flow through the vent is calculated based on standard equations for mass flow rate of ideal compressible gas through a tube, with an inlet pressure P (the

pressure of the upper drywell) and an outlet pressure $P_0 + \rho g Z_i$ (the hydrostatic pressure at the vent elevation). The loss of kinetic energy due to entrance, exit and friction is accounted by introducing the total loss coefficient K , which is the sum of losses due to flow entrance, turning, and exit, respectively. The actual vent rate G_{vent} is related to the ideal (no-loss) vent rate $G_{vent,ideal}$ by $G_{vent} = G_{vent,ideal}/(K+1)^{0.5}$. The value of K used in these calculations was 3, and no attempt was made to fit the data by varying this or the other parameter in the model ($C_{d,junc}$). The flow was checked for choking by the use of a critical pressure ratio of 2. At times that this condition was met the gas flow rate was set to that of ideal critical flow adjusted for losses by the same K factor.

B.3. Model Validation

As noted above the base values for the model parameters are $C_{d,junc} = 2$ and $K = 3$. Calculations show that variations in the range $1 < C_{d,junc} < 3$, and $1 < K < 6$ do not significantly influence the pressure transient. The results for the three tests considered are shown in Figures B.3.1 to B.3.3. Peak pressures and vent clearing times are summarized in Table B.3.1, along with the data, and the results of a previous benchmark exercise for the TRACG code (GE, 2003).

We can see first that the qualitative behavior of pressure rise and fall is predicted very well. Quantitatively the model slightly underestimates the rate of vent clearing and as a consequence overestimates the peak pressures reached by up to 12%, while the predictions remain consistently conservative for all three cases. Very likely this small error is due to gas breaking through the water slugs prior to complete vent clearing. The pressure oscillations that follow the main pressure event are of no interest here and their physics is not reflected in the formulation of the model.

Table B.3.1 Summary of Various Predictions against the Experimental Data.

Test Series	Description	Data	TRACG	Present
5703-01	a. Short-term peak pressure (kPA)	193	200	205
	b. Vent clearing time (s)			
	- Top vent	0.86	0.85	1.18
	- Middle vent	1.15	1.15	1.48
	- Bottom vent	DNC	DNC	DNC
5703-02	a. Short-term peak pressure (kPA)	200	227.5	230
	b. Vent clearing time (s)			
	- Top vent	1.14	1.05	1.42
	- Middle vent	1.52	1.35	1.68
	- Bottom vent	DNC	DNC	DNC
5703-03	a. Short-term peak pressure (kPA)	252	289.6	293
	b. Vent clearing time (s)			
	- Top vent	0.99	0.85	1.16
	- Middle vent	1.19	1.05	1.35
	- Bottom vent	1.60	1.30	1.93

DNC denotes vent "do not clear".

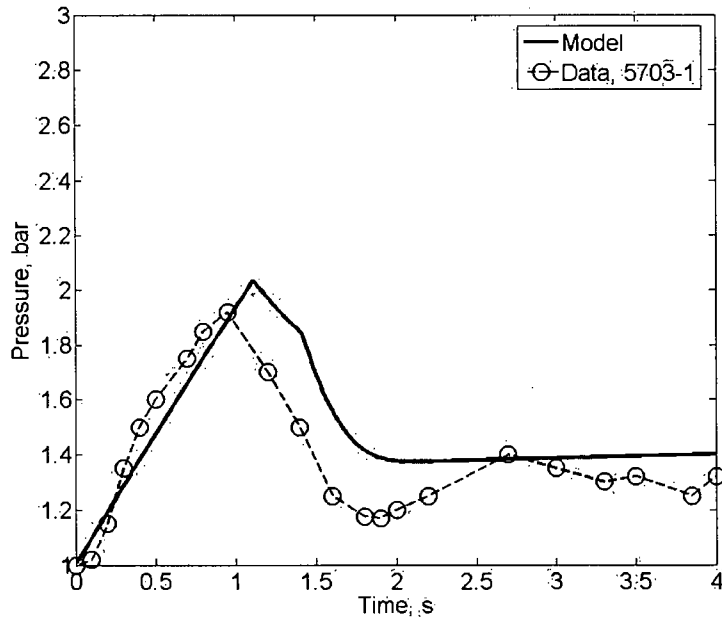


Figure B.3.1a Drywell pressure transient in Test 5703-1.

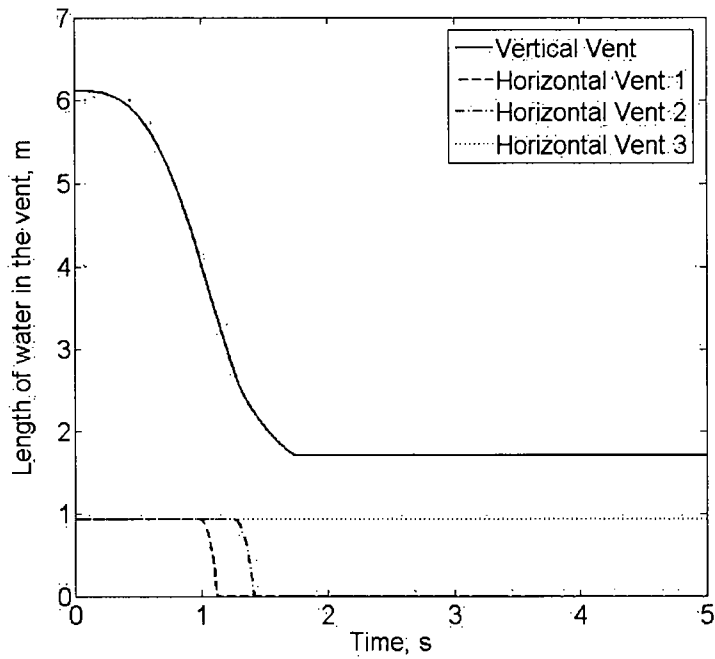


Figure B.3.1b. Predicted dynamics of vent clearing in Test 5730-1. The length is in m.

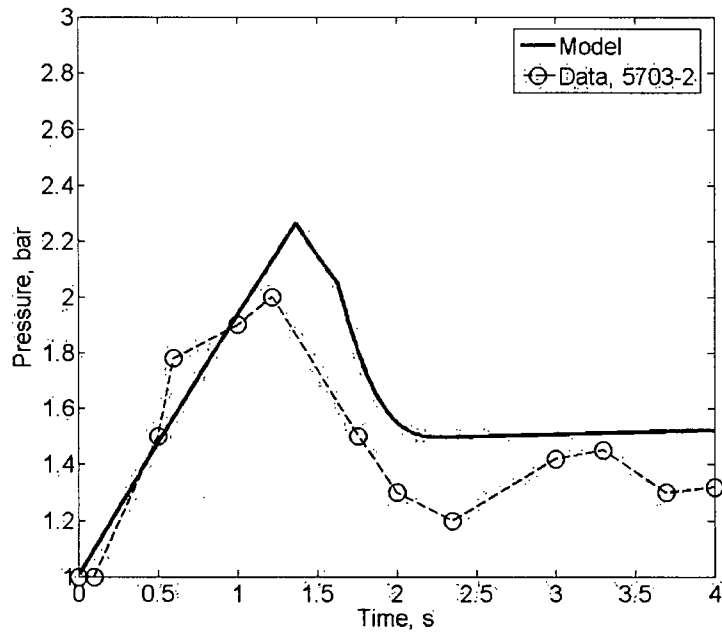


Figure B.3.2a Drywell pressure transient in Test 5703-2

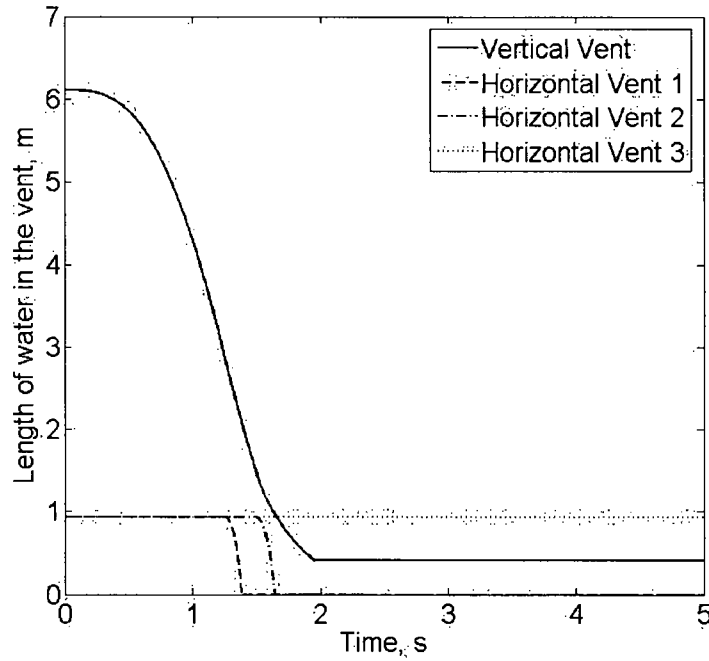


Figure B.3.2b. Predicted dynamics of vent clearing in Test 5730-2. (the length is in meters).

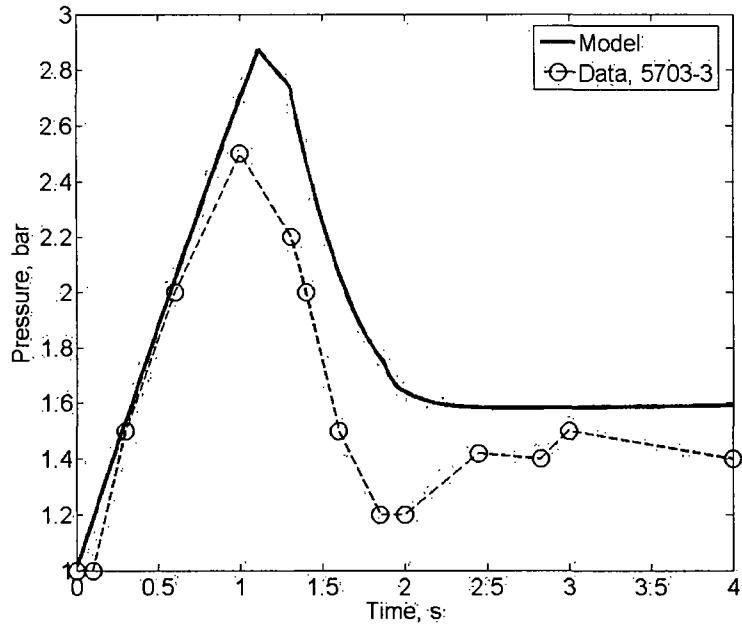


Figure B.3.3a. Drywell pressure transient in Test 5703-3.

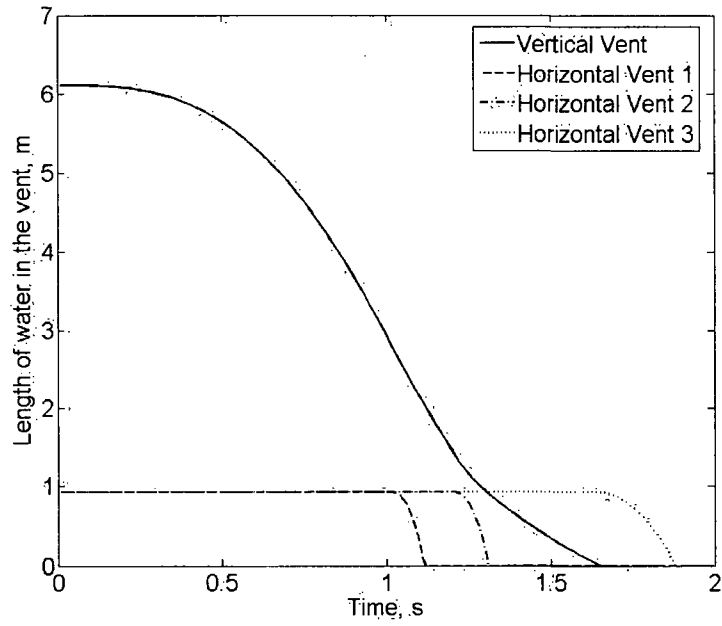


Figure B.3.3b. Predicted dynamics of vent clearing in Test 5730-3. (the length is in meters).

References for Appendix B

Batchelor G.K. (1967). An Introduction to Fluid Dynamics. Cambridge University Press.

GE (1974). Mark III Confirmatory Test Program, Phase I - Large Scale Demonstration Tests, Test Series 5701 through 5703, NEDM-13377, October 1974.

GE (1996). Licensing Topical Report, TRACG Model Description, NEDE-32176P, Revision 1, February 1996.

GE (2003). J.R. Fitch et al., TRACG Qualification for SBWR. Vol.1 and 2. NEDO-32725P Revision 1. (2003).

Appendix C

Validation of the Codes PM-ALPHA.L and ESPROSE-m

As noted in the main body of the report these codes have been extensively verified and reviewed during the ROAAM resolution of in-vessel steam explosion for AP600 (Theofanous, 1999c). There is very little to add here, except perhaps that in the meanwhile we participated in the SERENA OECD-sponsored joint code exercise (SERENA, 2004, 2005). Thus we limit ourselves to a very high level overview, and some indicative results.

An overall perspective of the verification effort is provided in Figures C.1 and C.2. We can see that in both cases we paid attention to separate key aspects, such as the rapid momentum, heat and mass transport, including phase changes, in the plunging of hot particle clouds in water pool (i.e. Figure C.3) for PM-ALPHA, and the wave dynamics in multiphase media (i.e. Figure C.4) for ESPROSE.m. Note that special attention has been paid to the numerical aspects, as they impose rather severe challenges to stability and accuracy of such simulations. Also note the extensive use made of analytical solutions as they constitute absolute standards for testing the numerical results. Finally we note that these reports also contain comparisons (and discussions) with all available integral experimental data steam explosions (both premixing and propagation).

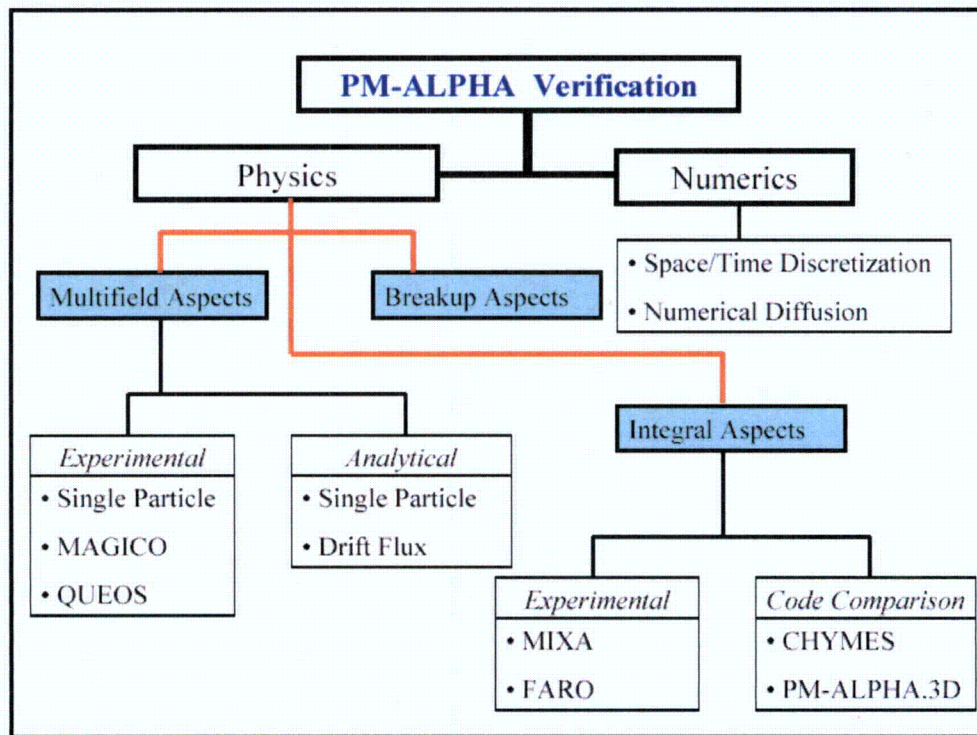


Figure C.1. Overview of the PM-ALPHA verification effort (Theofanous et al., 1999a).

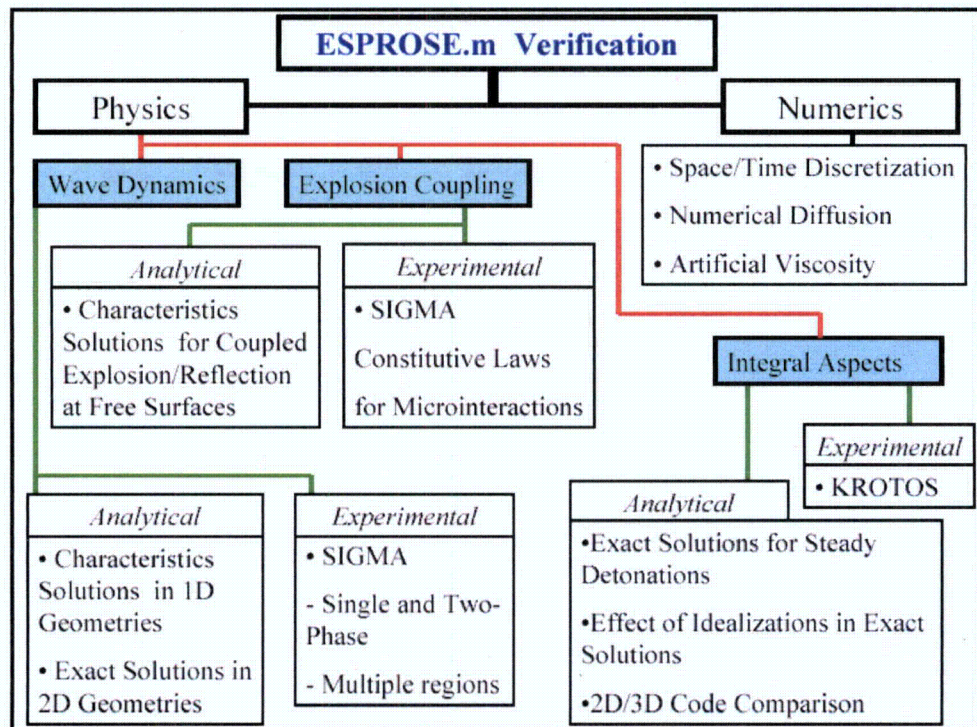


Figure C.2. Overview of the ESPROSE.m verification effort (Theofanous et al., 1999b).

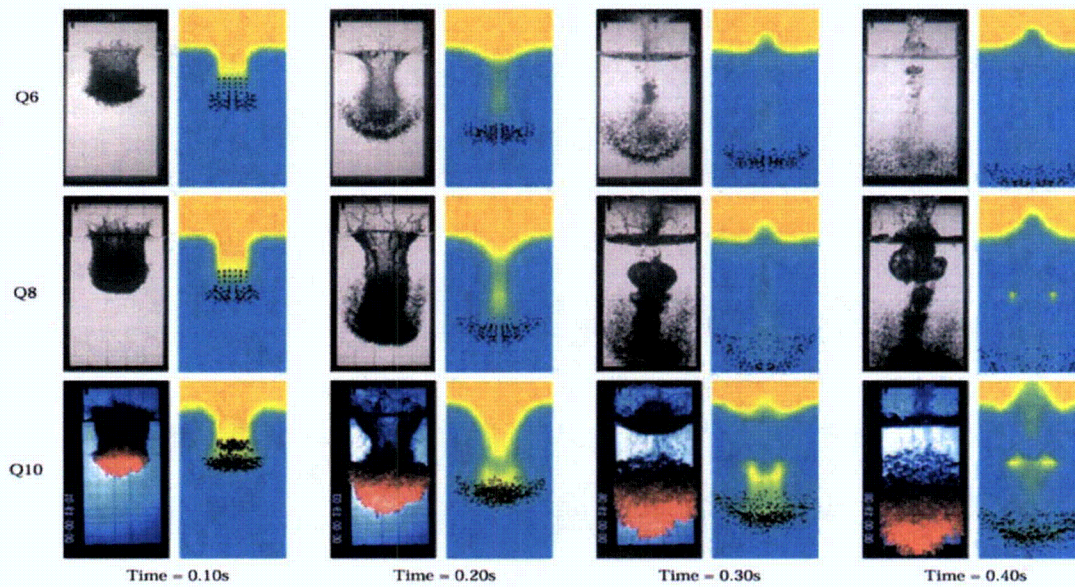


Figure C.3. PM-ALPHA simulation of particle clouds plunging into water pools (QUEOS experiments with different particle temperatures and coolant subcoolings). Note that the experimental images are in projection (external videos), while the simulations are shown in a vertical cross section.

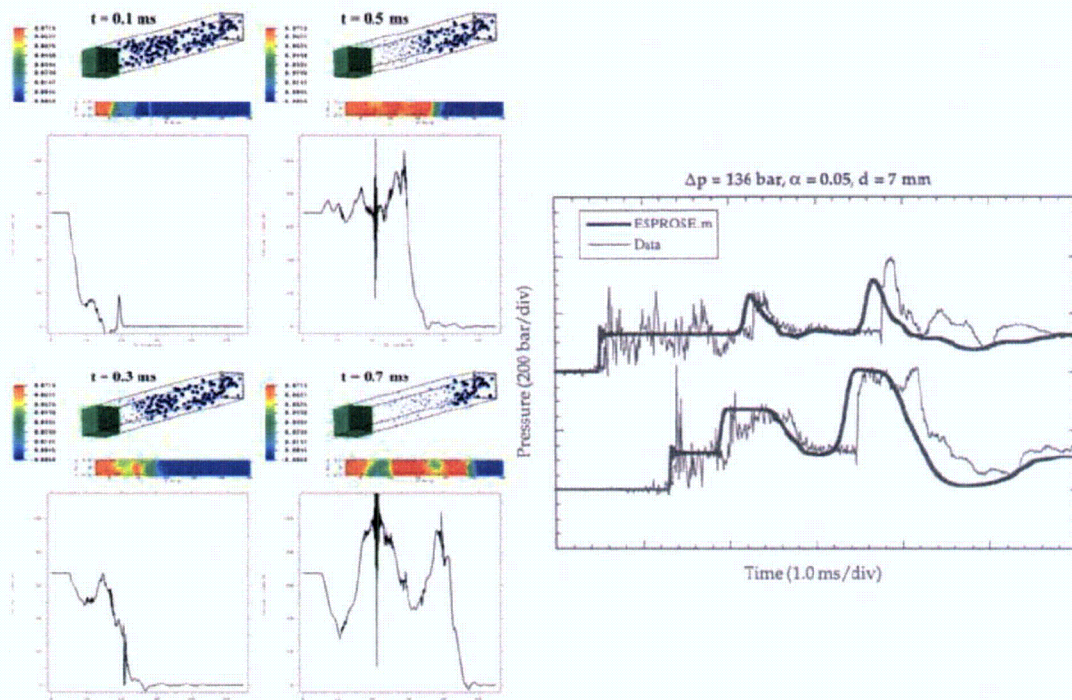


Figure C.4. Right: Pressure transient measured in a multi-void-region SIGMA run and ESPROSE.m simulation. Left: DNS [using ALE3D, an LLNL code] of this SIGMA run that captures also the pressure fluctuations due to collapsing bubbles.

References to Appendix C

Theofanous, T.G. W.W. Yuen and S. Angelini (1999a), "The Verification Basis of the PM-ALPHA Code," *Nuclear Engineering & Design*, 189 (1999) 59-102. (Also T.G. Theofanous, W.W. Yuen and S. Angelini, "Premixing of Steam Explosions: PM-ALPHA Verification Studies," DOE/ID-10504, June 1998.)

Theofanous, T.G. W.W. Yuen, K. Freeman and X. Chen (1999b), "The Verification Basis of the ESPROSE.m Code," *Nuclear Engineering & Design*, 189 (1999) 103-138. (Also T.G. Theofanous, W.W. Yuen, K. Freeman and X. Chen, "Propagation of Steam Explosions: ESPROSE.m Verification Studies," DOE/ID-10503, June 1998.)

Theofanous, T.G. W.W. Yuen, S. Angelini, J.J. Sienicki, K. Freeman, X. Chen and T. Salmassi, (1999c) "Lower Head Integrity Under Steam Explosion Loads," *Nuclear Engineering & Design*, 189 (1999) 7-57. (also T.G. Theofanous, W.W. Yuen, S. Angelini, J.J. Sienicki, K. Freeman, X. Chen and T. Salmassi, "Lower Head Integrity Under In-Vessel Steam Explosion Loads," DOE/ID-10541, June 1998).

SERENA (2004) Identification of Relevant Conditions and Experiments for Fuel-Coolant Interactions in Nuclear Power Plants - SERENA Co-ordinated Programme Phase 1 Task 1 Final Report NEA/CSNI/R(2004)7. Also in D. Magallon1, K-H Bang, S. Basu, G. Berthoud, M. Bürger, M.L. Corradini, H. Jacobs, R. Meignen, O. Melikhov, K. Moriyama, M. Naitoh, J-H. Song, N. Suh, T.G. Theofanous, "Status of International Program SERENA on Fuel-Coolant Interactions", International Conference on Advances in Nuclear Power Plants (ICAPP-05) Seoul, May 15-19, 2005.

SERENA (2005) Summary Record of the SERENA Task 4 Meeting. OECD/CSNI NEA/SEN/SIN/AMA(2005)13.

Appendix D

Validation of Natural Convection Model for Corium Melts

The purpose of this Appendix is to summarize evidence that our CFD simulations of natural convection in volumetrically heated pools, as carried out for purposes of this effort, are the culmination of long experience with this type of work both at the experimental as well as the computational fronts: Theofanous et al. (1996), Dinh and Nourgaliev (1997), Dinh et al (1997) and Theofanous and Angelini (2000).

The issues of particular concern here are (a) the up-to-downward power split, and (b) the heat flux distribution along the inclined boundaries of a volumetrically heated pool that is of the shape of a wedge. The conditions are turbulent convection, a regime characterized by very high values of the Rayleigh number, and a regime that has been difficult to approach in the past, both experimentally and computationally. The computational issues are those of grid resolution, as needed for keeping numerical diffusion from contaminating the actual transport involved. As a result computations are becoming more and more demanding as the Rayleigh numbers get bigger and bigger. The experimental issues had to do with achieving uniform volumetric heating in a large geometry, so as to match prototypic Rayleigh numbers of interest to reactor applications. The experimental problem was resolved by the ACOPO concept (Theofanous and Angelini, 2000), who also established the correspondence between the “external” (externally heated/cooled system) and the “internal” (volumetrically heated, externally cooled system) problems, and produced unified correlations valid up to the range of interest to whole-core reactor melt pools.

The computational issues turn out to be more insidious (Dinh and Nourgaliev, 1997), but eventually a reasonable understanding emerged, as verified by comparison to experiments (Dinh et al, 1997; Nourgaliev and Dinh, 1997). Heat transfer from the pool is driven by (a) fluid’s unstable stratification, which induces intense mixing in the bulk and near the upper cooled boundary, and (b), organized fluid motions, and “cold” boundary layers descending along the side and inclined lower boundaries.

In particular, we showed that mixing anisotropy is central to the understanding and modeling (Reynolds-type model) of high Rayleigh-number thermal convection of the type that is of primary interest in reactor applications. Further, analyses using a “no-model” (meaning no subgrid scale model) Large Eddy Simulation (LES) showed that, given sufficient resolution, the method works quite well in predicting mixing and heat transfer in volumetrically heated liquid pools, and for pools, such as the ACOPO

experiment, that approximate this condition by being subjected to externally-imposed transient cool-down (Nourgaliev et al. 1997a, 1997b and Figures D.1 and D.2).

It was also established that 2D simulations of thermal convection in volumetrically heated liquid pools are capable of capturing reasonably well the $Nu = f(Ra)$ dependence, although at the very high Rayleigh-number range ($Ra_E \sim 10^{12}$) the absolute values were somewhat lower than those measured in experiments. On the other hand, 3D simulations, which adequately capture all degrees of freedom, were found to improve both numerical convergence and energy balance. Based on our previous works, we favor the QUICK-modified, third-order bounded CCCT upwinded scheme (Nourgaliev and Dinh, 1997).

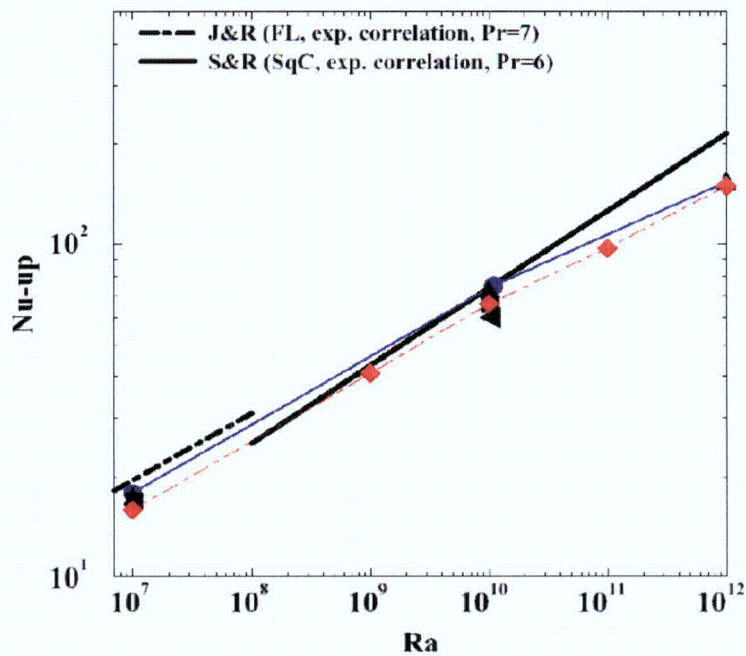


Figure D.1. Upward Nusselt number from an internally heated fluid layer. The numerical simulations utilize the no-model LES and the QUICK scheme. • – simulation for $Pr = 7$; ♦ – simulation for $Pr = 0.45$; ◀ – simulation for $Pr = 0.2$. As the Ra increases to the range of 10^{12} , the upward heat fluxes predicted by 2D simulations tend to be somewhat lower than experimental correlations (Steinberner and Reineke, 1978, Jahn and Reineke, 1974).

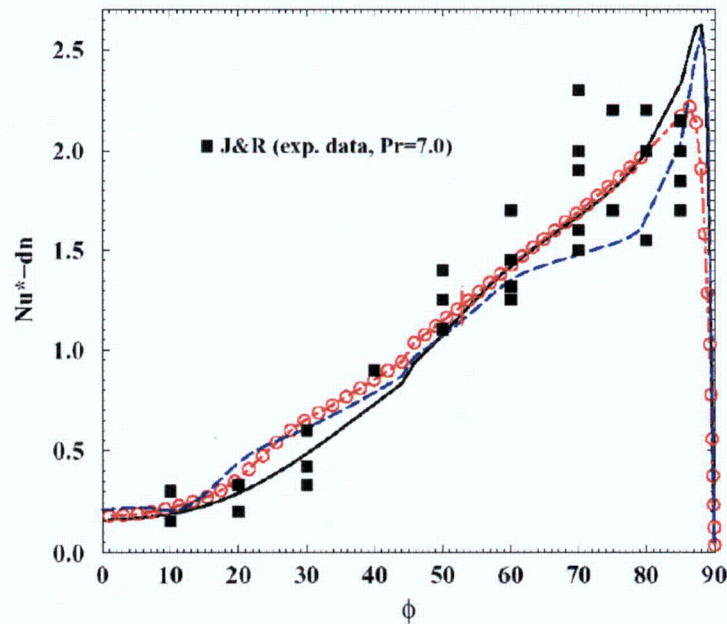


Figure D.2. Simulation of heat flux distribution (relative to the area-averaged value) on the downward surface in a volumetrically heated semicircular liquid pool (Jahn and Reineke data, 1974). (solid black line, red circles, and dotted blue line are simulations for $Pr = 7$; 1.2; 0.6, respectively).

More recently we have used the Fluent CFD code as a platform to further pursue these numerical issues in the scope of a new, unique, and highly sensitive experiment conducted in our laboratory at UCSB.

Named the BETA-NC experiment, the experimental approach stems from our work developed under a NASA grant to investigate pool boiling (Figure D.3). The objective is to gain insights into the physics of unstably stratified layers, and in particular to obtain transient data which characterize the emergence of flow structures. This kind of experiment and the approach are unique to enabling an *a priori* testing of fidelity of this type of (instability/self-organization) phenomena.

Uniform heat flux on the BETA heated surface is achieved by passing a direct electrical current through a 460nm-thin Titanium film, vapor-deposited on 130 μm borosilicate glass substrate. The Titanium film is highly uniform in thickness, and so is the surface heat flux due to Joule heating. Also, because of the small thickness of the Titanium film and the glass substrate, temperature response and measurement are on a millisecond time scale, which is much shorter than the time scale of the convection process (it occurs on a time scale of seconds). The test section used is a rectangular glass vessel, closed at the bottom by the heater element, it occupying the entire 27x40 mm^2 cross section of the vessel. We use an infrared camera to achieve a high-speed (1 KHz), high-resolution (30 μm), highly accurate ($\pm 0.3\text{K}$) thermometry of the heater surface (Dinh et al., 2004a, 2004b).

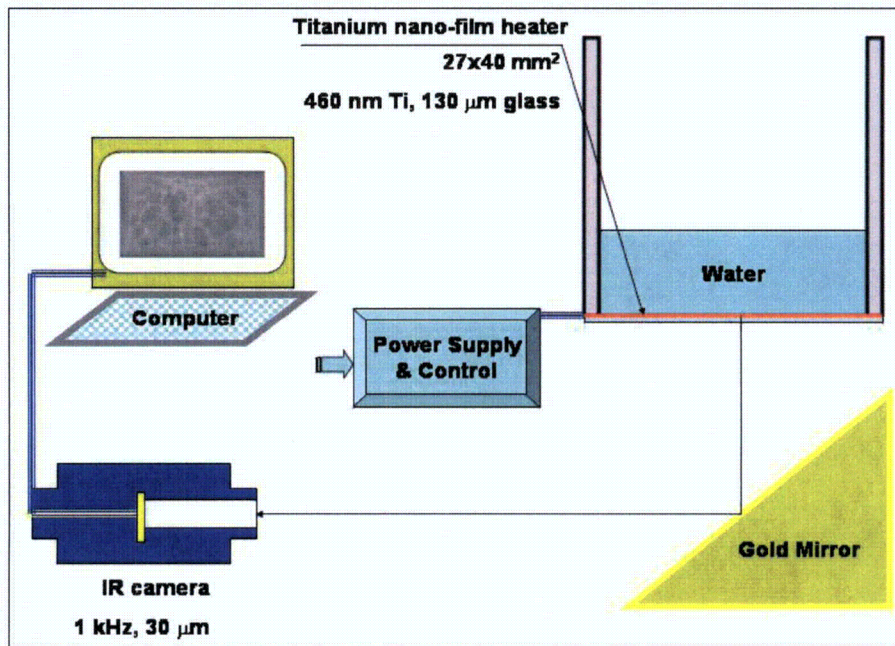


Figure D.3. BETA-NC experiment for the study of thermal convection.

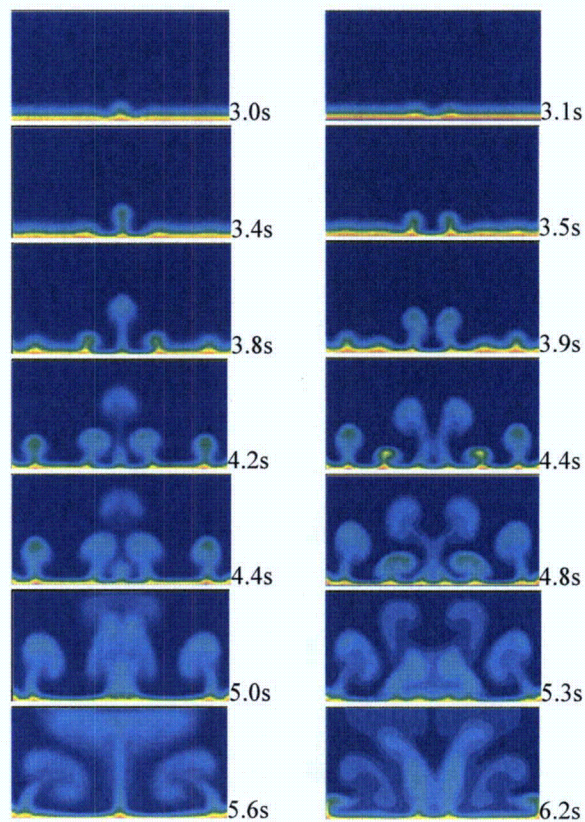
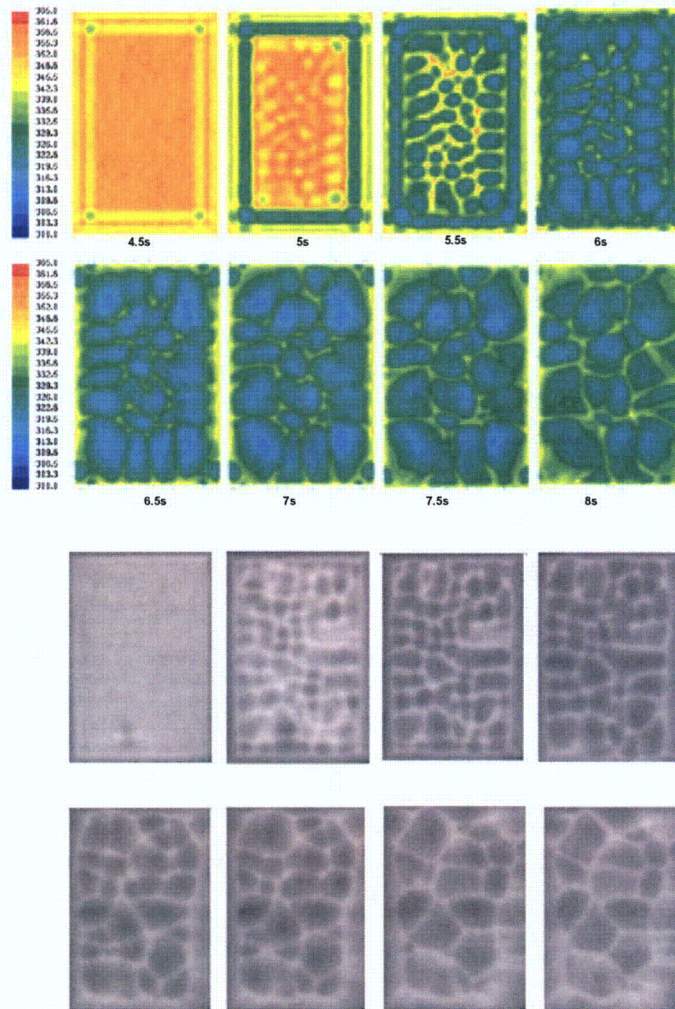


Figure D.4.a. Numerical simulation of fluid instability, and Rayleigh-Bernard convection in fluid layer heated from below.



*Figure D.4.b. Transient thermal convection patterns emergent upon heating, as visualized by temperature maps of the heating surface.
 Top: Surface temperature of a fluid layer as obtained from our numerical simulations.
 Bottom: Heater surface temperature as measured by a high-speed IR camera in a BETA-NC experiment (Dinh et al., 2004a). Both inception of instability and thermal patterns can be reproduced in this basic-principles simulation.*

For these BETA-NC simulations, we examined first-order (SIMPLE), second-order (SIMPLEC, QUICK) accurate numerical schemes, and tested the effect of parameters of spatial and time discretization. Figures D.4 provides a sample set of simulation results.

In Chapter 3 (BMP) heat transfer results obtained from natural convection simulation for BiMAC melt pool configurations were presented and used for the thermal load assessment. Additional perspectives on these numerical simulations are provided in Figures D.5 and D.6 addressing aspects of temporal and spatial resolution.

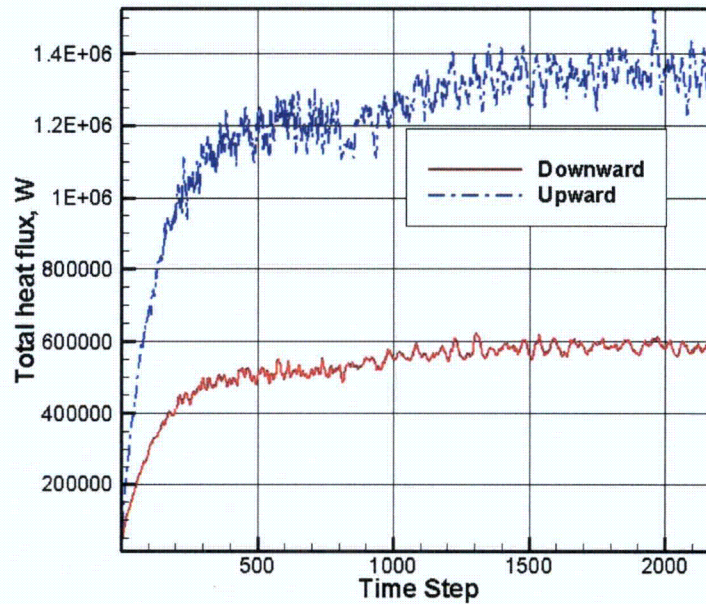


Figure D.5. Heat removal rates to top and bottom boundaries of a volumetrically heated liquid pool (Configuration C 2D simulation). During the first 800 time steps, the simulation was performed with a coarse time step, to establish the overall flow pattern, after which the time step was reduced by about an order of magnitude, to ensure adequate resolution of flow mixing in the unstably stratified region (top boundary). The refinement lead to an increase of both heat fluxes by $\sim 20\%$, so the energy split remained the same.

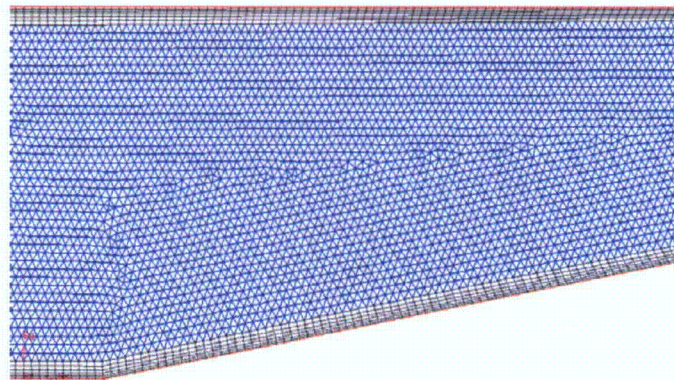


Figure D.6. Grid with refinement in the near-wall region. Sensitivity calculations were run on different grids to ensure that we achieved convergence .

References for Appendix D

Dinh T.N. and R. R. Nourgaliev, "Turbulence Modeling in Large Volumetrically Heated Liquid Pools", *Nuclear Engineering and Design*, **169** 131-150 (1997).

Dinh, T.N. R.R. Nourgaliev, and B.R. Sehgal, "On Heat Transfer Characteristics of Real and Simulant Melt Pool Experiments", *Nuclear Engineering and Design*, **169**, pp.151-164, 1997.

Dinh, T.N. Y.Z. Yang, J.P. Tu, R.R. Nourgaliev and T.G. Theofanous (2004a), "Rayleigh-Bénard Natural Convection Heat Transfer: Pattern Formation, Complexity and Predictability", 2004 International Congress on Advances in Nuclear Power Plants, Pittsburgh, PA, June 13-17, 2004.

Dinh, T.N. J.P. Tu, Y.Z. Yang, R.R. Nourgaliev and T.G. Theofanous (2004b), "Characterization and Predictability of Transient Heat Transfer in an Unstably Stratified Layer during Power Startup", 37th AIAA Thermophysics Conference, Portland, OR, June 27-30, 2004. AIAA-2004-2733.

Grenoble: (1994). OECD/CSNI/NEA Workshop on Large Molten Pool Heat Transfer, Nuclear Research Centre, Grenoble, France, March 9-11

FLUENT CFD Code. User Manual. 2003.

FLUENT 6.0 Validation Experience and Applications. Fluent and Fluent users websites.

Jahn M. and H.H. Reineke (1974), "Free Convection Heat Transfer with Internal Heat Sources: Calculations and Measurements", Proceedings of the 5th Int. Heat Transfer Conference, Tokyo, Japan , Vol.3, paper NC.2.8.

Nourgaliev, R.R. and T.N. Dinh, "The Investigation of Turbulence Characteristics in an Internally Heated Unstably Stratified Fluid Layers", *Nuclear Engineering and Design*, **178**:(1), 235-259 (1997).

Nourgaliev, R.R. T.N. Dinh, and B.R. Sehgal, "Simulation and Analysis of Transient Cooldown Natural Convection Experiments", *International Journal of Nuclear Engineering and Design*, **178**:(1), pp.13-27 (1997a).

Nourgaliev, R.R. T.N. Dinh, and B.R. Sehgal, "Effect of Fluid Prandtl Number on Heat Transfer Characteristics in Internally Heated Liquid Pools with Raleigh Numbers up to 10^{12} ", *Nuclear Engineering and Design* **169** 165-184 (1997b).

Steinberner U. and H.H. Reineke (1978), "Turbulent Buoyancy Convection Heat Transfer with Internal Heat Sources", Proceedings of the 6th Int. Heat Transfer Conference, Toronto, Canada, Vol.2, pp.305-310.

Theofanous, T. G. C. Liu, S. Additon, S. Angelini, O. Kymäläinen, and T. Salmassi, *In-Vessel Coolability and Retention of a Core Melt*, DOE/ID-10460, October 1996.

Theofanous, T. G. and S. Angelini, "Natural Convection for In-Vessel Retention at Prototypic Rayleigh Numbers," *Nuclear Engineering and Design* **200** 1-9 (2000).

Appendix E

Validation of 2-Phase Natural Circulation Model in BiMAC

E.1 Introduction

In this Appendix we examine aspects of two-phase natural circulation in BiMAC, as assessed by means of a model developed specifically for this work. The Model is described in Section E.2. A validation exercise using the pressure drop data from the SULTAN experiment is presented in Section E.3. Application to BiMAC is then given in Section E.4. Our principal interest is two-phase pressure drop in heated, low-inclination channels, with a characteristic dimension of ~ 0.10 m (large in comparison to most past experiments in this area).

E.2. The Two-Phase Flow Model

The governing equations for homogeneous two-phase flow in the 1D equilibrium approximation, are summarized in Table E.2.1 — the nomenclature can be found at the end of this appendix. The vapor quality x is the local equilibrium value according to energy conservation. The total pressure drop is obtained by integrating along the flow path (dl) the differential pressure gradients due to gravity, acceleration, and viscous losses, i.e.,

$$\frac{dp}{dl} = \frac{dp_b}{dl} + \frac{dp_f}{dl} + \frac{dp_a}{dl} \quad (\text{E.1})$$

The local void fractions, and two-phase viscous losses are from the Lockhart-Martinelli (1949) correlation applied in a quasi-steady fashion (see Wallis, 1969 as a more convenient reference). As a second approach, we also make use of an arbitrary specification of uniformly applied values of vapor slip, and using it, we obtain the local void fractions through the local quality. The correction for inclination (E.3) is similar to a generalization from data obtained on inclined pipes by Sneerova et al (1961).

Table E.2.1. Definition of the Two-Phase Flow Model.

Energy balance:

$$G \frac{d(xA)}{dl} = \frac{qU}{H_{fg}}$$

Void Fraction and Density

$$\beta = \frac{x}{x + \frac{(1-x)\rho_v}{\rho_w}}$$

$$\alpha_v = \frac{\beta}{\beta + s(1-\beta)}$$

$$\alpha_v = (1 + X_u + 1/F_l)^{-0.321} \quad (\text{E.2})$$

$$\text{where } X_u = \left(\frac{1-x}{x}\right)^{0.9} \left(\frac{\rho_v}{\rho_w}\right)^{0.5} \left(\frac{\mu_w}{\mu_v}\right)^{0.1}$$

$$\text{and } F_l = \left(\frac{x^3 G^2}{\rho_v^2 d g (1-x)}\right)^{0.5}$$

$$\alpha = \begin{cases} \alpha_v & \text{if } \theta = \pi/2 \\ \xi \cdot \alpha_v & \text{if } \theta < \pi/2 \end{cases} \quad (\text{E.3})$$

$$\text{where } \xi = \frac{\beta + s \cdot (1-\beta)}{\beta + Y \cdot s(1-\beta)}$$

$$Y = 1 + \left(1 - 5 \times 10^{-6} u_0 d^* \frac{\rho_l}{\mu_l}\right) \left(1 - \frac{\theta}{2\pi}\right)$$

$$d^* = \max \left(d, 20 \left(1 - \frac{\rho_v}{\rho_w}\right)^{1/4} \left(\frac{0.06}{\rho_w - \rho_v}\right)^{1/2} \right)$$

Contributions to the Pressure Gradient:

$$\frac{dp}{dl} = \frac{dp_b}{dl} + \frac{dp_f}{dl} + \frac{dp_a}{dl}$$

Pressure gradient due to gravity:

$$\frac{dp_h}{dl} = (\alpha \rho_g + (1-\alpha) \rho_l) g \sin \theta$$

Pressure gradient due to acceleration:

$$\frac{dp_a}{dl} = G^2 \frac{d}{dx} \left(\frac{x^2}{\rho_v \alpha} + \frac{(1-x)^2}{\rho_w (1-\alpha)} \right)$$

Pressure gradient due to viscous losses:

- Single phase:

$$\frac{dp_f}{dl} = \frac{2fG^2}{\rho d} \text{ where } f = \begin{cases} \frac{16}{\text{Re}} & \text{if } \text{Re} < 2000 \\ \frac{0.064}{\text{Re}^{0.2}} & \text{if } \text{Re} > 2000 \end{cases}$$

- Two phase, frictional pressure gradient (Lockhart-Martinelli):

$$\frac{dp_f}{dl} = \frac{1}{2} \left[\left(\frac{dp}{dz} \right)_w \phi_w^2 + \left(\frac{dp}{dz} \right)_v \phi_v^2 \right]$$

$$\left(\frac{dp}{dz} \right)_w = \frac{2f[(1-x)G]^2}{d \cdot \rho_w} \quad \text{and} \quad \left(\frac{dp}{dz} \right)_v = \frac{2f(x \cdot G)^2}{d \cdot \rho_v}$$

$$X^2 = \frac{(dp/dz)_w}{(dp/dz)_v} \quad \phi_w^2 = \frac{(dp/dz)_F}{(dp/dz)_w} = 1 + \frac{C}{X} + \frac{1}{X^2} \quad \phi_v^2 = \frac{(dp/dz)_F}{(dp/dz)_v} = 1 + CX + X^2$$

E.3. Interpretation of the SULTAN experiments

The SULTAN tests were designed to investigate basic (separate-effects) aspects of boiling convection. In particular the effects of several key thermo-hydraulic (e.g system pressure, heat flux, mass flow rate) and geometric parameters (e.g. channel dimensions) on pressure drop and critical heat flux (CHF) were systematically studied. These tests were conducted at the Grenoble Nuclear Research Centre (France/CEA/CENG) from 1994 to 1996. We make use here of the partial documentation available in the open literature (Rouge, 1997).

The overall facility is illustrated in Figure E.3.1a. The test section (Fig E.3.1.b) consists of a rectangular channel, heated from one of the side walls, and an outlet pipe. The heated side wall of the channel is a flat stainless steel plate 4 m x 0.15 m, and heat is supplied by the direct Joule effect. The distance between the heating side and the

opposite wall, termed “gap”, was varied between $\delta = 0.03$ m and $\delta = 0.15$ m. The cross-section hence varied from 0.15 m x 0.03 m to 0.15 m x 0.15 m. The test section orientation was also changed from the vertical ($\theta = 90^\circ$) to near horizontal ($\theta = 10^\circ$) – with the heated side on top — to capture the effects of inclination. Data on pressure drop and CHF were obtained for: pressures p , 0.1-0.5 MPa; inlet temperatures T_e , 50-150 °C; mass flow velocities G , 5-4400 kg/m²s; and heat fluxes, 100-1000 kW/m². We are interested here in the pressure drop measurements—besides these data being very appropriate to the inclined channels of the BiMAC, such information happens to be hardly available in previous two-phase pressure drop work.

In this section, our predictions of the pressure drop in the test section alone, and the total pressure drop including the outlet pipe, are evaluated against experimental data. Two sets of data were used for comparisons: (a) $\theta = 90^\circ$ at $p=0.5$ MPa with $\delta = 0.03$ m, and (b) $\theta = 10^\circ$ at $p=0.5$ MPa with $\delta = 0.15$ m. The results are summarized in Figures E.3.2 to E.3.7.

The Lockhart-Martinelli model appears to capture the general trend of the experimental data quite well. Calculations with $s = 10$ and $s = 40$ also yield good, in fact somewhat better predictions, especially for the low range of power levels which is of immediate interest here. This power dependency is as expected for the low inclination case—here we expect a stronger stratification, and/or slugging, with higher values of slip prevailing on the average.

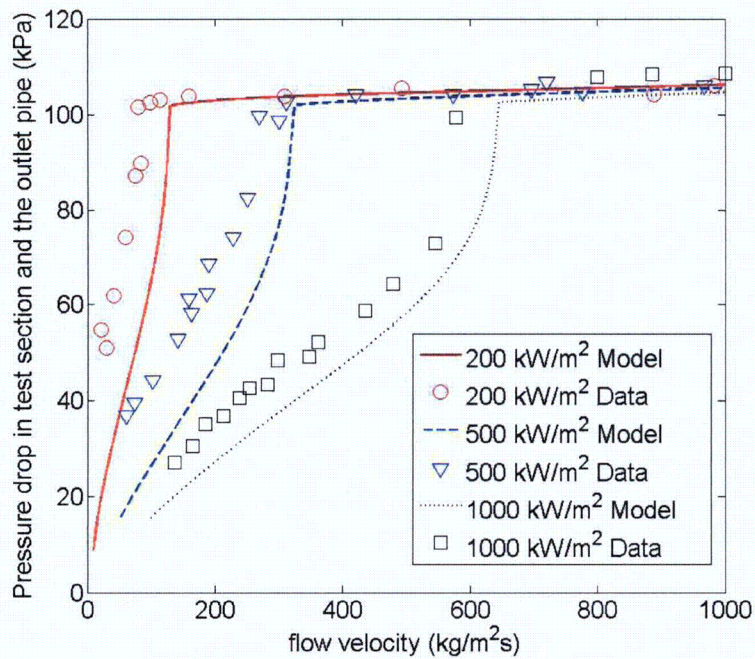
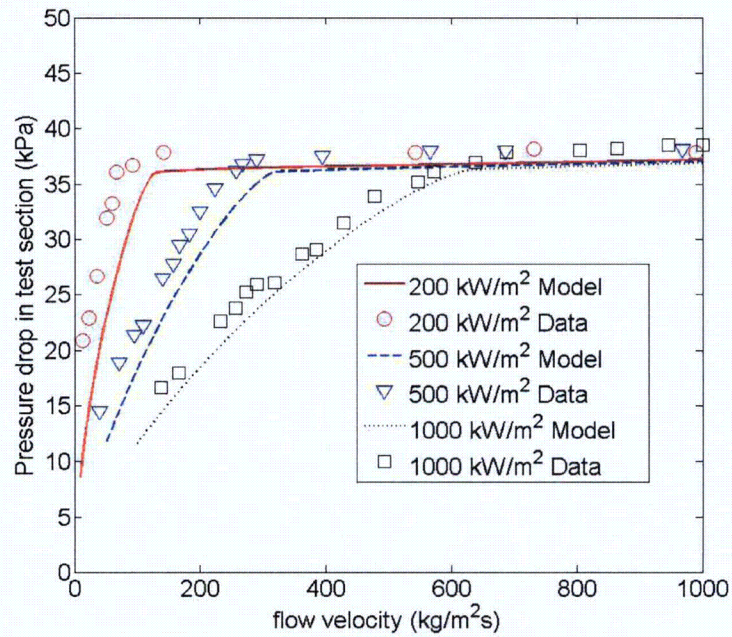


Figure E.3.2. Predictions of SULTAN experiments ($p = 0.5 \text{ MPa}$, $\theta = 90^\circ$, $\delta = 0.03 \text{ m}$, $T_e = 100^\circ\text{C}$). The slip is given by L-M, Eq.(E.2).

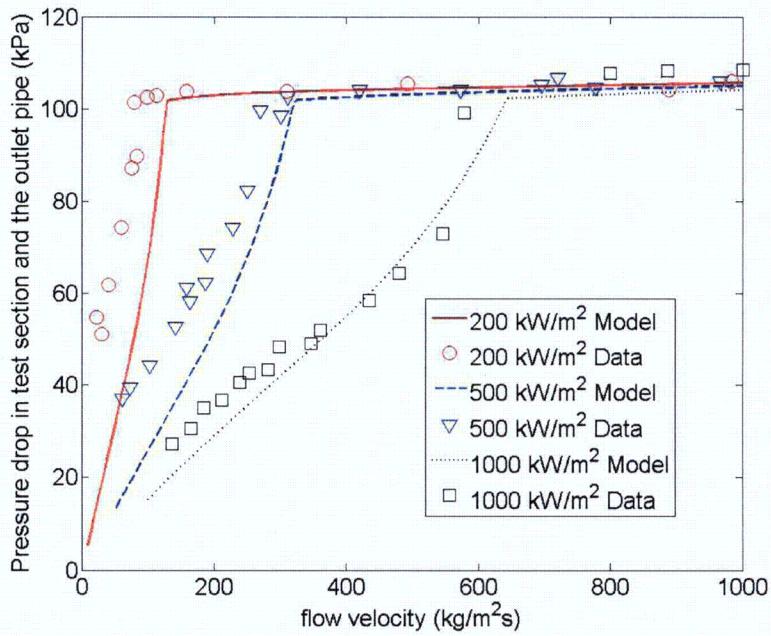
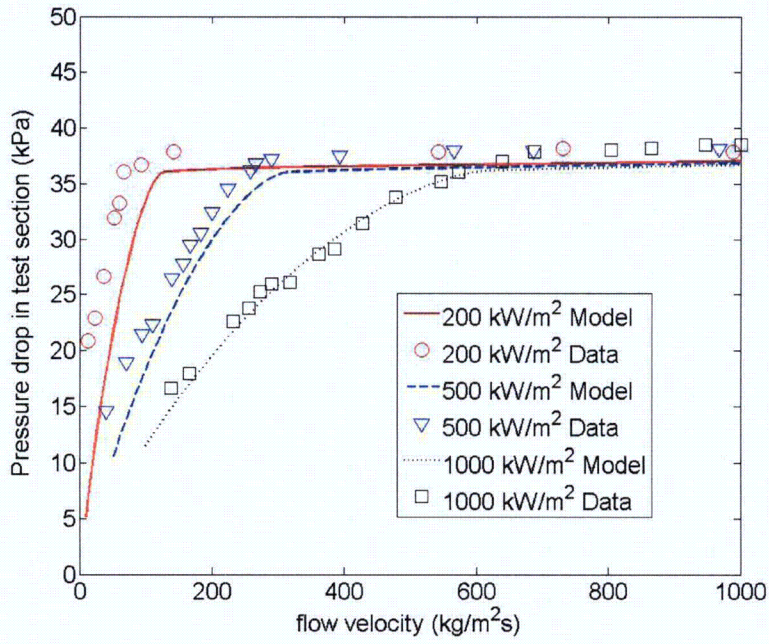


Figure E.3.3. Predictions of SULTAN experiments ($p = 0.5 \text{ MPa}$, $\theta = 90^\circ$, $\delta = 0.03 \text{ m}$, $T_e = 100^\circ\text{C}$). The slip is set at $s = 10$.

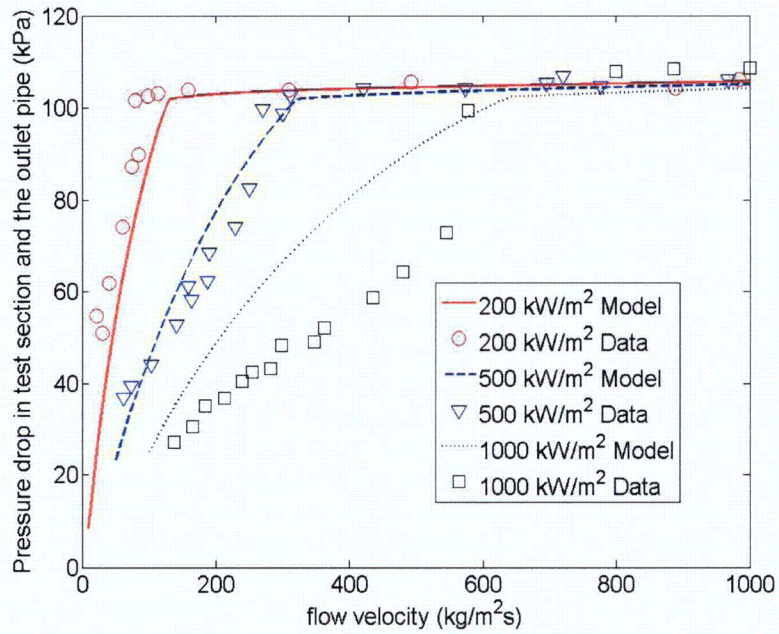
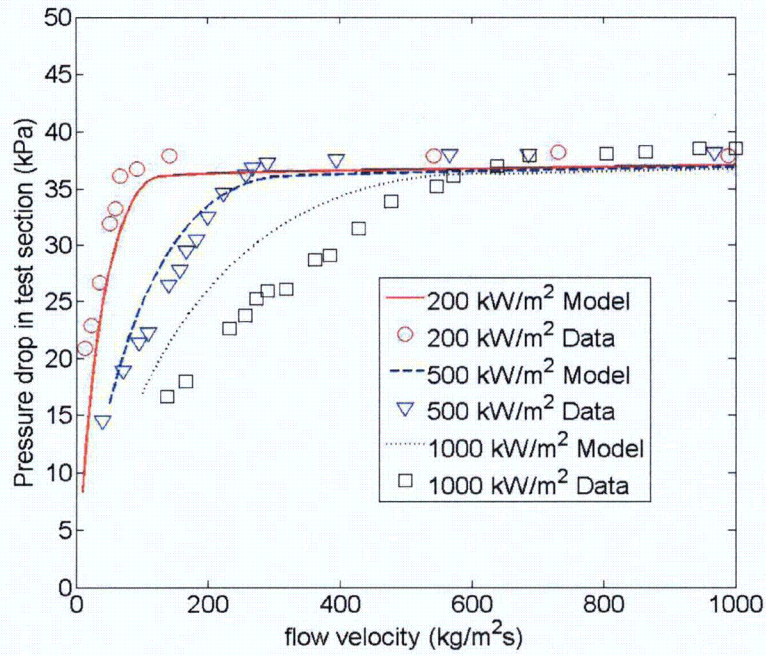


Figure E.3.4. Predictions of SULTAN experiments ($p = 0.5 \text{ MPa}$, $\theta = 90^\circ$, $\delta = 0.03 \text{ m}$, $T_e = 100^\circ\text{C}$). The slip is set at $s = 40$.

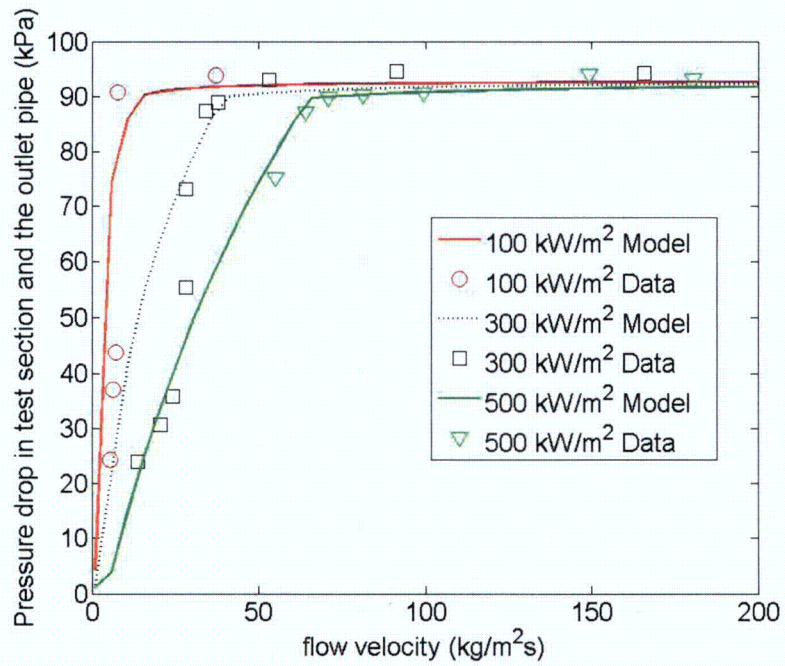
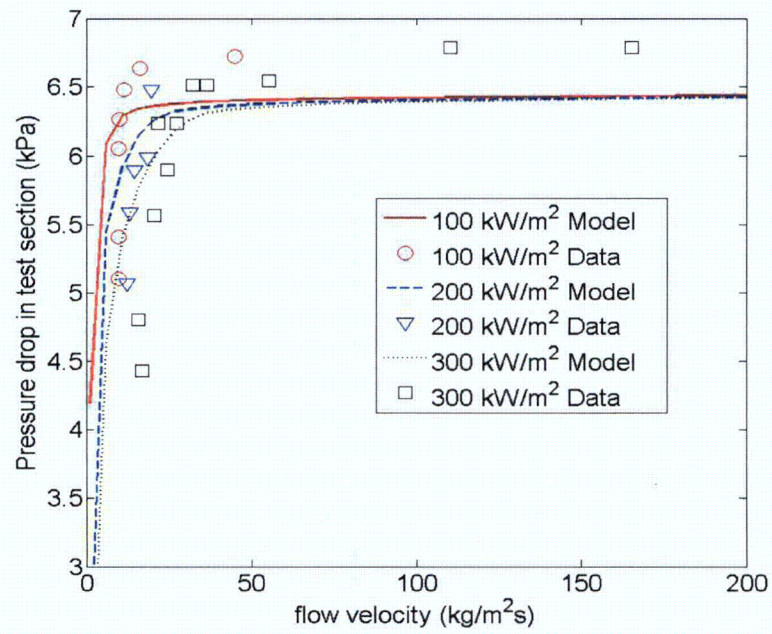


Figure E.3.5. Predictions of SULTAN experiments ($p = 0.5 \text{ MPa}$, $\theta = 10^\circ$, $\delta = 0.15 \text{ m}$, $T_e = 100^\circ\text{C}$). The slip is given by L-M, Eq.(E.2).

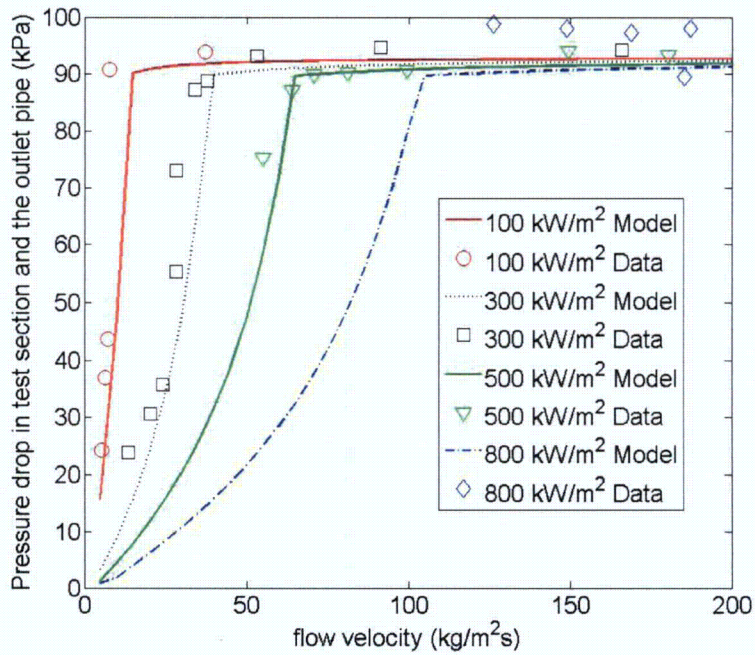
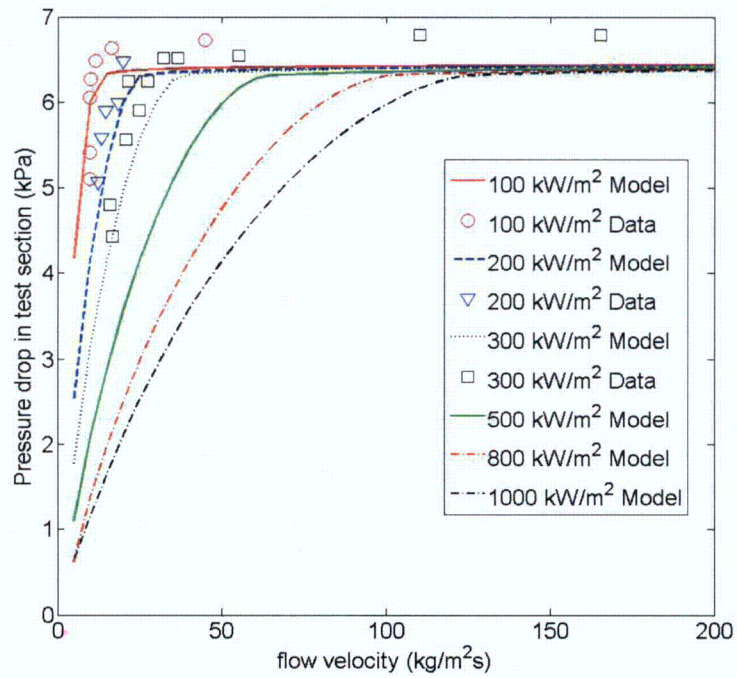


Figure E.3.6. Predictions of SULTAN experiments ($p = 0.5 \text{ MPa}$, $\theta = 10^\circ$, $\delta = 0.15 \text{ m}$, $T_e = 100^\circ\text{C}$). The slip is set at $s = 10$.

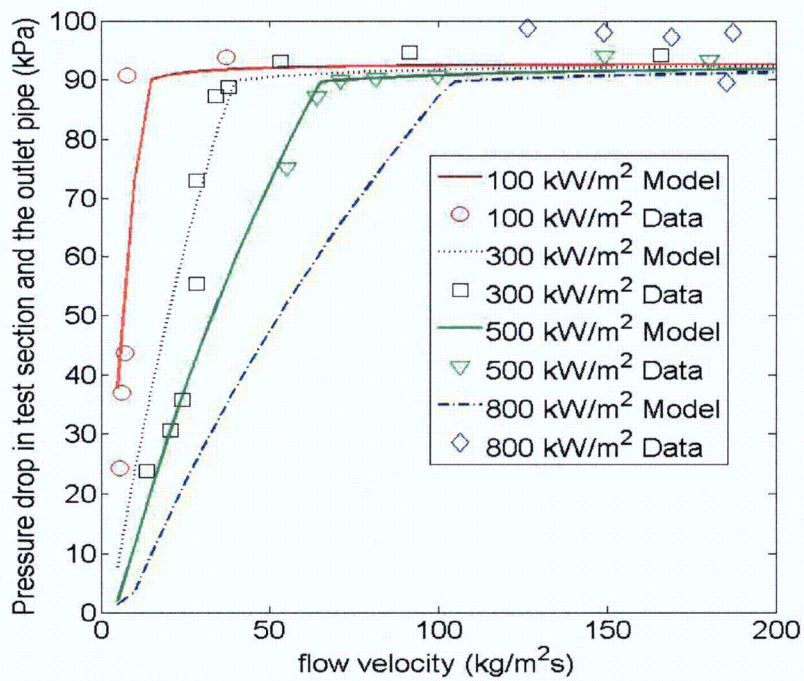
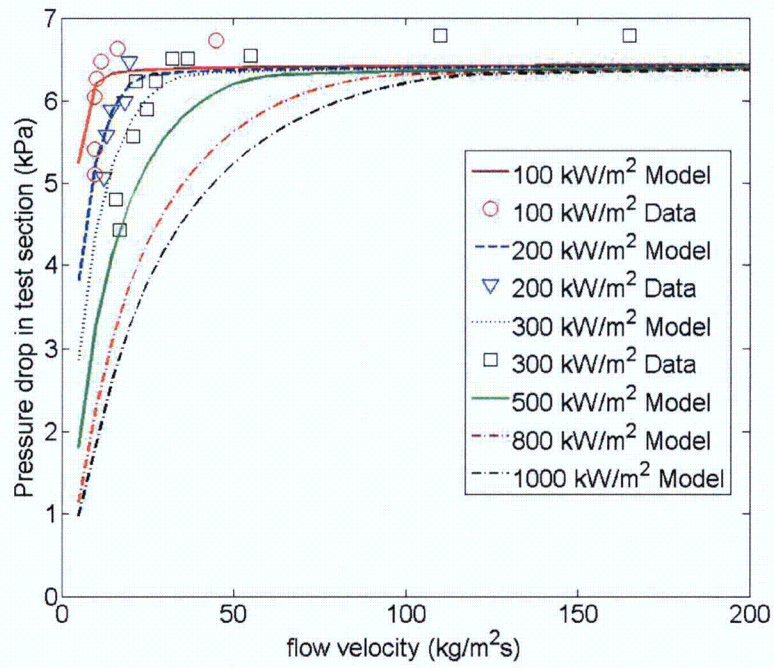


Figure E.3.7. Predictions of SULTAN experiments ($p = 0.5 \text{ MPa}$, $\theta = 10^\circ$, $\delta = 0.15 \text{ m}$, $T_e = 100^\circ \text{C}$). The slip is set at $s = 40$.

E.4. Two-Phase Natural Circulation Flow in the BiMAC .

As explained already in Chapter 3 (section 3.4.4), one of the keys to the BiMAC fragility is the performance of two-phase natural circulation through its pipes. The basic question is whether there can be excursive, Ledinegg-type, instabilities due to two-phase losses that could starve the flow for long-enough periods of time to cause local dryouts, and perhaps temperature excursions that may be hard to recover in the natural circulation mode of BiMAC operation.

Here we examine the most limiting case for this type of concern, and that is the performance of the longest pipe thermally loaded all along its length. We use the Lockhart-Martinelli-based model described above for both pressure drops and void fraction calculations (Table E.2.1). Steady-state solutions are found by matching the pressure drop requirements in the loop to the pressure head made available by boiling. Different values of the power level are considered to cover the range of interest; they are applied uniformly over the length of the pipe. The effect of non-uniformity is also examined. All important dimensions are summarized in Table E.4.1. Besides the flow rates, other important results of these calculations are the exit void fractions—they are needed to be sure there is enough liquid to keep the wall completely wetted. These results are presented in Figures E.4.3 (saturated water at the inlet), and Figures E.4.4 (10K subcooling at the inlet). The effect of heated (pipe) length is shown in Figures E.4.5.

As we can see in Figure E.4.3a, for saturated water at the inlet, there is a broad maximum in flow rate, which in fact is around the range of heat fluxes of interest here ($<100 \text{ kw/m}^2$). Moreover these results show that in this neighborhood, and even up to 600 kw/m^2 the gravity head dominates riser performance, so that the flow is self-adjusting, and self stabilizing—a decrease in flow would produce a more voided condition in the channel, and thus a driving force for an increase in flow. More specifically the “supply/demand” behavior for representative thermal loads on the BiMAC is shown in Figures E.4.6. We can see that the condition $|d \Delta P_R/d G| > |d \Delta P_D/d G|$ is satisfied, thus ensuring that any disturbances (of mass flow rate) do not escalate and rapidly return to the operating condition.

Finally, we must consider the size of downcomer flow area needed to supply all 100 pipes that make up the BiMAC jacket without significant pressure loss in the single-phase region of the flow loops. Sample results for an area of 0.06 m^2 feeding 30 and 60 pipes, at representative power loads are shown in Figures E.4.7. We can see that near-single pipe behavior can be obtained with rather modest downcomer flow area increases. The particular design choices will be subject to optimization, during the final design of BiMAC at the COL stage.

Table E.4.1 Geometric Parameters used in the BiMAC Flow Analyses.

Down-comer height/Diameter	1800/100 mm
Down-comer horizontal section length/Diameter	5500/100 mm
The riser length/Diameter	5000/100 mm
The height of the vertical section of the riser	830 mm

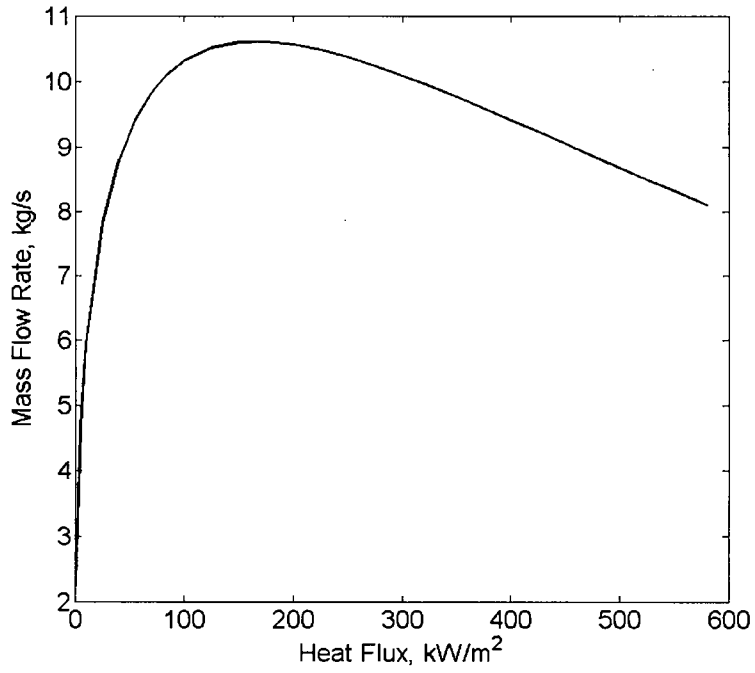


Figure E.4.3a. Prediction of mass flow rate as function of applied heat flux. $\Delta T_{sub} = 0$

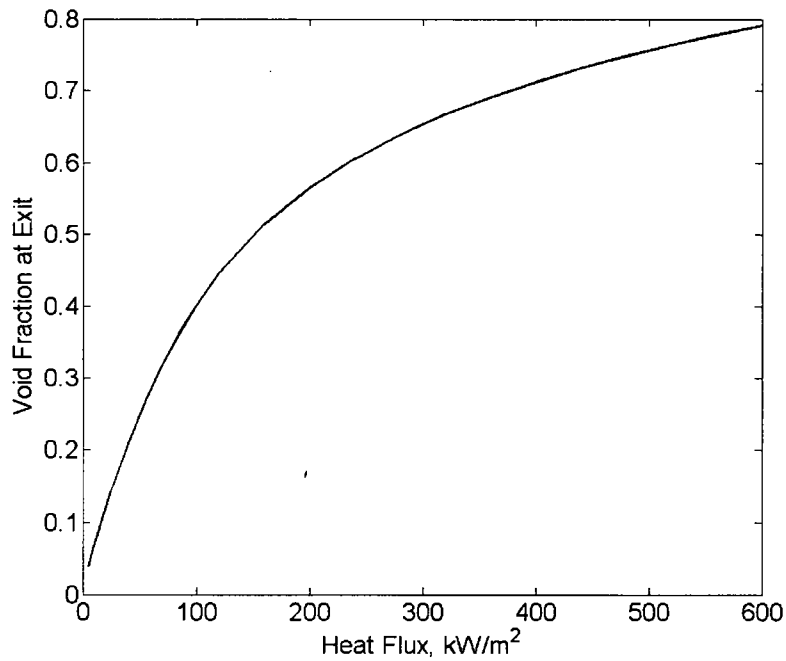


Figure E.4.3b. Prediction of exit void fraction as function of applied heat flux. $\Delta T_{sub} = 0$

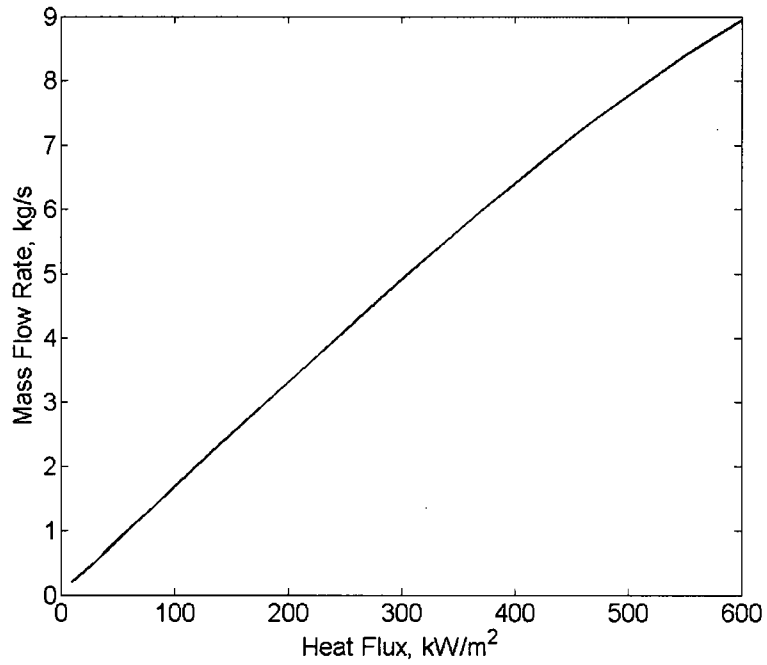


Figure E.4.4a. Predictions of flow rate as function of applied heat flux. $\Delta T_{sub} = 10$ K

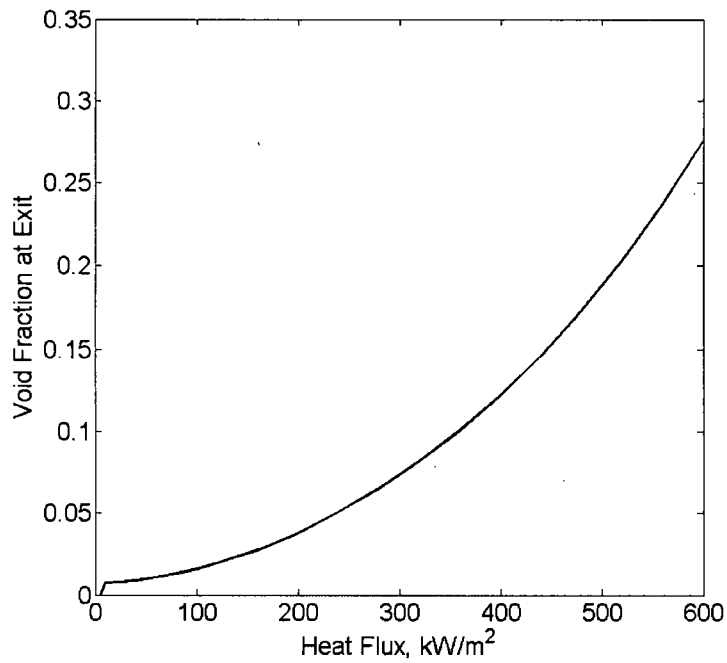


Figure E.4.4b. Predictions of exit void fraction as function of applied heat flux
 $\Delta T_{sub} = 10$ K

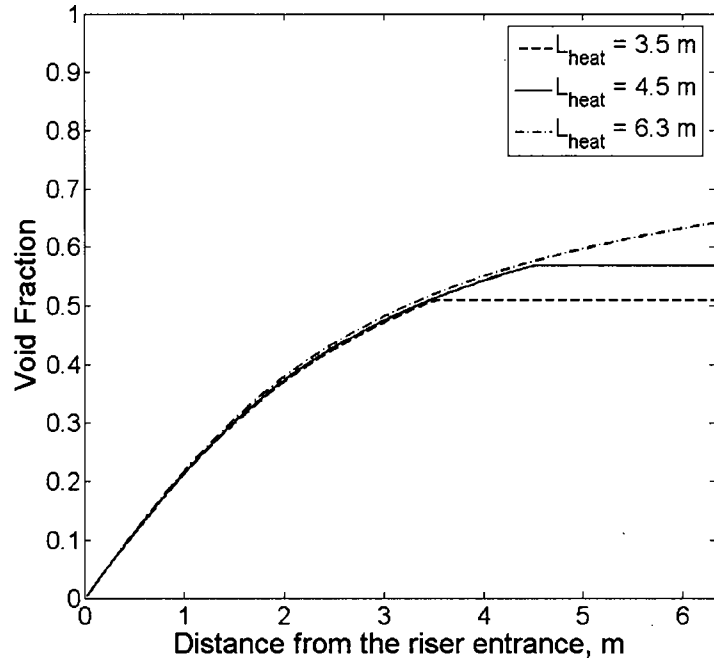


Figure E.4.5. Distribution of void fraction in the riser as function of the heated length. Averaged heat flux 200 kW/m^2 . The water is saturated at the entrance.

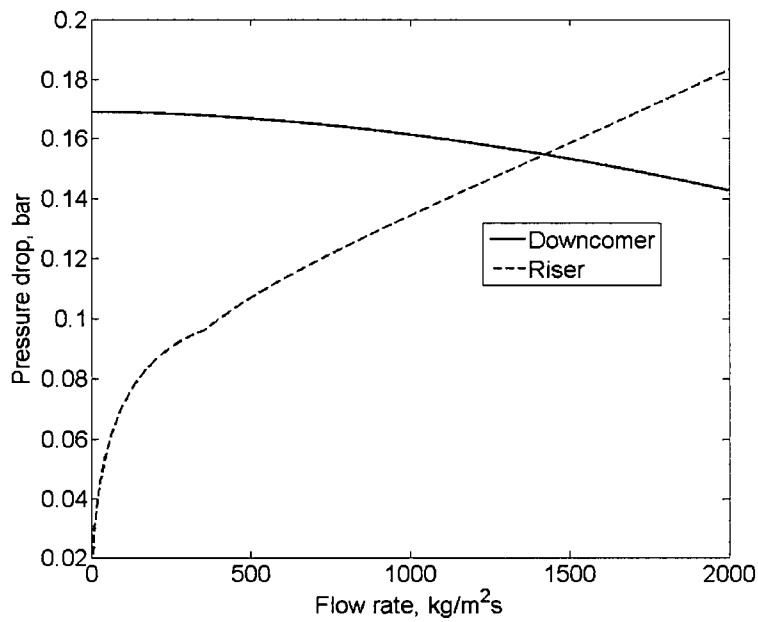


Figure E.4.6a. Pressure drop in the Downcomer and the Riser. $q = 100 \text{ kW/m}^2$.

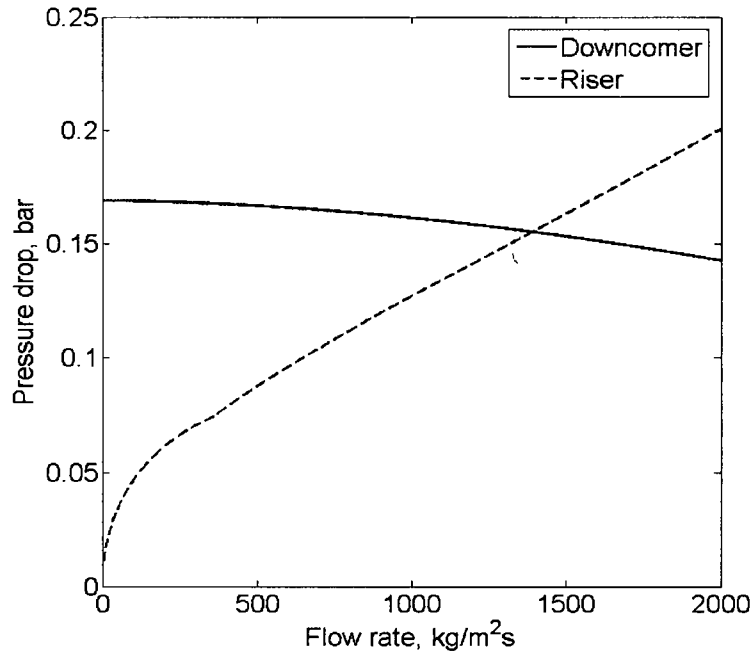


Figure E.4.6b. Pressure drop in the Downcomer and the Riser. $q = 200 \text{ kW/m}^2$.

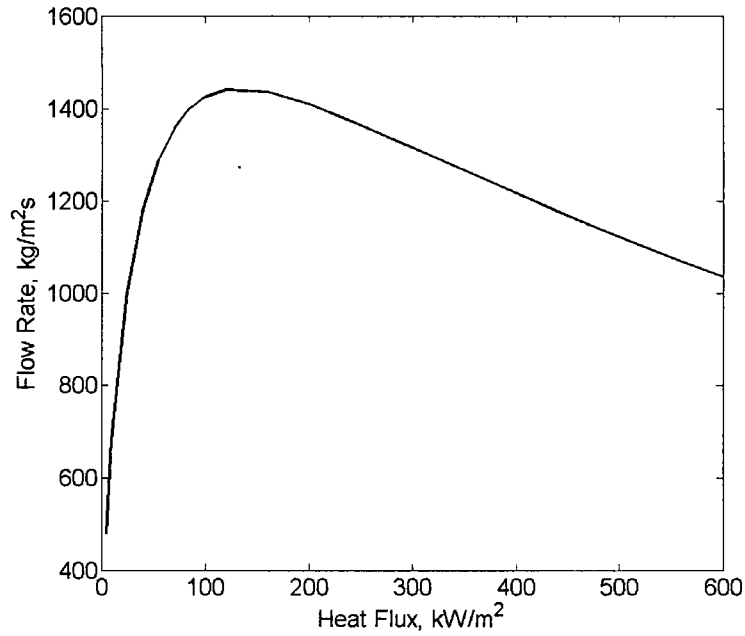


Figure E.4.7a. Predictions of mass velocity as function of applied heat flux. Single-pipe loop with Downcomer flow area of 0.06 m^2 . $\Delta T_{sub} = 0$

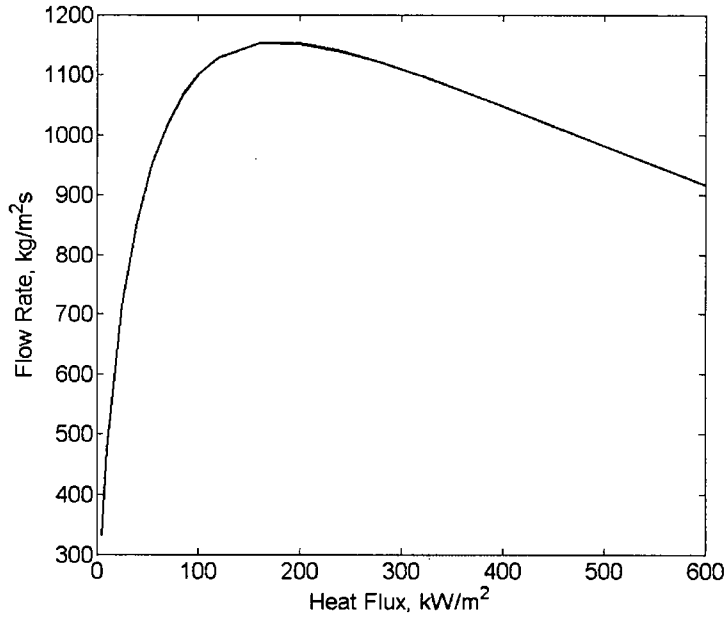


Figure E.4.7b. Predictions of mass velocity as function of applied heat flux. A loop with 30-pipes for Riser and a Downcomer flow area of 0.06 m^2 . $\Delta T_{sub} = 0$

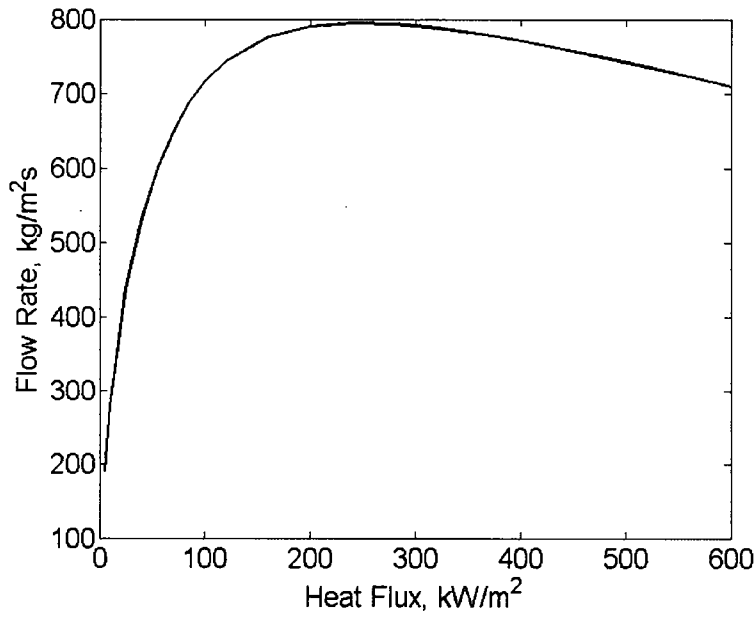


Figure E.4.7c. Predictions of mass velocity as function of applied heat flux. A loop with 60-pipes for Riser and a Downcomer flow area of 0.06 m^2 . $\Delta T_{sub} = 0$

E.5. Conclusions

We have shown that the pressure drop data obtained in the SULTAN facility are readily interpretable by means of a slip-equilibrium flow model using the Lockhart-Martinelli correlation for pressure drop and void fraction. This “benchmarking” is important because this experiment is matched quite well to the inclination and dimensions of a BiMAC channel, including that heating was supplied from above.

Applied to BiMAC, this model yields results that indicate stable operation under natural circulation conditions, while the flow and void fraction levels provide strong assurance that the heated wall would remain well-wetted, and not be subject to dryouts. Moreover sample calculations show that the downcomer flow areas needed to supply the riser flows are rather modest: they will be subject to optimization, along with other BiMAC parameters during final design at the COL stage.

Symbol	Description	Unit
d	Hydraulic diameter of pipe	m
f	Friction factor	–
G	Mass flux	kg/(m ² .s)
L	Length of pipe	m
\dot{m}	Mass flow rate	kg/s
p	Pressure	Pa
Re	Reynolds number	–
s	Slip ratio	–
x	Vapor (mass) quality	–
X_{tt}	Lockhart-Martinelli parameter	–
Y	Coefficient, see Eq. (15)	–
z	Pipe length	m
α	Void fraction	–
α_v	Void fraction in vertical riser	–
β	Vapor volumetric flow ratio	–
ϕ^2	Two-phase friction multiplier	–
μ	Viscosity	Pa.s
θ	Inclination angle of the riser	degree
ρ	Density	kg/m ³
ξ	Coefficient, see Eq. (16)	–

Subscripts

w	Water
v	Vapor
F	Two-phase mixture

References for Appendix E

Lin Z.H. (1992), "Characteristics of Gas-Liquid Two-Phase Flow In Pipelines and Their Engineering Applications", Xian Jiaotong Univ. Press.

Lockhart R.W. and R.C. Martinelli (1949), "Proposed Correlation of Data for Isothermal Two-Phase Two-Component Flow in Pipes", *Chem. Eng. Progr.* 45, 39-48.

Rouge, S. (1997). "SULTAN test facility for large-scale vessel coolability in natural convection at low pressure". *Nuc. Eng. Des.* 169: 185-195.

Sneerova, P.I. A.P. Svars, E.L. Miropolski, *Thermal Engineering*, 1961, v.4 (reference [25] in Lin, 1992)..

Wallis, G.B. 1969. *One-Dimensional Two-Phase Flow*: McGraw-Hill, 51-54.

DYNA3D Finite Element Analysis of Steam Explosion Loads on a Pedestal Wall Design

Charles R. Noble

January 22, 2007

This work was performed under the auspices of the U.S. Department of Energy by the University of California, Lawrence Livermore National Laboratory under contract No. W-7405-Eng-48.

1.0 Objective

The objective of this brief report is to document the ESBWR pedestal wall finite element analyses that were performed as a quick turnaround effort in July 2005 at Lawrence Livermore National Laboratory and describe the assumptions and failure criteria used for these analyses [Ref 4]. The analyses described within are for the pedestal wall design that included an internal steel liner. The goal of the finite element analyses was to assist in determining the load carrying capacity of the ESBWR pedestal wall subjected to an impulsive pressure generated by a steam explosion.

2.0 Model Description

The DYNA3D (ParaDyn) [Ref 2] finite element model used 1/8 symmetry and 523,887 solid hexahedral elements for the concrete and rebar materials, 13,200 shell elements for the liner, and 501,600 nodes. The finite element model is shown in Figure 1. A summary of the material properties assumed for each material at the time of the simulation is presented in Table 1. A kinematic isotropic elastic plastic material model was used for the steel liner and rebar materials and the Karagozian & Case nonlinear constitutive model was used for the concrete. Symmetry boundary conditions were applied to the sides of the finite element domain and the base of the pedestal wall was assumed to be completely fixed in all three global directions.

3.0 Material Model Descriptions and Damage Metrics

3.1 Material Models

The K&C concrete model was developed by Javier Malvar, Jim Wesevich, and John Crawford of Karagozian and Case, and Don Simon of Logicon RDA [Ref 3]. The concrete model uses three independent fixed surfaces to define the plastic behavior of concrete (see Figure 2). The three surfaces are defined by pressure on the horizontal axis and deviatoric

stress on the vertical axis. These three surfaces define three important regions of concrete behavior. It can be seen easily if one plots the stress-strain response for a uniaxial unconfined compression test (see Figure 2). The material response is considered linear up until point 1, or first yield. After yielding, a hardening plasticity response occurs until point 2, or maximum strength, is reached. After reaching a maximum strength, softening occurs until a residual strength, which is based on the amount of concrete confinement, is obtained.

For this analysis, complete concrete damage is defined as concrete which has reached the residual strength of the concrete material. The post-processor will use the color red to denote concrete which has reached point 3 (Figure 2). Furthermore, this concrete material model takes into account strain-rate enhancement. At high strain rates, the apparent strength of concrete and the corresponding strain at peak stress both increase. It has been shown by experimental tests that there are different rate enhancements for tensile and compressive loading. The strain rate enhancement factors used are those determined by the Air Force and are shown in Figure 3. For a more detailed discussion on this concrete damage model, please refer to the attached appendix. Extensive verification and validation of this material model has also been performed by Karagozian & Case [Ref 1].

A kinematic isotropic/elastic-plastic material model was used for the steel liner and rebar materials. Material failure for this model is determined in the post-processing step of the analysis and is not modeled within the constitutive model itself. During the post-processing step, material failure may be determined by thresholding the steel effective plastic strain at various values, with a value of 0.2 or 20% being the typical value assumed.

model includes 10 m high by 45 degrees by 2.4 m thick section of reinforced concrete

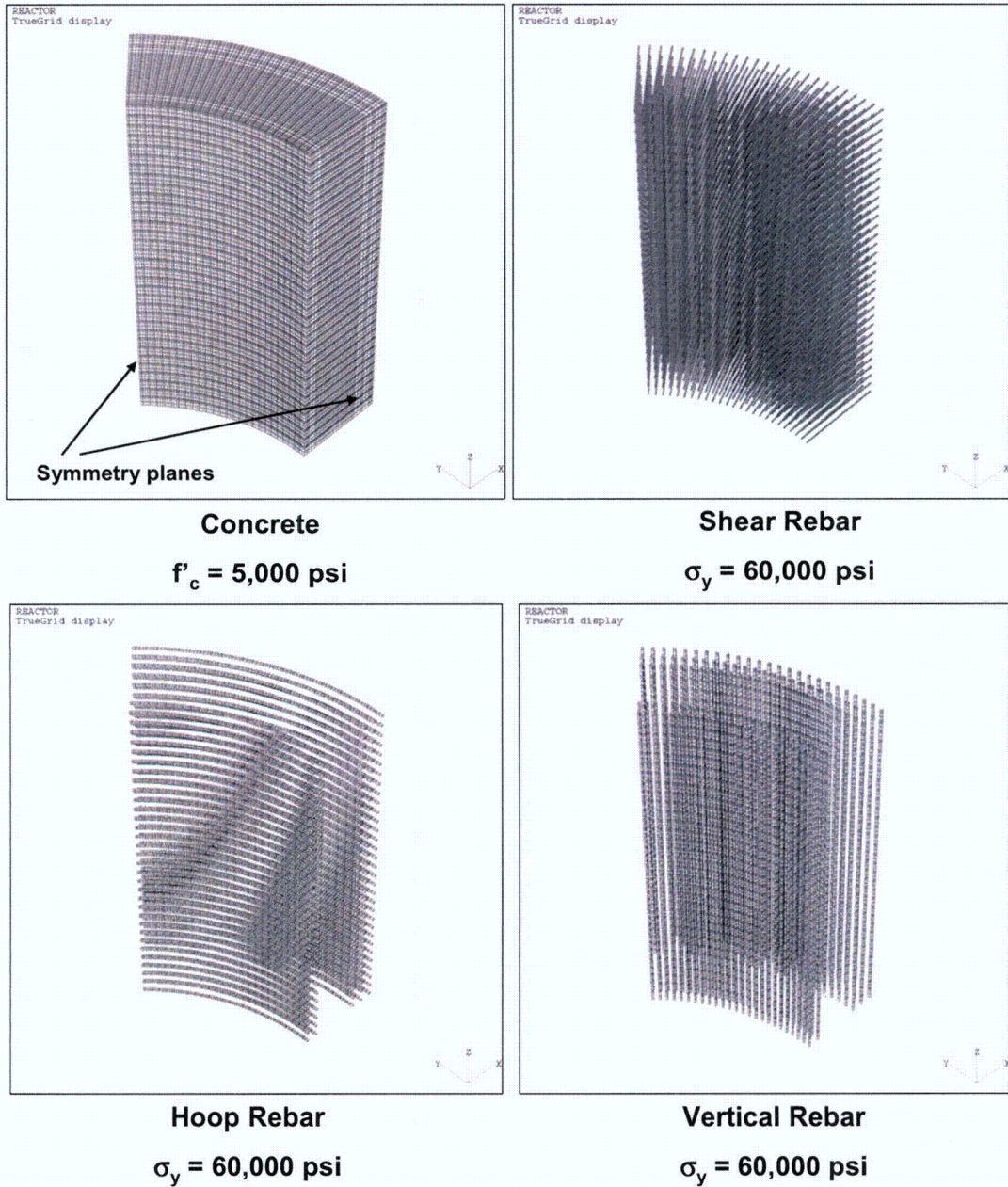


FIGURE 1. DYNA3D finite element model.

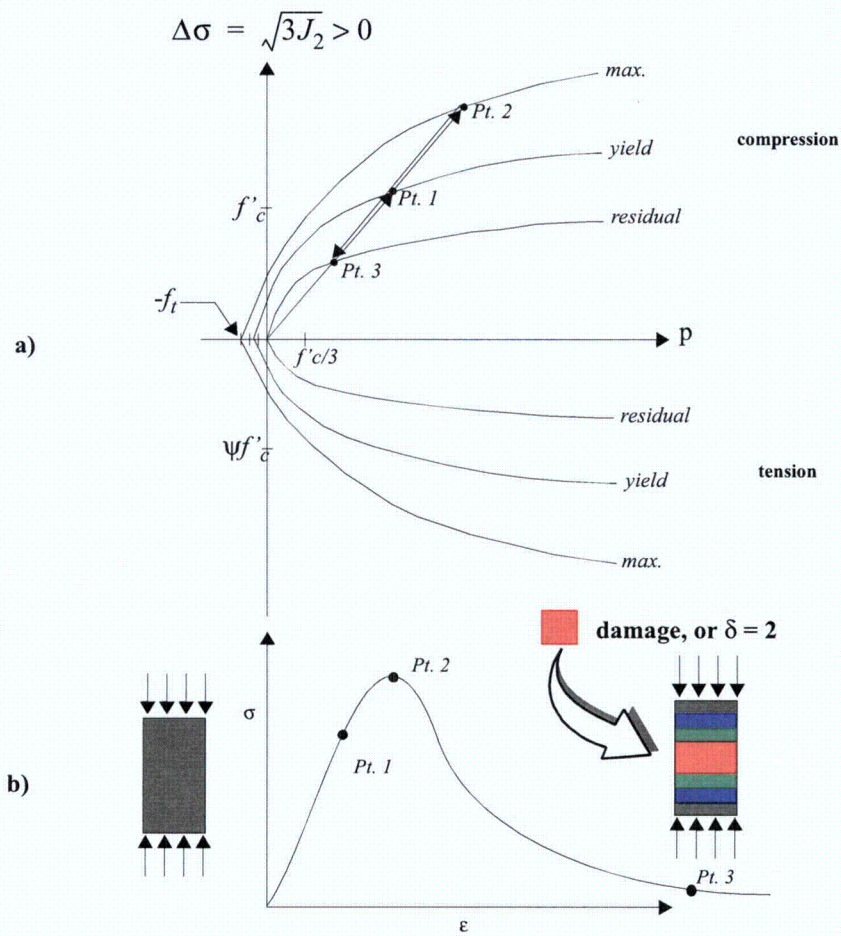


FIGURE 2. a). Three independent fixed failure surfaces for DTRA concrete material model; b). Uniaxial representation of concrete stress-strain curve.

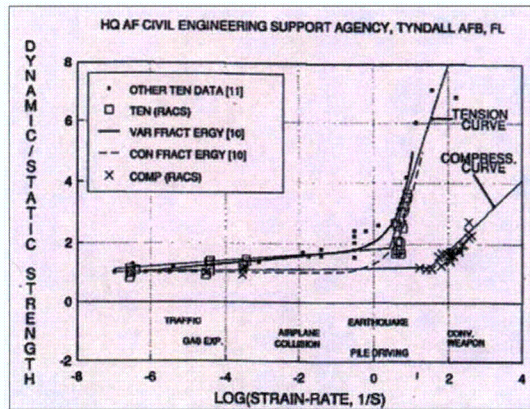


FIGURE 3. Strain rate effects on tensile and compressive strengths determined by Air Force.

TABLE 1. Assumed Finite Element Material Properties

Material Property	Value	Units
Concrete compressive strength	5000	psi
Concrete tensile strength	500	psi
Rebar modulus of elasticity	29e+06	psi
Rebar Poisson's ratio	0.29	
Rebar yield strength	60000	psi
Rebar tangent modulus	110800	psi
Steel liner modulus of elasticity	27.2e+06	psi
Steel liner Poisson's ratio	0.3	
Steel liner yield strength	33140	psi
Steel liner tangent modulus	556000	psi

3.2 Failure Criteria for Pedestal Wall

Multiple criteria was used to determine failure of the pedestal wall. The first criteria was the concrete damage parameter within the Karagozian & Case material model. The damage parameter shows, in a simplified sense, at what location on the stress-strain curve the concrete is at. For example, undamaged concrete or concrete that has not reached first yield, is shown in a blue color. Material that has reached maximum yield is shown in a green color, and material that has reached its residual strength is shown in a red color. Unfortunately, a concrete damage parameter, by itself, is not necessarily a good indicator of structural integrity after an extreme loading event. In other words, a concrete damage criterion, either using an internally calculated "damage parameter" or a shear criterion, does not give the structural analyst an indication of the remaining strength in the other structural members, such as the rebar or the steel liner. Effective plastic strain was the variable used to evaluate the damage to the steel. In the original simulations, it was

assumed that the rebar would fail if the effective plastic strain was 20% or higher. The failure strains for the steel liner was assumed to be a higher value of 30%, due to the ductility that was assumed for this material at the time of the calculation. Total failure of the pedestal wall is assumed to occur if the concrete is fully damaged and the rebar has reached 20% effective plastic strain throughout the entire wall section.

4.0 Simulations

This brief report will discuss only the three simulations that included an internal steel liner. The only difference between the three simulations was the impulse applied to the structure. The pressure time histories used for the three different cases are shown in Figure 4. The three different pressure time histories have three different impulses: approximately 200 KPa-sec, 300 KPa-sec, and 600 KPa-sec. A brief damage summary is presented for all three cases in Table 2.

5.0 200 KPa-sec Case

Figures 5 through 8 show the concrete damage, steel liner effective plastic strain, and rebar effective plastic strain pseudocolor plots for the 200 KPa-sec impulse case at a simulation time of 0.039 seconds. The concrete is significantly damaged at the bottom portion of the pedestal wall. The concrete that is shown in red is at its residual strength and is considered completely damaged, which for this constitutive relationship means that the concrete has some strength based on the amount of confining pressure the concrete is experiencing. If the concrete is not confined and is fully damaged, the concrete has virtually no strength. Therefore, material that is not confined by rebar, such as the cover concrete on the backside of the pedestal wall, is most likely going to spall off of the structure. The steel liner has a peak effective plastic strain value of 9.81% at the base of the structure where the finite element model is fixed. This value is therefore the maximum value shown in the pseudocolor plot legend shown in Figure 6. The maximum rebar effective plastic strain is shown to be 12.89%, which also occurs at the base of the pedestal wall. None of the rebar strains come close to the assumed failure criterion of 20%. The outer hoop rebar strains are shown to have values near 4%, based on the pseudocolor plot shown in Figure 8.

6.0 300 KPa-sec Case

Figures 9 through 12 show the concrete damage, steel liner effective plastic strain, and rebar effective plastic strain pseudocolor plots for the 300 KPa-sec impulse case at a simulation time of 0.038 seconds. The calculation predicts the concrete to be fully damaged at the base of the pedestal wall. To evaluate whether the pedestal wall has been fully ruptured, the rebar strains must be analyzed similar to the 200 KPa-sec case. If the rebar strains are not predicted to be near rebar rupture strain levels, the majority of the damaged concrete may be confined within the rebar cage and total failure of the pedestal wall may not be predicted. A significant amount of the axial rebar at the base of the pedestal wall

has reached the assumed failure strain of 20%. From the pseudocolor plots, however, it appears that the outermost axial rebar has not reached 20% effective plastic strain levels and the outermost hoop rebar is experiencing strain levels near 7%. This can all be seen by closely examining Figure 12. It is therefore predicted that although the concrete is fully damaged throughout the entire bottom section of the wall, the rebar may have some residual strength to provide concrete confinement and prevent total failure of the wall. This simulation predicts peak steel liner strains near 20-24% at the base of the pedestal wall.

7.0 600 KPa-sec Case

Figures 13 through 16 show the concrete damage, steel liner effective plastic strain, and rebar effective plastic strain pseudocolor plots for the 600 KPa-sec impulse case at a simulation time of 0.024 seconds. Again, the concrete is predicted to have extensive damage throughout the base of the pedestal wall. The steel liner effective plastic strains have reached a level of 30% or higher at the base of the pedestal wall and is predicted to rupture. The strain levels have reached 20% or higher for all of the axial rebar at the base of the pedestal wall and is not expected to carry any further load. Significant strains reaching levels near 20% are also predicted for the outermost hoop rebar (shown in Figure 16) and is also not expected to carry any further load. Definite wall failure is predicted for this impulse level.

TABLE 2. Damage summary.

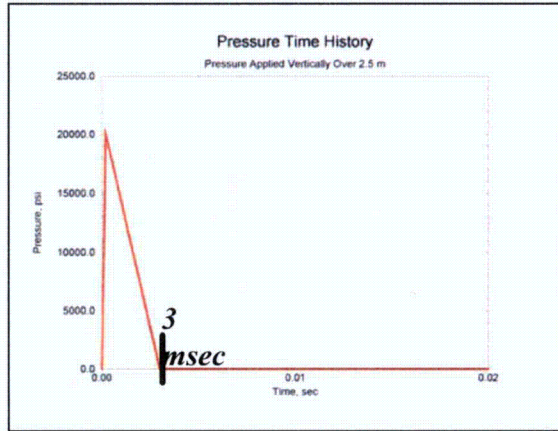
Impulse Level KPa-sec	Concrete Damage at Base	Axial Rebar Strains at Base (EPS) ^a	Hoop Rebar Strains at Base (EPS)	Liner Strains at Base (EPS)
200	Fully Damaged	12.89%	4%	9.81%
300	Fully Damaged	Outermost rebar has not reached 20% strain levels	7%	20-24%
600	Fully Damaged	20% or higher	20% or higher	30% or higher

a. Effective Plastic Strain

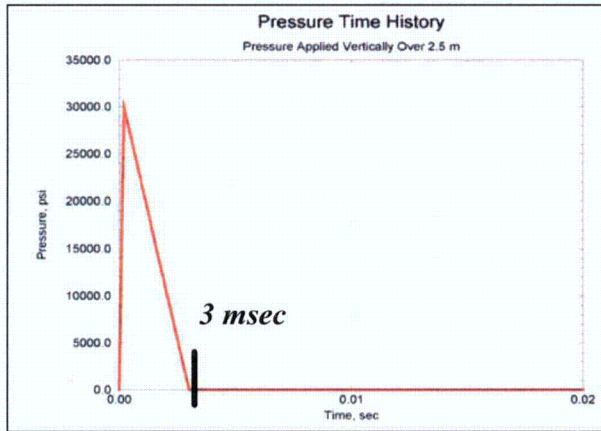
8.0 References

1. Crawford, J.E., L.J. Malvar, Shi, Y. Verification and Validation for DYNA3D Models of RC Components Subjected to Cased and Uncased Munitions. Karagozian & Case, TR-99-10.3, October 26, 2004.
2. Lin, J., DYNA3D: A Nonlinear, Explicit, Three-Dimensional Finite Element Code for Solid and Structural Mechanics User's Manual, UCRL-MA-107254, January 2005.
3. Malvar, L.J., Crawford, J.E., Wesevich, J.W., Simons, D. A Plasticity Concrete Material Model for DYNA3D. Int. J. Impact Engng, Vol. 19, Nos. 9-10, pp. 847-873, 1997.

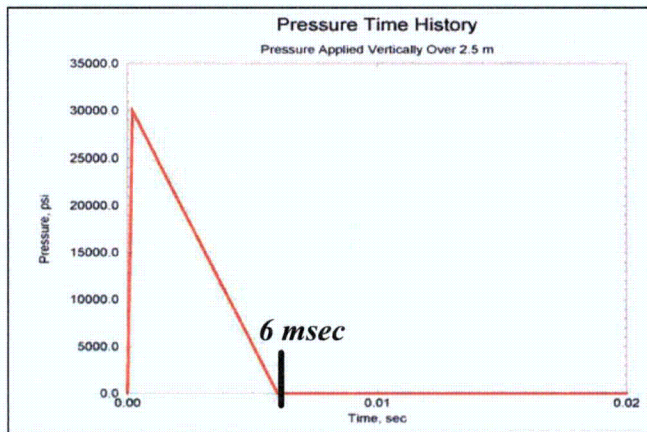
4. Noble, C.R. Finite Element Analysis of Nuclear Reactor Components. Lawrence Livermore National Laboratory, UCRL-PRES-214986, August 1, 2005.



200 KPa-s



300 KPa-s



600 KPa-s

FIGURE 4. Pressure time histories applied to structure.

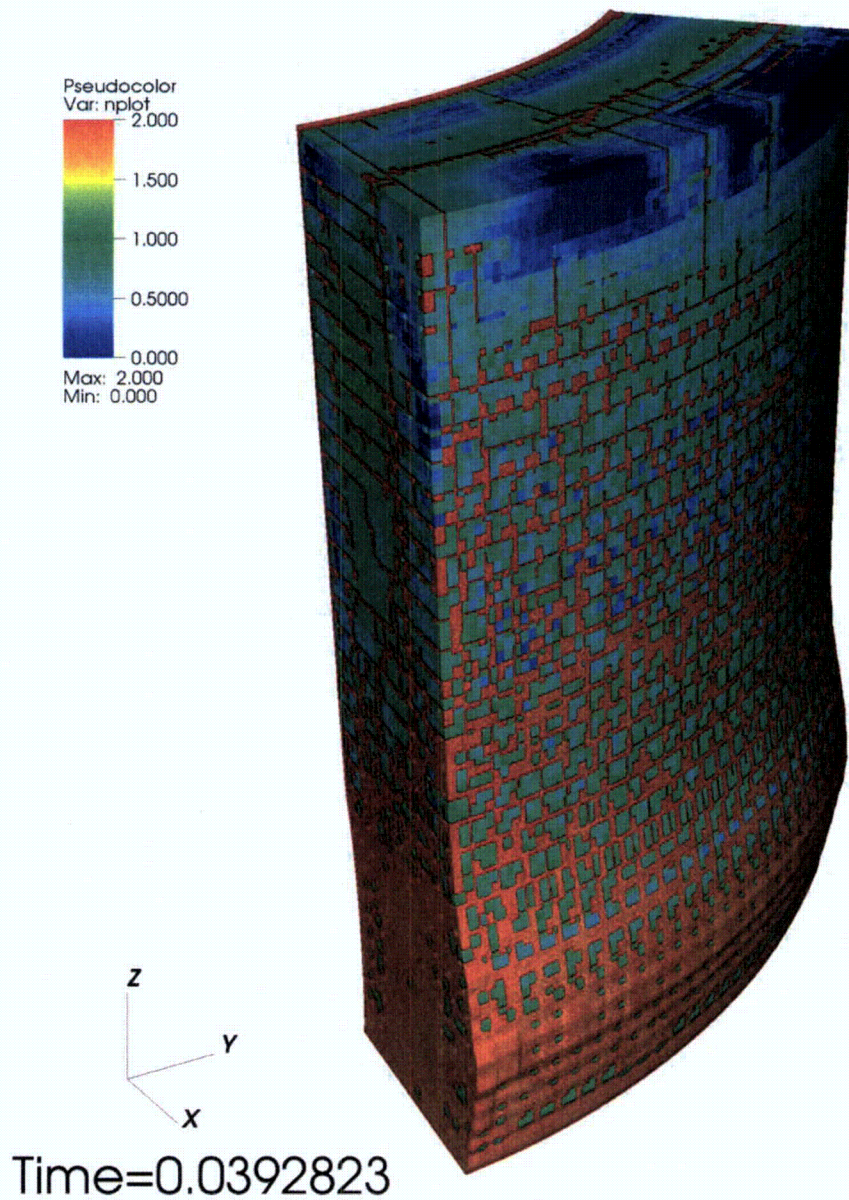


FIGURE 5. Concrete damage pseudocolor plot for 200 KPa-sec case.

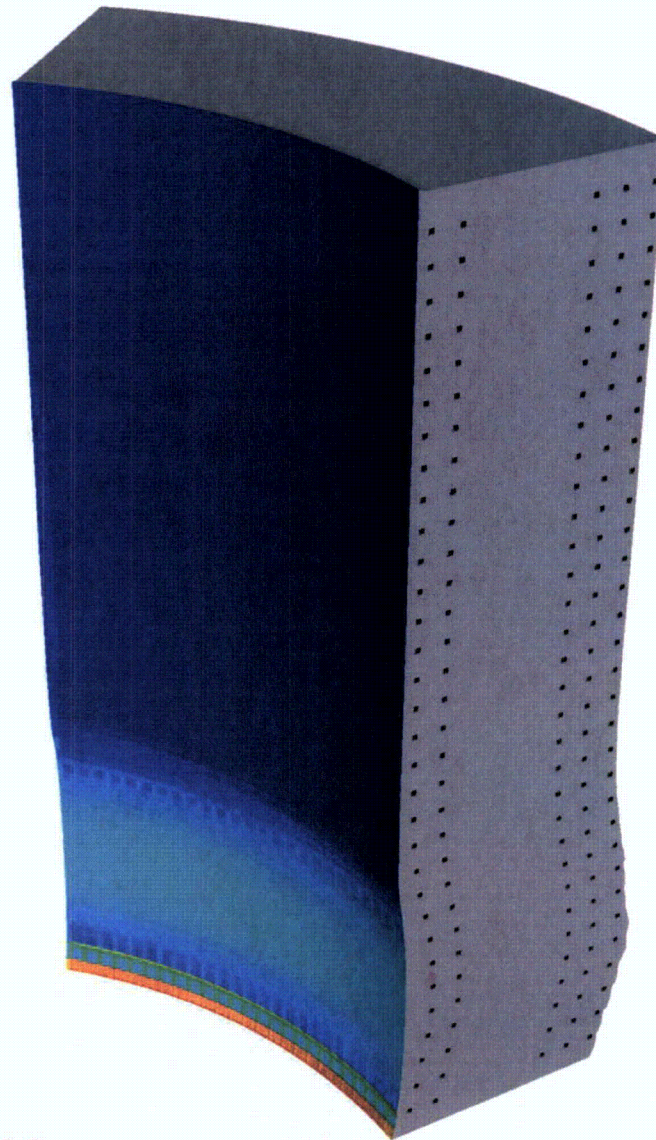
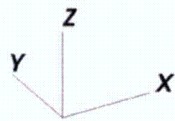
Filled Boundary
Var: materials1

- mat1
- mat2
- mat4

Pseudocolor
Var: eeff_mid

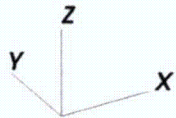
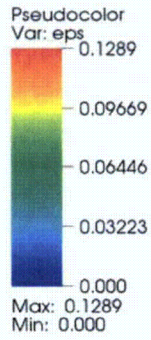
0.09806
0.07355
0.04903
0.02452
0.000

Max: 0.09806
Min: 0.000



Time=0.0392823

FIGURE 6. Steel liner effective plastic strain pseudocolor plot (taken at the mid-point of the shell element) for the 200 KPa-sec case.



Time=0.0392823

FIGURE 7. Rebar effective plastic strain pseudocolor plot for 200 KPa-sec case.

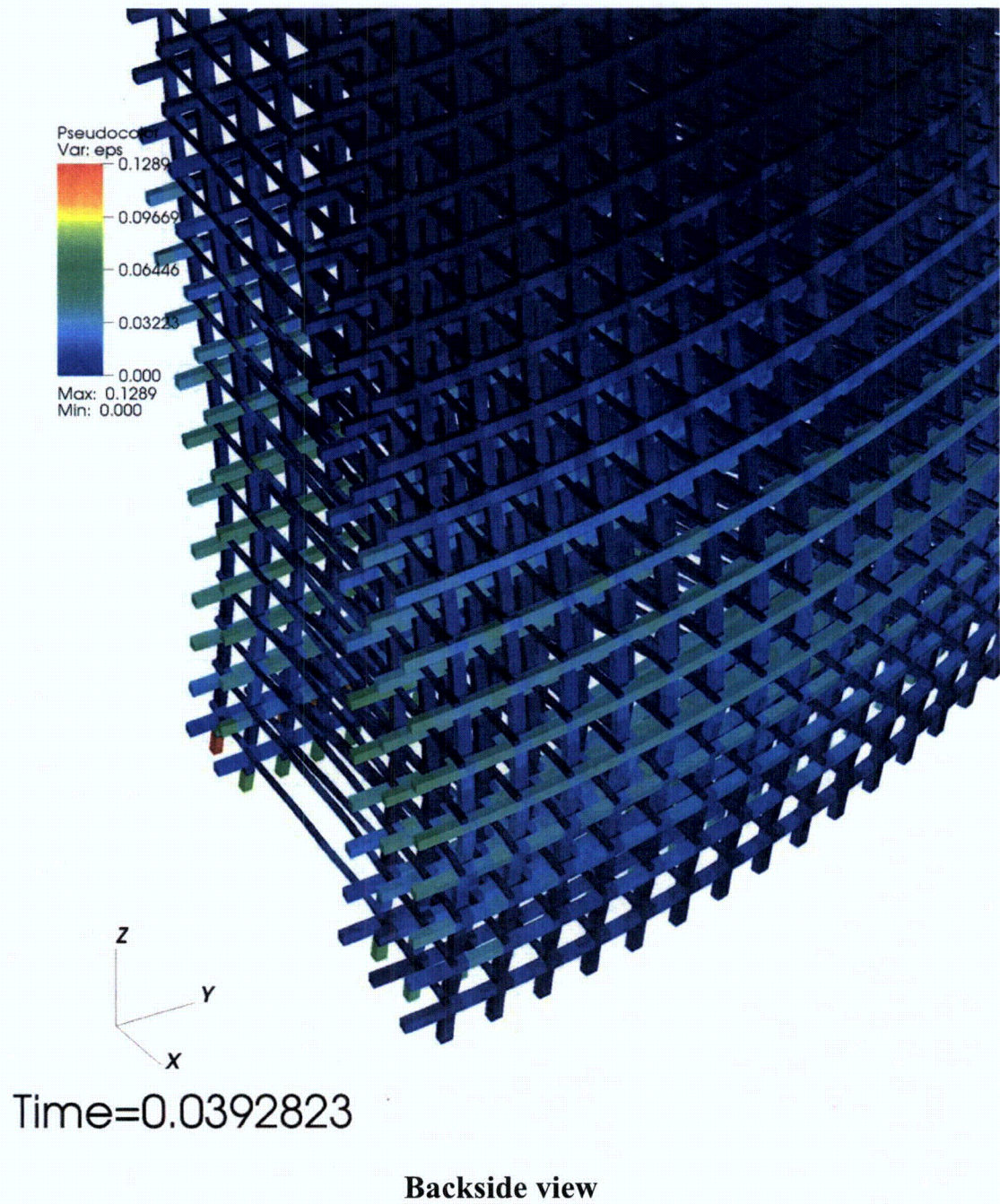


FIGURE 8. Blown up view of rebar effective plastic strain at base of model for 200 KPa-sec case.

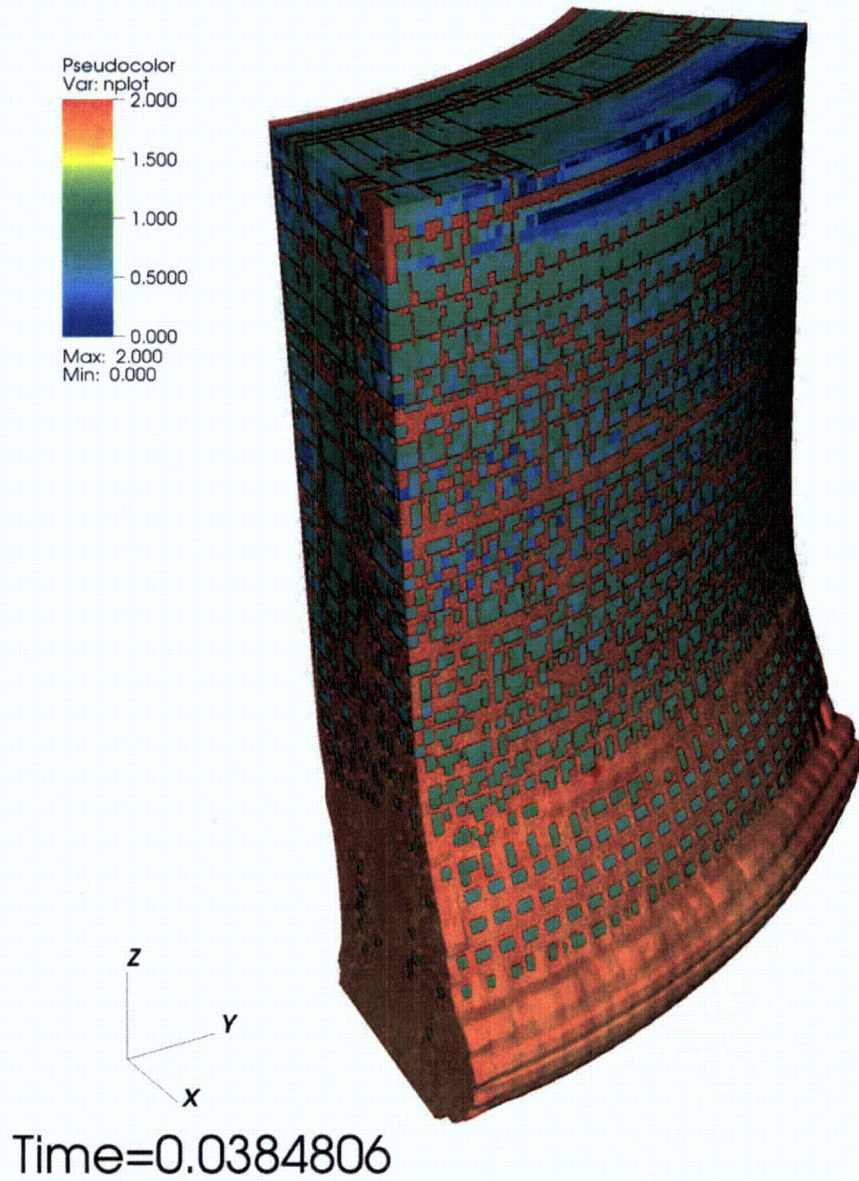


FIGURE 9. Concrete damage pseudocolor plot for 300 KPa-sec case.

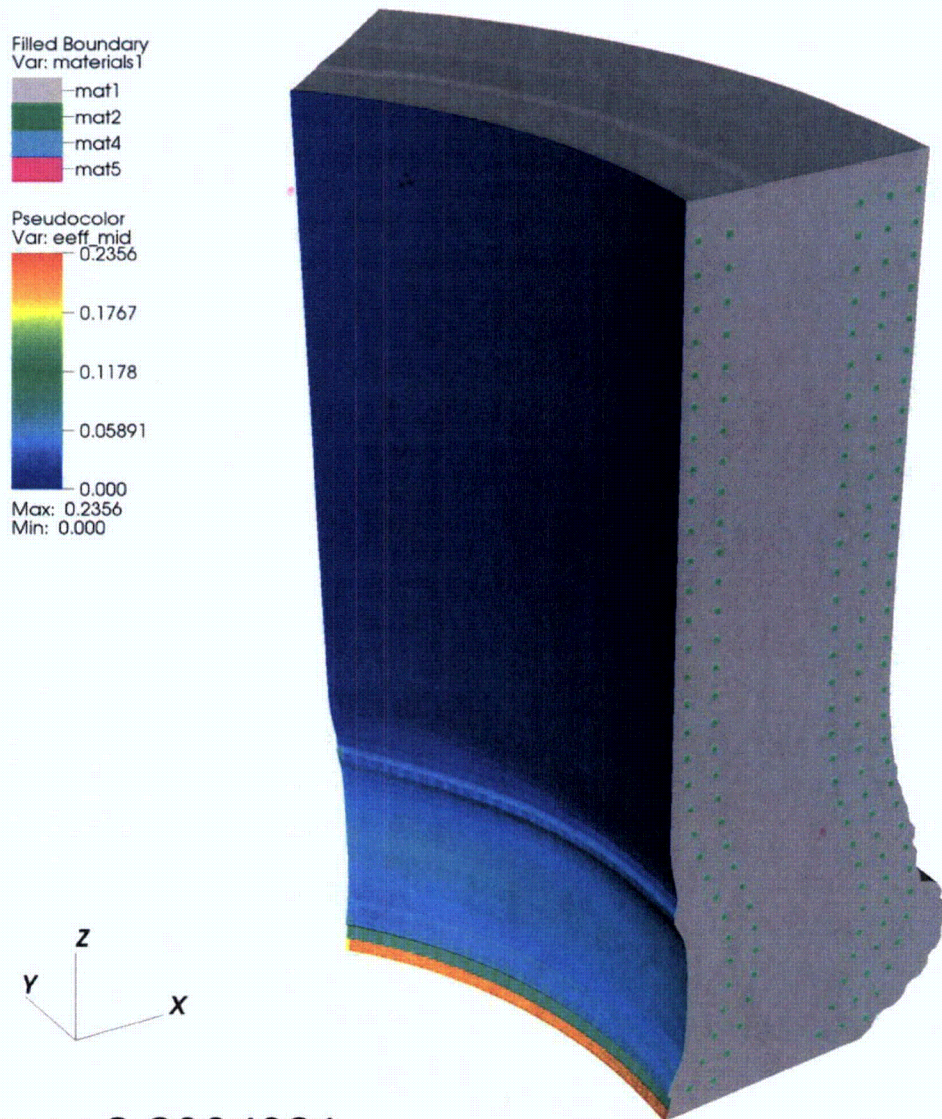
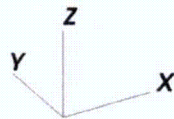
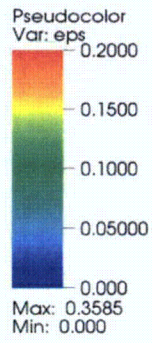


FIGURE 10. Steel liner effective plastic strain pseudocolor plot (taken at the mid-point of the shell element) for the 300 KPa-sec case.



Time=0.0384806

FIGURE 11. Rebar effective plastic strain pseudocolor plot for 300 KPa-sec case.

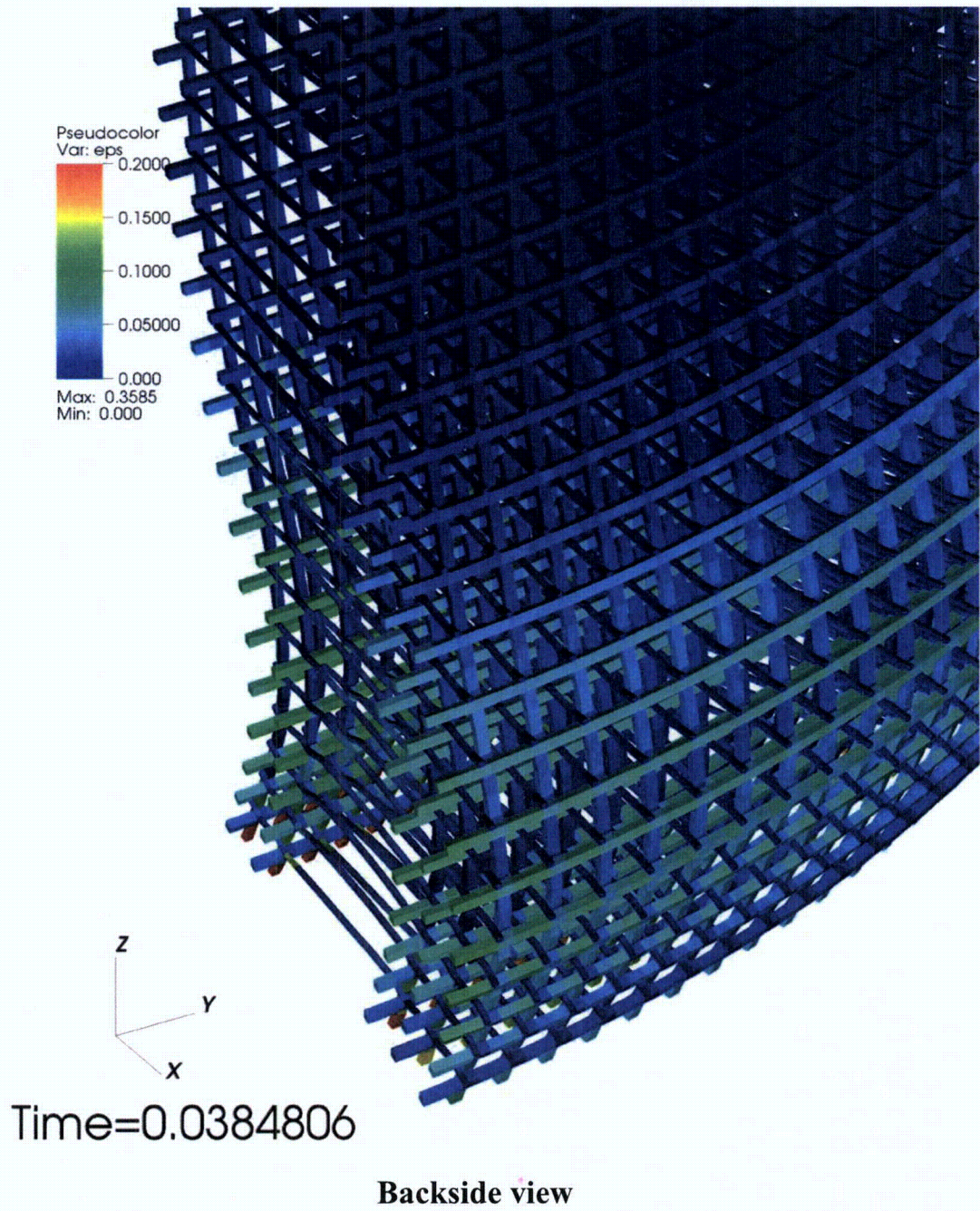


FIGURE 12. Blown up view of rebar effective plastic strain at base of model for 300 KPa-sec case.

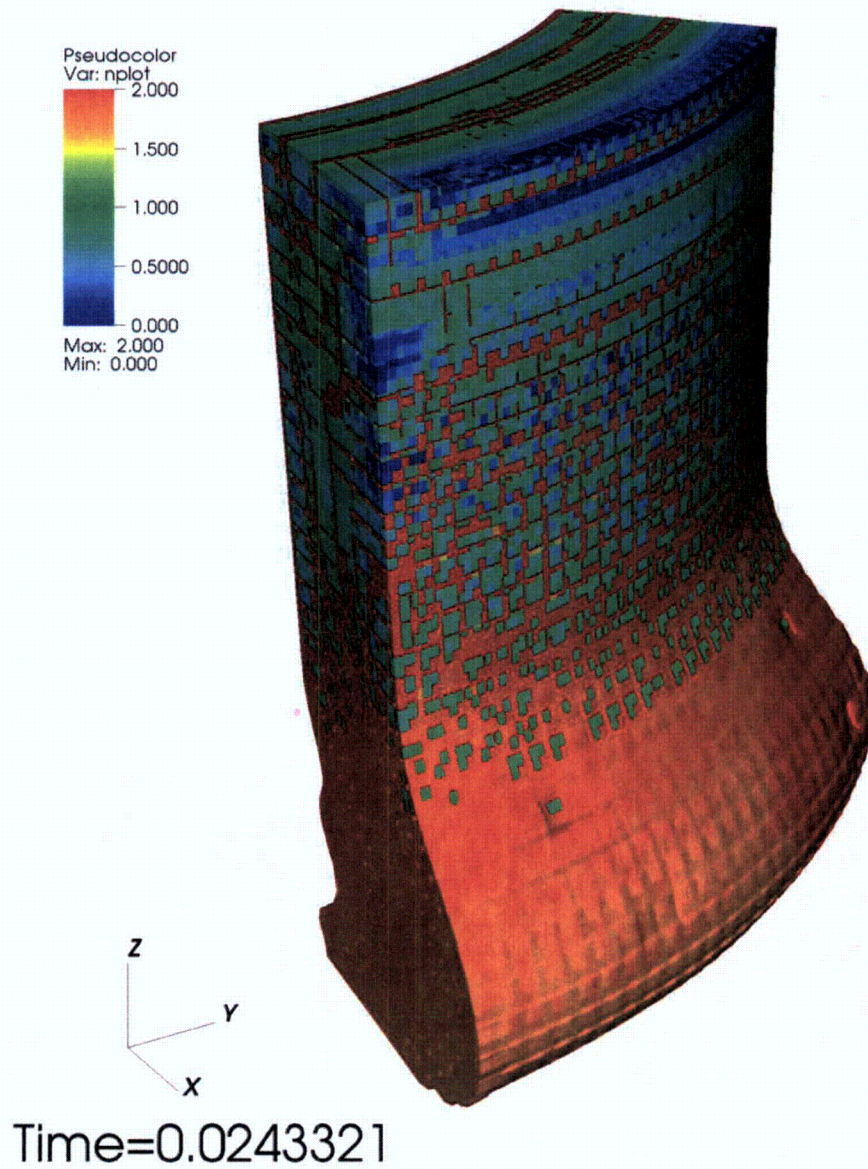
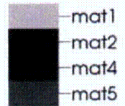
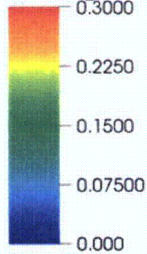


FIGURE 13. Concrete damage pseudocolor plot for 600 KPa-sec case.

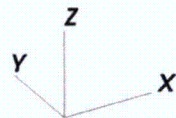
Filled Boundary
Var: materials1



Pseudocolor
Var: eeff_mid

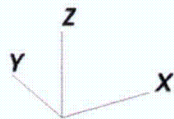
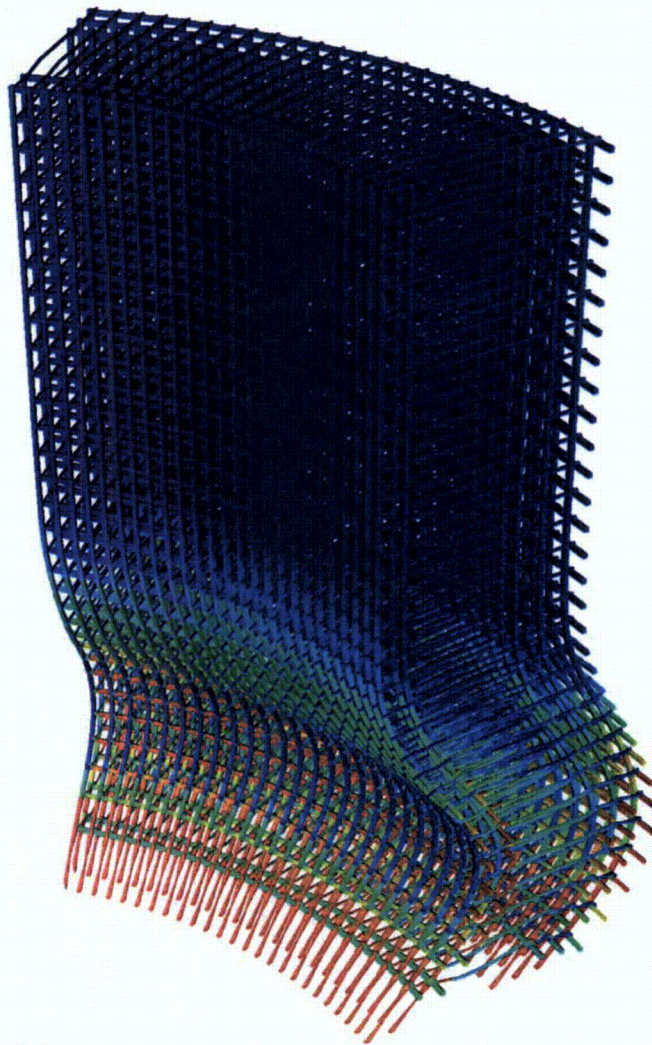
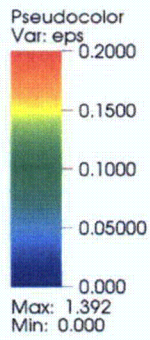


Max: 0.8211
Min: 0.000



Time=0.0243321

FIGURE 14. Steel liner effective plastic strain pseudocolor plot (taken at the mid-point of the shell element) for the 600 KPa-sec case.



Time=0.0243321

FIGURE 15. Rebar effective plastic strain pseudocolor plot for 600 KPa-sec case.

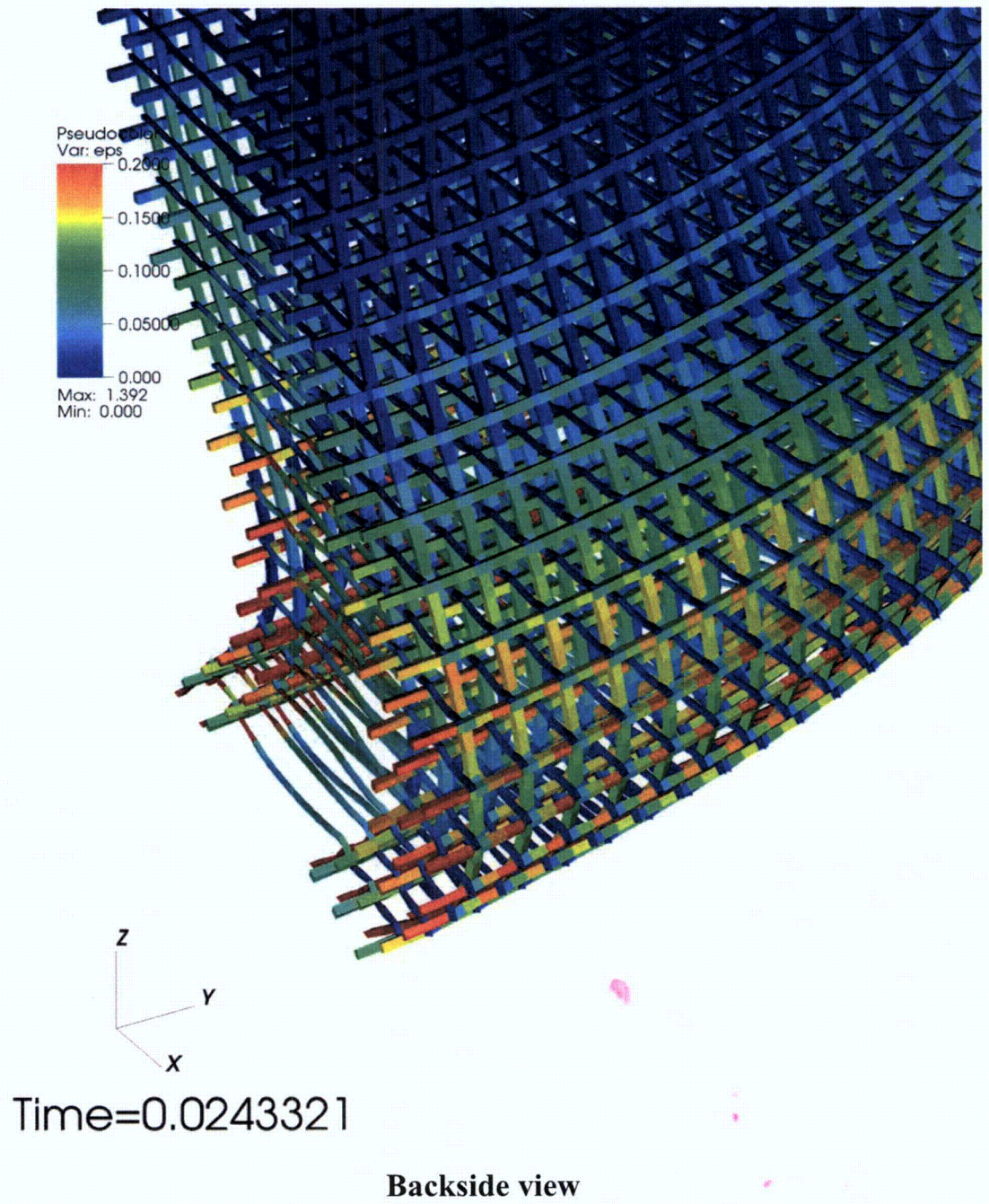


FIGURE 16. Blown up view of rebar effective plastic strain at base of model for 600 KPa-sec case.